Stability Control of Electric Vehicles with In-wheel Motors

by

Kiumars Jalali

A thesis
presented to the University of Waterloo
in fulfillment of the
thesis requirement for the degree of
Doctor of Philosophy
in
Mechanical Engineering

Waterloo, Ontario, Canada, 2010

I hereby declare that I am the sole author of this thesis. This is a true copy of the thesis, including any required final revisions, as accepted by my examiners.

I understand that my thesis may be made electronically available to the public.

Kiumars Jalali

Abstract

Recently, mostly due to global warming concerns and high oil prices, electric vehicles have attracted a great deal of interest as an elegant solution to environmental and energy problems. In addition to the fact that electric vehicles have no tailpipe emissions and are more efficient than internal combustion engine vehicles, they represent more versatile platforms on which to apply advanced motion control techniques, since motor torque and speed can be generated and controlled quickly and precisely.

The chassis control systems developed today are distinguished by the way the individual subsystems work in order to provide vehicle stability and control. However, the optimum driving dynamics can only be achieved when the tire forces on all wheels and in all three directions can be influenced and controlled precisely. This level of control requires that the vehicle is equipped with various chassis control systems that are integrated and networked together. Drive-by-wire electric vehicles with in-wheel motors provide the ideal platform for developing the required control system in such a situation.

The focus of this thesis is to develop effective control strategies to improve driving dynamics and safety based on the philosophy of individually monitoring and controlling the tire forces on each wheel. A two-passenger electric all-wheel-drive urban vehicle (AUTO21EV) with four direct-drive in-wheel motors and an active steering system is designed and developed in this work. Based on this platform, an advanced fuzzy slip control system, a genetic fuzzy yaw moment controller, an advanced torque vectoring controller, and a genetic fuzzy active steering controller are developed, and the performance and effectiveness of each is evaluated using some standard test maneuvers. Finally, these control systems are integrated with each other by taking advantage of the strengths of each chassis control system and by distributing the required control effort between the in-wheel motors and the active steering system. The performance and effectiveness of the integrated control approach is evaluated and compared to the individual stability control systems, again based on some predefined standard test maneuvers.

Acknowledgements

This research has been carried out in the Motion Research Group at the University of Waterloo, in Canada. I am pleased to acknowledge the financial support that I received from AUTO21, a Canadian Network of Centres of Excellence, and the Natural Sciences and Engineering Research Council of Canada (NSERC). The financial support from these organizations allowed me to focus on my research and carry it out to completion.

There are a number of people to whom I would like to express my gratitude. First of all, I owe a great deal of gratitude to my supervisors, Prof. Steve Lambert and Prof. John McPhee, for giving me great freedom in selecting my research topics and who, through a combination of patience and persistence, have enabled me to grow more than I knew possible during the course of my Ph.D. This work is a result of their unlimited support and encouragement, and the faith they put in me. It was a long journey that I'm happy to have experienced.

Special thanks go to the present (Tom Uchida, Matthew Millard, Sukhpreet Sandhu, Ramin Masoudi, Willem Petersen, Joydeep Banerjee, Mohammad Sharif Shourijeh, Mohammadreza Saeedi, and Mike Boos) and past (Kevin Morency, Mathieu Léger, Mike Wybenga, Adel Izadbakhsh, William Bombardier, Akram Abdel-Rahman, Dr. Nasser Azad, Dr. Yi Liu, and Dr. Chad Schmitke) lab mates at the Motion Research Group. I have had a great time working with you guys and hope that we keep in touch in the future.

Tom Uchida, I had a great time working with you and, without your enthusiasm, patience, and constant support, this thesis would be neither half as good nor half as finished by now. I hope I will be able to repay you soon.

Chad Schmitke, it was my honor to work with you on a variety of projects, and I thank you for your support throughout my thesis.

Kevin Morency, thank you for the great support you provided me during your stay in Waterloo. It was a great time having you as my lab mate and roommate at the same time.

Last but not least, I would like to thank my parents, Robabeh Djalali and Amir Hossein Jalali, for the unlimited love and support you provided me throughout my life. I am who I am just because of you. Without your unconditional support, care, and belief in

me, I would not have made it this far in life. You have been there for me every step of the way and have aided me through all of my decisions.

Thank You!

Waterloo, April 2010
Kiumars Jalali

Dedication

This thesis is dedicated to my father, who has raised me to be the person I am today. You have been with me every step of the way, through good times and bad. Thank you for all the unconditional love, guidance, and support that you have always given me, helping me to succeed and instilling in me the confidence that I am capable of doing anything I put my mind to.

Thank you for everything. I love you!

Table of Contents

List of Figures

List of Tables

1 Introduction and Background

During the last two decades, advances in electronics have revolutionized many aspects of automobiles, especially in the areas of engine management and vehicle dynamics safety systems such as the anti-lock braking system (ABS), traction control system (TCS), and electronic stability control (ESC) system. In these cases, the signals generated by the brake or accelerator pedal are modulated by an electronic control unit in order to control the tire slip of individual wheels in emergency braking (ABS) or emergency acceleration (TCS) situations, or to control the vehicle yaw rate through individual wheel braking (ESC). It is important to note that the U.S. National Highway Traffic Safety Administration (NHTSA) has passed a new Federal legislation that makes installation of ESC mandatory on all passenger cars, multipurpose passenger vehicles, trucks, and buses by 2012 [FMV07]. The move to improve the safety, comfort, and performance of vehicles has led to an increase in the use of electronic control systems and the introduction of drive-by-wire systems. Today, the value added to the modern vehicle by electronic systems is approximately 20 percent. In luxury vehicles, for example, more than 90 control systems are used to control a variety of actuators. It is expected that this rate will consistently increase, reaching over 40 percent by the year 2015 [ATZ06].

Integrating various electronic control systems offers the potential to optimize driving behaviour independently of the driving maneuver through the individual control and allocation of traction, steering, and braking forces. These unique features open new horizons for controlling the driving dynamics of a vehicle in a way that has never been possible. For example, integrating the active braking and active steering systems can avoid the vehicle side-pushing behaviour when braking on a μ-split road [Koe06]. In addition, by integrating different chassis control systems, individual sensor signals can be used by the entire system, thereby avoiding sensor redundancy and reducing costs.

Recently, electric vehicles (EVs) have attracted a great deal of interest as an elegant solution to environmental and energy problems. Thanks to great improvements in electric motor and battery technologies, EVs have achieved sufficient driving performance and efficiency in comparison to conventional internal combustion engine (ICE) vehicles. EVs have no tailpipe emissions because they have no fuel, combustion, or exhaust systems. In fact, EVs are virtually maintenance-free because they never need oil

changes, air filters, tune-ups, mufflers, timing belts, or emission tests. Critics proclaim that EVs are simply "elsewhere emission vehicles" because they transfer emissions from the tailpipe to the smokestack. Although there are emissions associated with coal- and oil-fired power plants, the smokestack emissions associated with charging EVs are very low [Bra94]. However, in the ideal scenario, EVs would be charged from renewable energy sources such as hydro, solar, and wind power, or even zero-emission nuclear power.

Even EVs recharging from fossil-fuel power plants, such as those powered by coal and oil, have unique efficiency advantages over ICE vehicles. As a system, EVs and power plants are twice as efficient as ICE vehicles and the system that refines gasoline (Table 1-I). At current U.S. energy prices, with the cost of gasoline at 3 dollars per gallon and the national average cost of electricity at 8.5 cents per kilowatt per hour, a plug-in EV runs on an equivalent of 75 cents per gallon. According to an interesting study revealed in 2005, half the cars on U.S. roads are driven no more than 25 miles a day (Figure 1-1). Therefore, an EV with just a 20-mile-range battery could reduce the national fuel consumption by approximately 60 percent [Gri98]. In addition, EVs are the most exciting platforms on which to apply advanced motion control techniques, since the torque of an electric motor can be generated and controlled quickly and precisely in an efficient way. Note that the torque response of an electric motor is several milliseconds and, therefore, 10 to 100 times faster than that of the ICE, or even hydraulic braking systems [Hor04]. Furthermore, the installation of small but powerful direct-drive in-wheel motors into each wheel will produce a novel all-wheel-drive (AWD) system in which even bidirectional torques on the left and right wheels can be generated. This flexibility can be used to support the driver's steering wheel movements and reduce response times in tight cornering and lane-change maneuvers.

	EVs and Power Plants	ICE and Fuel Refining
Processing	39% (Electricity Generation)	92% (Fuel Refining)
Transmission Lines	95%	–
Charging	88%	–
Vehicle Efficiency	88%	15%
Overall Efficiency	29%	14%

Table 1-I: Operating efficiency of EVs and ICE vehicles [Gri98]

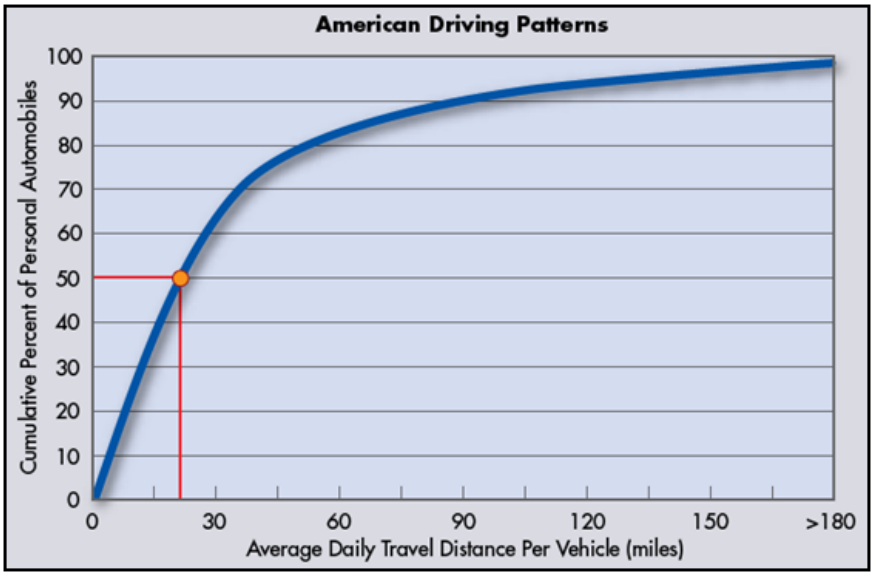

Figure 1-1: American driving patterns [San05]

This novel powertrain concept represents a very advanced torque vectoring system, enabling any desired torque distribution between all four wheels, and allowing the realization of many advanced stability control systems. Moreover, such a powertrain concept can support a very advanced AWD system, ensuring the optimal traction of each wheel by controlling the motor torque in all driving conditions. Further benefits of such an EV include a reduction of noise pollution and the minimization of the noise, vibration, and harshness (NVH) of the vehicle due to the elimination of the ICE and other powertrain components.

In summary, replacing the ICE and the entire conventional powertrain system with two or four electric motors and batteries will bring entirely new perspectives to the discipline of vehicle design. The batteries can be placed into the chassis as a modular package which, likewise, can be built as a modular unit. This concept will allow the designer to combine the modular chassis with different body frames to realize different vehicle types. The Hy-wire concept car developed by GM is an example of this type of chassis, where the vehicle structure is classified into two separate groups. The first group is designed with the vehicle bodywork and chassis together, and is called the rolling chassis. The second group is the driving chassis, which is a functional module that houses the electric motors, power source, steering, and suspension systems (Figure 1-2).

This research focuses on the development and verification of innovative vehicle stability control strategies for an electric all-wheel-drive drive-by-wire vehicle. The

vehicle is being designed as part of an AUTO21 research project to examine the use and development of collaborative design tools.

Figure 1-2: GM Hy-wire concept car with rolling and driving chassis [Elb04]

1.1 State-of-the-art drive-by-wire technologies

Since 1986, an increasing number of vehicle engines have been manipulated by an electronic pedal and an electrically-driven throttle or injection, which represent the first drive-by-wire components [Jur06]. Such systems are equipped with a fail-safe function whereby the throttle spring system automatically closes the throttle in the event of electronic failure. Other mechatronic units have been developed to allow an automatic transmission to control a hydraulic torque converter as well as gear shifting functions. The successful use of fly-by-wire technology in the aviation industry, positive experience with the throttle-by-wire and electronically-controlled transmissions in automobiles, and various electronic driver assistance systems for braking and power steering are the incentives for the future development of complete drive-by-wire systems without mechanical backup. Such a scheme is usually not fail-safe but, rather, has fault-tolerant properties [Ise02]. The lower reliability and different fault behaviour inherent in the electronic and electrical components used in drive-by-wire systems without mechanical backup have made the transition from systems with mechanical backup extremely challenging. Nevertheless, fault-tolerant electronic systems must be incorporated to meet the high safety requirements set by governments, especially in the developed countries. Figure 1-3 illustrates the hazard severity of failures for different electronic and electrical driving systems [Rie99]. As shown, the hazard severity increases considerably when drive-by-wire systems are used. Note that the brake and steering systems in a vehicle are safety-critical systems that must continue to operate in the event of a failure, without

endangering human life. However, the hazard severity of the steer-by-wire system is the highest among the drive-by-wire systems simply because, in contrast to the braking system, it consists of only a single unit, so a malfunction causes the driver to lose all steering control of the vehicle. In contrast, if a single braking actuator fails, three alternate units remain, providing the driver with 75 percent of the normal braking force. Moreover, new functions such as collision avoidance, autonomous driving, lane-keeping assistance, and advanced stability control systems require vehicles to be equipped with full by-wire systems, where all actuators can be controlled through electronic control units to enable the application of driver-independent signals to the system. Therefore, the hazard severity of such systems is equally elevated.

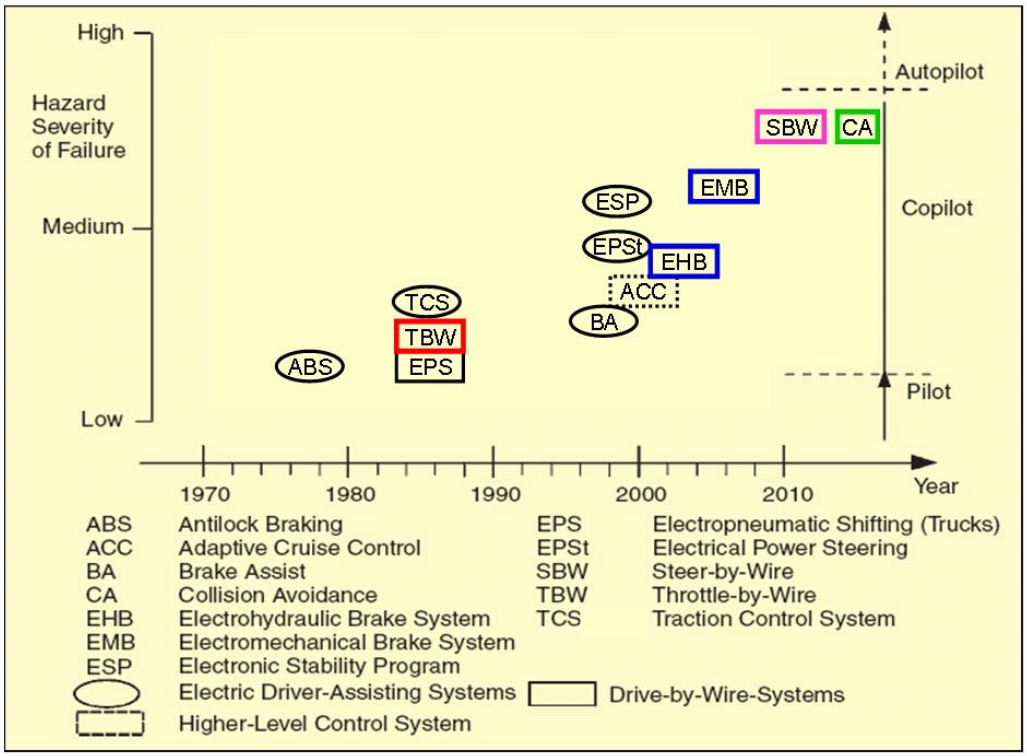

Figure 1-3: Hazard severity of failures in drive-by-wire and higher-level control systems [Rie99]

1.1.1 Brake-by-wire systems

With the exception of the electronic parking brake (EPB), brake-by-wire systems can be divided into two classes: electro-hydraulic brakes (EHB) and electro-mechanical brakes (EMB). Although EPB and EHB systems are already standard features for many car manufacturers, EMB systems are still in the development stage [Elb04].

In EHB systems, the input from the brake pedal is replaced with an electronically controlled actuator. This actuation is attainable using a hydraulic system, where control is

achieved by operating the pump and various control valves (Figure 1-4-a). The input from the driver would be provided by a position sensor, taking any form required (e.g., a traditional pedal or even a joystick) [Ham03]. The sensor converts the braking request of the driver into an electrical signal and sends it to an EHB unit at each wheel. The brake unit consists of an electric motor, a pump, and a hydraulic tank. In the event of a failure, a standard hydraulic brake system is activated as a fail-safe system, which provides the minimum braking power prescribed by legal braking regulations [Elb04]. In EMB systems, the hydraulic system is completely removed and the braking force is generated at each wheel by a high-power electric actuator. All electric motors are controlled through an electronic control unit (ECU), where the driver input would, again, come from a suitable sensor similar to those used in EHB systems. A feedback actuator at the brake pedal provides force feedback to the driver (Figure 1-4-b). Note that an EMB system fully decouples the driver from the braking system. The ECU plays a central role, converting the brake request of the driver into an electrical signal and adopting tasks such as ABS control. Since each wheel has its own electronic module that controls the respective brake independently of the others, the system can maintain 75 percent of its total potential even after an actuator fails whereas, in a typical dual-circuit hydraulic brake system, a failure will cause half of the brakes to become ineffective. For safety reasons, an EMB system has a backup power circuit and a backup ECU. Both types of brake-by-wire system have the following advantages over their conventional counterparts [Elb04]:

- easy incorporation with anti-lock braking and traction control systems,
- faster response and improved performance,
- disturbance-independent pedal force characteristics,
- improved package and NVH performance,
- improvement of ergonomics and crash behaviour,
- modular structure, and
- environmental friendliness and improved maintenance for the EMB due to the elimination of hydraulic fluid.

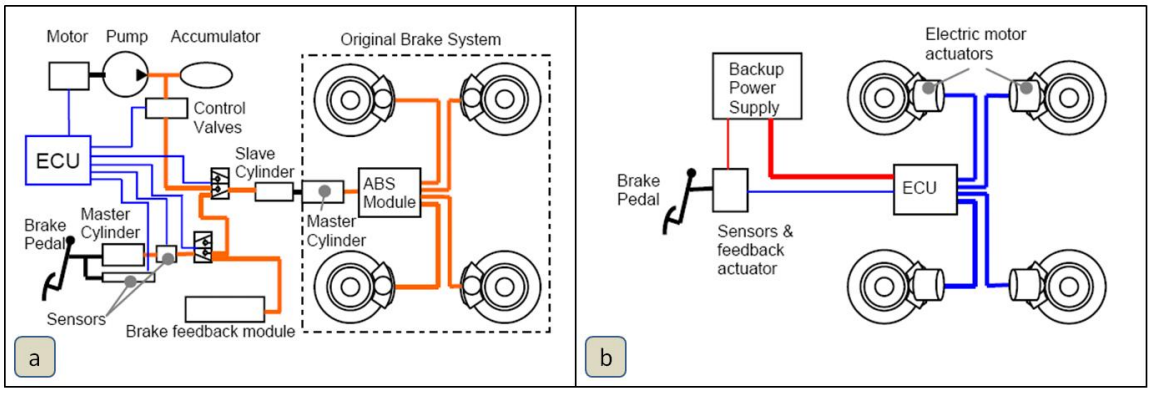

Figure 1-4: (a) Electro-hydraulic braking (EHB) and (b) electro-mechanical braking (EMB) concepts for brake-by-wire technology [Ham03]

Brake-by-wire technology can be used to realize anti-lock braking (ABS), traction control (TCS), and stability control (ESC) systems by controlling the longitudinal slip of the tires. Note that an ABS system only uses braking intervention to control the longitudinal dynamics of the vehicle, whereas TCS and ESC systems use both motor management and braking intervention to control, respectively, the longitudinal and lateral dynamics of the vehicle.

1.1.2 Steer-by-wire systems

Automotive steering systems have evolved from mechanical steering systems to hydraulic power steering assist systems and, recently, to electric power steering systems. Electro-hydraulic power steering is becoming more popular than hydraulic power steering since, due to the electronically-controlled operation of the power pack, energy consumption is reduced by 70 percent in comparison to conventional hydraulic steering systems. Electro-mechanical power steering systems have recently been introduced to the market, and have the benefit of eliminating all the hydraulic components and the environmentally unfriendly hydraulic fluid. Electro-mechanical power steering systems consume 85 percent less energy than conventional hydraulic systems, because the electrical systems only operate when steering, and are lighter and more compact than their hydraulic counterparts [Elb04].

The next step in steering evolution is the complete elimination of the mechanical linkage between the steering wheel and the rest of the steering system. Since torque feedback and the self-centering effect are important characteristics that a driver expects to experience when steering a vehicle, force feedback actuators must be installed at the steering wheel to generate an artificial steering torque based on the actual aligning

moment on the tires. Torque feedback is essential to the driver for estimating the driving conditions, and the self-centering effect should occur when the driver releases the steering wheel while exiting a turn. Electronics allow the amount of feedback steering torque to be set independently of the actual aligning moment, and can be tuned for different driving styles. Furthermore, the absence of the steering column greatly simplifies the interior design of the car, since the steering wheel can then be assembled modularly into the dashboard on either the left or right side. Removal of the steering column also frees up space in the engine compartment and improves the frontal crash behaviour of the vehicle. Additionally, the elimination of the steering column prevents the transmission of NVH from the road to the driver through the steering wheel [Yih05].

The steer-by-wire system has the ability to electronically augment the steering input of the driver and, thus, is capable of providing variable steering ratio and active steering functionalities during normal driving situations as well as emergency maneuvers. The following three architectures have been applied in concept cars to realize a steer-by-wire system [JB04]:

- electro-hydraulic actuation (Figure 1-5-a),
- purely hydraulic actuation (Figure 1-5-b), and
- electro-mechanical actuation (Figure 1-5-c).

One method of realizing a steer-by-wire system is to replace the input from the steering column to the steering rack with an electric motor attached to the rack and pinion, adding an additional force feedback actuator on the steering wheel, and retaining all other conventional steering system components (Figure 1-5-a). Although this solution provides a relatively easy method of converting a conventional vehicle into a steer-by-wire vehicle, it suffers from packaging and weight issues. The purely hydraulic method, shown in Figure 1-5-b, enables steering actuation by adding a series of hydraulic control valves to the power-assisted steering rack, thereby providing control over the rack position; however, this solution still suffers from packaging and weight issues due to the retention of the conventional power steering system. The most sensible way to achieve a steer-by-wire system is to completely remove the hydraulic system and replace it with a powerful direct-drive electric motor. The wheel actuation can be accomplished with one

motor controlling both wheels through a steering rack or with one motor controlling each wheel, the latter of which allows the independent control of each wheel (Figure 1-5-c).

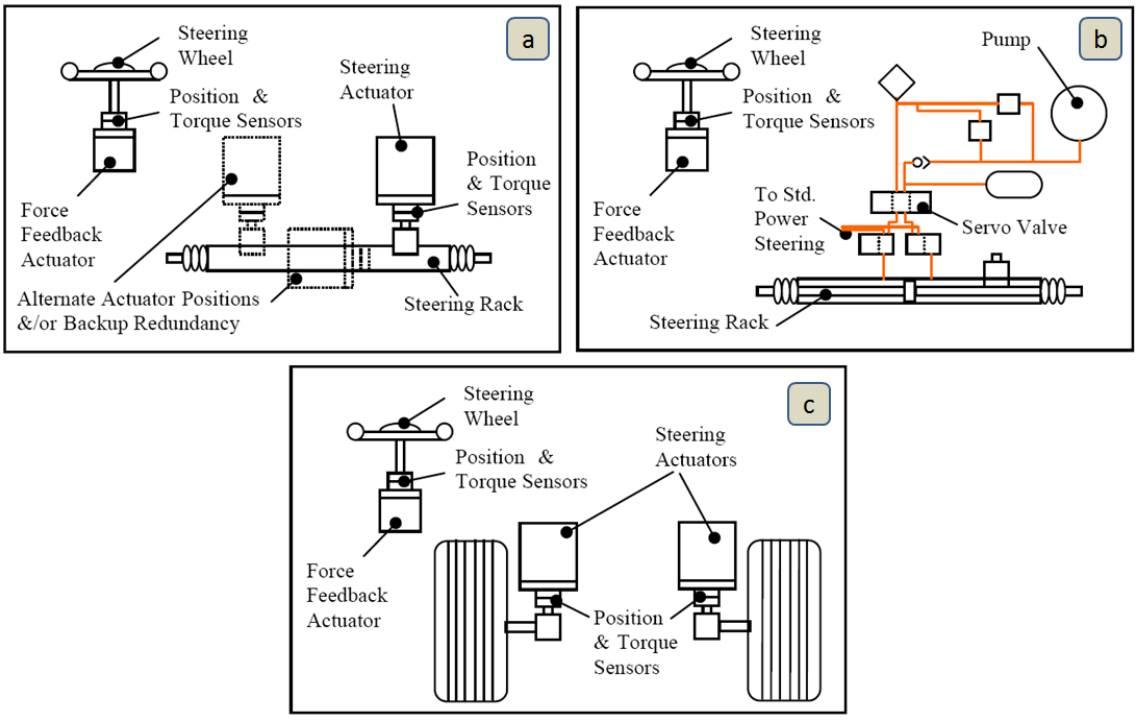

Figure 1-5: (a) Electro-hydraulic actuation, (b) pure hydraulic actuation, and (c) electro-mechanical actuation concepts for steer-by-wire technology [JB04]

1.2 Conventional slip control systems

In the last 30 years, advances in electronics have revolutionized many aspects of the automobile industry. Thanks to the advancements in automotive braking technologies, drivers now rely on electronic support to help them not only to decelerate and accelerate, but also to stabilize their vehicles while in motion. In this regard, slip control systems, such as anti-lock braking systems (ABS) and traction control systems (TCS), have received particular attention. These safety systems involve the use of electronic control units to modulate the brake and accelerator pedal inputs provided by the driver in order to control the slip of individual tires during emergency braking (ABS) or acceleration (TCS). The primary task of a slip control system is to influence the longitudinal dynamics of a vehicle by preventing the tires from locking up when braking and spinning out when accelerating, thereby enhancing the stability and steerability of the vehicle. A comprehensive overview of the history, operation, and types of slip control systems can be found in [Bow93, Bur93, Pen96, Mit82].

According to a study conducted by the Monash University Accident Research Centre, ABS has reduced the risk of multiple vehicle crashes by 18 percent and the risk of run-off-road crashes by 35 percent [Bur04]. Another study conducted by the National Highway Traffic Safety Administration (NHTSA) confirms that a statistically significant decrease in multi-vehicle crashes and fatal pedestrian strikes is achievable using an ABS system [Maz01]. As a result, the European Automobile Manufacturers Association has been committed to equipping all new vehicles with ABS since 2003 [Bur04]. Figures also indicate that about 95 percent of all-new vehicles in the United States have been equipped with ABS since 2003 [Vel01].

1.2.1 Anti-lock braking system

ABS is by no means a new innovation, and its development and acceptance has occurred over a number of decades. The first ABS system was developed by Dunlop Maxaret in 1952, and was used on aircraft landing systems [Vel01]. In 1978, Robert Bosch GmbH introduced the modern anti-lock braking system for passenger vehicles [Mar02-a, Mar02-b]. By the 1990s, ABS was a common option on many vehicles, and is now a standard feature on nearly all new vehicles.

An ABS system detects the onset of wheel lock-up due to a high braking force, and then limits the braking pressure to prevent wheel lock-up. An ABS system is considered a stand-alone system (i.e., it can be installed independently of other control systems), and consists of a wheel speed sensor, a hydraulic modulator, and an electronic control unit (ECU) for signal processing, control, and triggering the actuators in the hydraulic modulator [Bos07]. The ECU recognizes wheel lock-up by detecting sharp increases in wheel deceleration, and reduces the braking force in a closed-loop process until the lock-up situation vanishes. The cyclic application and reduction of the braking force ensures that the brakes operate at or near their most efficient operating point and the vehicle maintains steering control. This cyclic application is also responsible for the pulsation that a driver feels through the brake pedal when the system is activated. Note that the driver can be isolated from this pulsation in a brake-by-wire system.

In general, when a driver presses the brake pedal, the brake slip increases until the point of maximum friction between the tire and the road surface is reached, which is the limit between the stable and unstable regions. At this point, any increase in brake pressure will reduce the friction between the tire and the road surface, and the wheel will

tend towards skidding. In a vehicle with a conventional braking system, as the wheels tend towards lock-up, the lateral force potential of the tires (which enables steering) is greatly reduced, and approaches zero when the wheels are fully locked. By preventing wheel lock-up, the lateral force potential of the tires is maintained at a high level, allowing the driver to retain steering control during emergency braking. Thus, the task of an ABS system is to use the friction coefficient between the tires and the road surface in an optimal fashion in order to minimize the braking distance while retaining steerability.

1.2.2 Traction control system

In 1971, the Buick division of GM introduced *MaxTrac* as the first TCS, which was used to detect rear wheel spin and modulate the engine power delivered to those wheels in order to provide the most traction possible. Since then, more sophisticated TCS systems have been developed by different companies, such as Cadillac and Robert Bosch GmbH, and involve an engine management controller that cooperates with the brake system in order to prevent the driven wheels from spinning out.

Tire slip can also be controlled in an acceleration mode using a combination of the hydraulic brake system and the engine management controller to prevent tire spin-out. This task is accomplished by a TCS system, which is a constructive add-on to an existing ABS system and cannot be installed alone. In a TCS, the ECU recognizes wheel spin-out by detecting sharp increases in wheel acceleration. The ECU then reduces the engine torque through the engine management controller in a closed-loop process to reduce the traction force on the driven wheels. If the ECU is unable to prevent a spin-out situation using this first method of intervention, it applies the brakes in order to stop the wheels from spinning out. The closed-loop control process and the cooperation between the engine management controller and the brake system together ensure that the friction coefficient between the tires on the driven wheels and the road surface is used in an optimal fashion, maximizing the traction force while retaining stability and steerability. Note that the aim of a TCS system is defined based on the vehicle configuration. In a front-wheel-drive (FWD) vehicle, TCS aims to maximize the traction force while retaining steerability, whereas in a rear-wheel-drive (RWD) vehicle, TCS intends to maintain vehicle stability while maximizing the traction force.

1.2.3 Methods of adjusting the tire slip ratio

One method of adjusting the tire slip ratio in a slip control system is to limit the maximum possible slip ratio to a fixed amount. This strategy is shown in Figure 1-6, where the longitudinal force (F_x) and lateral force (F_y) of the tire are plotted as functions of the longitudinal slip ratio of the tire [Bei00]. The bold vertical line in Figure 1-6 highlights the limited slip ratio control strategy. The advantage of this method is that the tire slip angle (α) reasonably controls the relation between the longitudinal and lateral tire forces. In other words, at a fixed slip ratio, when the tire slip angle increases, the longitudinal tire force decreases and, at the same time, the lateral force potential of the tire increases, which improves the lateral stability of the vehicle (Figure 1-6).

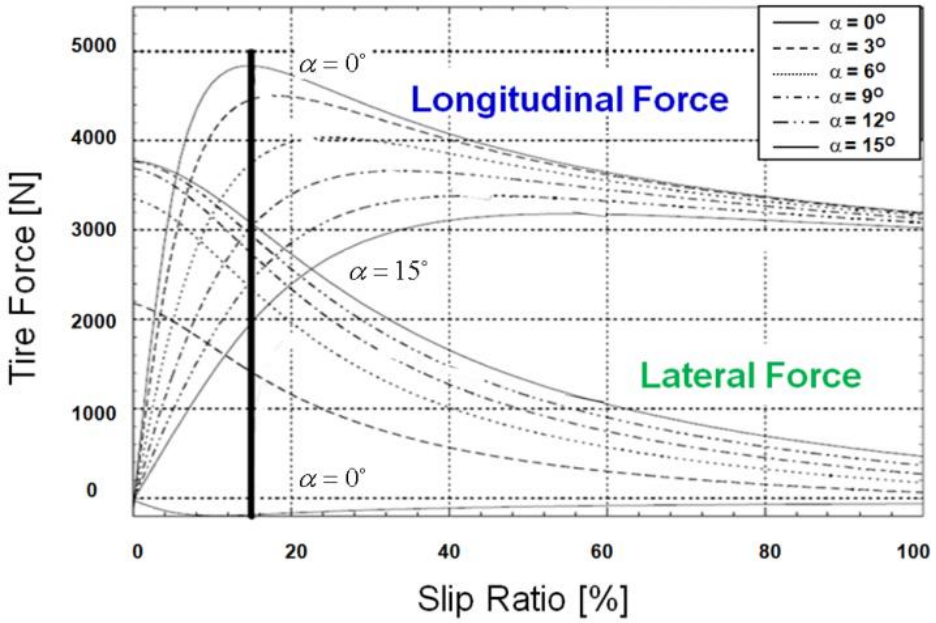

Figure 1-6: Characteristics of the tire longitudinal and lateral forces as a function of tire slip ratio for constant tire slip angles; used for a slip control system with limited slip ratio [Bei00]

An alternative approach is to adjust the tire slip ratio such that the maximum possible traction force can be generated at all slip angles. This method prioritizes the longitudinal tire force over the lateral tire force and ensures that the maximum possible traction force is attained at every sideslip angle [Bei00]. In other words, if the tire slip ratio is adjusted such that the maximum longitudinal force can be generated when the tire slip angle increases, the lateral force potential will not always increase. This situation is shown in Figure 1-7, where the upper bold-dashed line indicates the peak tire forces in the longitudinal direction at every slip angle, and the lower bold-dashed line indicates the corresponding lateral force of the tire.

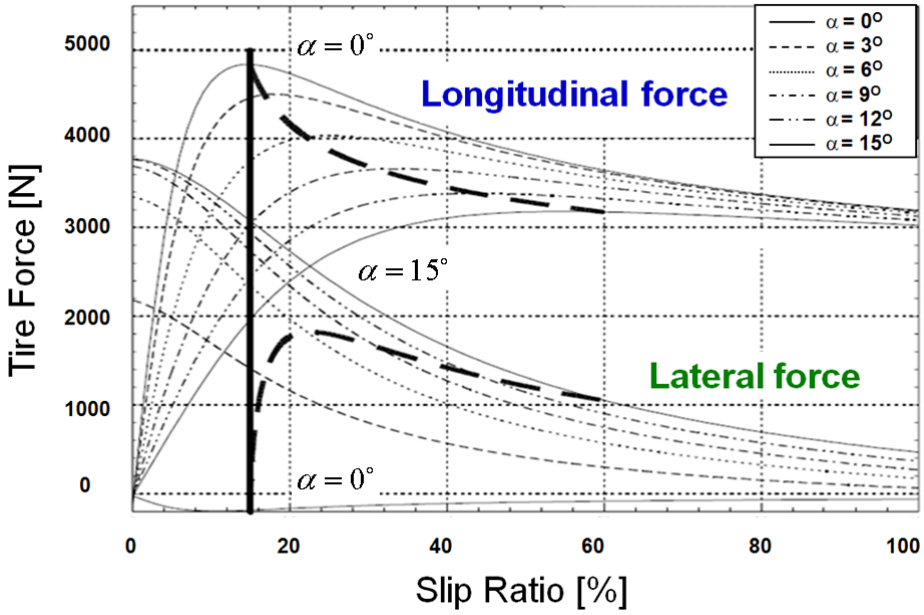

Figure 1-7: Characteristics of the tire longitudinal and lateral forces as a function of tire slip ratio for constant tire slip angles; used for a slip control system with adjustable slip ratio [Bei00]

1.3 Conventional stability control systems

Electronic stability control systems represent another breakthrough technology that has evolved and incorporated the slip control systems. These stability enhancement systems are designed to improve the lateral stability of the vehicle by electronically monitoring vehicle states and automatically assisting drivers in dangerous situations and under slippery road conditions. In general, most drivers are used to operating a vehicle with their "linear range" skills, the range of lateral acceleration in which a given steering wheel angle produces a proportional change in the heading of the vehicle [FMV07]. In this range, heading adjustments are easy to achieve because the response of the vehicle is proportional to the driver's steering input, and the lag time between the input and the response is very small. Therefore, the driver feels that he is in control and the vehicle travels in the direction in which it is pointed. However, when driving an ordinary vehicle at higher lateral accelerations (above 0.4g on a dry road), the relationship between the driver's steering input and the response of the vehicle changes, and the lag time of the vehicle response can lengthen [Wal05]. As a result, when an average driver encounters these changes in a panic situation, it is more likely that he will lose control and crash because the familiar actions learned when driving in the linear range are no longer valid. Electronic stability control systems augment the driver's inputs so that actions learned in

linear-range driving remain the correct actions for controlling the vehicle in panic situations [FMV07].

Electronic stability control systems use sensors that monitor the speed of each wheel, the steering wheel angle, and the overall yaw rate and lateral acceleration of the vehicle. Data from the sensors are used to estimate the intended course of the driver by monitoring the yaw rate and sideslip angle of the vehicle using a reference bicycle model and comparing that to the actual motion of the vehicle. Comparing the desired and actual data, an electronic stability control system can intervene early in the impending loss-of-control situation, generating a corrective yaw moment and restoring yaw stability before the driver has the opportunity to make an overcorrection or other error. In this way, an electronic stability control system prevents a vehicle from changing its heading from the desired path in a way that would induce further panic in a driver facing a critical situation [Lie05]. Different types of electronic stability control systems exist for generating a corrective yaw moment. For example, a corrective yaw moment can be generated by braking individual wheels using an electronic stability control (ESC) system, by superimposing the steering angle of the driver with a correction using an active steering control (ASC) system, by modifying the steering angles on an axle using a four-wheel-steering (4WS) system, or by varying the available drive torques on the driven wheels using a torque vectoring control (TVC) system [Zan00, Alb96, And06, Ack99, Rey03].

Several studies from around the world have confirmed that ESC is highly effective at preventing crashes. The following list summarizes some results from these global studies:

- Germany: ESC would prevent 80 percent of skidding crashes and 35 percent of all vehicle fatalities [Rie05].
- Sweden: ESC would prevent 16.7 percent of all injury crashes, excluding rear-end collisions, and 21.6 percent of serious and fatal crashes [Lib05].
- Japan: ESC would prevent 35 percent of single-vehicle crashes and 50 percent of fatal single-vehicle crashes. In addition, ESC would prevent 30 percent of head-on crashes and 40 percent of fatal head-on crashes [Aga03].
- United States: ESC would prevent 41 percent of single-vehicle crashes and 56 percent of fatal single-vehicle crashes [Far04]. In addition, ESC would reduce the

rates of fatal single-SUV crashes by 50 percent and fatal single-passenger-car crashes by 30 percent. Corresponding reductions for non-fatal single-vehicle crashes are 70 percent for SUVs and 55 percent for passenger cars [Gre06].

As a result of these studies, in March 2007, the U.S. National Highway Traffic Safety Administration (NHTSA) passed a new Federal Motor Vehicle Safety Standard (FMVSS No. 126) that makes the installation of ESC mandatory on all passenger cars, multipurpose passenger vehicles, trucks, and buses with a gross vehicle weight rating of 4,536 kg or less by 2012 [FMV07]. Note that ESC was equipped on about 29 percent of model year 2006 light vehicles sold in the U.S., and manufacturers intend to increase this amount to 71 percent by 2011.

1.3.1 Braking-based electronic stability control system

Although electronic stability control (ESC) systems have been known by a number of different trade names, such as Dynamic Stability Control (DSC), Dynamic Stability and Traction Control (DSTC), Electronic Stability Program (ESP), Vehicle Dynamic Control (VDC), Vehicle Stability Assist (VSA), Vehicle Stability Control (VSC), Vehicle Skid Control (VSC), Vehicle Stability Enhancement (VSE), and Porsche Stability Management (PSM), their function and performance are similar. All these systems use computers to control individual wheel brakes, thereby helping the driver maintain control of the vehicle during extreme maneuvers, keeping the vehicle headed in the intended direction even when the vehicle nears or reaches the limits of road traction.

When a driver attempts a sudden maneuver (for instance, to avoid an obstacle or crash, or due to misjudgment of the severity of a curve), the driver may lose control if the vehicle responds differently as it nears the limits of its handling than it does in ordinary driving situations. The driver's loss of control may be the result of the vehicle spinning out (oversteering) or plowing out (understeering). As long as there is sufficient traction between the tires and the road, a professional driver can maintain control of an unstable vehicle (oversteered or understeered) by using counter-steering and by performing a sequence of corrections based on the vehicle response. An average driver, on the other hand, tends to correct the spinning motion of an unstable vehicle through inappropriate steering inputs that, in most cases, make the situation even worse [FMV07]. An ESC system automatically applies braking torques to individual wheels to generate a corrective

yaw moment, adjusting the heading of the vehicle if it departs from the direction in which the driver is steering. Thus, ESC prevents the heading from changing too quickly (oversteering) or not quickly enough (understeering). Although ESC cannot increase the available traction, it supports the driver in his efforts to keep the vehicle under control and on the road in an emergency maneuver, using only the driver's ordinary driving actions learned in linear-range driving. Note that keeping the vehicle on the road prevents single-vehicle crashes, and roadway departure is the situation that leads to most rollovers [Dan04]. However, the activation of an ESC system is often at the expense of reducing the vehicle speed which, in general, is perceived by the driver as being annoying.

Figure 1-8-a illustrates the operation of an ESC system during a left-hand turn in order to stabilize an oversteered vehicle, where the rear of the vehicle begins to slide. In a vehicle equipped with ESC, the system immediately detects that the heading of the vehicle is changing more quickly than is appropriate given the driver's intended path, and it momentarily applies the front outside brake to generate a corrective yaw moment that turns the heading of the vehicle back to the intended path. In addition, braking the front outside tire simultaneously reduces the lateral force potential of that tire, which also helps to generate the required corrective yaw moment. Note that braking the rear outside tire is not an appropriate action in this situation because, in an oversteered vehicle, reducing the lateral force potential on the rear axle will lead to further instability.

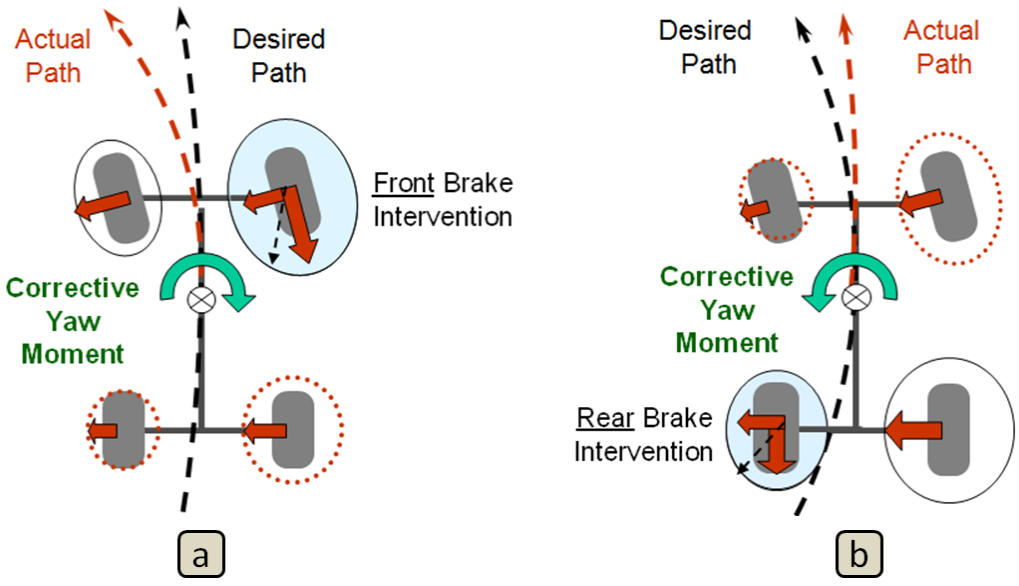

Figure 1-8: Braking intervention of an ESC system (a) in an oversteered vehicle and (b) in an understeered vehicle (the ellipse on each tire demonstrates the adhesion potential of that tire; a dotted ellipse indicates that the adhesion potential has been exceeded)

Figure 1-8-b illustrates an understeered vehicle during a left-hand turn, whose response as it nears the limits of road traction involves sliding at the front and plowing out. In this situation, the ESC system detects that the heading of the vehicle is changing less quickly than is appropriate given the driver's intended path, and immediately applies the left inside brake to turn the heading of the vehicle back to the desired path. Once again, the braking force and the reduced lateral force potential on the rear inside tire are both used to generate the corrective yaw moment that is required to stabilize the vehicle. Note that braking intervention using the front inside tire is not an appropriate action since, in an understeered vehicle, the adhesion potential has already been exceeded on the front axle.

1.3.2 Steering-based electronic stability control system

In 2004, BMW introduced its first commercial active steering system in its 5-series class of vehicles. Active steering fills the gap between conventional steering system and steer-by-wire technologies. Although an active steering system allows driver-independent steering intervention, the mechanical linkage between the steering wheel and the rack-and-pinion system on the front axle remains in place, acting as a fail-safe mechanism. Figure 1-9 illustrates the active steering system developed by BMW, which is comprised of a rack-and-pinion steering system, a double planetary gear, and an electric motor as the actuator. An active steering system facilitates the implementation of two major functions: a variable steering ratio, and maintaining vehicle stability and maneuverability during emergency maneuvers or when driving conditions call for a change in the steering response [Koe04].

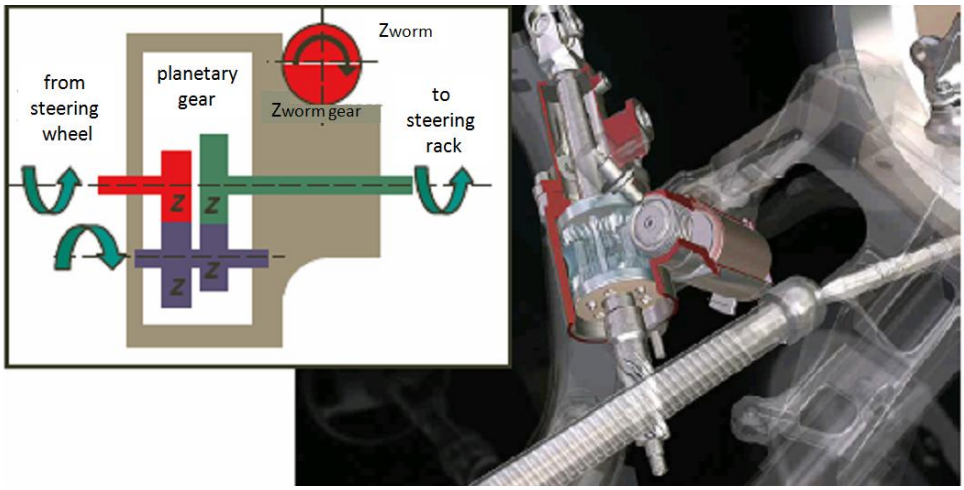

Figure 1-9: Design concept and mechanical layout of the BMW active steering system [Koe04]

The basic design trade-off associated with conventional steering systems involves choosing a suitable geometric steering ratio, which affects not only the steering effort required during low-speed maneuvering, but also has a significant influence on the vehicle dynamics at higher speeds. An active steering system resolves this conflict by increasing the steering ratio at higher speeds to enhance the responsiveness of the vehicle, and decreasing it at lower speeds to enhance the maneuverability. This adjustment is accomplished using a double planetary gear and an electric motor. The active steering system adds a slight steering angle to the driver's input at low speeds and counter-steers slightly at higher speeds, thereby avoiding hand-over-hand steering when parking while ensuring an essentially constant steering effort in the medium- and high-speed ranges, where a more conservative steering system is required. The variable steering ratio of the active steering system developed by BMW is illustrated in Figure 1-10. As can be seen, the active steering system reduces the steering ratio to 1:10 at lower speeds to provide the driver with a more direct steering feel, and increases the ratio to 1:20 in the high-speed range to support the driver with a more sensitive steering system. Note that conventional steering systems can only offer fixed steering ratios, which are typically between 1:14 and 1:18.

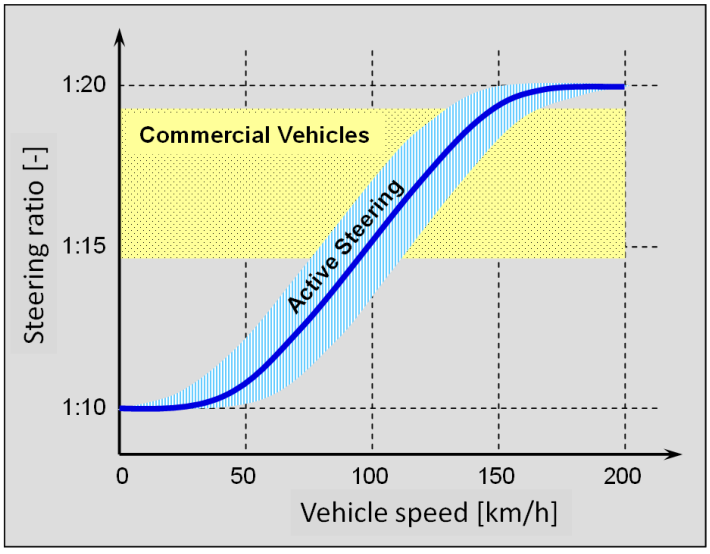

Figure 1-10: Variable steering ratio caused by an active steering system [Koe04]

Another significant advantage of an active steering system is its ability to electronically augment the driver's steering input to stabilize the vehicle. In general, steering intervention is faster than braking individual wheels, as is done in an ESC system, since a certain amount of time is required to build up hydraulic brake pressure. In

comparison to braking intervention, modifying the reaction of the vehicle using steering intervention is generally a continuous process and is not perceived by the driver – or, at least, is not perceived as being annoying [Koe04]. Figure 1-11 compares the effectiveness of ESC and active steering systems for correcting an oversteered vehicle, where the rear tires have reached their limit of adhesion during a left turn. In such a situation, an ESC system applies a braking force (F_B) to the front outside tire to generate the required corrective yaw moment (M_z), which is calculated as follows [Yih05]:

$$M_z = F_B \cdot \frac{t_f}{2} \tag{1.1}$$

where t_f is the front track-width of the vehicle. An active steering system, on the other hand, applies a counter-steering angle in order to generate the same corrective yaw moment (M_z) but, in this case, the moment is generated using the lateral forces (F_y) of the front tires:

$$M_z = 2F_y \cdot a \tag{1.2}$$

where a is the distance between the front axle and the vehicle center of mass. Assuming that the same corrective yaw moment is generated by these two systems, and knowing that the track-width of most passenger cars is very close to the distance between the vehicle center of mass and the front axle, the required lateral force on the front tires is only one-fourth of the required braking force:

$$F_y = \frac{F_B}{4} \tag{1.3}$$

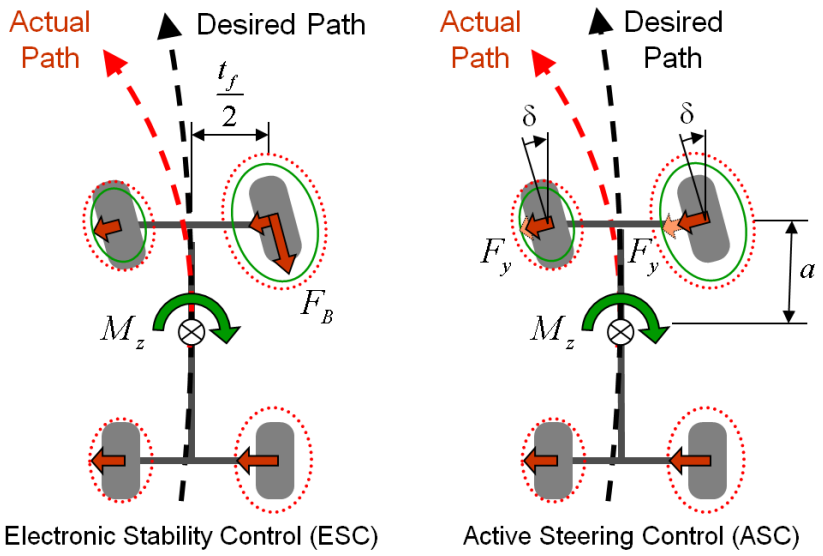

Figure 1-11: Generation of a corrective yaw moment through braking intervention using an ESC system (left) and through steering intervention using an active steering system (right)

Therefore, it is actually advantageous to use steering intervention rather than braking intervention to generate a corrective yaw moment when controlling a vehicle on slippery surfaces, where the limits of adhesion are easily reached. In addition, active steering can also be used when driving on a μ-split road in order to correct the side-pushing effect that appears due to the different traction forces on the two sides of a vehicle. However, the effectiveness range of the active steering system is very restricted due to the actuator range limit. For instance, the active steering system developed by BMW is only able to apply up to 3^o of steering angle on the front wheels [Koe04].

1.3.3 Torque vectoring control system

In conventional four-wheel-drive (4WD) vehicles, either all the wheels of the vehicle are permanently driven, which is referred to as an all-wheel-drive (AWD) vehicle, or one of the two axles is always linked to the engine and the second can be engaged manually or automatically when needed. In both cases, in order to transmit the available engine torque to the wheels, inter-axle differentials or clutches must be installed on the propshaft, between the front and rear axles, and on both drive axles in order to split the torque between the left and right wheels. A comprehensive overview of the drivelines and differentials available for 4WD and AWD vehicles can be found in [Whe02, Whe05]. Although these powertrain configurations can enhance the traction and driving dynamics on various road conditions, they suffer from higher costs, weight, and power consumption, as well as inefficiency.

In recent years, the market for AWD vehicles has evolved and expanded, and customer expectations of the driving dynamics and stability of such vehicles have increased drastically. In addition, consumers are increasingly willing to request AWD on their new cars at extra cost [Pel05]. In order to meet these requirements and remain competitive in the market, active differentials for driveline systems are being introduced, which are able to distribute the engine torque to the front and rear axles, as well as to the left and right wheels of each axle, depending on the driving maneuver or road conditions. The possibility of actively influencing the distribution of the available engine torque based on the driving situation and traction conditions has led to an upheaval of the AWD market [Wun05]. However, the pressure to reduce CO_2 emissions and increase fuel efficiency standards force the weight, cost, and power requirements of these actuators to be minimized.

Torque vectoring is the term introduced by the Ricardo Company [Whe05] to describe a means of varying the distribution of engine torque between two outputs of a differential unit by controlling the torque over a relatively small speed difference between the outputs. Torque is directed in proportion to the relative shaft speeds, and can be biased seamlessly from one output to the other. Later on, active torque vectoring systems were introduced into the powertrain system, presenting torque-on-demand capabilities, where a center differential distributes the available engine torque to the front and rear axle differentials. Each axle differential can be equipped with an active torque vectoring system as well, which can be used to distribute the torque between the left and right wheels. An active center differential apportions the torque depending on the driving dynamics and the traction potentials on each axle, whereas an active axle differential distributes the torque based on the vehicle dynamics and the traction potential on each wheel of a single axle.

The benefits of active torque vectoring technology are twofold: the enhancement of vehicle traction and the enhancement of vehicle stability. On the one hand, torque vectoring can be used to modulate the individual wheel speeds to keep each tire operating in its optimal longitudinal slip range for the best traction. On the other hand, torque vectoring can be used to enhance the vehicle handling response by generating a corrective yaw moment to influence the vehicle yaw behaviour [Rey03]. For instance, Figure 1-12 illustrates an active powertrain with an active center differential, an active rear differential, and an open front differential [Jal04]. In normal driving conditions, where the differential actuators are not active, the center differential splits the torque generated by the engine by a fixed ratio of 40:60 percent to the front and rear axles, respectively, using a planetary gear. This fixed torque distribution ratio can be established based on the axle-load ratios, the design philosophy of the vehicle, or the desired handling characteristics of the vehicle [Rei02]. In addition, the front and rear differentials split their received torques in half using open differentials. Using torque vectoring technology for traction enhancement, the torque vectoring ratios on the center and rear differentials can vary depending on the traction potentials available on each axle or tire, such that the highest traction force on each wheel is attained. Figure 1-13 illustrates the case where the front tires are on ice with almost no traction, and more traction is available on the rear right tire than the rear left tire. As can be seen, the active center differential is capable of

sending 90 percent of the available engine torque to the rear axle, where more traction is available. The active rear differential, on the other hand, splits the torque received from the center differential asymmetrically by a ratio of 20:80 percent for the left and right wheels of the rear axle, respectively.

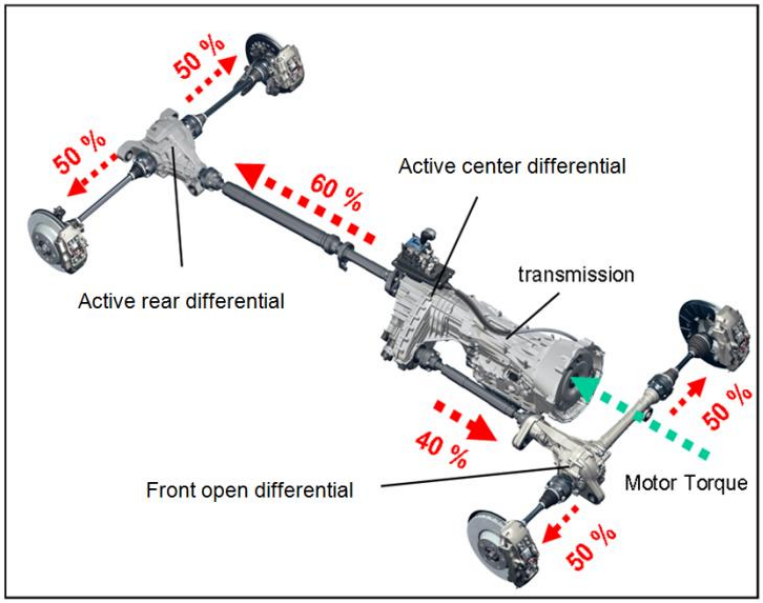

Figure 1-12: An active powertrain system with active center and rear differentials [Jal04]

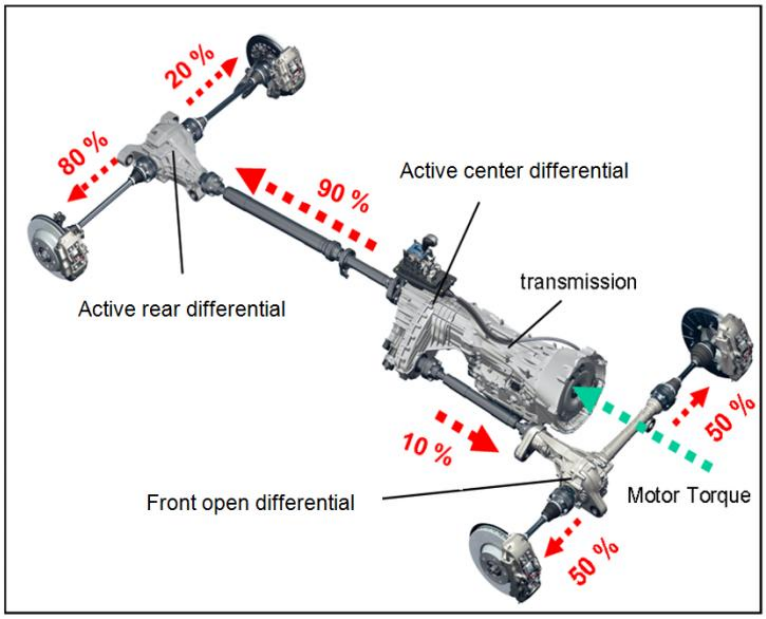

Figure 1-13: Torque vectoring in an active powertrain to enhance the vehicle traction [Jal04]

Torque vectoring can also be used as a stability control system, where the available drive torque is distributed among the wheels in order to generate a corrective yaw moment about the vertical axis of the vehicle. The corrective yaw moment can be

generated in a left-to-right torque vectoring mode, where the available drive torque is distributed asymmetrically to the left and right wheels of an axle, or in a front-to-rear mode, where the available engine torque is distributed asymmetrically to the front and rear axles. For instance, an oversteering situation, in which the adhesion potential has been reached at the rear axle, can be corrected using left-to-right torque vectoring on the front axle, where more torque is transmitted to the front inside tire (Figure 1-14-a). Conversely, an understeering situation, in which the adhesion potential has been exceeded on the front axle, can be corrected by using left-to-right torque vectoring on the rear axle, in which a higher percentage of the available axle torque is transmitted to the rear outside tire in order to generate the required corrective yaw moment (Figure 1-14-b).

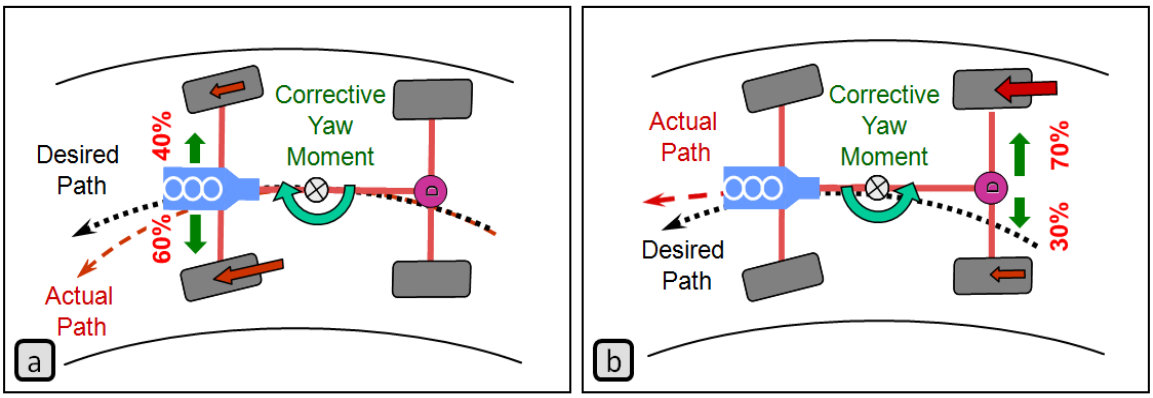

Figure 1-14: (a) Stability control of an oversteered vehicle through side-to-side torque vectoring on the front axle, and (b) stability control of an understeered vehicle through side-to-side torque vectoring on the rear axle

The driving dynamics of a vehicle can also be influenced by varying the front-to-rear torque distribution. The front-to-rear torque vectoring mode takes advantage of the interconnection between the longitudinal and lateral tire forces, where changing one force will automatically influence the other. For instance, an understeered vehicle can be controlled by transmitting more of the engine torque to the rear axle than the front axle. This strategy not only increases the lateral force potential at the front axle and, simultaneously, enhances the steerability of the vehicle, but it also reduces the lateral force potential of the rear axle by increasing the longitudinal traction force. The lateral force difference between the two axles generates the required corrective yaw moment about the vertical axis of the vehicle, helping the vehicle to travel in the direction in which it is pointed (Figure 1-15-a). Conversely, an oversteered vehicle can be controlled by transmitting more of the available engine torque to the front axle, thereby increasing

the essential lateral force potential on the rear axle. At the same time, this strategy will reduce the lateral force potential on the front axle by elevating its longitudinal force, thus helping the vehicle to develop more understeering behaviour (Figure 1-15-b).

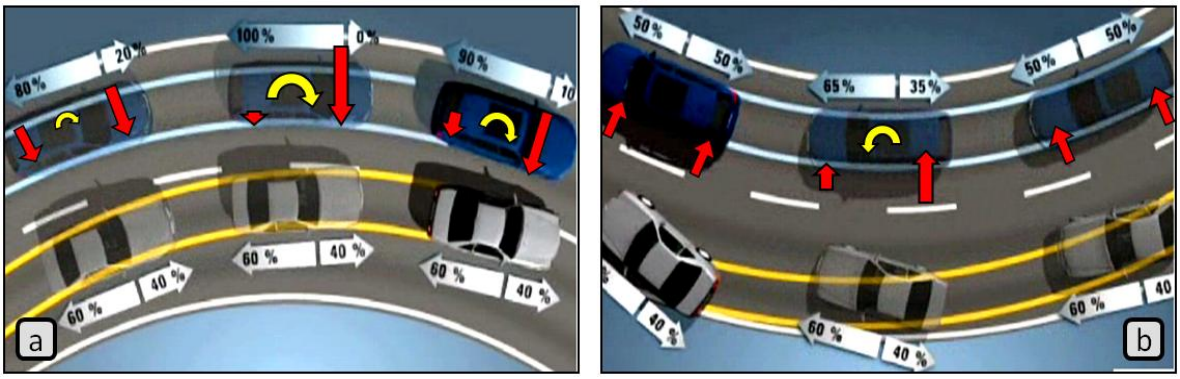

Figure 1-15: Front-to-rear torque vectoring (a) in an understeered vehicle, and (b) in an oversteered vehicle [Wal06]

Although the theory behind the torque vectoring technique is similar to that used for an ESC system, torque vectoring is more effective, especially for generating a corrective yaw moment at higher vehicle speeds and during emergency maneuvers near the handling limits of the vehicle [Rey03]. In general, torque vectoring can affect the vehicle driving dynamics and traction while causing almost no change in the total driving force of the vehicle. Active braking, on the other hand, is hampered by a net braking effect and drive torque reduction, which not only increases the inefficiency of the vehicle by eliminating power that has already been produced, but it has also been reported by drivers as being disruptive due to the unexpected speed reduction. Moreover, in contrast to active braking, which is allowed only a limited operation time to ensure a safe reserve of fade-free braking performance, torque vectoring can be employed much more actively to enhance driving dynamics and vehicle traction even in normal driving conditions and everyday driving experience. However, it is important to note that a torque vectoring system can only be effective when a driving torque exists in the first place. In other words, torque vectoring is not able to intervene when the driver releases the throttle or brakes the vehicle. In such cases, an ESC system must maintain the stability of the vehicle. Therefore, torque vectoring and active braking should be considered to be complementary technologies whose full potential can only be realized if a holistic approach is used to operate both systems under a common supervisory controller.

In summary, to control the vehicle traction and driving dynamics during both braking and acceleration maneuvers, the vehicle should be equipped with ABS, TCS,

ESC, and torque vectoring control systems, and all of these systems should be networked together in an integrated fashion. However, equipping a vehicle with all the aforementioned control systems and actuators is a very expensive and complex task. It is for this reason that such a degree of vehicle control is only available in luxury-class vehicles, where the customer is prepared to pay for the required technologies.

1.4 Advanced stability control system through networked chassis

Until the 1980s, chassis technology, which directly determines the dynamic performance of a vehicle, advanced exclusively within the mechanical engineering framework. After the mid-1980s invention and practical application of the four-wheel-steering system (4WS), the vehicle dynamics performance field became a main stream of research and development for control technology. Since then, research and development of vehicle dynamics performance has been carried out as a collaborative technology of mechanical engineering and control engineering.

Current chassis control systems are distinguished by the way the individual subsystems work. Each individual subsystem can generally be assigned to an individual dynamic domain, such as longitudinal, lateral, or vertical dynamics. However, individual subsystems often influence two of the three domains, as illustrated in Figure 1-16. For instance, a torque vectoring system can influence both the longitudinal and lateral dynamics of a vehicle. Furthermore, the influences of individual subsystems, especially during extreme maneuvers, are interconnected and coupled through the tire-road characteristics. Thus, the optimum driving dynamics can only be achieved when the tire forces on all four wheels and in all three directions can be influenced and controlled precisely. In order to achieve this level of control, the vehicle must not only be equipped with various active chassis subsystems, but these subsystems must be networked together in order to control the tire forces and meet the instantaneous driving dynamics, safety, and comfort requirements [Sem06].

Taking advantage of the benefits and strengths of each subsystem, the ideal stability control system can be obtained by activating the most effective subsystem or subsystems based on the driving maneuver and road conditions. For example, an ESP system uses braking intervention of individual wheels in order to influence the longitudinal forces on the tires and, ultimately, the yaw behaviour of the vehicle.

However, in order to obtain stabilization, vehicle braking is not necessary in all situations. In particular, if the vehicle speed must be maintained at the same level while turning in a curve, torque vectoring techniques can be used to affect the driving dynamics. Furthermore, the influences of individual subsystems, especially during extreme maneuvers, are interconnected and coupled through the tire-road characteristics. Figure 1-17 demonstrates the interdependencies of longitudinal, lateral, and vertical dynamics. For example, a friction ellipse couples the lateral and longitudinal tire forces, whereas a "longitudinal friction coefficient versus slip ratio" relationship couples the longitudinal and vertical tire forces, and a "lateral friction coefficient versus slip angle" relationship couples the lateral and vertical forces of a tire. Thus, most vehicle control principles can be related to the linear and nonlinear characteristics of the tire-road contacts. The factors influencing the nature of this contact can be summarized as direct effects of the steering angle, slip angle, and camber angle of the tires on lateral forces, and direct effects of traction and braking intervention on longitudinal forces. The wheel vertical load, however, influences both longitudinal and lateral forces directly by defining the maximum possible adhesion potential.

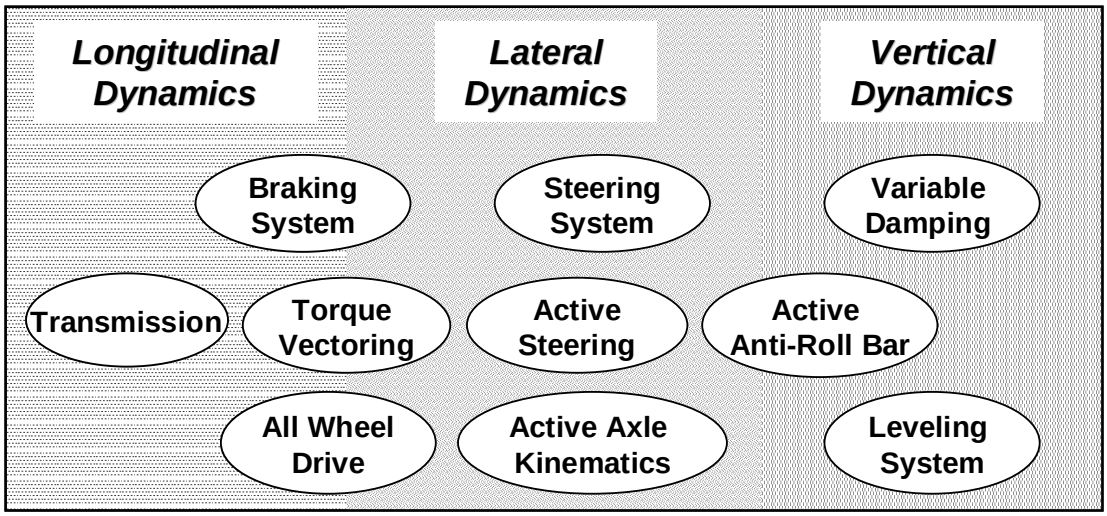

Figure 1-16: Domain structure of driveline and chassis systems [Sem06]

The fundamental question of which configurations are both effective and feasible given a specific set of driving conditions can only be answered if the strengths and limitations of each active chassis subsystem have been identified. A popular method of addressing such issues is by presenting the effects of each subsystem on the resulting tire-road friction ellipse or circle. Since the driver is limited by the friction constraints of the tires, the vehicle controls are expected to provide the driver with predictable authority

over longitudinal and lateral accelerations, within the physical constraints of the vehicle "friction circle", and subject to perceived customer acceptability of the frequency and amplitude dependence of the vehicle responses [Gor03]. Therefore, given that friction limits change with speed, road surface conditions, and so forth, these vehicle control systems are required to provide adequate feedback of such changes. The concepts illustrated in Figure 1-18, presented by Toyota [Yam91], indicate the domain of operation of some typical vehicle control systems. Although the diagrams should not be taken too literally, they clearly underline the fact that integrated control can enlarge the dynamic response domain of the vehicle by taking advantage of the control system with the most effectiveness for a particular driving maneuver and set of road conditions.

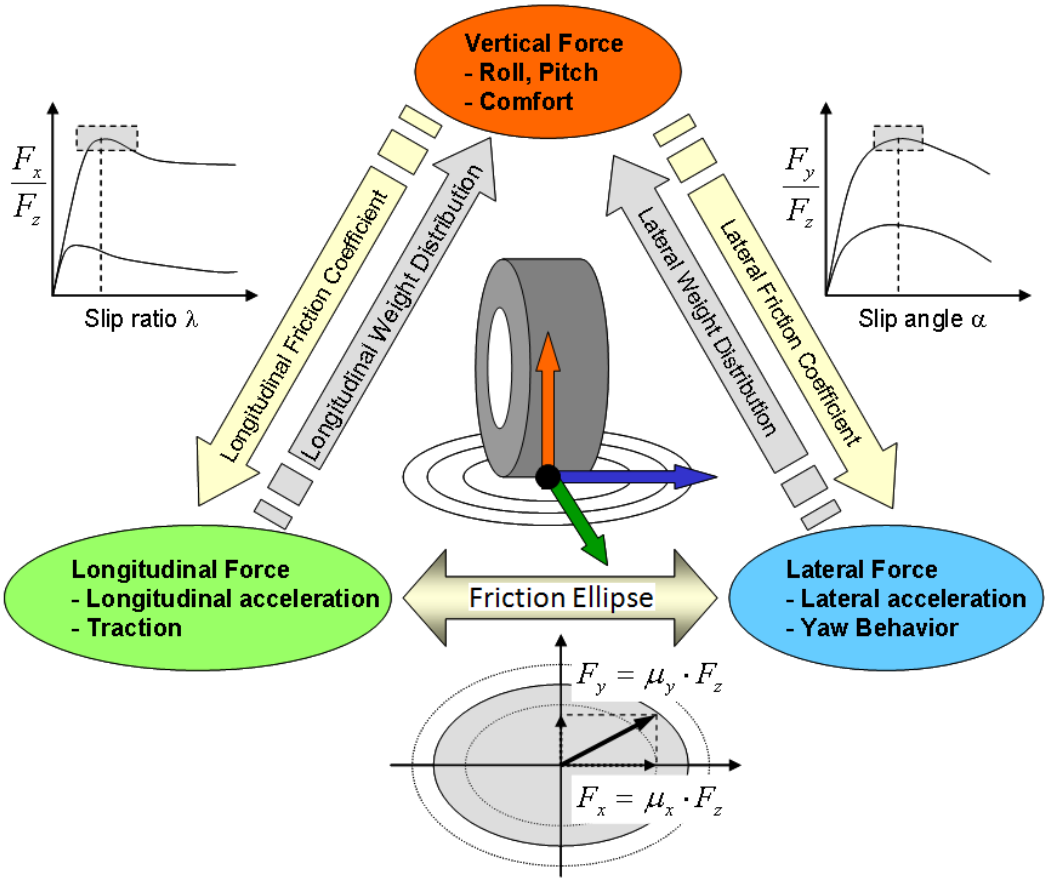

Figure 1-17: Interdependencies among longitudinal, lateral, and vertical dynamics

The majority of the stability control systems currently on the market stabilize the vehicle in critical driving situations by intervening with only one type of active chassis subsystem at a time, which limits the performance of the vehicle. Recently, there has been a move towards networking the individual subsystems in order to take advantage of synergies and increase the performance of the vehicle. Until very recently, however,

mainly due to marketing strategies, chassis subsystems have been treated as stand-alone systems in a so-called "coexistence" architecture, which requires no overhead but still suffers from suboptimal performance. This architecture can lead to a situation in which, for instance, a vehicle with four active chassis subsystems is equipped with as many as four independent sets of sensors, state estimators, reference models, and state controllers [Sem06, Koe06]. Since the simultaneous actuation of these subsystems may affect the same degrees-of-freedom of the vehicle and have counterproductive results, the overlapping of actuator effort must be addressed in a more coordinated way. One solution to this problem is a "hierarchical coexistence" of the subsystems with a unidirectional information flow, where one system acts independently and the others adapt as necessary.

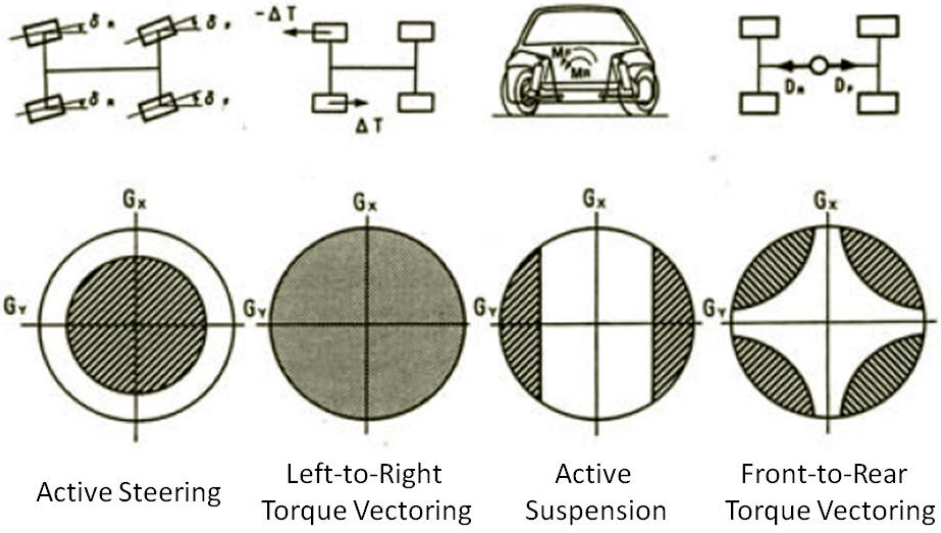

Figure 1-18: Effective range of various control concepts based on the resulting tire-road friction circle [Yam91]

An "integrated approach" is a more sophisticated means of addressing the coordination of several actuators [And06, Gor03]. In this approach, each of the chassis subsystems has one basic function. In contrast to the coexistence approach, there is only one set of sensors, one state estimator, one reference model, and one state controller. Based on the desired and actual behaviour of the vehicle, the system can calculate the required generalized forces and moments to maintain the course desired by the driver. These generalized forces and moments are then applied by the actuators based on their effectiveness, ensuring the best overall safety, ride quality, and driving pleasure.

1.5 Thesis outline and contributions

In order to investigate effective and feasible control configurations given a specific set of driving conditions, the performance and limitations of several active chassis subsystems have been analyzed and evaluated. These subsystems have been specifically designed for the AUTO21EV, which is equipped with four direct-drive in-wheel motors and an active steering system on the front axle.

To this end, a set of test maneuvers is developed in Chapter 2 for evaluating vehicle handling and performance. In addition, path-following and speed-control driver models are developed and implemented, which allow the simulation of closed-loop test maneuvers.

In Chapter 3, an advanced fuzzy slip controller is developed for the AUTO21EV that combines the functionalities of an ABS, a TCS, and the brake system of the vehicle. Furthermore, the performance and functionalities of the developed fuzzy slip control system are evaluated using four test maneuvers.

In Chapter 4, a 14-degree-of-freedom (DOF) vehicle model is developed to allow for the testing of different control strategies, and for applying a genetic tuning algorithm to the development of the fuzzy yaw moment controller. The genetic tuning procedure is applied to the developed fuzzy yaw moment controller to improve its performance. The genetic fuzzy yaw moment controller determines the corrective yaw moment that is required to stabilize the vehicle and applies a virtual yaw moment around the vertical axis of the vehicle. The effectiveness and performance of the genetic fuzzy yaw moment controller is evaluated using a variety of test maneuvers.

Chapter 5 describes the development of an advanced torque vectoring controller based on the previously developed genetic fuzzy yaw moment controller. The objective of the advanced torque vectoring controller is to generate the required corrective yaw moment through the torque intervention of the individual in-wheel motors to stabilize the vehicle during normal and emergency driving maneuvers. A novel algorithm is developed for the left-to-right torque vectoring control on each axle, and a PD controller is introduced for the front-to-rear torque vectoring distribution action. Several maneuvers are simulated to demonstrate the performance and effectiveness of the advanced torque vectoring controller, and the results are compared to those obtained using the genetic fuzzy yaw moment controller.

In Chapter 6, the simplified 14-DOF vehicle model introduced in Chapter 4 is used to develop a fuzzy active steering controller. Use of this simplified vehicle model facilitates the testing of different control strategies and the application of a genetic algorithm procedure to the development of the fuzzy active steering controller. The performance of the fuzzy active steering controller is improved by tuning the membership functions of the fuzzy controller using a genetic tuning procedure. The performance and effectiveness of the genetic fuzzy active steering controller are confirmed by simulating a variety of maneuvers, and the results are compared to those obtained using the genetic fuzzy yaw moment controller and the advanced torque vectoring controller.

Chapter 7 presents an activation function that integrates the control efforts of the advanced torque vectoring and genetic fuzzy active steering controllers. Several test maneuvers are simulated to demonstrate the performance and effectiveness of this integrated control approach. It is confirmed that the integrated control approach produces better results than all of the individual control systems.

Finally, Chapter 8 summarizes the work, highlights the contributions, and discusses directions for future work in this thesis.

2 Test Maneuvers and Analytical Driver Models

The driver of a passenger car is responsible not only for controlling the vehicle speed by actuating the brake and accelerator pedals, but also for controlling the direction in which the vehicle is travelling. Thus, the tasks of the driver are threefold: navigation, path following, and vehicle stability [Wal05]. In order to travel between two points, a driver must first choose a suitable route. Criteria such as route length and travelling time might be used to select the desired route. Navigation systems can help a driver plan a route between two points, but the ultimate decision about which route to select is still made by the driver. The second task of a driver is to define the desired path for the vehicle within the chosen route based on additional information that is gathered along the way, such as traffic conditions, traffic signs, and unexpected obstacles. Despite technological advancements in this area, the path-following task cannot be fully automated using control systems such as path-following cameras or inductive highway striping. The final task of a driver is to keep the vehicle on the desired path using the available actuators (the steering wheel, brake pedal, and accelerator pedal). Moreover, the driver is responsible for the stability of the vehicle while driving through the desired path. The stability control systems available on the market are either designed to maintain the stability of the vehicle, or at least to support the driver in accomplishing this task. Since the driver must perform the three aforementioned tasks simultaneously, a stability control system not only helps the driver maintain the stability of the vehicle, but also indirectly helps him accomplish the route-planning and path-following tasks. In the ideal case, a stability control system will allow the driver to devote all his attention to the other two tasks.

From a control systems perspective, the driver and vehicle can be modelled as a control loop, where the driver acts as a controller that is responsible for the stability of the plant, which is the vehicle (Figure 2-1). In such a control loop, some disturbances act on the driver (such as the relative motion between the vehicle and the driver, driver distractions, and line-of-sight obstructions), and others act on the vehicle (such as cross wind, different coefficients of friction on the road, and road roughness). In terms of the lateral dynamics, the actuating variable that must be corrected by the driver is the steering wheel angle; in terms of the longitudinal dynamics, the actuating variables are the brake and accelerator pedal positions. The control deviation that must be corrected by the driver

in the lateral dynamics domain is the difference between the desired and actual paths, while in the longitudinal dynamics domain, the deviation between the desired and actual speeds must be corrected. Moreover, the driver-vehicle-environment control loop is considered to be a dynamic closed-loop system, whose stability depends mostly on the vehicle behaviour and the capabilities of the driver. In other words, the stability of this control loop depends on the ability of the controller (the driver) to handle large errors, the behaviour of the control system under fast control actions, and the stability of the system under the influence of external disturbances.

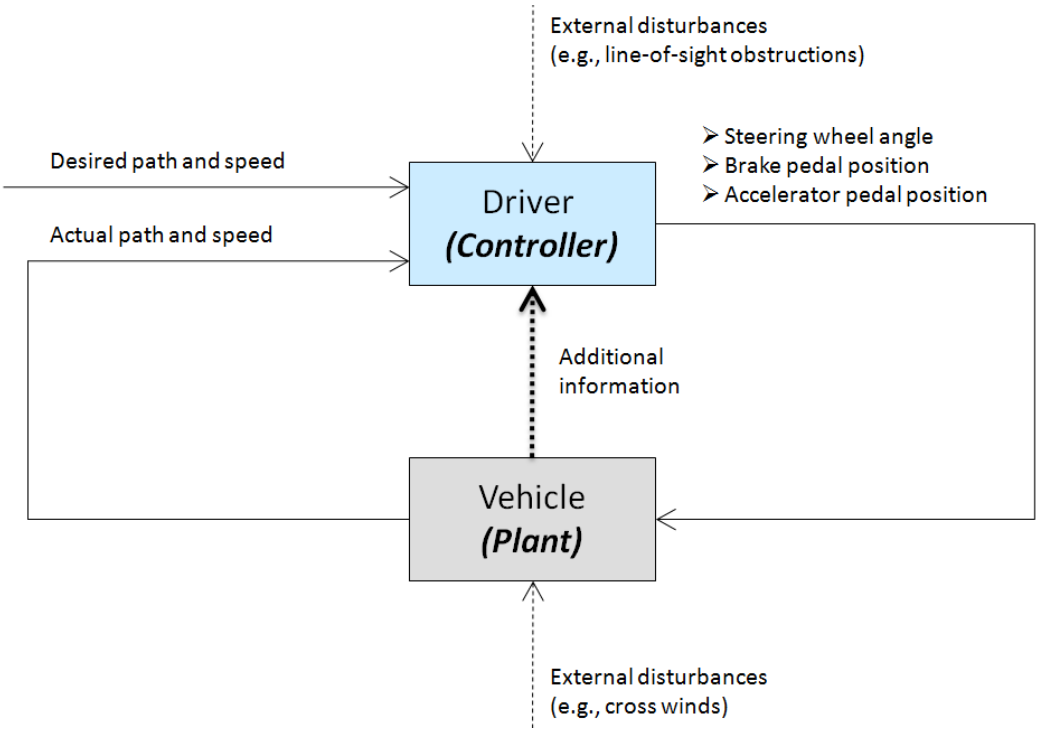

Figure 2-1: Graphical representation of the driver-vehicle-environment control loop

In general, the dynamic characteristics of the vehicle must match the capabilities of the driver. The quality of this match defines the vehicle handling and performance characteristics. In this regard, a vehicle is considered to have a good handling characteristic if the following arguments are true [Wal05]:

1. There must be a good correlation between the steering wheel variation and the lane-change behaviour of the vehicle. This property defines the transfer function behaviour of the vehicle as the plant of the control loop.
2. The driver must receive reasonable information about the condition of the vehicle in order to predict its behaviour. For instance, changes in the steering wheel feedback

torque, the vehicle sideslip angle, as well as tire squeak before reaching the physical limit of adhesion will all help the driver predict the behaviour of the vehicle and, ultimately, react correctly.

3. The external disturbances acting on the vehicle should cause little or no change in the course of the vehicle – that is, the vehicle should be inherently stable.
4. The vehicle must have a high lateral acceleration limit, which defines the lateral stability reserve of the vehicle; the larger this limit, the more stable the vehicle will be.

It is important to note that there are no standard legal regulations about the vehicle handling and performance characteristics, and every car manufacturer is free to set its own specifications in this area. Looking at the vehicle handling and performance from the driver's perspective, it is a completely subjective evaluation that can change from one driver to another. Therefore, it is very difficult to set a standard criterion for quantifying the quality of these evaluations. In fact, there is no comprehensive, objective definition for the dynamic characteristics associated with the driver-vehicle-environment control loop, as adequate data on the precise control characteristics of the human element are still not available [Bos07]. For this reason, in practice, the assessment of the vehicle is performed by expert drivers who can subjectively evaluate the measured data gathered through a series of standard test maneuvers.

2.1 Test maneuvers for evaluating vehicle handling and performance

Many test maneuvers have been developed for evaluating the quality of the handling and performance characteristics of a vehicle. Many of these test maneuvers are based on ideal driving conditions, and some of them are motivated by the examination methods typically used for control systems, such as step-steer and swept-sine-steer maneuvers (Figure 2-2). An extensive overview of different test maneuvers and their detailed descriptions can be found in the publications of Roenitz, Braess, and Zomotor [Roe77, Roe98].

The test maneuvers that describe the vehicle behaviour in terms of the driver-vehicle-environment control loop are known as 'closed-loop' test maneuvers. To evaluate these maneuvers, the quality of the match between the dynamic behaviour of the vehicle and the driver's capabilities must be considered. These test maneuvers require a

professional driver who can make judgments on the handling qualities of the vehicle based on the combination of diverse subjective impressions. In the simulation environment, an appropriate driver model is used, which can simulate the required behaviour of a specific driver (professional or average driver) in following a desired predefined path, in place of a test driver. If, on the other hand, the actuation variables in a test maneuver are defined to be pure functions of time, and the dynamic behaviour of the vehicle has no influence on the driver's response, then the test maneuver is known as an 'open-loop' maneuver. In an open-loop test maneuver, the driver is replaced by a specific, objectively quantifiable interference factor, and the handling data derived from the maneuver provides objective information about the handling qualities of the vehicle. Open-loop test maneuvers also provide insight into the stability of the vehicle and the sensitivity of the vehicle to external disturbances.

Driving Situation	Test Maneuvers	Closed-loop	Open-loop
Cornering Events	Steady-state constant radius cornering	N	Y
	Load-cycle changes	Y	Y
	Transient constant radius cornering	Y	Y
	Braking-in-turn	Y	Y
	Aquaplaning (μ-split road)	Y	Y
Straight-line Events	Directional stability	Y	Y
	Straight-line acceleration	Y	Y
	Aquaplaning (μ-split road)	Y	Y
	Straight-line braking	Y	Y
	Cross wind	Y	Y
	Load-cycle changes	Y	Y
	Responsiveness test	Y	N
Dynamic Performance Tests	Step-steer	N	Y
	Impulse-steer	N	Y
	Single-lane-change	Y	N
	ISO double-lane-change	Y	N
	Driving in a curve	Y	N
	Driving out of a curve	Y	N
Transient Behaviour Tests	Sine steer	N	Y
	Swept-sine steer	Y	N
	Step-steer and acceleration	N	Y
	Obstacle avoidance test	Y	N

Figure 2-2: Different test maneuvers for evaluating vehicle handling and performance characteristics [Roe77] (Y = yes and N = no)

It can be concluded that each test maneuver provides some information about the dynamic behaviour of the vehicle in one or several respects, such as vehicle handling, stability, path following, and longitudinal dynamics. Therefore, a comprehensive

evaluation of the dynamic characteristics of a vehicle is only possible by examining the results obtained from several different test maneuvers.

2.1.1 Selection and evaluation of chosen test maneuvers

As mentioned above, many test maneuvers are used in industry, and can provide insight into the dynamic behaviour of the vehicle under different conditions (Figure 2-2). However, a comprehensive evaluation of the dynamic characteristics of a vehicle and the effectiveness of different chassis control systems can only be achieved when the results obtained from different test maneuvers are combined and evaluated as a whole. Therefore, a number of different test maneuvers are used in this work to provide important information about different aspects of the dynamic behaviour of the vehicle and the effectiveness of each individual chassis control system, as well as the effectiveness of integrated chassis control management strategies. These test maneuvers are chosen such that all aspects of vehicle dynamics are addressed. In other words, the chosen test maneuvers act to clarify the performance and effect of different chassis control systems on the driver-vehicle-environment control loop, and quantify the advantages of each control method. The chosen test maneuvers are described in the following.

1) ISO double-lane-change Maneuver

The ISO double-lane-change is a closed-loop test maneuver that is used to evaluate the lateral dynamics of a vehicle based on the subjective evaluations of professional drivers. The specifications of the ISO double-lane-change maneuver are described in the ISO 3888 standard, and the test track design is illustrated in Figure 2-3. As described in [Pai05, Bau99], the driver starts this maneuver at a particular speed and releases the throttle. The driver then attempts to negotiate the course without striking the cones. The test speed is progressively increased until either instability occurs or the course can no longer be negotiated. Since a severe double-lane-change maneuver effectively demonstrates the cornering capability of a vehicle when driving at the friction limit in both directions, many car manufacturers and research institutions consider it to be a suitable test maneuver for assessing electronic stability controllers.

In this work, the desired vehicle trajectory in a double-lane-change maneuver is defined as a function of forward displacement using two fifth-order splines that are connected with a straight line segment in the middle [Bod06]:

$$y = f(x) = \begin{cases} 0 & if \quad x < 18.5 \\ c_1x^5 + \cdots + c_5x + c_6 & if \quad 18.5 \le x < 42 \\ 3.0425 & if \quad 42 \le x < 43 \\ c_7x^5 + \cdots + c_{11}x + c_{12} & if \quad 43 \le x < 65.5 \\ 0 & if \quad x \ge 65.5 \end{cases} \tag{2.1}$$

where c_1 to c_{12} denote parameters that are determined by enforcing boundary conditions on the splines. This desired vehicle trajectory is, in fact, the predefined target trajectory to which the driver model refers while driving through the test maneuver, and is indicated by a dashed line in Figure 2-3. Note that the second lane-change is more aggressive than the first one and, thus, asymmetric steering inputs are required to follow the desired path. In addition, the road is considered to be flat and dry with a coefficient of friction of $\mu = 1$.

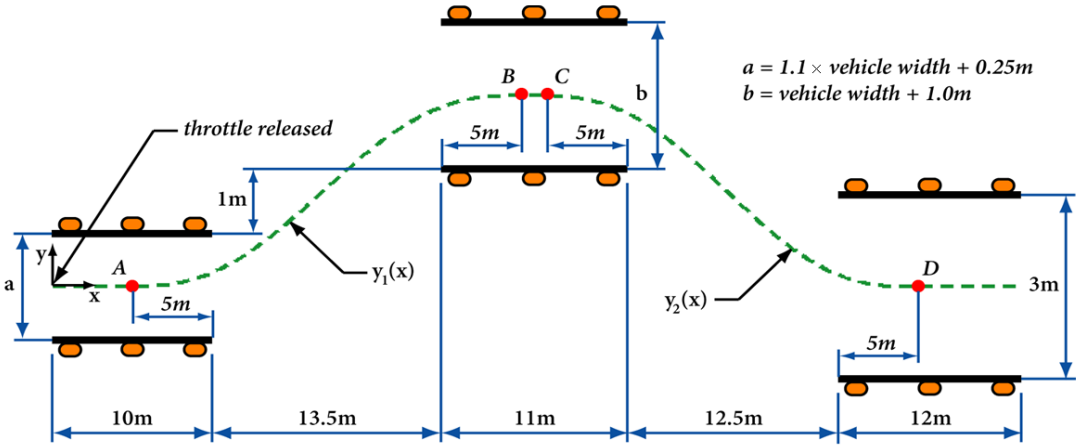

Figure 2-3: ISO 3888 double-lane-change maneuver test track design [Bau99]

Due to the importance of the double-lane-change maneuver, six different plots will be used to evaluate the performance of the vehicle and its different chassis control systems.

1. Actual and desired vehicle trajectories: This plot is used to determine whether the actual vehicle trajectory matches well with the predefined desired trajectory, and whether the driver is able to negotiate the course without striking the cones.
2. Actual and desired vehicle yaw rate and sideslip angle as functions of time: Based on these two plots, the quality of the match between the actual reaction of the vehicle and the reaction of the reference bicycle model is evaluated. In this regard, the

maximum sideslip angle ($|\beta|_{\max}$) and maximum yaw rate ($|\dot{\psi}|_{\max}$) of the vehicle must be observed, both of which should be small.

3. Lateral acceleration of the vehicle as a function of time: This plot reveals whether the vehicle reaches its physical limit when driving through the maneuver. The maximum lateral acceleration ($|a_y|_{\max}$) is observed, and should be a large number. A large lateral acceleration at a given steering wheel angle indicates that the traction potential on each tire is widely used to hold the vehicle on its desired path or, in other words, the vehicle is able to follow the driver's steering request even during emergency maneuvers [Bei00].
4. Driver's steering wheel input as a function of time: The gradient of this plot indicates the driver's effort during the maneuver and is an important factor when evaluating the quality of the handling and agility of the vehicle. In addition, the maximum steering wheel angle ($|\delta_{SW}|_{\max}$) is observed, which should be small. A small maximum steering wheel angle ensures that the driver is not exhausted or over-demanded when driving through an emergency maneuver.
5. Vehicle yaw rate as a function of steering wheel angle: This plot is a Lissajous figure that demonstrates the relationship between the input signal (the steering wheel angle) and the output signal (the vehicle yaw rate) of the driver-vehicle-environment control system. The resulting pattern in a Lissajous figure is a function of the ratio of the input and output signal frequencies [Cun89]. In addition, the hysteresis of the resulting pattern describes the phase shift between the input and output signals. Hence, this plot is considered to be a handling performance plot, where a smaller amount of hysteresis indicates a phase shift between the driver's steering wheel input and the yaw rate response of the vehicle, and better agility and responsiveness of the vehicle. The size of the hysteresis ($\Delta\dot{\psi}_H$) serves as a quantitative measure for comparing the performance of different chassis control systems.
6. Vehicle speed as a function of time: By observing the vehicle speed as a function of time, the effect of each chassis control system on vehicle speed is evaluated. The gradient of the speed plot indicates whether the activation of a chassis control system would have a detrimental effect on the vehicle longitudinal speed. Note that such a speed reduction is perceived by the driver as being annoying. Moreover, the speed

lost by the vehicle at the end of the maneuver ($v_{lost} = v_{start} - v_{end}$) is determined, and should be as small as possible.

Table 2-I summarizes the requirements for a desirable vehicle response during a double-lane-change maneuver.

Parameter	$\lvert\beta\rvert_{\max}$	$\lvert\dot{\psi}\rvert_{\max}$	$\lvert a_y\rvert_{\max}$	$\lvert\delta_{SW}\rvert_{\max}$	$\Delta\dot{\psi}_H$	v_{lost}
Requirement	small	small	large	small	small	small

Table 2-I: Criteria for desirable vehicle response during a double-lane-change maneuver

2) Step-steer response maneuver

A step-steer response is an open-loop test maneuver used to examine both transient and steady-state vehicle behaviour. In this test, the vehicle is driven in a straight line at a constant speed of 90 km/h, and a sudden limited steering wheel input is applied. The road is considered to be flat and dry, with a coefficient of friction of $\mu = 1$. Note that the rate of change of the steering wheel input is limited to 300^{o}/s, which corresponds to a driver's reaction time. Therefore, the step-steer is, in fact, a steep ramp input that is applied to the steering wheel. The steering wheel angle is determined such that a lateral acceleration of $a_y = 4$ m/s^2 is reached [Wal05]. The vehicle speed is kept constant by the speed controller.

The criteria for evaluating test results from this maneuver are similar to those described in the literature for a step response of a dynamic system. In this regard, a fast response of the vehicle yaw rate and lateral acceleration, with a sufficient amount of damping, is desirable. From a multitude of different performance measures that are defined in the literature for evaluating the step response of a dynamic system [Bol95], two measures are chosen to describe the performance of a step-steer response: rise time and percentage overshoot. The rise time ($t_{\dot{\psi}}$) is defined as the time required for the yaw rate response to rise from zero to 90% of the steady-state value. Rise time is a measure of how fast the vehicle responds to the steering input. The overshoot is the maximum amount by which the response exceeds the steady-state value. The overshoot is often written as a percentage of the steady-state value, which is then called percentage overshoot (PO) and is calculated as follows:

$$\mathrm{PO} = \frac{\dot{\psi}_{\max} - \dot{\psi}_{ss}}{\dot{\psi}_{ss}} \times 100\% \tag{2.2}$$

where $\dot{\psi}_{\max}$ is the maximum yaw rate and $\dot{\psi}_{ss}$ is the steady-state value of the yaw rate. Both of these performance measures, $t_{\dot{\psi}}$ and PO, must be small, which indicates a small phase delay and a good damping behaviour of the vehicle.

In addition, the maximum sideslip angle ($|\beta|_{\max}$) and the rise time of the lateral acceleration response of the vehicle (t_{a_y}) are also observed, both of which should, again, be small numbers. Table M-II summarizes the requirements for a desirable vehicle response during a step-steer test maneuver.

Parameter	$t_{\dot{\psi}}$	$\mathrm{PO} = \frac{\dot{\psi}_{\max} - \dot{\psi}_{ss}}{\dot{\psi}_{ss}} \times 100\%$	$\lvert\beta\rvert_{\max}$	t_{a_y}
Requirement	small	small	small	small

Table 2-II: Criteria for desirable vehicle response during a step-steer maneuver

3) Brake-in-turn maneuver

The brake-in-turn test maneuver simultaneously considers both the lateral and longitudinal dynamics of the vehicle. Brake-in-turn is one of the most critical maneuvers encountered in everyday driving. The reaction of the vehicle to this maneuver reveals the compromise between steerability, stability, and deceleration [ISO85].

In this work, the brake-in-turn maneuver is considered to be a closed-loop test maneuver, and begins with the vehicle being driven at a constant speed of 75 km/h into a curve with a radius of 60 m. Once the vehicle has reached a steady-state lateral acceleration, the driver intends to slow the vehicle to 20 km/h with a deceleration rate of 6 m/s^2. The path-following driver model attempts to keep the vehicle on the predefined circular path, while the speed controller reduces the vehicle speed at the predefined deceleration rate. The road is considered to be flat and dry with a coefficient of friction of $\mu = 1$.

Four plots are used to evaluate the behaviour of the vehicle in a brake-in-turn maneuver. First, the vehicle trajectory is plotted and the maximum lateral deviation of the vehicle with respect to the desired path ($\Delta y_{\mathbf{max}}$) is measured. The lateral deviation should be as small as possible. Second, the driver's steering wheel input is plotted as a function

of time. The gradient of this plot indicates the driver's effort to keep the vehicle on the desired path or, in other words, how easily the driver can control the vehicle when braking in a turn. The maximum steering wheel angle ($|\delta_{SW}|_{\max}$) is observed, which is an important indicator of driver effort. The final two plots illustrate the vehicle yaw rate and sideslip angle as functions of time. Due to the weight transfer away from the rear axle, the vehicle yaw rate and sideslip angle grow as the vehicle progresses toward larger deceleration rates. Again, the maximum yaw rate ($|\dot{\psi}|_{\max}$) and sideslip angle ($|\beta|_{\max}$) are observed, and should remain small. Table 2-III summarizes the requirements for a desirable vehicle response during a brake-in-turn maneuver.

Parameter	$\Delta y_{\max}$	$\lvert\delta_{SW}\rvert_{\max}$	$\lvert\dot{\psi}\rvert_{\max}$	$\lvert\beta\rvert_{\max}$
Requirement	small	small	small	small

Table 2-III: Criteria for desirable vehicle response during a brake-in-turn maneuver

4) Straight-line braking on a μ-split road

In order to better differentiate between the performance and effects of different chassis control systems on vehicle behaviour, a straight-line braking maneuver on a μ-split road is conducted [Roe98]. Braking on a μ-split road is a very critical test maneuver, since the vehicle will experience severe instability if the driver does not react immediately to correct the course of the vehicle. During this test, due to the asymmetric braking forces generated on the left and right tires, the vehicle will be pushed to the side of the road that has a higher coefficient of friction. In most cases, the asymmetric braking forces are high enough to cause the vehicle to turn around its vertical axis, which is a very dangerous situation. In general, a real instability of this nature is corrected by inexperienced drivers through the application of an inappropriate single steering wheel input that, in most cases, makes the situation even worse. An experienced driver, on the other hand, can avoid such a dangerous situation by performing a sequence of corrections based on the vehicle response, thereby regaining control of the vehicle. In this work, the straight-line braking on a μ-split road is considered as an open-loop test maneuver, in which the vehicle is driven at a constant speed of 80 km/h while the steering wheel is held fixed. The driver then attempts to stop the vehicle in an emergency braking situation on a μ-split road,

which has a black ice patch ($\mu_{ice} = 0.1$) on the left side and is dry ($\mu_{dry} = 1.0$) on the right side. The road is considered to be flat and the length of the ice patch is 10 meters.

In order to evaluate the performance of the vehicle and its chassis control systems, three plots are examined. First, the trajectory of the vehicle is analyzed to determine whether the vehicle becomes unstable and leaves the predefined road. The maximum lateral deviation of the vehicle with respect to the desired straight-line trajectory (Δy_{max}) is measured. This lateral deviation should be as small as possible. In addition, the braking distance of the vehicle ($\Delta x_{braking}$) is measured, which indicates the efficiency of a stability controller in emergency braking situations. The braking distance is the distance that the vehicle travels after the start of the braking action, and should be kept as small as possible. Next, the yaw rate and sideslip angle of the vehicle are plotted as functions of time. The gradients of these two plots indicate whether the vehicle becomes unstable and the extent to which the vehicle is sensitive to external disturbances. Moreover, the maximum yaw rate ($|\dot{\psi}|_{max}$) and sideslip angle ($|\beta|_{max}$) are measured from these plots. It is desirable to have small values for these two factors. Note that, in cases where an active steering system is used, it is also necessary to plot the steering angle of the vehicle as a function of time so that the activity of the active steering system can be analyzed. Table 2-IV summarizes the requirements for a desirable vehicle response during a straight-line braking maneuver on a μ-split road.

Parameter	Δy_{max}	$\Delta x_{braking}$	$\|\dot{\psi}\|_{max}$	$\|\beta\|_{max}$
Requirement	small	small	small	small

Table 2-IV: Criteria for desirable vehicle response during a straight-line braking maneuver on a μ-split road

2.1.2 Comprehensive evaluation of chosen test maneuvers

As mentioned earlier, a comprehensive evaluation of the dynamic characteristics of a vehicle and the effectiveness of different chassis control systems can only be obtained when the results of different test maneuvers are combined and evaluated as a whole. Four test maneuvers are used in this work to provide important information about different aspects of the dynamic behaviour of the vehicle and the effectiveness of each chassis control system. The results of these test maneuvers are evaluated with respect to four main performance characteristics: handling, stability, path-following capability, and

longitudinal dynamics. Such an approach makes it possible to evaluate the influence of each chassis control system on the reaction of the vehicle to the steering wheel input (handling), as well as the stability, path-following capability, and longitudinal dynamics of the vehicle during a maneuver. In this regard, each parameter measured during a test maneuver is assigned to one or more of the four main performance characteristics, as illustrated in Figure 2-4. The improvements in the dynamic behaviour of the vehicle are evaluated with respect to the uncontrolled vehicle, and the effectiveness of each chassis control system is estimated using the following quantitative assessment:

3 = very useful, very effective

2 = useful, effective

1 = useful and effective to some extent

0 = no influence, ineffective

Once the effectiveness of each candidate controller has been evaluated based on the four aforementioned driving maneuvers and with respect to the four main performance characteristics, a final comprehensive evaluation is performed in which the mean value of all individual test results within a category is calculated. In this way, each candidate controller can be compared to the others in terms of the four main performance characteristics.

Characteristic / Maneuver	Handling	Stability	Path following	Longitudinal dynamics
Double-lane-change	$\lvert\beta\rvert_{\max}$, $\lvert\dot{\psi}\rvert_{\max}$, $\lvert\delta_{SW}\rvert_{\max}$ $\Delta\dot{\psi}_H$, $\lvert a_y\rvert_{\max}$	$\lvert\beta\rvert_{\max}$, $\lvert\dot{\psi}\rvert_{\max}$		v_{lost}
Step-steer	$t_{\dot{\psi}}$, t_{a_y}, PO, $\lvert\beta\rvert_{\max}$			
Brake-in-turn	$\lvert\beta\rvert_{\max}$, $\lvert\dot{\psi}\rvert_{\max}$, $\lvert\delta_{SW}\rvert_{\max}$	$\lvert\beta\rvert_{\max}$, $\lvert\dot{\psi}\rvert_{\max}$	$\Delta y_{\max}$	
Straight-line braking on a μ-split road		$\lvert\beta\rvert_{\max}$, $\lvert\dot{\psi}\rvert_{\max}$	$\Delta y_{\max}$	$\Delta x_{braking}$

Figure 2-4: Important properties of the dynamic behaviour of the vehicle evaluated by each test maneuver

2.2 Modelling the behaviour of a driver

In order to evaluate the handling and performance of the vehicle in the design stage and the effectiveness of different chassis control subsystems before implementing them in a

real vehicle, the simulation of a large number of different maneuvers is necessary. As discussed above, there is a significant difference between open-loop test maneuvers, which are defined by chronological control inputs and are routinely used for the subjective evaluation of handling performance, and closed-loop test maneuvers, which primarily involve a path-following task. However, in order to realize these test maneuvers in the simulation environment, not only is a mathematical vehicle model needed for every test maneuver, but a driver model must also be designed to simulate the closed-loop test maneuvers. The role of the driver model is to calculate the control inputs required to successfully follow a predefined path. Such a driver model can be implemented as an inverse dynamics problem [Dix96] or by a representation of a driver that can look ahead, preview the path, and change the steering wheel angle accordingly [Guo93, Oez95].

There exist a variety of controllers suitable for modelling driver behaviour, some of which are more complex than the others. Therefore, one should first choose the level of modelling fidelity required to achieve the task at hand, based on the needs of the simulation. In general, driver models fall into two main categories: optimum control models and moment-by-moment feedback models [Blu04]. Optimum control models use some form of penalty function as a measure to assess the quality of the control achieved. These models use repeated simulations of a specific event and numerical optimization methods to tune the parameters of the driver model such that the value of the defined penalty function is minimized over the duration of the event of interest. Although optimum control models are suitable for learned events, such as the circuit driving of race cars, some care must be exercised with their use for evaluating the performance of regular passenger cars. Since the average driver of a passenger vehicle is generally unskilled, the application of modelling techniques in which repeated simulations are used to discover the so-called ‘best’ way of achieving a maneuver may not be an appropriate way of simulating an emergency situation, where the driver has only one attempt to complete the maneuver [Guo93, Mac96]. Moment-by-moment feedback models are a subset of the optimum control models, with the difference being that the feedback parameters of the controller are set once by the analyst and remain constant thereafter. Although these models are less appropriate for predicting the driver behaviour for circuit racing, they add clarity in understanding the vehicle behaviour and driver inputs when driving through a test maneuver [Sha00]. Such driver models are also more appropriate for understanding

the effects of different chassis control systems on both the vehicle and the driver when driving through closed-loop test maneuvers.

2.2.1 Development of a path-following driver model

With these facts in mind, a moment-by-moment feedback driver model that is similar to the model described in [Oez95] is developed in this work, but is enhanced with a more sophisticated path previewing technique. The driver model described in [Oez95] uses a single-preview-point steering control model, whose objective is to steer a ground vehicle along a reference line located in the middle of the lane to be followed. In this regard, a single arbitrary look-ahead point is defined along the local longitudinal axis of the vehicle, and the distance between the look-ahead point and the reference path is defined as the "look-ahead offset". The required steer angle is then calculated as a function of the look-ahead offset, vehicle longitudinal velocity, and various vehicle parameters. A linear bicycle model is used, as illustrated in Figure 2-5, to obtain the following linear state-space equation [Oez95]:

$$\begin{bmatrix}\dot{v}\\ \dot{r}\end{bmatrix}=\begin{bmatrix}-\dfrac{C_{\alpha f}+C_{\alpha r}}{m_{CG}\cdot u} & -u+\dfrac{b\cdot C_{\alpha r}-a\cdot C_{\alpha f}}{m_{CG}\cdot u}\\ \dfrac{b\cdot C_{\alpha r}-a\cdot C_{\alpha f}}{I_z\cdot u} & -\dfrac{a^2\cdot C_{\alpha f}+b^2\cdot C_{\alpha r}}{I_z\cdot u}\end{bmatrix}\cdot\begin{bmatrix}v\\ r\end{bmatrix}+\begin{bmatrix}\dfrac{C_{\alpha f}}{m_{CG}}\\ \dfrac{a\cdot C_{\alpha f}}{I_z}\end{bmatrix}\cdot\delta \tag{2.3}$$

where $\vec{u}$, $\vec{v}$, and $\vec{r}$ are, respectively, the longitudinal, lateral, and yaw rate vectors of the vehicle, and $u=|\vec{u}|$, $v=|\vec{v}|$, and $r=\dot{\psi}=|\vec{r}|$ are the magnitudes of these vectors. In addition, *a* and *b* are the distances of the front and rear axles to the vehicle center of gravity, m_{CG} is the vehicle mass, I_z is the yaw moment of inertia, δ is the steering angle of the front wheel, and $C_{\alpha f}$ and $C_{\alpha r}$ are the total cornering stiffnesses of the front and rear tires, respectively. As illustrated in Figure 2-5, $\vec{V}$ indicates the velocity vector of the vehicle's center of gravity, whose magnitude is $V=|\vec{V}|=\sqrt{u^2+v^2}$. Note that the vehicle coordinate axes are in accordance with the ISO 4130 and DIN 70000 standards, where the Z direction points upwards, the X-axis is along the vehicle longitudinal axis and points towards the front of the vehicle, and the Y-axis points left when viewing along the positive X direction.

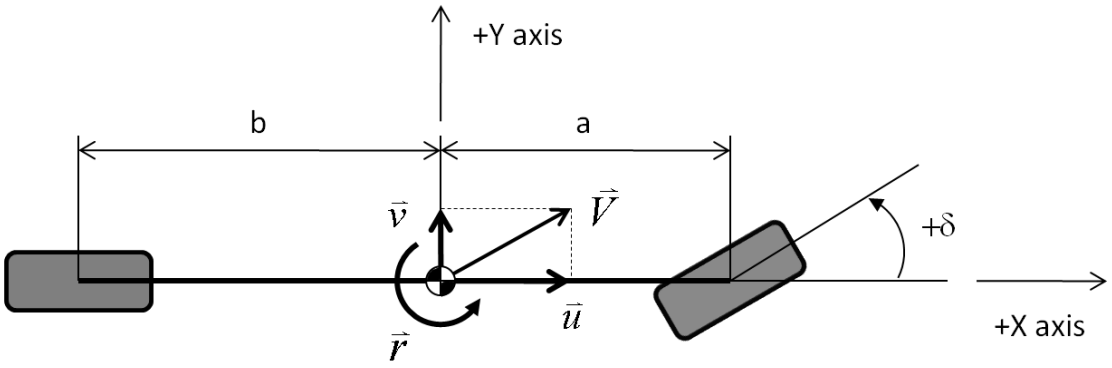

Figure 2-5: Linear bicycle model used for developing the driver model

Figure 2-6 illustrates the vehicle motion along a desired circular path of radius *R*, where the distance between the center of gravity of the vehicle and the look-ahead point is defined as look-ahead distance (*d*), the distance between the look-ahead point and the point on the curve closest to it is defined as look-ahead offset (*o*), and the distance between the look-ahead point and the center of the curve is defined as *h*. By considering the steady-state motion of the vehicle along the curve, where the vehicle perfectly tracks the desired path, explicit expressions are obtained for the variables v_{ss}, r_{ss}, V_{ss}, δ_{ss}, o_{ss}, and h_{ss}. All of these expressions are in terms of the vehicle longitudinal speed *u*, the radius of curvature *R*, and the vehicle parameters. Note that the subscript '*ss*' indicates that the values are calculated when the vehicle is in a steady-state condition, where $\dot{v} = \dot{r} = 0$, the center of gravity of the vehicle perfectly tracks the desired curve, the velocity vector *V* is tangent to the curve, and the longitudinal velocity *u* is held constant. At steady-state, equation (2.3) becomes the following:

$$-\begin{bmatrix} -\dfrac{C_{\alpha f}+C_{\alpha r}}{m_{CG}\cdot u} & -u+\dfrac{b\cdot C_{\alpha r}-a\cdot C_{\alpha f}}{m_{CG}\cdot u} \\ \dfrac{b\cdot C_{\alpha r}-a\cdot C_{\alpha f}}{I_z\cdot u} & -\dfrac{a^2\cdot C_{\alpha f}+b^2\cdot C_{\alpha r}}{I_z\cdot u} \end{bmatrix}\cdot\begin{bmatrix} v_{ss} \\ r_{ss} \end{bmatrix}=\begin{bmatrix} \dfrac{C_{\alpha f}}{m_{CG}} \\ \dfrac{a\cdot C_{\alpha f}}{I_z} \end{bmatrix}\cdot\delta_{ss} \tag{2.4}$$

From equation (2.4), the steady-state lateral velocity (v_{ss}) can be calculated as a function of the steady-state yaw rate (r_{ss}) as follows [Oez95]:

$$v_{ss}=T\cdot r_{ss},\ \text{where}\ \ T=b-\frac{a\cdot m_{CG}\cdot u^2}{C_{\alpha r}\cdot(a+b)} \tag{2.5}$$

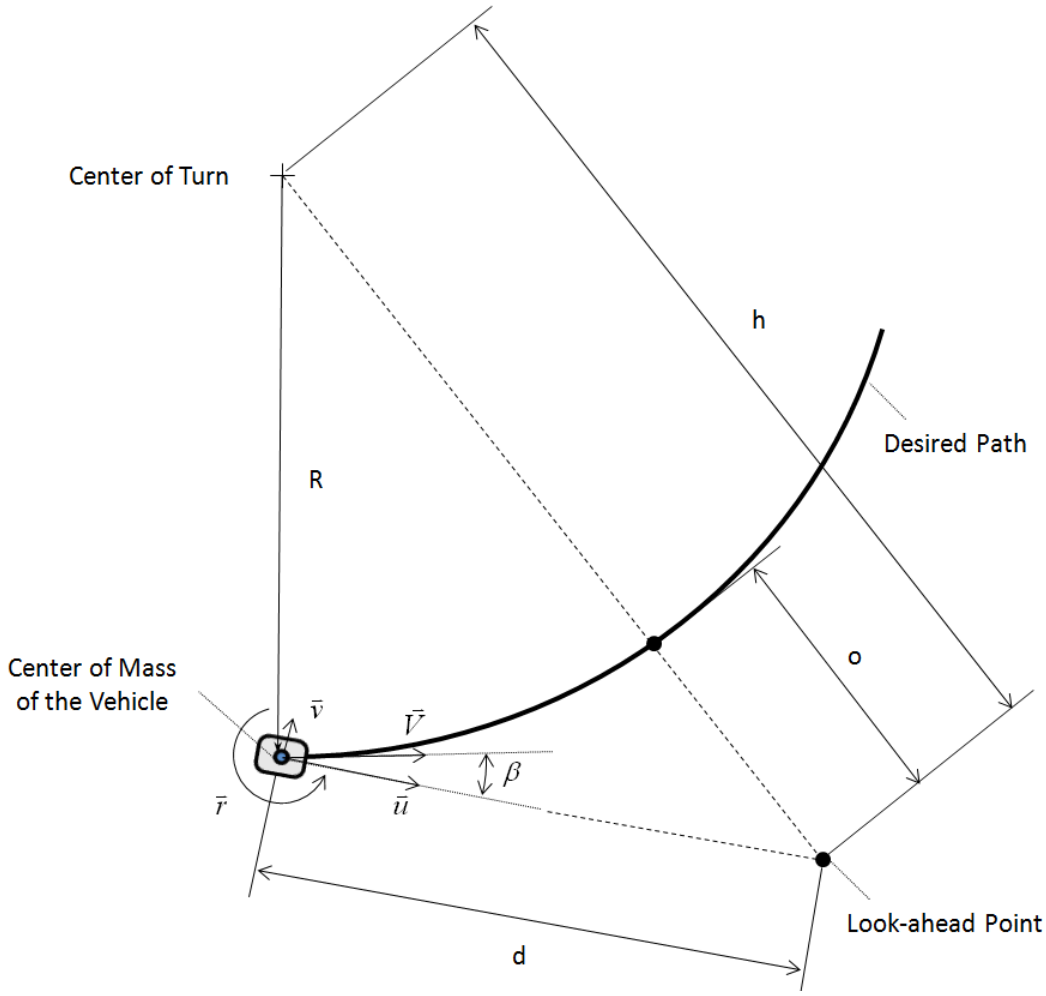

Figure 2-6: Steady-state vehicle motion along a circular path of radius R

In general, the following statements can be made for a vehicle in steady-state circular motion [Oez95]:

$$V_{ss} = \sqrt{u^2 + v_{ss}^2} \tag{2.6}$$

$$V_{ss} = R \cdot r_{ss} \tag{2.7}$$

One can now obtain new expressions for r_{ss} and δ_{ss} from equations (2.4) to (2.7) that are only in terms of the vehicle longitudinal speed u, the radius of curvature R, and vehicle parameters [Oez95]:

$$r_{ss} = \frac{u}{\sqrt{R^2 - T^2}} \tag{2.8}$$

$$\delta_{ss} = \frac{1}{\sqrt{R^2 - T^2}} \cdot \left(a + b - \frac{m_{CG} \cdot u^2 \cdot \left(a \cdot C_{\alpha f} - b \cdot C_{\alpha r} \right)}{(a+b) \cdot C_{\alpha f} \cdot C_{\alpha r}} \right) \tag{2.9}$$

According to equation (2.5), the largest value for T is always less than b, which is the distance of the rear axle to the vehicle center of gravity. Since, in reality, a vehicle with front steering system can never have a radius of curvature less than its wheelbase, equations (2.8) and (2.9) will never encounter a singularity problem.

In order to calculate an appropriate expression for the steady-state look-ahead offset o_{ss}, where $o_{ss} = h_{ss} - R$, an expression for h_{ss} is first defined as follows [Oez95]:

$$h_{ss} = \sqrt{d^2 + R^2 - 2R \cdot d \cdot \cos\left(\frac{\pi}{2} + \beta\right)} = \sqrt{d^2 + R^2 - 2R \cdot d \cdot \frac{v_{ss}}{V_{ss}}} \tag{2.10}$$

Using equations (2.5), (2.7), and (2.10), the final expressions for h_{ss} and o_{ss} are obtained as follows [Oez95]:

$$h_{ss} = \sqrt{d^2 + R^2 + 2 \cdot d \cdot T} \tag{2.11}$$

$$o_{ss} = \sqrt{d^2 + R^2 + 2 \cdot d \cdot T} - R \tag{2.12}$$

Finally, from equations (2.9) and (2.12), the ratio between the desired steering input δ_{ss} and the look-ahead offset o_{ss} is calculated as follows [Oez95]:

$$\frac{\delta_{ss}}{o_{ss}} = \frac{\frac{1}{\sqrt{R^2 - T^2}} \cdot \left(a + b - \frac{m_{CG} \cdot u^2 \cdot \left(a \cdot C_{\alpha f} - b \cdot C_{\alpha r} \right)}{(a+b) \cdot C_{\alpha f} \cdot C_{\alpha r}} \right)}{\sqrt{R^2 + d^2 + 2 \cdot d \cdot T} - R} \tag{2.13}$$

At this point, two important assumptions are made by the authors of [Oez95] in order to simplify equation (2.13). First, using Taylor's expansion:

$$\forall x, \varepsilon \in \mathbb{R},\ x > 0\text{: if } \frac{|\varepsilon|}{x} \ll 1 \Rightarrow \sqrt{x + \varepsilon} = \sqrt{x} + \frac{\varepsilon}{2\sqrt{x}} \tag{2.14}$$

and assuming that $\frac{|d \cdot (d + 2 \cdot T)|}{R} \ll 1$, equation (2.13) can be rewritten as follows [Oez95]:

$$\frac{\delta_{ss}}{o_{ss}} = \frac{2 \cdot \left(a + b - \frac{m_{CG} \cdot u^2 \cdot \left(a \cdot C_{\alpha f} - b \cdot C_{\alpha r} \right)}{(a+b) \cdot C_{\alpha f} \cdot C_{\alpha r}} \right)}{\sqrt{1 - \frac{T^2}{R^2}} \cdot d \cdot (d + 2 \cdot T)} \tag{2.15}$$

Next, by assuming that $\frac{|T|}{R} \ll 1$ and, thus, $\sqrt{1 - \frac{T^2}{R^2}} \approx 1$, equation (2.15) can be further simplified as follows [Oez95]:

$$\delta_{ss} \approx \frac{2 \cdot \left(a + b - \frac{m_{CG} \cdot u^2 \cdot \left(a \cdot C_{\alpha f} - b \cdot C_{\alpha r} \right)}{(a+b) \cdot C_{\alpha f} \cdot C_{\alpha r}} \right)}{d \cdot (d + 2 \cdot T)} \cdot o_{ss} \tag{2.16}$$

Equation (2.16) indicates that the steering angle required to keep the vehicle on a circular path when in steady-state motion is a function of the look-ahead offset o_{ss}, the vehicle longitudinal velocity u, the look-ahead distance d, and various vehicle parameters. It is important to notice that equation (2.16) is independent of the radius of curvature R, which makes it attractive for use in a driver model that is suitable for every possible road profile. Moreover, since equation (2.16) is a function of vehicle forward velocity, it updates itself as the vehicle speed changes, as in a gain scheduling controller. The stability of this steering controller has been proven analytically in [Oez95] using the Routh-Hurwitz technique.

Many researchers believe that using a single preview point for describing a driver model is unrealistic and, therefore, unsatisfactory [Guo93, Mac96, Sha00]. If the look-ahead point is too far in front of the vehicle, it will be inappropriate to act on the preview information at the time of its acquisition, and the information has been lost by the time it is useful. On the other hand, if the look-ahead point is too close to the vehicle, it necessarily causes very poor control, especially at higher speeds. Moreover, if the road profile is complex, a single-preview-point model can result in a situation where its information does not coincide with the current state of the vehicle, even with a proper look-ahead distance (Figure 2-7-a). Realistically, one cannot imagine that a human driver only uses the information from a single look-ahead point in order to make an appropriate decision on how to adjust the steering wheel.

In order to solve this problem, the single-preview-point driver model described by equation (2.16) is enhanced in this work by taking two additional steps. First, the look-ahead distance is redefined to be a function of the vehicle longitudinal velocity and the driver's reaction time, as described in the following:

$$d_{look-ahead}(t) = d_{const} + t_{driver} \cdot u(t) \tag{2.17}$$

where d_{const} is a constant distance that the driver will look ahead, even at lower velocities, t_{driver} is the reaction time of the driver, and u is the vehicle longitudinal velocity. Notably, the constant distance that the driver looks ahead is chosen to be 4 meters and the reaction time of the driver is 0.7 seconds. Equation (2.17) indicates that the faster the vehicle is

driven, the longer the look-ahead distance will be, which corresponds well with the reaction of a real driver. In the second step, five preview points are defined on the "optical lever" of the driver, which is along the local longitudinal axis of the vehicle, between the vehicle center of gravity and the look-ahead distance. The coordinates of the preview points on the optical lever of the driver are calculated as follows [Sha00]:

$$\begin{cases} x_{pp,i}(t) = x_{CG}(t) + K_i \cdot d_{look-ahead}(t) \cdot \cos(\psi(t)) \\ y_{pp,i}(t) = y_{CG}(t) + K_i \cdot d_{look-ahead}(t) \cdot \sin(\psi(t)) \end{cases} \tag{2.18}$$

where $x_{pp,i}(t)$ and $y_{pp,i}(t)$ are the coordinates of the i^{th} preview point, and $x_{CG}(t)$ and $y_{CG}(t)$ define the coordinates of the vehicle center of gravity at time t in the global reference frame, respectively. K_i is the relative distance between the i^{th} preview point and the vehicle center of gravity on the optical lever, $d_{look-ahead}(t)$ is the look-ahead distance defined in equation (2.17), and $\psi(t)$ is the vehicle yaw angle at time t. The lateral offset of each preview point from its corresponding point on the desired path is calculated as the distance between the preview point and the desired path, measured along a line that is perpendicular to the optical lever, as shown in Figure 2-7-b.

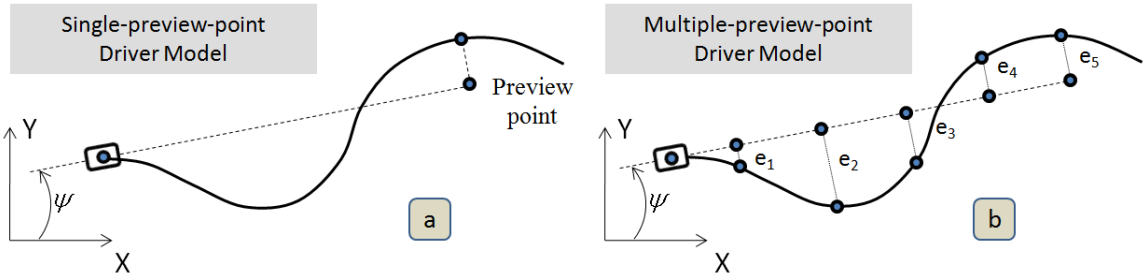

Figure 2-7: (a) Single-preview-point and (b) multiple-preview-point driver models

The new look-ahead offset is then defined as the weighted sum of all the lateral offsets:

$$e_i(t) = \left(y_{R,i}(t) - y_{pp,i}(t)\right) \cdot \cos\left(\psi(t)\right) - \left(x_{R,i}(t) - x_{pp,i}(t)\right) \cdot \sin\left(\psi(t)\right) \tag{2.19}$$

$$o(t) = \sum_{i=1}^{5} \left(G_i \cdot e_i(t)\right) \tag{2.20}$$

where $e_i(t)$ is the lateral offset, $x_{R,i}(t)$ and $y_{R,i}(t)$ are the coordinates of the intersection between the line perpendicular to the optical lever and the desired path, and G_i is the control gain of the i^{th} preview point. Note that the control gains of the driver model are derived in an ad hoc fashion based on intuition, not on any formal optimization scheme. The following control gains are chosen for the driver model: $G_1 = 3$, $G_2 = 5$, $G_3 = 4$, $G_4 =$

1, and G_5 = 0.5. The new driver model is described by combining equations (2.16) and (2.20) as follows:

$$\delta_{ss}(t) = \frac{2 \cdot \left(a + b - \frac{m_{CG} \cdot u^2(t) \cdot \left(a \cdot C_{\alpha f} - b \cdot C_{\alpha r} \right)}{(a+b) \cdot C_{\alpha f} \cdot C_{\alpha r}} \right)}{d_{look-ahead}(t) \cdot \left(d_{look-ahead}(t) + 2 \cdot \left(b - \frac{a \cdot m_{CG} \cdot u^2(t)}{C_{\alpha r} \cdot (a+b)} \right) \right)} \cdot \sum_{i=1}^{5} \left(G_i \cdot e_i(t) \right) \tag{2.21}$$

It is important to note that one can also add an orientation error, the error between the desired and actual vehicle yaw angles, to equation (2.20) in order to make the steering input of the driver model a function of position error as well as orientation error. However, in this work, only position error is considered.

2.2.2 Development of a speed-control driver model

As mentioned earlier, one of the tasks of a driver model is to adjust the brake and accelerator pedal positions such that the deviation between the desired and actual vehicle speeds is minimized. In order to do this, a gain scheduling PID controller is developed as the speed controller for the AUTO21EV. PID controllers are very popular and are widely used in industry because of their simple structure and robust performance in a wide range of operating conditions. The design of such controllers requires the specification of three parameters: the proportional, integral, and derivative gains. The important problem of tuning a PID controller involves finding appropriate settings for these three gains. The conventional approach to defining the PID parameters is to study a mathematical model of the dynamic system and attempt to derive a fixed set of gain parameters that are valid in a wide range of operating conditions. One well-known example of such an approach is the Ziegler-Nichols method [Zie42]. Such a method works well for processes or dynamic systems that can be modelled using linear first- or second-order systems; however, most real industrial processes or dynamic systems have characteristics such as higher-order dynamics, dead-zones, or nonlinearity that make modelling them with simple linear systems inaccurate. Therefore, in the last couple of decades, there have been some efforts to find and improve tuning methods that can update the gain parameters of PID controllers at any instant based on a structurally fixed parameter-evolving process model.

One of these tuning methods is adaptive control, which uses a control scheme that is capable of modifying its behaviour in response to changes in the dynamic system. There are three well-known adaptive control schemes: gain scheduling, model-reference

adaptive control, and self-tuning regulators. The gain scheduling technique is based on the adjustment of controller parameters in response to the operating conditions of a dynamic system. This type of control system is particularly useful when the variations in the dynamic system are predictable and when the control parameters need to be adjusted quickly in response to these variations [Kar04]. Figure 2-8 shows a block diagram of the gain scheduling speed controller developed in this work. As shown in the figure, the difference between the driver's speed request and the actual vehicle speed is measured and amplified by the PID controller at each time step; the PID controller then outputs the required motor torque at each wheel accordingly. At this stage, it is assumed that the torque calculated by the gain scheduling speed controller ($T_{Driver,req}$) is applied to each wheel. In other words, the total amount of torque that is applied to the vehicle is equal to the following:

$$T_{total} = 4 \times T_{Driver,req} \tag{2.22}$$

In this case, the required motor torque ($T_{Driver,req}$) is the input to the in-wheel motor controller described in [Vog07]. However, it is important to note that the required motor torque at each wheel may be modified by the advanced slip controller and/or the advanced torque vectoring system, which will be discussed later, depending on the traction potential of the tire or the vehicle driving dynamics.

The proportional (K_P^*), integral (K_I^*), and derivative (K_D^*) gains of the gain scheduling PID controller are all defined to be proportional to the vehicle forward speed, as follows:

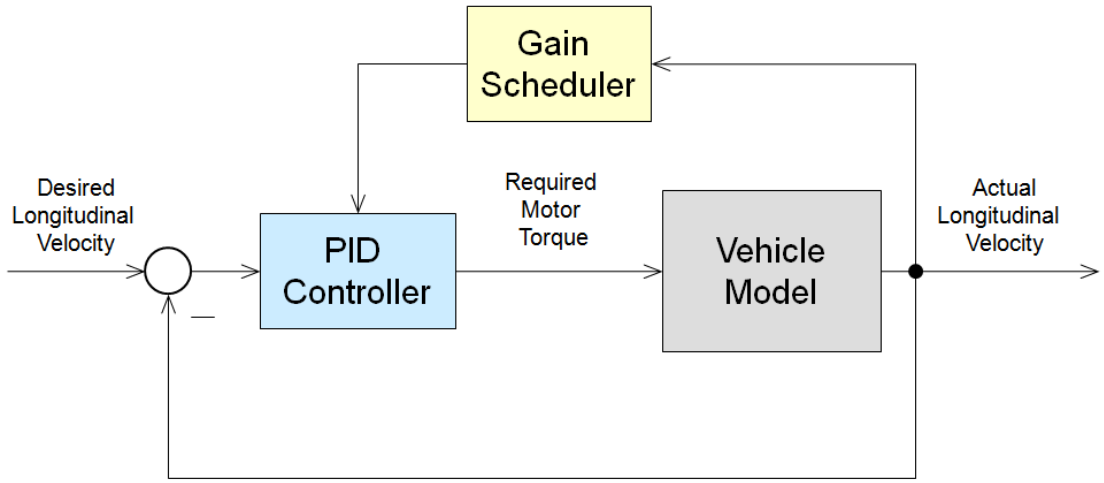

Figure 2-8: Block diagram of the gain scheduling speed controller

$$K_P^* = K_P \cdot u_{act} \tag{2.23}$$

$$K_I^* = K_I \cdot u_{act} \tag{2.24}$$

$$K_D^* = K_D \cdot u_{act} \tag{2.25}$$

where $K_P = 70$, $K_I = 0.05$, and $K_D = 0.05$ are constant gains and u_{act} is the actual longitudinal speed of the vehicle. Thus, the following equation describes the output of the gain scheduling PID controller:

$$T_{req}(t) = K_P^* \cdot e + K_I^* \cdot \int e \cdot dt + K_D^* \cdot \frac{de}{dt} \tag{2.26}$$

where $e = u_{des} - u_{act}$ is the difference between the desired (u_{des}) and actual (u_{act}) vehicle speed. Since the proposed gain scheduling PID controller is part of a digital control system, the derivative and integral parts of the controller are approximated as follows:

$$\int_{t-T_s}^{t} e \cdot dt \approx \frac{1}{2}\left(e(t) + e(t-T_s)\right) \cdot T_s \tag{2.27}$$

$$\frac{de}{dt} \approx \frac{e(t) - e(t-T_s)}{T_s} \tag{2.28}$$

where t is the current simulation time and T_s is the sampling time. It is important to notice that the controller gain parameters, namely K_P, K_I, and K_D, are tuned manually using a trial-and-error approach such that a sufficiently fast response with no overshoot is obtained over the entire speed range.

2.3 Evaluation of the path-following and speed-control driver models

The performance of the proposed path-following driver model, described in equation (2.21), is evaluated using two test maneuvers. First, a severe ISO double-lane-change maneuver with obstacle avoidance is used to evaluate the performance of the driver model. As mentioned before, the ISO double-lane-change maneuver is a closed-loop test maneuver typically used to adjust the dynamics of a vehicle based on the subjective evaluations of professional drivers. In addition, the complexity of the course used in this maneuver is a good example for demonstrating the performance of the path-following driver model.

Figure 2-9 illustrates the concept behind the path-following driver model. At each time step, the driver model looks ahead along the vehicle longitudinal axis and calculates

the look-ahead offset as the weighted sum of five lateral offsets. As mentioned earlier, each lateral offset is calculated as the distance between the preview point and the desired path measured along a line that is perpendicular to the optical lever. Using equation (2.21), the driver model changes the steering wheel angle based on the look-ahead offset, the vehicle longitudinal speed, the look-ahead distance, and vehicle parameters.

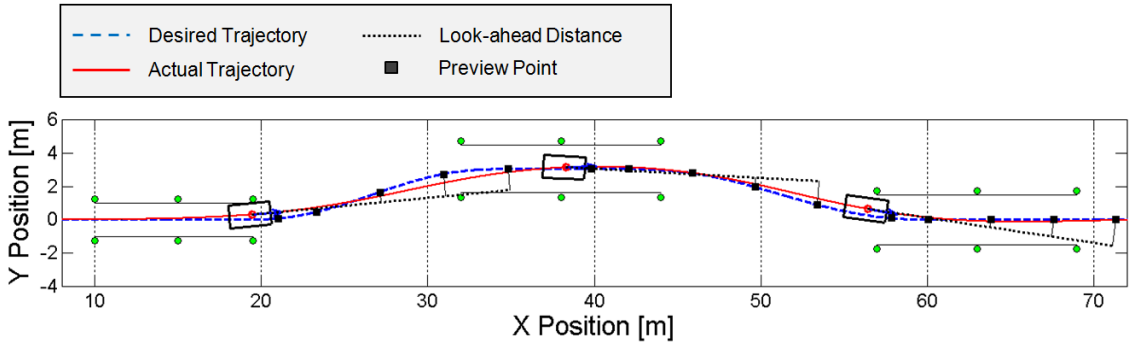

Figure 2-9: Path-following driver model concept in a double-lane-change maneuver

Figure 2-10-a illustrates the vehicle trajectory when driving through the double-lane-change maneuver at 40 km/h. In this simulation, the full AUTO21EV vehicle model developed in the ADAMS/View environment is used (Appendix A), which is equipped with tires using the *Pacejka* 2002 [Pac02] tire model. The simulation time is 8 seconds with a sample time of 1 millisecond. A fixed-step fourth-order Runge-Kutta solver is used to integrate the dynamic equations of motion. As shown in the figure, the path-following driver model is able to steer the vehicle through the desired path such that the actual vehicle trajectory matches well with the desired one. Figure 2-10-b illustrates the steering wheel input applied by the driver model, and Figure 2-10-c shows the vehicle yaw rate with respect to the driver's steering wheel input. Note that the steering system has a gear ratio of 1:18 (Appendix A). Figure 2-10-c demonstrates the handling capabilities of the vehicle, as the closer this plot is to a straight narrow line, the more the vehicle behaves like its reference bicycle model, which indicates better responsiveness of the vehicle to the driver's steering input. Looking at the vehicle yaw rate and sideslip angle shown in Figure 2-11, it is clear that the actual vehicle yaw rate is very close to the desired yaw rate, which is calculated using the reference bicycle model (Chapter 4, equation 4.12). Moreover, the vehicle sideslip angle is very small – less than 0.4 degrees – which indicates a slight understeering behaviour of the vehicle.

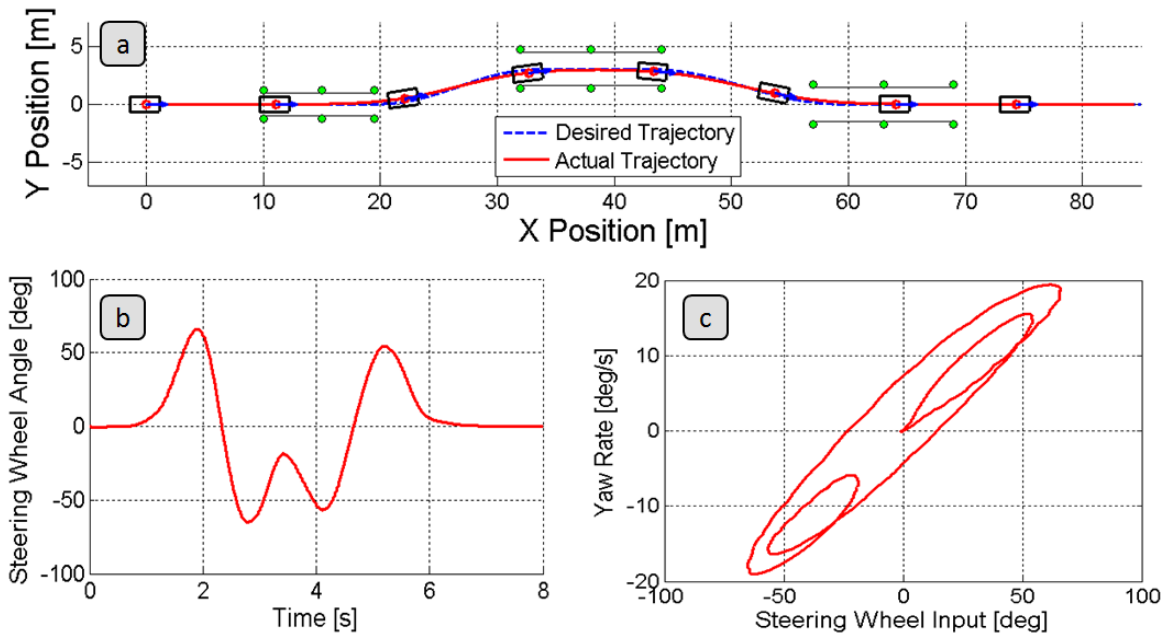

Figure 2-10: (a) Desired and actual vehicle trajectories, (b) driver's steering wheel input, and (c) vehicle yaw rate with respect to the steering wheel angle when driving through a double-lane-change maneuver at 40 km/h using the path-following driver model

In order to investigate the behaviour of the driver model in the nonlinear operating regime of the vehicle, the double-lane-change maneuver is repeated at a speed of 75 km/h. Figure 2-12-a illustrates the vehicle trajectory when driving through the double-lane-change maneuver. Due to the fact that the vehicle is operating at its physical limit, the path-following driver model is unable to exactly match the actual vehicle trajectory with the desired one; however, the driver model is able to keep the vehicle under control throughout the entire maneuver, using counter-steering at some points. Figure 2-12-b shows the driver's steering wheel input which, in comparison to that shown in Figure 2-10-b, is much larger. Figure 2-12-c illustrates the vehicle yaw rate with respect to the driver's steering wheel input, which is considered to be a handling performance figure. Comparing this plot with Figure 2-10-c, it is clear that the phase shift between the vehicle yaw rate and the driver's steering wheel input is much larger when driving through the double-lane-change maneuver at a high speed, which ultimately indicates that the vehicle responsiveness has been reduced. Figure 2-13 illustrates the vehicle yaw rate and sideslip angle for this maneuver, and confirms that the vehicle was operating within its physical limits.

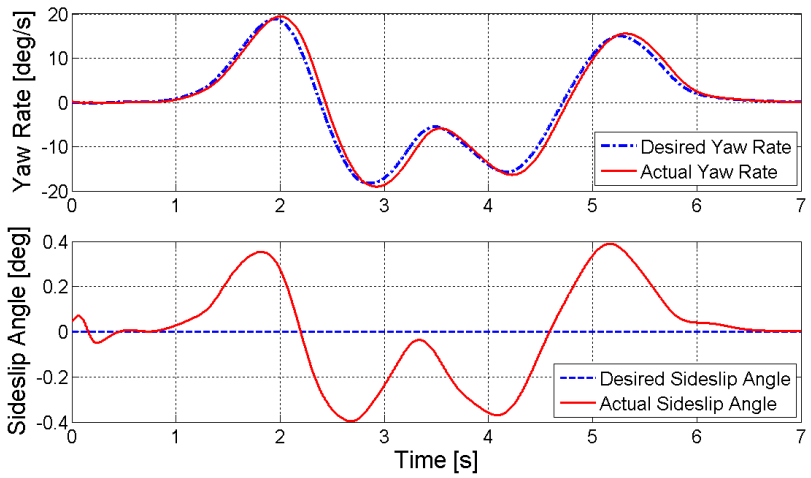

Figure 2-11: Desired and actual vehicle yaw rate (top) and sideslip angle (bottom) when driving through a double-lane-change maneuver at 40 km/h using the path-following driver model

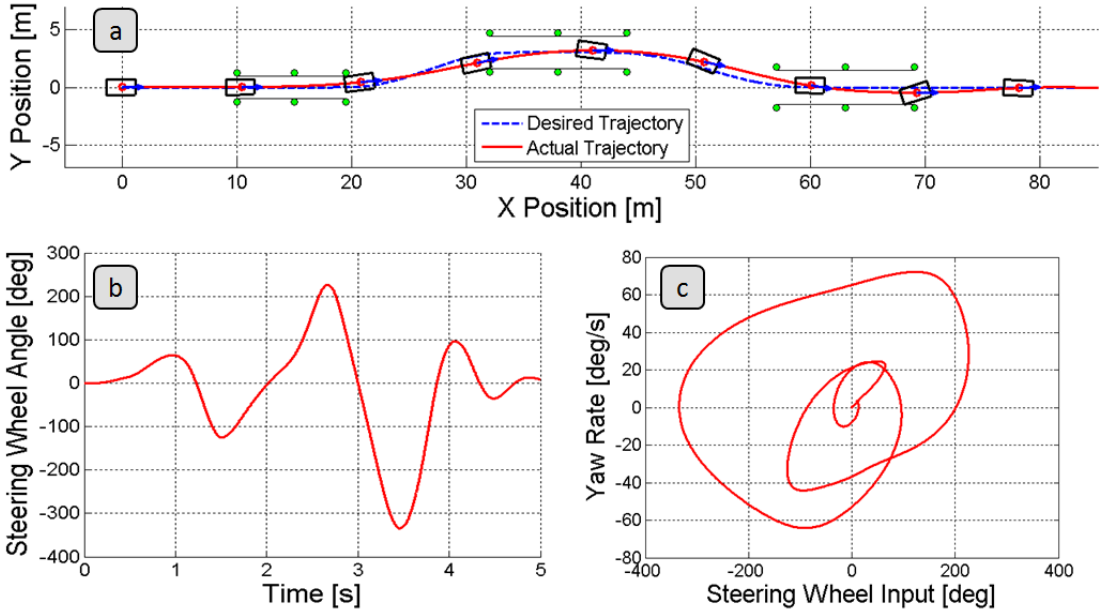

Figure 2-12: (a) Desired and actual vehicle trajectories, (b) driver's steering wheel input, and (c) vehicle yaw rate with respect to the steering wheel angle when driving through a double-lane-change maneuver at 75 km/h using the path-following driver model

The second test maneuver that is used to evaluate the performance of the multiple-preview-point path-following driver model is a steady-state constant radius cornering maneuver. Here, the AUTO21EV is driven through a circular path with a radius of 75 meters. The driver model attempts to keep the vehicle on the predefined path while the vehicle speed is continuously increasing from an initial speed of 5 km/h to a maximum speed of 90 km/h. As illustrated in Figure 2-14-a, the driver model is able to keep the vehicle on the predefined circular path even at higher velocities. Figure 2-14-b shows the steering wheel angle that the driver model applies to keep the vehicle on the circular path.

As can be seen, the driver model continuously adjusts the steering wheel angle in order to keep the vehicle on the desired path. As the vehicle speed is increased, the driver model applies a larger steering wheel angle, thereby generating larger lateral forces on the front axle in order to compensate for the larger centripetal acceleration. Figure 2-14-c illustrates the desired and actual vehicle forward speeds as functions of time. This figure confirms the performance of the gain scheduling PID speed controller, as the actual vehicle speed precisely follows the driver's speed request.

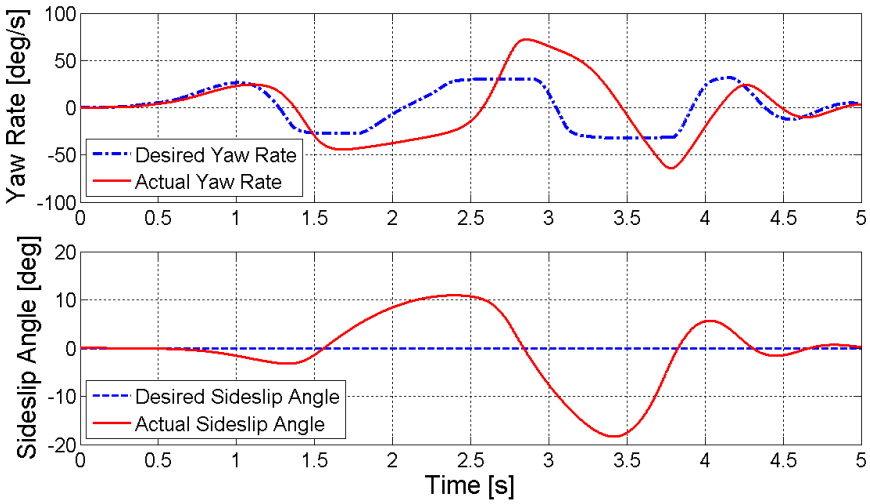

Figure 2-13: Desired and actual vehicle yaw rate (top) and sideslip angle (bottom) when driving through a double-lane-change maneuver at 75 km/h using the path-following driver model

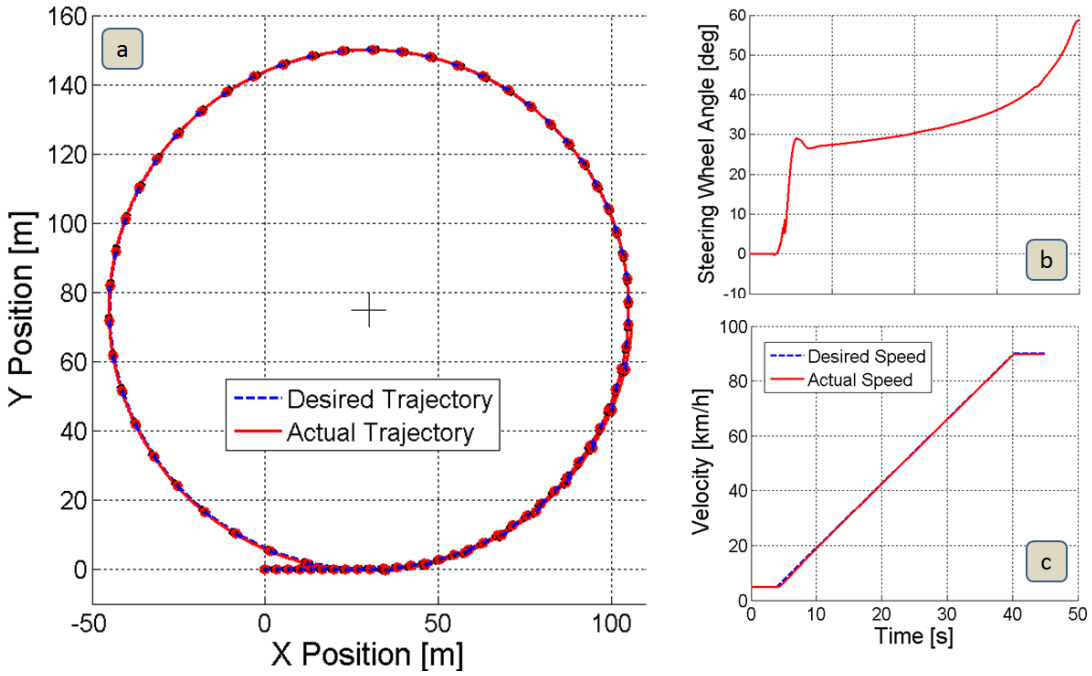

Figure 2-14: (a) Desired and actual vehicle trajectories, (b) required steering wheel angle applied by the driver model, and (c) desired and actual vehicle longitudinal speeds when driving through the steady-state constant radius maneuver using the path-following and speed-control driver models

The steering wheel angle applied by the driver model as a function of vehicle lateral acceleration is illustrated in Figure 2-15-a. It is apparent that the steering wheel angle has a linear gradient up to a lateral acceleration of 4 m/s^2 and then progressively increases as lateral acceleration grows. This plot very clearly indicates the understeering characteristic of the AUTO21EV. In fact, the slope of the linear region of this curve is equal to the understeering gradient of the vehicle calculated in the design stage [Bod06]. As illustrated in Figure 2-15-b, the gradient of the sideslip angle is approximately linear for the majority of the lateral acceleration range, which indicates good vehicle handling. The maximum sideslip angle of the vehicle is measured as $|\beta|_{\max} = 5.7^\circ$, which is acceptable. Moreover, the maximum lateral acceleration is calculated to be 8.3 m/s^2, which is acceptable for a small vehicle like the AUTO21EV. This value indicates a good usage of the adhesion potential on all tires in order to keep the vehicle on its desired path. The steering ratio can be calculated as the ratio of the steering wheel angle at the beginning of the circular path ($\delta_{SW} = 25.8^\circ$), where the lateral acceleration is small, and the Ackermann angle ($\delta_A = \frac{a+b}{R} = \frac{1.8}{75} = 1.375^\circ$), as follows:

$$i_S = \frac{\delta_{SW}}{\delta_A} = \frac{25.8^\circ}{1.375^\circ} = 18.8 \tag{2.29}$$

This ratio agrees well with the steering ratio of the AUTO21EV calculated in the design stage [Bod06].

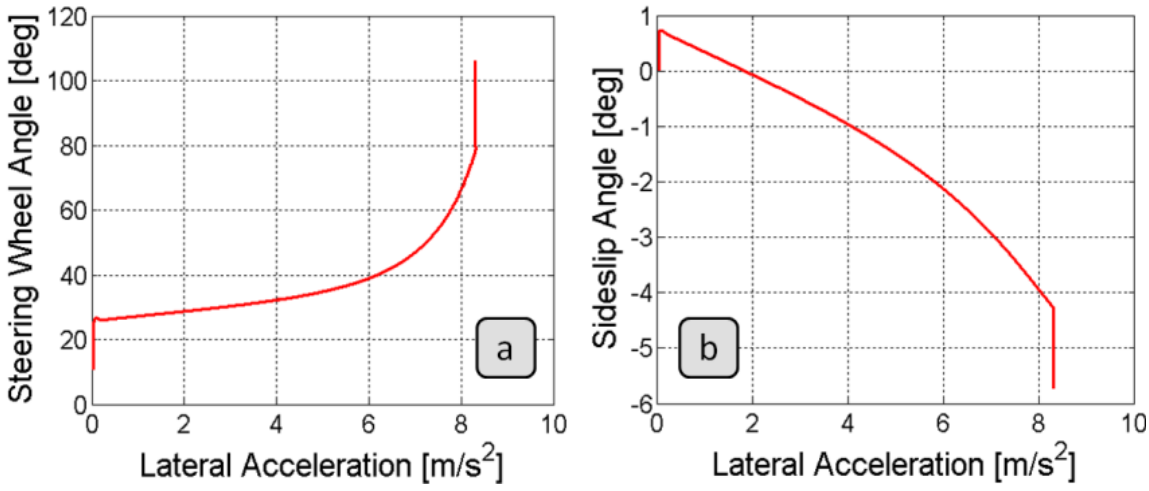

Figure 2-15: (a) Driver's steering wheel input and (b) vehicle sideslip angle as functions of vehicle lateral acceleration when driving through the steady-state constant radius maneuver using the path-following and speed-control driver models

In order to further evaluate the performance of the gain scheduling PID speed controller, the vehicle is accelerated and then braked in a stepwise speed-variation mode while driving in a straight line. In this test, the driver first increases the vehicle speed from 10 km/h to the maximum speed of 90 km/h in increments of 20 km/h. Next, the driver reduces the vehicle speed back to 10 km/h, again in a stepwise manner. Figure 2-16 illustrates the driver's speed request and the actual vehicle speed response for this maneuver. As can be seen, the actual vehicle velocity follows the driver's request very well, without causing any overshoot or significant over-damped conditions. Note that the torque of the in-wheel motors reduces as the vehicle drives faster as a result of the undesirable induction voltage produced by the permanent magnets. Consequently, the acceleration response at lower speeds is faster than that at higher speeds (Figure 2-16). This effect is confirmed by Figure 2-17, which illustrates the motor torques during this maneuver. Note that, at the beginning and end of the test maneuver, where the vehicle is travelling at lower speeds, the maximum motor torque is available at each wheel; as the vehicle speed increases, the maximum possible motor torque decreases. It is important to notice that the slip controllers on the front axle have limited the motor torques at the beginning of the maneuver in order to avoid tire spin-out, and the slip controllers at the rear wheels have limited the motor torques at the end of the maneuver in order to avoid tire lock-up [Jal10]. The development of the fuzzy slip controller is the subject of the next chapter.

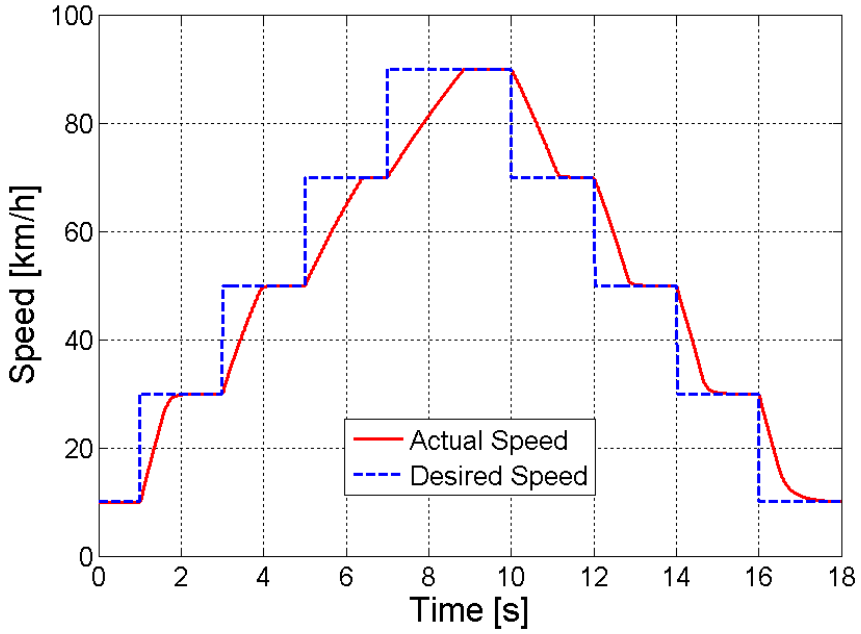

Figure 2-16: Stepwise speed request from the driver model and the actual speed of the vehicle

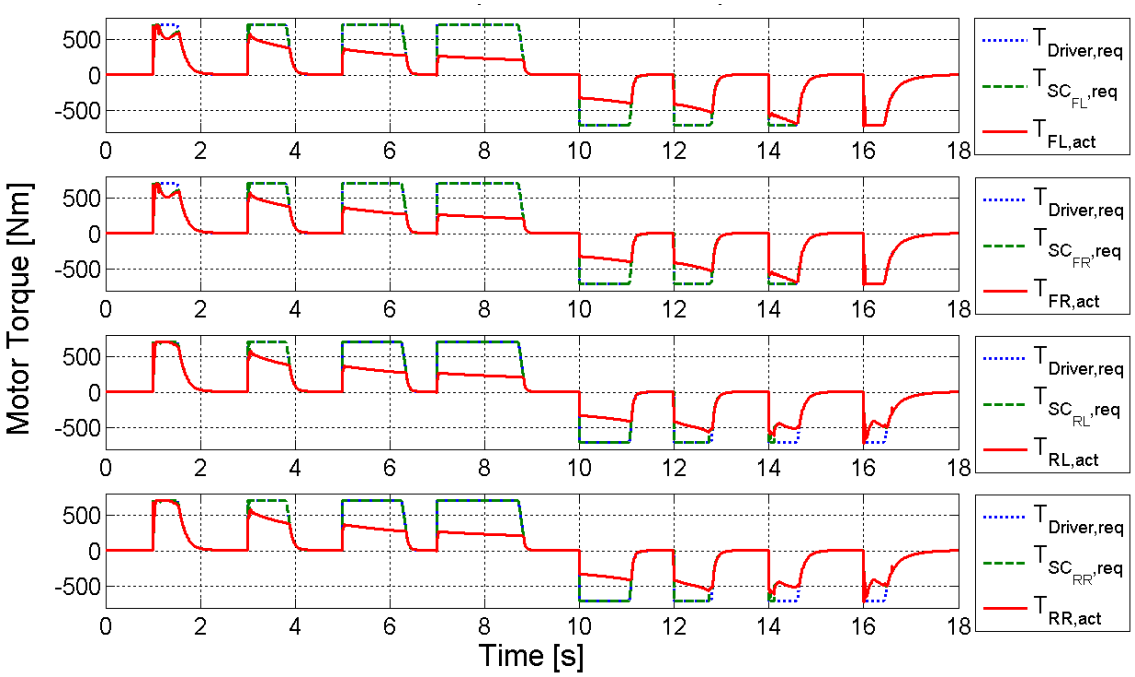

Figure 2-17: Motor torques during the stepwise speed variation test when driving in a straight line

3 Advanced Fuzzy Slip Control System

In the last 30 years, advances in electronics have revolutionized many aspects of the automobile industry. Areas like engine management and safety systems, such as anti-lock braking systems (ABS), traction control systems (TCS), and electronic stability control (ESC) systems, have received particular attention. These safety systems involve the use of electronic control units to modulate the brake and accelerator pedal inputs provided by the driver in order to control the slip of individual tires during emergency braking (ABS) or accelerating (TCS), or to control the stability of the vehicle by braking individual wheels (ESC) [Zan00, Alb96, Ack99].

ABS is by no means a new innovation, and its development and acceptance has occurred over a number of decades. The first ABS system was developed by Dunlop Maxaret in 1952, and was used on aircraft landing systems [Vel01]. In 1978, Robert Bosch GmbH introduced the modern anti-lock braking system for passenger vehicles [Mar02-a, Mar02-b]. By the 1990s, ABS was a common option on many vehicles, and is now a standard feature, or at least an optional feature, on nearly all new vehicles. In 1971, the Buick division of GM introduced *MaxTrac* as the first TCS, which was used to detect rear wheel spin and modulate the engine power delivered to those wheels in order to provide the most traction possible. Since then, more sophisticated TCS systems have been developed by different companies, such as Cadillac and Robert Bosch GmbH, and involve an engine management controller that cooperates with the brake system in order to prevent the driven wheels from spinning out. A comprehensive overview of the history, operation, and types of slip control systems can be found in [Bur93].

The primary task of a slip control system, such as ABS or TCS, is to influence the longitudinal dynamics of a vehicle by preventing the tires from locking up when braking or spinning out when accelerating, thereby enhancing the directional stability of the vehicle. According to a study conducted by the Monash University Accident Research Centre, ABS has reduced the risk of multiple vehicle crashes by 18% and the risk of run-off-road crashes by 35% [Bur04]. Another study conducted by the National Highway Traffic Safety Administration (NHTSA) confirms that a statistically significant decrease in multi-vehicle crashes and fatal pedestrian strikes is achievable using an ABS system [Maz01]. As a result, the European Automobile Manufacturers Association has been

committed to equipping all new vehicles with ABS since 2003 [Bur04]. Figures from the United States suggested that about 95% of new vehicles were equipped with ABS in 2003 [Vel01].

3.1 Conventional slip control systems

Conventional slip control systems use the hydraulic brake system and/or the engine management controller in order to control the tire slip ratio, thereby influencing the longitudinal dynamics of the vehicle. Slip control systems are closed-loop control devices that prevent tire lock-up and spin-out during braking and acceleration, respectively. In a closed-loop control system, the measured response of a physical system is compared to a desired response, and the difference between these two responses initiates actions that will cause the actual response of the system to approach the desired response. Preventing tire lock-up and spin-out helps maintain the stability and steerability of the vehicle.

An ABS system detects the onset of wheel lock-up due to a high braking force, and then limits the braking pressure to prevent wheel lock-up. An ABS system is considered a stand-alone system (it can be installed independently of other control systems), and consists of a wheel speed sensor, a hydraulic modulator, and an electronic control unit (ECU) for signal processing, control, and triggering the actuators in the hydraulic modulator [Bos07]. The ECU recognizes wheel lock-up by detecting sharp increases in wheel deceleration, and reduces the braking force in a closed-loop process until the lock-up situation vanishes. The cyclic application and reduction of the braking force ensures that the brakes operate at or near their most efficient operating point and the vehicle maintains steering control. This cyclic application is also responsible for the pulsation that a driver feels through the brake pedal when the system is activated. In general, when a driver presses the brake pedal, the brake slip increases until the point of maximum friction between the tire and the road surface is reached, which is the limit between the stable and unstable regions. At this point, any increase in brake pressure will reduce the friction between the tire and the road surface, and the wheel will tend towards skidding. In a vehicle with a conventional braking system, as the wheels tend towards lock-up, the lateral force potential of the tires that enables steering is greatly reduced, and approaches zero when the wheels are fully locked. By preventing wheel lock-up, however, the lateral force potential of the tires is maintained at a high level, allowing the

driver to retain steering control during emergency braking. Therefore, the task of an ABS system is to use the friction coefficient between the tires and the road surface in an optimal fashion in order to minimize the braking distance while retaining steerability.

Tire slip can also be controlled in an acceleration mode using a combination of the hydraulic brake system and the engine management controller to prevent tire spin-out. This task is accomplished by a TCS system, which is a constructive add-on to an existing ABS system and cannot be installed alone. In a TCS, the ECU recognizes wheel spin-out by detecting sharp increases in wheel acceleration. The ECU then reduces the engine torque through the engine management controller in a closed-loop process to reduce the traction force on the driven wheels. If the ECU was unable to prevent a spin-out situation using this first method of intervention, it operates the brakes in order to stop the wheel from spinning out. The cyclic application and the cooperation between the engine management controller and the brake system together ensure that the friction coefficient between the tires on the driven wheels and the road surface is used in an optimal fashion, maximizing the traction force while retaining stability and steerability. Note that the aim of a TCS system is defined based on the vehicle configuration. In a front-wheel-drive (FWD) vehicle, TCS aims to maximize the traction force while retaining steerability, whereas in a rear-wheel-drive (RWD) vehicle, TCS intends to maintain vehicle stability while maximizing the traction force.

3.2 Development of an advanced fuzzy slip control system

In Chapter 1, two different methods of adjusting the tire slip ratio in a slip control system are explained. As explained earlier, the tire slip ratio can be controlled either by limiting the maximum possible slip ratio to a fixed amount or by adjusting the tire slip ratio such that the maximum possible traction force can be generated at all slip angles. On the other hand, the adhesion coefficient versus tire slip ratio plot shown in Figure 3-1 suggests that the maximum adhesion coefficient for different road conditions can be generated at a slip ratio of about 15%. Although this limit closely corresponds to the position of the peak adhesion coefficient for only a dry road, the descending slopes associated with other road conditions are small up to this slip limit; thus a slip ratio of 15% can be considered to represent the maximum traction at other road conditions as well. With this in mind, and noting that higher vehicle stability is more advantageous than maximum traction when

driving in a curve, the limited tire slip ratio method from Chapter 1 has been chosen for the advanced fuzzy slip controller of the AUTO21EV.

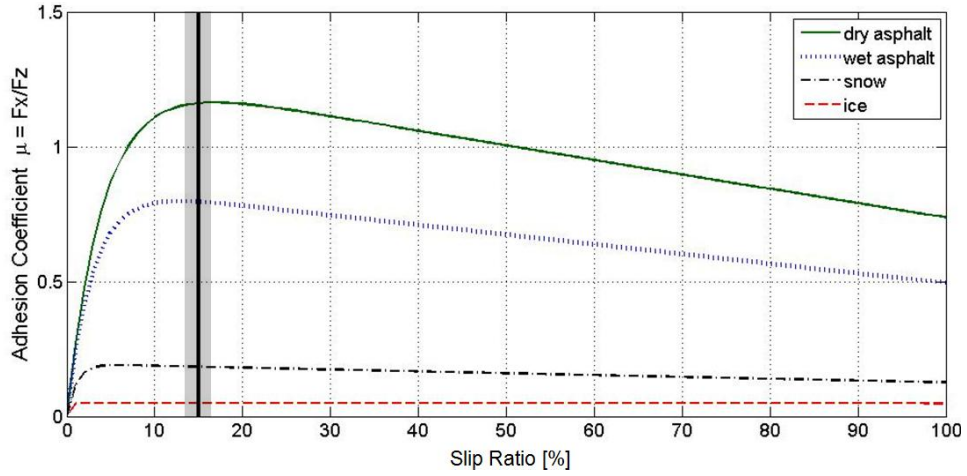

Figure 3-1: Typical adhesion coefficient characteristics as a function of tire slip ratio for different road conditions

The actual slip ratio of each tire is calculated as a positive number using the following equations for brake and acceleration modes, respectively:

$$\lambda_{brake,\,i} = \frac{v_{w,x_i'} - \omega_{w,i} r_{dyn,i}}{v_{w,x_i'}} \quad \text{if } v_{w,x_i'} \geq 0,\ \omega_{w,i} \geq 0, \text{ and } \omega_{w,i} r_{dyn,i} \leq v_{w,x_i'} \tag{3.1}$$

$$\lambda_{accel,\,i} = \frac{\omega_{w,i} r_{dyn,i} - v_{w,x_i'}}{\omega_{w,i} r_{dyn,i}} \quad \text{if } v_{w,x_i'} \geq 0,\ \omega_{w,i} \geq 0, \text{ and } \omega_{w,i} r_{dyn,i} \geq v_{w,x_i'} \tag{3.2}$$

where $i \in \{\text{FL, FR, RL, RR}\}$, $v_{w,x_i'}$ is the speed of the wheel center along the wheel plane, r_{dyn} is the dynamic tire radius, and ω_w is the angular velocity of the tire. It is important to note that, although all of the variables mentioned above are accessible in a simulation environment, they must be measured or estimated in real life. The dynamic tire radius, which is also known as the effective tire radius, is the ratio of the linear velocity of the wheel center in the longitudinal direction to the angular velocity of the wheel [Blu04]. Although the dynamic tire radius has to be estimated in real life, in this work for simplicity, the calculated dynamic tire radius is deployed directly from the tire model at each time step. Note that the static loaded tire radius, which is the loaded radius of a stationary tire inflated to the normal recommended pressure, is also used in the literature, but it is associated with high inaccuracy [Bei00, Kie05]. If the vehicle travels in a straight line and the tires roll freely without skidding and without any torque applied to them, the speed of the wheel center along the wheel plane is equivalent to the speed of the center of

gravity of the vehicle. In the presence of simultaneous longitudinal and lateral wheel slips, however, the wheel center speeds are estimated by transferring the vehicle velocity ($\vec{v}_{CG}$) to the wheel centers [Kie05].

Figure 3-2 illustrates a two-track model of the vehicle in the horizontal plane, which can be used to calculate the wheel speeds. The vehicle velocity $\vec{v}_{CG}$ and the magnitudes of the longitudinal $a_{CG,x}$ and lateral $a_{CG,y}$ accelerations are calculated as follows:

$$\vec{v}_{CG} = v_{CG,x} \cdot \vec{e}_x + v_{CG,y} \cdot \vec{e}_y \tag{3.3}$$

$$a_{CG,x} = \dot{v}_{CG,x} - v_{CG,y} \cdot \dot{\psi} \tag{3.4}$$

$$a_{CG,y} = \dot{v}_{CG,y} + v_{CG,x} \cdot \dot{\psi} \tag{3.5}$$

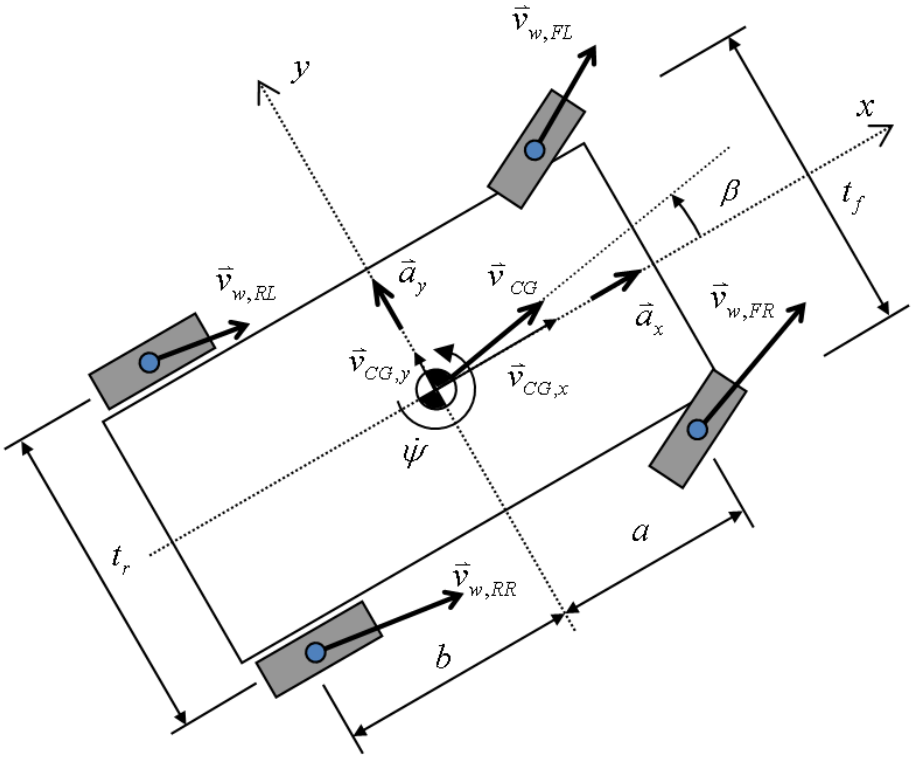

Figure 3-2: Planar two-track vehicle model

where $\vec{e}_x$ and $\vec{e}_y$ are unit vectors along the longitudinal and lateral axes of the vehicle, respectively, $v_{CG,x}$ and $v_{CG,y}$ are the longitudinal and lateral speeds of the vehicle, and $\dot{\psi}$ is the vehicle yaw rate. In real life, the longitudinal ($\dot{v}_{CG,x}$) and lateral ($\dot{v}_{CG,y}$) accelerations of the vehicle are measured with two accelerometers, which are positioned at the center of mass of the vehicle along the longitudinal and lateral vehicle axes,

respectively. The yaw rate $\dot{\psi}$ is measured using a gyroscope positioned at the center of gravity of the vehicle, along its vertical axis. It is important to note that, in real life, the vehicle velocity ($\vec{v}_{CG}$) must be estimated as well. Three common methods of estimating the vehicle velocity are as follows [Kie05, Bos07]:

- Transforming the measured wheel speeds to the center of gravity of the vehicle and fusing the data from all rotational wheel speeds with the integrated longitudinal acceleration signal,
- Using a Kalman filter, and
- Using a fuzzy estimator.

In this work, however, for the sake of accuracy and simplicity, the vehicle velocity is obtained directly from the simulation environment and is not estimated.

The sideslip angle (β) of the vehicle, which is the angle between the direction of motion of the vehicle and its longitudinal axis, cannot be measured directly using a sensor. In this work, a neural network similar in structure to that proposed by Durali and Bahramzadeh [Dur03] is used to estimate this angle. The neural network is constructed using 3 layers and 5 hidden nodes, and is able to estimate the vehicle sideslip angle at the current time step given the current steering wheel input, the current and two previous lateral and longitudinal accelerations, and the two previous estimates of the sideslip angle (Figure 3-3). This neural network is trained with data obtained by driving the vehicle through several maneuvers at different speeds. As demonstrated by Figure 3-4, the resulting neural network provides a reliable vehicle sideslip angle calculation when driving through different maneuvers. Knowing the sideslip angle of the vehicle, the longitudinal and lateral speeds of the vehicle are calculated as follows:

$$v_{CG,x} = v_{CG} \cdot \cos(\beta) \tag{3.6}$$

$$v_{CG,y} = v_{CG} \cdot \sin(\beta) \tag{3.7}$$

Looking at Figure 3-2, the wheel center velocities $\vec{v}_{w,i}$ can be calculated as follows [Kie05]:

$$\vec{v}_{w,FL} = \left(v_{CG,x} - \dot{\psi} \cdot \frac{t_f}{2} \right) \vec{e}_x + \left(v_{CG,y} + \dot{\psi} \cdot a \right) \vec{e}_y \tag{3.8}$$

$$\vec{v}_{w,FR} = \left(v_{CG,x} + \dot{\psi} \cdot \frac{t_f}{2} \right) \vec{e}_x + \left(v_{CG,y} + \dot{\psi} \cdot a \right) \vec{e}_y \tag{3.9}$$

$$\vec{v}_{w,RL} = \left(v_{CG,x} - \dot{\psi} \cdot \frac{t_r}{2} \right) \vec{e}_x + \left(v_{CG,y} - \dot{\psi} \cdot b \right) \vec{e}_y \tag{3.10}$$

$$\vec{v}_{w,RR} = \left(v_{CG,x} + \dot{\psi} \cdot \frac{t_r}{2} \right) \vec{e}_x + \left(v_{CG,y} - \dot{\psi} \cdot b \right) \vec{e}_y \tag{3.11}$$

Note that all of these wheel center velocities are calculated with respect to the local coordinate system of the vehicle.

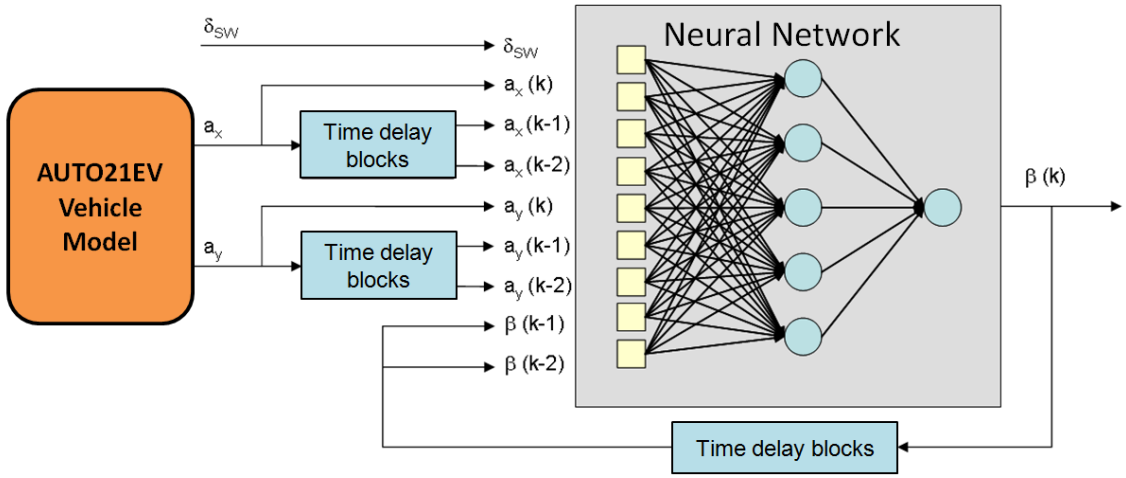

Figure 3-3: Block diagram of neural network sideslip estimator proposed by Durali and Bahramzadeh [Dur03]

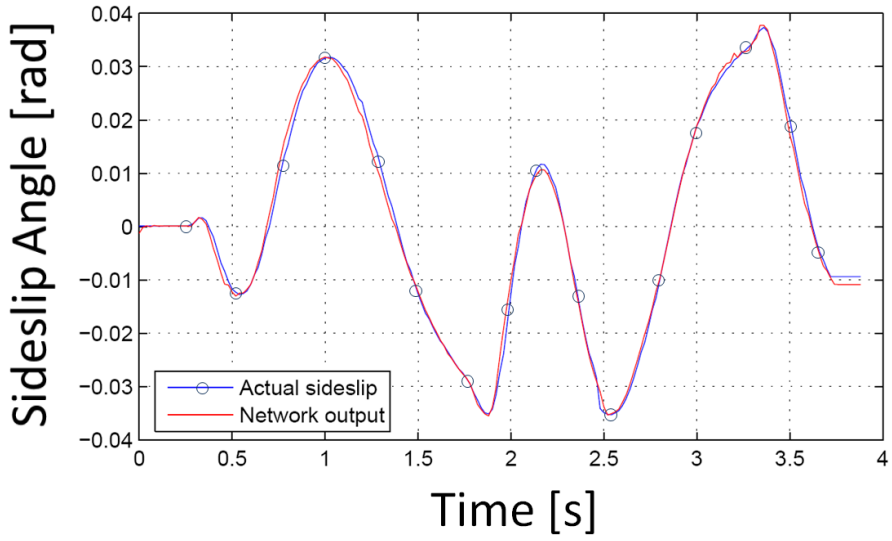

Figure 3-4: Performance of the neural network sideslip angle estimator during a double-lane-change maneuver

According to equations (3.1) and (3.2), the slip ratio of a tire is calculated along the wheel plane. Since the rear wheels do not steer, their local coordinate systems are

parallel to the vehicle coordinate system. Thus, the portion of the wheel center velocity along the x-axis from equations (3.10) and (3.11) can be used directly to calculate the wheel slip for the rear tires:

$$v_{w,x_{RL}} = v_{w,x'_{RL}} = v_{CG,x} - \dot{\psi} \cdot \frac{t_r}{2} \tag{3.12}$$

$$v_{w,x_{RR}} = v_{w,x'_{RR}} = v_{CG,x} + \dot{\psi} \cdot \frac{t_r}{2} \tag{3.13}$$

Note that $v_{w,x'_{RL}}$ and $v_{w,x'_{RR}}$ indicate the wheel center velocities of the rear-left and rear-right tires with respect to the local coordinate systems of the wheels. The local coordinate systems of the front wheels are rotated by the steering angle δ, so equations (3.8) and (3.9) must be transformed into the appropriate wheel coordinate systems. Looking at Figure 3-5, the wheel center velocities of the front wheels can be calculated as follows:

$$v_{w,x'_{FL}} = v_{w,x_{FL}} \cdot \cos(\delta) + v_{w,y_{FL}} \cdot \sin(\delta) = \left(v_{CG,x} - \dot{\psi} \cdot \frac{t_f}{2} \right) \cdot \cos(\delta) + \left(v_{CG,y} + \dot{\psi} \cdot a \right) \cdot \sin(\delta) \tag{3.14}$$

$$v_{w,x'_{FR}} = v_{w,x_{FR}} \cdot \cos(\delta) + v_{w,y_{FR}} \cdot \sin(\delta) = \left(v_{CG,x} + \dot{\psi} \cdot \frac{t_f}{2} \right) \cdot \cos(\delta) + \left(v_{CG,y} + \dot{\psi} \cdot a \right) \cdot \sin(\delta) \tag{3.15}$$

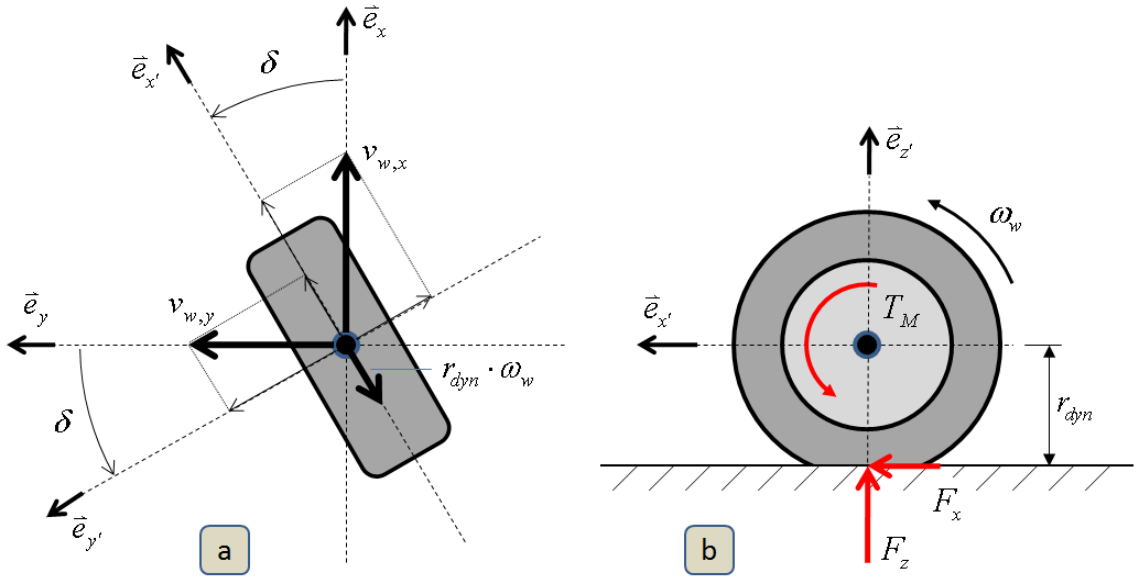

Figure 3-5: (a) Translational and (b) rotational tire motion

One advantage of the AUTO21EV is that both ABS and TCS systems can be realized through the available in-wheel motors without using the conventional brake system or engine management controller. The torque response of an electric motor is several milliseconds, which is 10 to 100 times faster than that of an internal combustion

engine or even a hydraulic brake system [Hor04]. When coupled with the ability to individually control the wheel slip at each corner of the vehicle, this platform has allowed us to design a very advanced slip control system for the AUTO21EV using its in-wheel motors. Figure 3-6 illustrates the block diagram that is used to calculate the actual slip ratio of the front-left (FL) tire as an example.

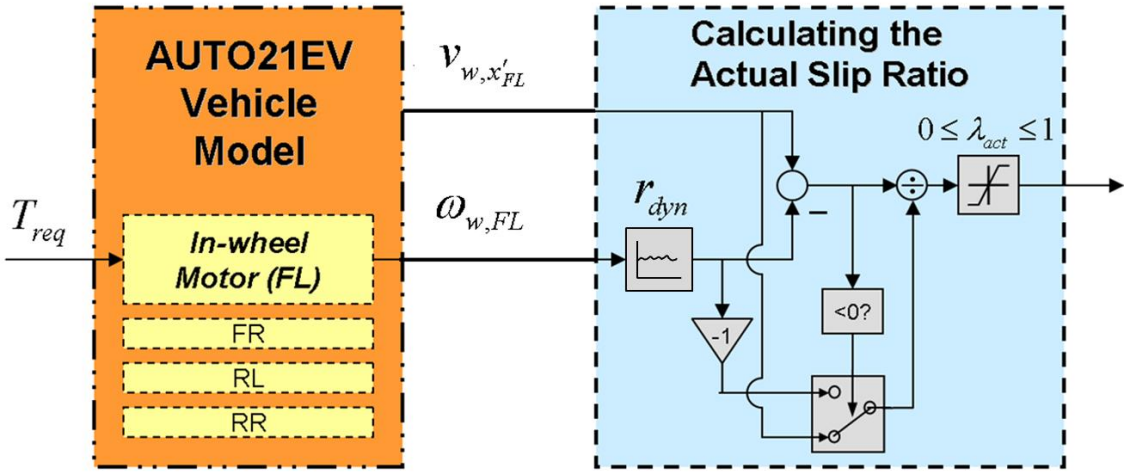

Figure 3-6: Block diagram for calculating the actual slip ratio of the front-left tire

Fuzzy logic control systems are robust and flexible inference methods that are well suited for tackling complicated nonlinear dynamic control problems. As such, they are ideal candidates for controlling the highly nonlinear behaviour inherent in vehicle dynamics. Fuzzy control systems can tolerate imprecise information and can describe expert knowledge in vague linguistic terms, which suits the subjective nature of vehicle dynamics and slip control systems [Kar04].

The rule base of the fuzzy slip controller was designed using the slip ratio error $e(\lambda)$ and the rate of change of the slip ratio error $\dot{e}(\lambda)$ as the inputs; the corrective motor torque T_{corr} is the output of the slip controller (see Table 3-I). The tire slip ratio error is calculated by comparing the actual tire slip with the desired slip limit at every time step. The rate of change of the slip ratio error is calculated by subtracting the previous slip ratio error from the current one, and dividing the result by the sample time of the controller.

Variable	Definition
Input 1	$e(\lambda) = \lambda_{lim} - \lambda_{act}$
Input 2	$\dot{e}(\lambda) = \frac{e(\lambda)_k - e(\lambda)_{k-1}}{\text{sample time}}$
Output	T_{corr}

Table 3-I: Definition of the input and output variables of the fuzzy slip controller

The controller inputs and output are normalized to simplify the definition of the fuzzy sets. Four and seven fuzzy sets are used for the slip ratio error and the rate of change of the slip ratio error, respectively, in order to provide enough rule coverage. Nine fuzzy sets are used to describe the output of the fuzzy slip controller.

The fuzzy inference system processes the list of rules in the knowledge base using the fuzzy inputs obtained from the previous time step of the simulation, and produces the fuzzy output which, once defuzzified, is applied in the next time step. The Mamdani fuzzy inference method is used, which is characterized by the following fuzzy rule schema:

$$\text{IF } e(\lambda) \text{ is } A \text{ AND } \dot{e}(\lambda) \text{ is } B \text{ THEN } T_{corr} \text{ is } C \tag{3.16}$$

where *A*, *B*, and *C* are fuzzy sets defined on the input and output domains. The control rule base of the proposed fuzzy slip controller is developed based on expert knowledge and extensive investigation. Figure 3-7 illustrates the control rule base and control surface of the fuzzy slip controller. The linguistic terms that have been used in this table are listed in Table 3-II. The shape and distribution of the membership functions used for the input and output variables of the fuzzy slip controller are shown in Figure 3-8. Since only positive membership functions have been used for $e(\lambda)$ and the slip controller is only activated when $e(\lambda)$ is negative (i.e., when the actual slip ratio of a tire is greater than the slip limit), the slip ratio error must be converted into a positive number before entering the fuzzy slip controller. This procedure is shown in Figure 3-9, where the block diagram of the entire slip control system is illustrated.

Control Rule Base		e(λ)			
		ZE	PS	PM	PL
ė(λ)	NL	ZE	ZE	ZE	ZE
	NM	ZE	ZE	ZE	NS
	NS	ZE	ZE	NS	NM
	ZE	ZE	NS	NM	NL
	PS	NM	NL	NVL	NVL
	PM	NL	NVL	NVL	NVL
	PL	NVL	NVL	NVL	NVL

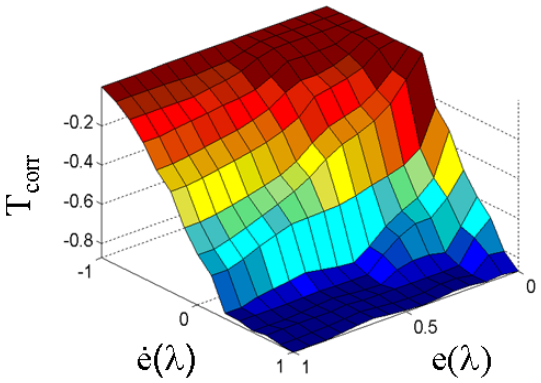

Figure 3-7: Control rule base (left) and control surface (right) of the fuzzy slip control system

Acronym	Linguistic Variable
NVL	Negative Very Large
NL	Negative Large
NM	Negative Medium
NS	Negative Small
ZE	Zero
PS	Positive Small
PM	Positive Medium
PL	Positive Large
PVL	Positive Very Large

Table 3-II: Linguistic variables used in the fuzzy rules

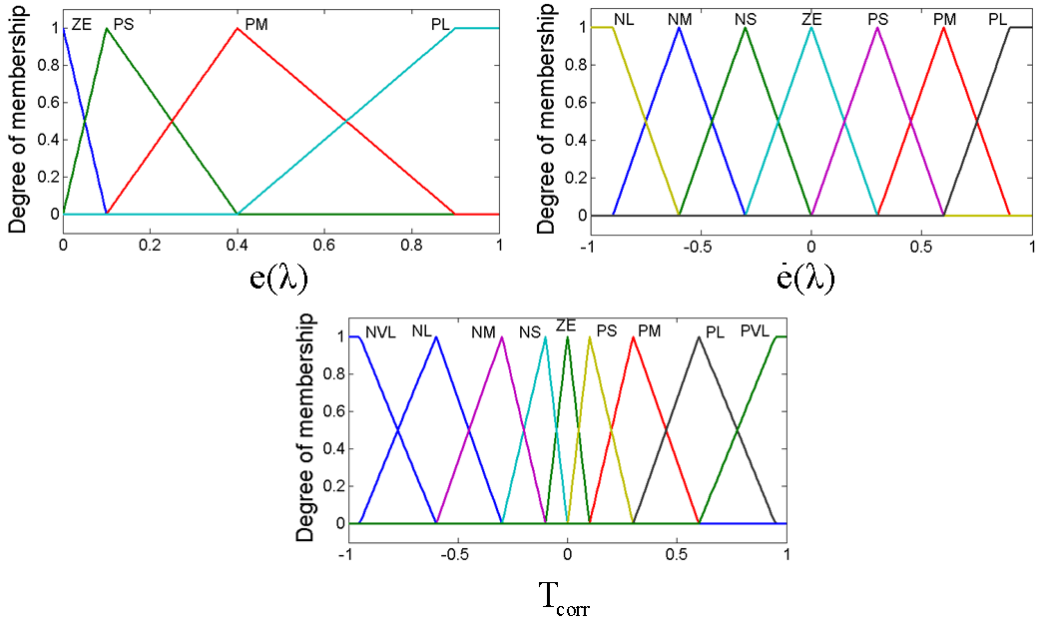

Figure 3-8: Shape and distribution of membership functions for the input and output variables of the fuzzy slip controller

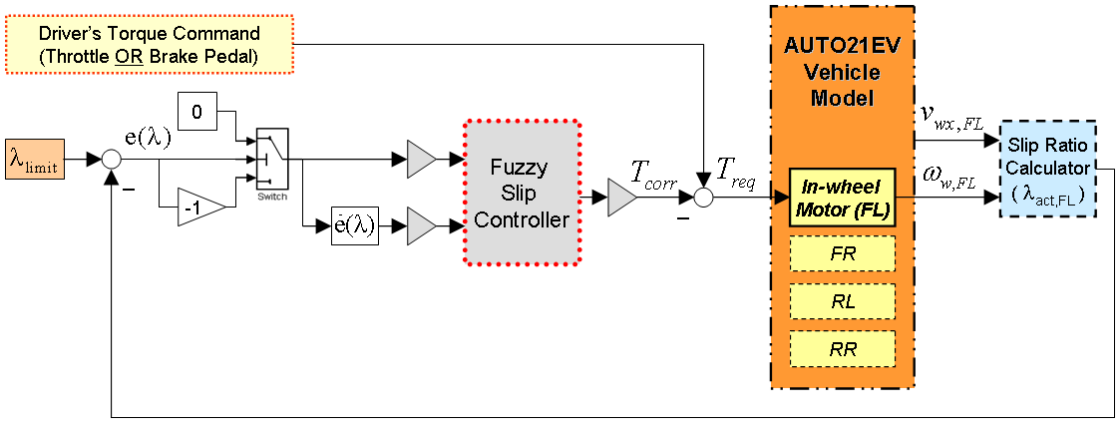

Figure 3-9: Block diagram of the advanced slip control system for the front-left tire

3.3 Evaluation of the advanced fuzzy slip control system

The performance of the fuzzy slip controller is tested using four different maneuvers. First, the AUTO21EV is accelerated in a straight line from 5 km/h to its maximum speed of 90 km/h. The acceleration starts at 0.5 seconds into the simulation and the vehicle reaches its maximum speed after 5 seconds (Figure 3-10-a). As illustrated in Figure 3-10-b, a maximum acceleration of about 0.85g is achievable up to a speed of 28 km/h, where the maximum motor torques are available.

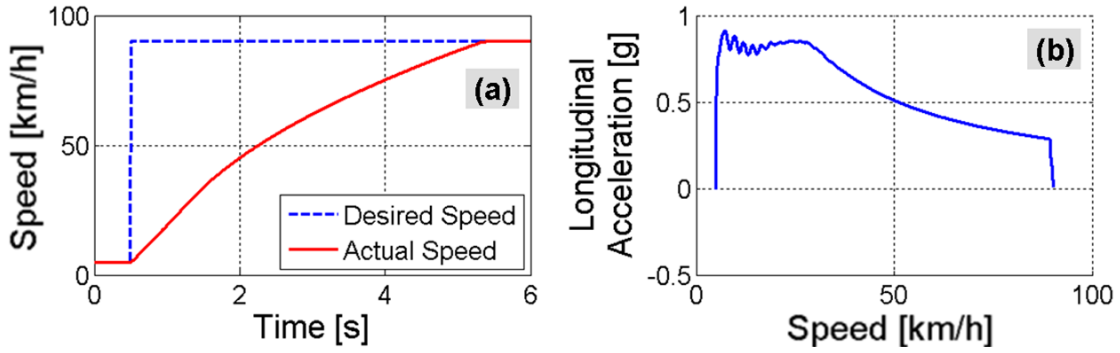

Figure 3-10: (a) Vehicle speed and (b) vehicle longitudinal acceleration versus forward speed during the straight-line acceleration maneuver

Figure 3-11 illustrates the slip ratio of each tire during the straight-line acceleration maneuver. The plots shown in Figure 3-11 clearly indicate that the slip controllers on the front wheels have limited the tire slips after the start of acceleration up to about 1 second, where tire spin-out would have otherwise occurred due to the availability of high motor torques and the dynamic weight shift to the rear axle. Moreover, the slip controllers on the rear wheels are activated for a short period of time (0.1 seconds) in order to generate the maximum possible traction force while preventing

any tire spin-out. The activation of the slip controllers can also be verified by looking at the motor torque histories in Figure 3-12. The required torque from the driver model ($T_{Driver,req}$) is modified by the slip controllers ($T_{SC_i,req}$) such that, during a period of about 0.1 seconds after the start of the acceleration, the rate of change of each motor torque is limited by its respective slip controller to prevent spin-out. The slip controllers on the front wheels have continued limiting the motor torques up to about 1.3 seconds of the simulation, at which point the maximum motor torques are automatically reduced due to the induction voltages and magnetization losses that occur at higher motor speeds. On the rear wheels, however, the actual torque of the motors is restricted by the maximum torque limit, not by the slip controllers. Moreover, due to the shifting of weight to the rear axle of the vehicle, the traction potentials of the rear tires have increased, thereby preventing these tires from spinning out. Note that the oscillatory behaviour of the slip ratios of the rear tires in the first second of the simulation is caused by the tire model and not the controllers. Notice that the Pacejka 2002 tire model that is used in this work is not very suitable for low speeds and ABS braking control applications (see Figure A-18 in the Appendix). However, it was the best tire model that was available for this work.

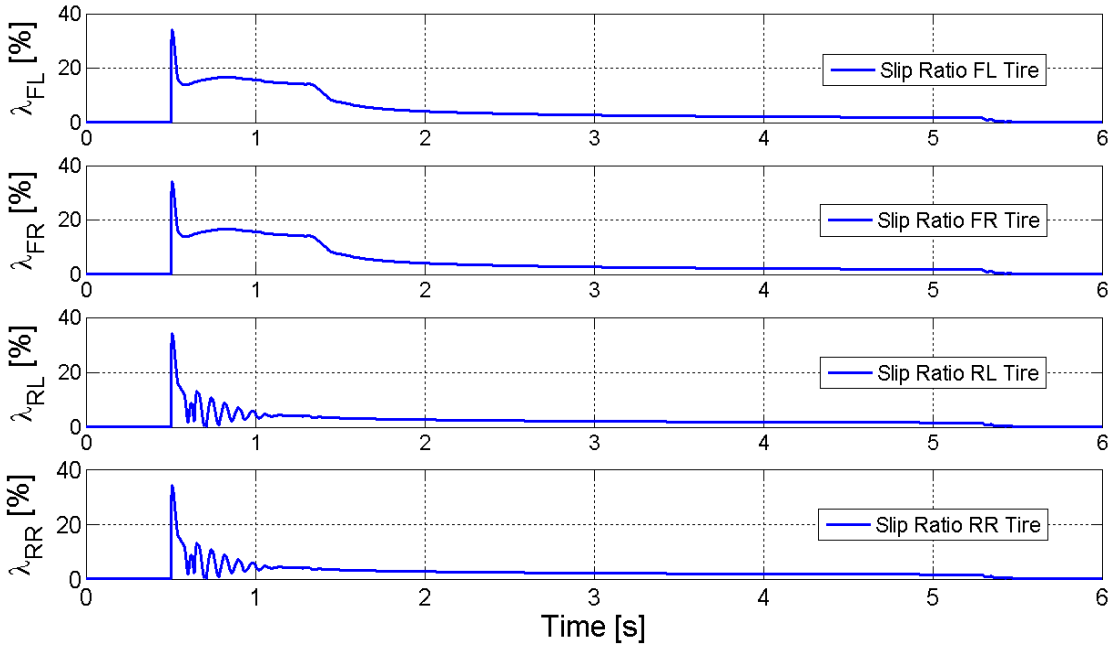

Figure 3-11: Tire slip ratios during the straight-line acceleration maneuver

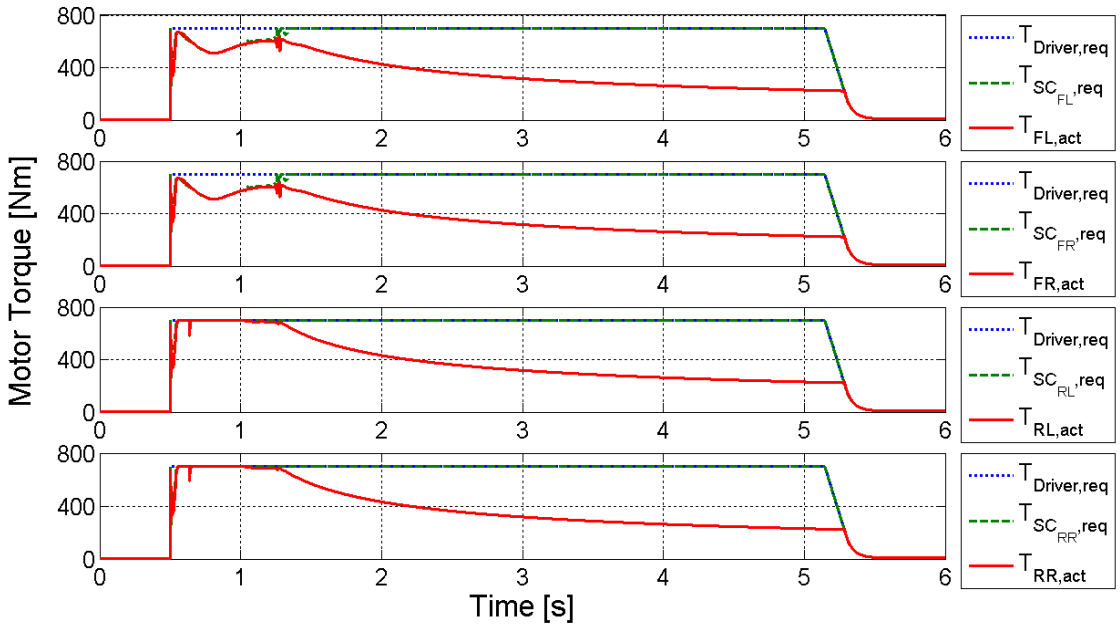

Figure 3-12: Motor torques during the straight-line acceleration maneuver

The second maneuver used to evaluate the performance of the slip control design is a straight-line braking test. In this test, the driver intends to stop the AUTO21EV from a maximum speed of 80 km/h in an emergency braking situation. Figure 3-13-a indicates that the braking distance is about 39.7 meters, which is a very impressive result considering the regulations on braking systems for passenger vehicles in the European Union (EU). As stated in the EU directives and regulations for braking systems, the braking distance of passenger-type vehicles must be less than 50.7 meters for an initial test speed of 80 km/h [Bos07]. It takes about 4 seconds to bring the vehicle to a final speed of 5 km/h (Figure 3-13-b), during which time none of the tires lock up. Note that the vehicle speed is only reduced to 5 km/h due to the instability of the Pacejka tire model at low speeds. Figure 3-13-c indicates that a maximum deceleration of 0.82g is achievable at speeds lower than 45 km/h. These results confirm that the proposed slip controller is capable of replacing the conventional brake system in the AUTO21EV. In other words, the in-wheel motors are capable of taking over the entire functionality of a conventional brake system for the entire speed range. As a fail-safe back-up, however, a redundant hand-brake system must be installed in the AUTO21EV.

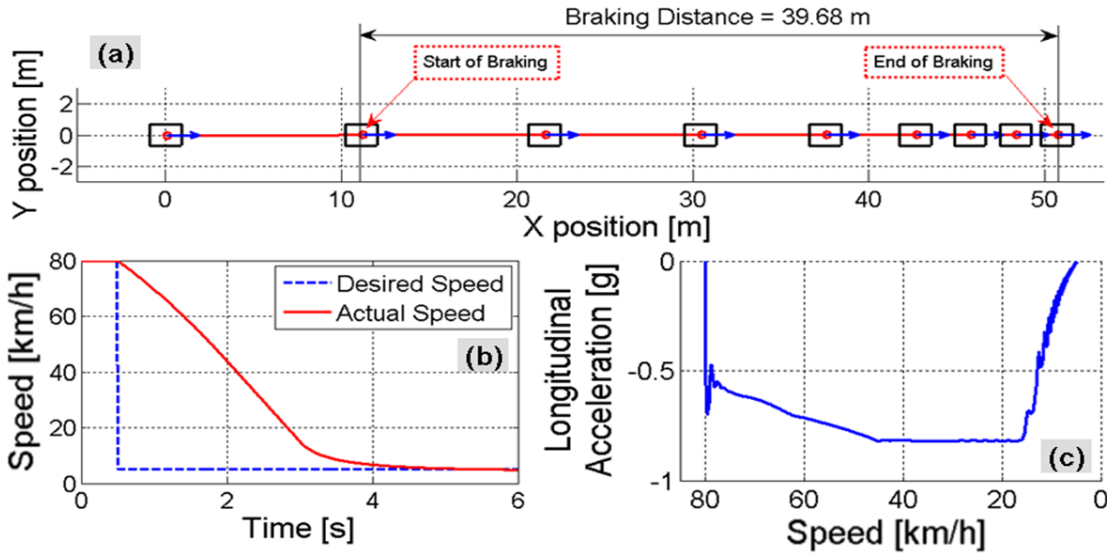

Figure 3-13: (a) Braking distance, (b) vehicle speed, and (c) vehicle longitudinal deceleration versus forward speed during the straight-line braking test

As illustrated in Figure 3-14, the slip controllers are only activated on the rear tires at about 1.4 seconds, where tire lock-up would have otherwise occurred due to the dynamic weight shift to the front axle and higher available braking torques at lower speeds. This control effort is also apparent in Figure 3-15, in which the motor torques at the rear wheels are shown to be restricted to about 500 Nm, while the in-wheel motors on the front axle are permitted to apply the maximum torque of 700 Nm. In addition, since the slip controllers prevent any tire lock-up, there is no need to introduce an extra braking force distribution technique, as is common in conventional brake systems. As mentioned earlier, the rapid oscillations in the slip ratio plots that occur after the third second of the simulation (when the vehicle speed is about 10 km/h) are caused by the tire model and not the controllers.

The third test for the fuzzy slip controller is performed on a μ-split road, where the road is dry on the right side and icy on the left side. In this test, the driver holds the steering wheel fixed and accelerates the vehicle in a straight line from an initial speed of 10 km/h. The road is considered to be dry before x = 15 m and after x = 25 m. As shown in Figure 3-16, a black ice patch is present on the left side of the road for 15 m < x < 25 m. Although the intention of the driver is to travel in a straight line, the car is pushed to the left side of the road due to the asymmetrical traction forces on the left and right sides of the vehicle. In order to keep the vehicle on the road, this side-pushing effect must be corrected either through a counter-steering input from the driver or by an

active stability control system. Note that the slip control system has done its job by maximizing the available acceleration.

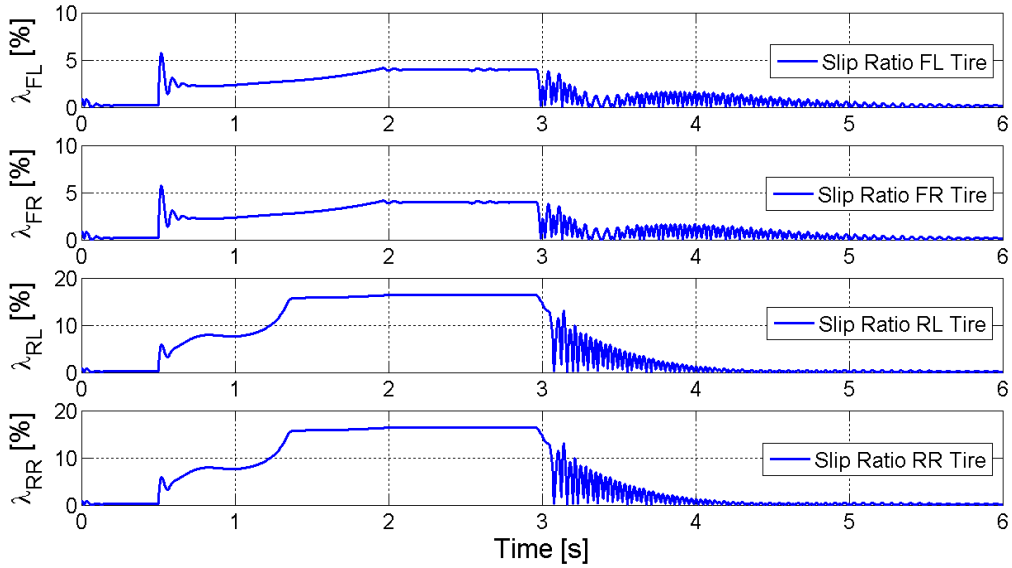

Figure 3-14: Tire slip ratios during the straight-line braking maneuver

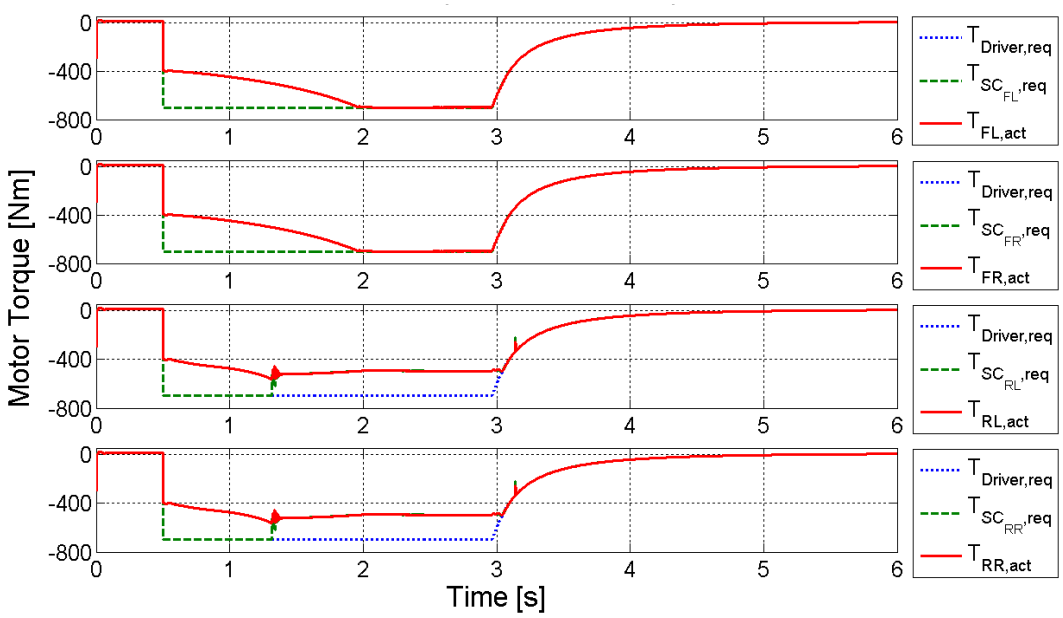

Figure 3-15: Motor torques during the straight-line braking maneuver

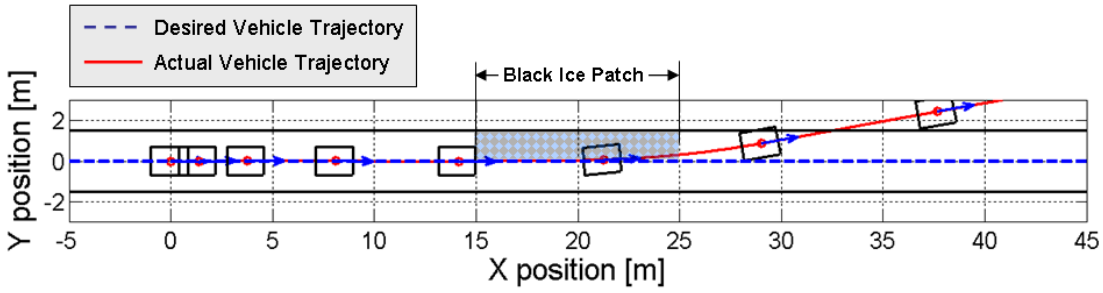

Figure 3-16: Vehicle trajectory when accelerating on a μ-split road

Figure 3-17 illustrates the tire slips of the vehicle during this acceleration maneuver. The slip controllers have limited the tire slips on the front axle at the beginning of the acceleration, where tire spin-out would have occurred due to the available high motor torques and the dynamic weight shift to the rear axle. In addition, the slip controllers on the left side of the vehicle are activated when the vehicle drives over the black ice patch, thereby preventing tire spin-out while still generating the maximum possible traction force on the ice patch. As shown in Figure 3-18, the motor torques on the front wheels are limited by the slip controllers for about 0.6 seconds after the start of the acceleration. When driving over the black ice patch, the motor torques on the left side of the vehicle are reduced to about 40 Nm to avoid tire spin-out.

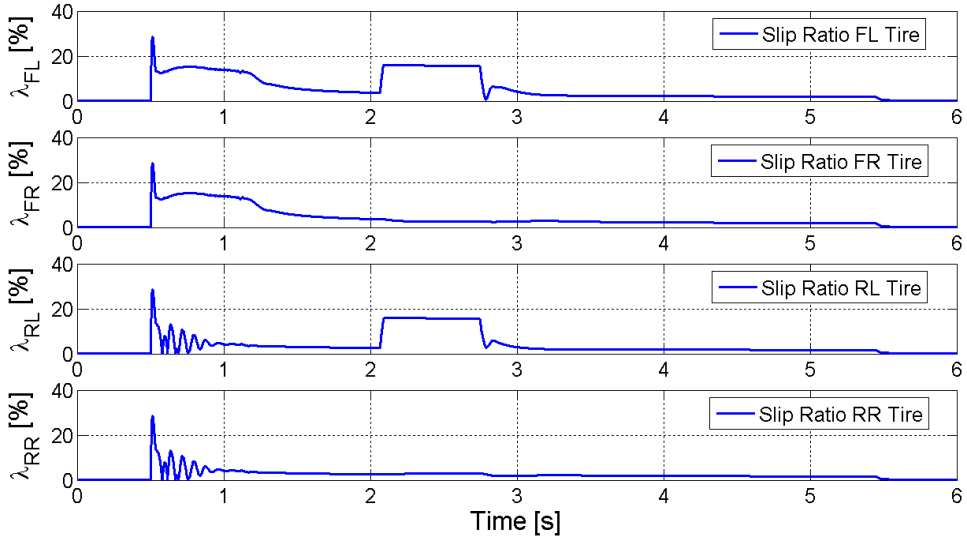

Figure 3-17: Tire slip ratios during the straight-line acceleration maneuver on a µ-split road

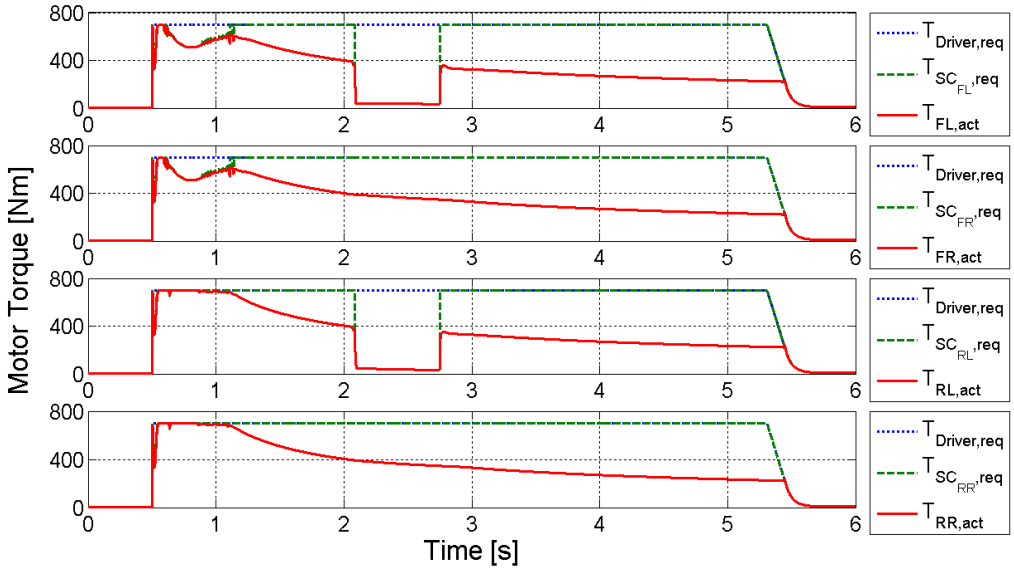

Figure 3-18: Motor torques during the straight-line acceleration maneuver on a µ-split road

The final test for the fuzzy slip controller is braking on a μ-split road, which is a very critical test since the vehicle will experience severe instability if the driver does not react immediately to correct the course of the vehicle. In this test, the driver holds the steering wheel fixed and attempts to stop the vehicle in an emergency braking situation from 80 km/h on a road that has a black ice patch on the left side for 15 m < x < 25 m. As illustrated in Figure 3-19, the vehicle is pushed to the right side of the road due to the asymmetrical braking forces on the left and right sides of the vehicle. More important is the fact that these asymmetrical braking forces are high enough to turn the vehicle around its vertical axis. In order to avoid such a dangerous situation, a driver must correct the course of the vehicle through a sequence of steering corrections based on the vehicle response, which is a very difficult task for an average driver. Although the slip controller has done its job to maximize the braking forces, further control is needed to maintain a safe trajectory.

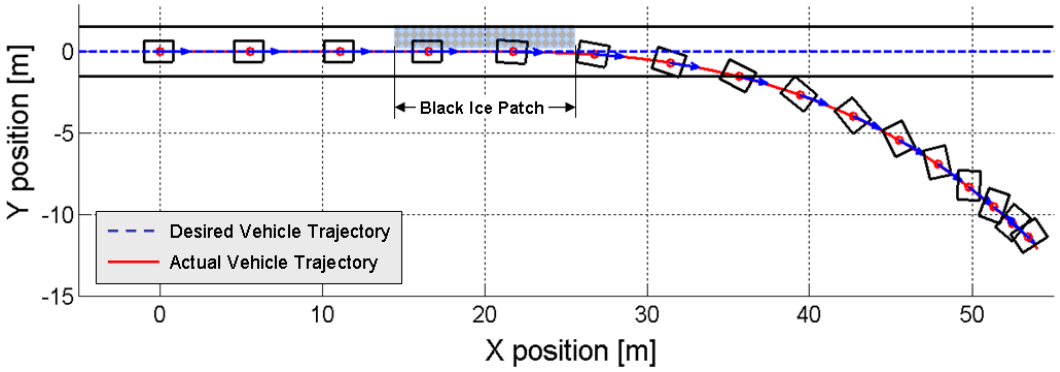

Figure 3-19: Vehicle trajectory when braking on a μ-split road

As shown in Figure 3-20, the slip controllers on the left side of the vehicle have limited the tire slips when driving over the μ-split portion of the road, which occurs between 0.7 and 1.2 seconds after the start of the simulation. The rear-right tire will also begin experiencing a lock-up situation due to the shifting vehicle weight and a high braking torque at around 1.1 seconds, which is prevented by the rear-right slip controller. Furthermore, since the vehicle starts to turn around its vertical axis, large lateral forces are generated on all tires, which simultaneously reduce the braking force potential on all four tires. This yawing motion explains why the front-left, front-right, rear-left, and rear-right slip controllers are becoming active at around 1.95, 1.4, 1.6, and 1.1 seconds, respectively, to prevent tire lock-up. The activation of the slip controllers is also confirmed by Figure 3-21, which illustrates the motor torques. Note that, due to the

vehicle spin occurring in this test, only the meaningful range of data has been plotted in Figures 3-20 and 3-21.

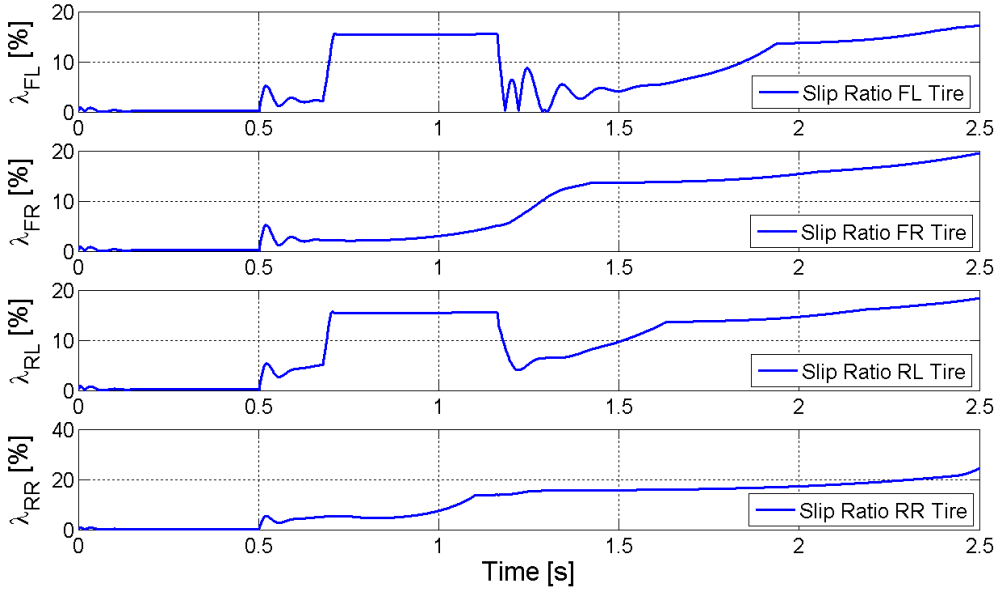

Figure 3-20: Tire slip ratios during the straight-line braking maneuver on a μ-split road

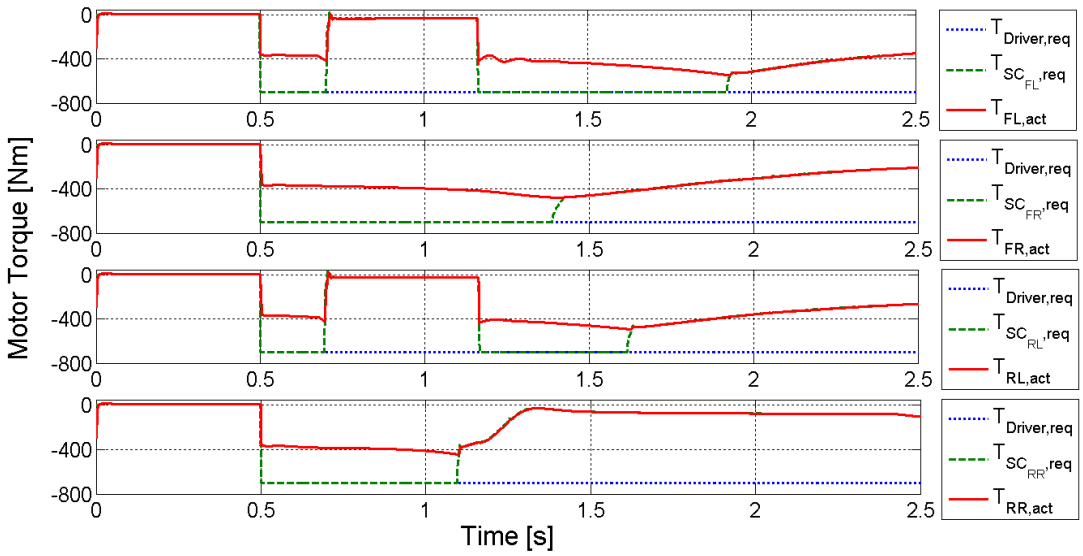

Figure 3-21: Motor torques during the straight-line braking maneuver on a μ-split road

3.4 Chapter summary

In this chapter, an advanced fuzzy slip controller is developed for the AUTO21EV that combines the functionalities of an ABS, a TCS, and the brake system of the vehicle. Since the developed fuzzy slip controller is able to control the slip ratio of all four tires in all driving conditions, thereby realizing the most advanced All-Wheel-Drive system. The developed fuzzy slip controller is based on a chassis platform that has four individual

electric drives, the reaction time of this slip controller is much faster than that of any other conventional slip control system based on a hydraulic brake system or internal combustion engine. The performance and functionality of the developed fuzzy slip control system have been evaluated using four test maneuvers.

4 Genetic Fuzzy Yaw Moment Controller

As mentioned in Chapter 1, most stability control systems generate a corrective yaw moment around the vertical axis of the vehicle by affecting the linear or nonlinear characteristics of the tire-road contact forces. A corrective yaw moment can be created directly using the lateral force of the tires by manipulating the steering or camber angle of the tires, such as in an active steering or active camber system, or using the longitudinal force of the tires by manipulating the drive or brake torque of individual wheels, such as in an electronic stability control (ESC) or torque vectoring control system. It is important to notice that longitudinal and lateral tire forces can both be influenced indirectly by manipulating the wheel load and defining the maximum possible transfer force, such as in an active suspension or an active anti-roll bar system. Regardless of the means by which forces are applied, generating a corrective yaw moment around the vertical axis of the vehicle is the main objective of all these systems.

Having this in mind, a yaw moment controller is designed for the AUTO21EV that acts as a high-level supervisory module, assigning tasks to the low-level controllers and actuators. This hierarchical approach addresses the complexities of integrated chassis control management and allows the low-level controllers and actuators, such as the torque vectoring controllers and the in-wheel motors, to be designed simply as tracking controllers that track the reference signals generated by the supervisory yaw moment controller. In addition, since such a yaw moment controller represents an ideal controller, in that the required corrective yaw moment can be generated directly without being restricted by the performance and limitations of actuators, the performance of this yaw moment controller can be used as a reference against which the performance of other stability control systems can be compared.

In this chapter, a genetic fuzzy yaw moment controller (YMC) is developed for the AUTO21EV, the objective of which is to calculate the corrective yaw moment required to minimize the sideslip angle and yaw rate errors of the vehicle, comparing the actual values from the vehicle to those obtained using a reference bicycle model. At this stage, the calculated corrective yaw moment is applied to an imaginary torque driver that is placed at the center of mass of the vehicle, acting about its vertical axis.

4.1 Simplified vehicle model with in-wheel motors

A full vehicle model, such as the AUTO21EV model created in the ADAMS environment (Appendix A), involves a large number of both equations and parameters, which makes it difficult for a control engineer to investigate the effects of different control strategies and discover the source of possible problems. In fact, from a vehicle motion control perspective, it is more desirable to start with a simpler vehicle model and increase the level of fidelity once the effectiveness of a control strategy has been confirmed. In addition, numerical formulation techniques, such as those employed in the ADAMS software, are very computationally expensive because these techniques generate system matrices that are only valid for an instant of time and, thus, must be reformulated at every time step of a simulation. Furthermore, the optimization of control parameters using a genetic algorithm procedure involves many simulation runs, which can be a time-consuming process, especially when the system model is complicated.

With this in mind, a fast simulation model was desired to allow for the testing of different control strategies, and for applying a genetic algorithm procedure to the development of the chassis control systems. Therefore, an alternative 14-degree-of-freedom (DOF) vehicle model was developed using DynaFlexPro, a Maple package that uses symbolic formulation procedures and linear graph theory to generate computationally efficient simulation code [Sch04]. Symbolic formulation techniques combine the system parameters and modelling variables to create sets of equations that describe a dynamic system for all time. Therefore, such approaches are ideal for real-time applications, such as hardware- and human-in-the-loop scenarios, which require a fast computation time. In addition, the 14-DOF vehicle model used herein was recommended by Sayers [Say96] for analyzing the handling and stability behaviour of vehicles, and has been adopted by several commercial software packages such as CarSim [Sch08].

The AUTO21EV was modelled in the DynaFlexPro environment with independent suspensions, four direct-drive in-wheel motors, and a steering system on the front axle, as shown in Figure 4-1. Note that the in-wheel motors are integrated directly in the vehicle model, combining the mechanical and electrical domains of this mechatronic system together. The topology of the vehicle model was defined in block diagram form using ModelBuilder, a graphical user interface companion for DynaFlexPro. The generated DynaFlexPro model of the vehicle was later imported into the

MATLAB/Simulink environment, and different chassis control systems and in-wheel motor controllers were added to it. Note that DynaFlexPro has been superseded by the Multibody package in MapleSim.

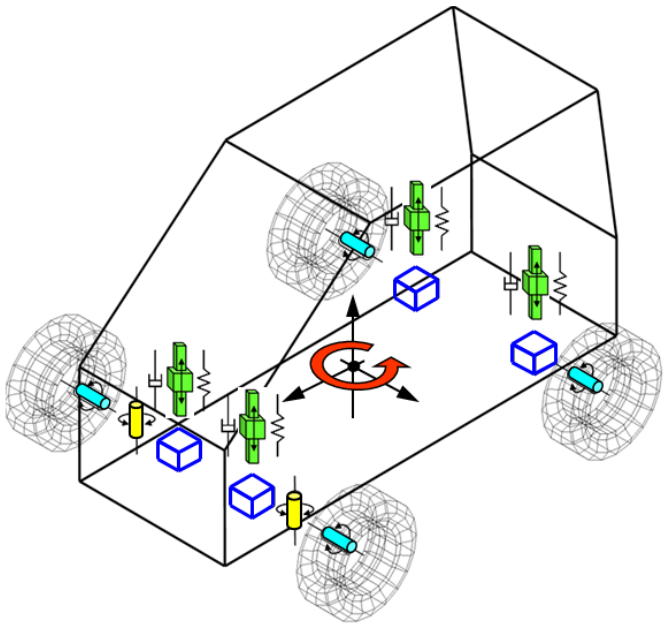

Figure 4-1: AUTO21EV vehicle model implemented in DynaFlexPro

The sprung mass of the vehicle is considered to be a single rigid body, which will be referred to herein as the chassis. The position and orientation of the chassis, measured with respect to a global reference frame, account for 6 DOF. The suspension system is modelled using four lumped masses that are connected to the chassis via four prismatic joints, each of which is associated with a linear spring and damper, representing the suspension compliance. Together, these components add another 4 DOF to the vehicle model. Note that these four lumped masses consist of those components of the suspension and steering system that are considered to belong to the unsprung mass, including the stator of the in-wheel motors. Each wheel consists of a tire, a rim, and the rotor of the in-wheel motor, and is connected to its corresponding lumped mass with a revolute joint that allows the wheel to spin around its rotation axis, thereby adding another 4 DOF to the model. The steering system is modelled with two independent motion drivers on the front axle, which facilitate the use of an Ackermann steering configuration using look-up tables. Since the driver specifies the input to the steering system, these motion drivers do not add any DOF to the model. The Pacejka 2002 tire model, which is the most comprehensive version of the Magic Formula tire model [Pac02], is used in this vehicle model. Pacejka 2002 is considered to be the state-of-the-art for modelling tire-road

contact forces in vehicle dynamics applications and, thus, is recommended for all generic vehicle handling and stability simulations, including steady-state cornering, double-lane-change, braking-in-turn, straight-line μ-split braking, and ABS braking maneuvers [ADA02]. It is important to note that all the masses and moments of inertia of different parts and subsystems of the vehicle and in-wheel motors, including the spring and damper rates of the suspension system and the Ackermann steering behaviour, are taken directly from the full vehicle model developed in ADAMS. Finally, a torque driver is added at the center of mass of the vehicle around its vertical axis, which represents the imaginary corrective yaw moment. As mentioned earlier, this torque driver represents only the ideal case, where any required corrective yaw moment can be generated and acts directly at the center of mass of the vehicle. Note that the required corrective yaw moment must ultimately be generated by individual tire forces. More details about the DynaFlexPro model of the AUTO21EV can be found in [Vog07].

4.2 Soft computing and hybrid techniques

As the complexity of an engineering problem increases, so does the need for more advanced analytical control techniques. Many of the dynamic systems studied in recent applications involve nonlinear, time-variant, and chaotic behaviour. While conventional mathematical model-based control techniques can effectively address linear time-invariant problems, their efficacy when applied to more complex nonlinear time-variant problems is limited. The tools of soft computing have been shown to be highly effective in situations where the performance of conventional techniques is poor [Kar04].

The term “soft computing” refers to a family of computational techniques, namely fuzzy logic, evolutionary computation, and neural networks. These techniques have been conceptualized and developed over the past forty years. Contrary to hard computational techniques, which are characteristically rigid in structure, soft computing techniques have the ability to operate in environments that are subject to uncertainty and imprecision. In fact, in many applications, the precision offered by conventional techniques can comfortably be sacrificed in order to arrive at more economical and intuitive solutions. Each soft computing technique has its own set of strengths and weaknesses, some of which are illustrated in Figure 4-2. While the tools of soft computing share some common characteristics, these techniques are considered to be complementary, as

desirable features lacking in one approach may be present in another. Although many problems have been solved by using only one technique, many real-world problems require the integration of two or more techniques in order to achieve the required speed and accuracy for a given application. Therefore, by combining individual soft computing techniques together, new and powerful hybrid techniques can be generated that exploit the strengths of the constituent paradigms while reducing the effects of their weaknesses. Figure 4-3 illustrates some of the possible hybrid techniques that can be obtained through the fusion of two or more soft computing paradigms. Since building a genetic fuzzy YMC is the main focus of this chapter, a brief overview of fuzzy logic and the genetic algorithms is presented below.

Fuzzy Logic	✓ Intuitive representation of knowledge ✓ Tolerates imprecise information × Unable to learn or adapt × Design of knowledge base is difficult
Genetic Algorithm	✓ Covers the entire search space ✓ Does not require differentiability × Converges slower than other methods × Obtains only approximate solutions
Neural Network	✓ Excellent learning and generalization ✓ Can adapt to changing environments × Unintuitive representation of knowledge × Size and structure unknown a priori

Figure 4-2: Advantages and disadvantages of soft computing techniques

Fuzzy Logic: Since their initial development by Prof. L.A. Zadeh in the mid-1960s [Kar04], the principles of fuzzy logic have been applied to a wide variety of applications. In contrast to conventional Boolean or crisp methods, in which truth is represented by the state 1 and falsity is represented by the state 0, fuzzy logic represents approximate knowledge, and can be considered to be an extension of crisp two-state logic. Fuzzy logic is based on fuzzy set theory in a manner that is similar to how crisp two-state logic is based on crisp set theory. A fuzzy set is represented by a membership function. A particular 'element' value in the range of definition of the fuzzy set will have a grade of membership, which gives the degree to which the particular element belongs to the set. In this manner, it is possible for an element to belong to the set (to some degree) and,

simultaneously, to not belong to the set (to a complementary degree), thereby allowing a non-crisp, fuzzy membership [Kar04].

As the complexity of a system increases, the ability to develop precise analytical models of the system diminishes until a threshold is reached, beyond which analytical modelling simply becomes intractable. Under such circumstances, where precise model-based decision-making is not practical, fuzzy knowledge-based decision-making is particularly suitable. Fuzzy logic provides an approximate, yet practical, means of representing knowledge about a system that is too complex or ill-defined and, therefore, not easy to handle using precise mathematical means. At the same time, fuzzy logic provides a means of making inferences using approximate knowledge, which can be used to make decisions regarding the system and carry out appropriate actions. These features allow fuzzy logic to effectively handle human-oriented knowledge.

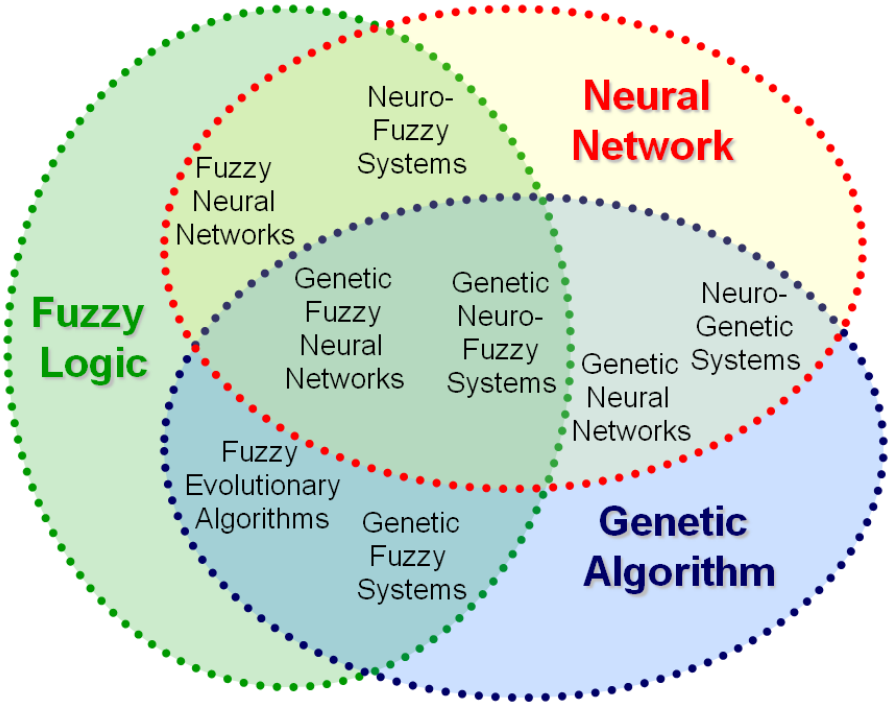

Figure 4-3: Hybrid techniques possible through the combination of soft computing paradigms

Fuzzy inference systems represent knowledge in the simple and intuitive form of '*if-then*' rules, and are able to approximate human reasoning capabilities given imprecise information. As such, fuzzy systems tend to be more robust than traditional control systems, and can be used to model and control complex nonlinear dynamic systems without requiring a complex analytical model of the system. Although many applications can be found in industry, fuzzy systems can only be used in situations where expert

knowledge is available. However, as the complexity of a system increases, it becomes more challenging to determine the correct set of fuzzy rules and the appropriate shape of the membership functions. Unfortunately, fuzzy systems have no inherent learning or adapting capabilities, so the fuzzy rules and membership functions must be designed and tuned manually if a fuzzy system is implemented on its own.

Figure 4-4 illustrates the structure of a fuzzy rule-based system. As can be seen, a fuzzy controller consists of four parts: fuzzification, the knowledge base, the inference engine, and defuzzification. The inputs to the fuzzy controller are most often crisp measurements obtained from some measuring equipment, so a preprocessor is necessary for preparing the measurements before entering the controller. Some possible preprocessing methods are as follows [Jan98]:

- Quantization in connection with sampling or rounding to integers;
- Normalization or scaling onto a particular standard range;
- Filtering to remove noise;
- Averaging to obtain long-term or short-term tendencies; and
- Differentiation and integration, or their discrete equivalences.

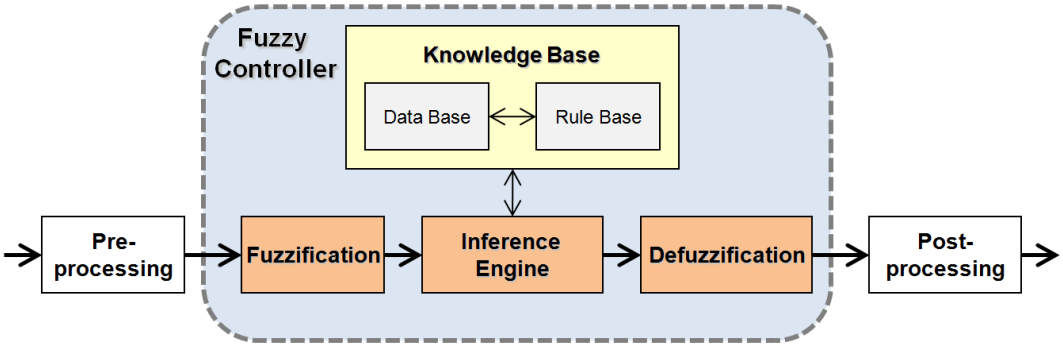

Figure 4-4: Block diagram of a fuzzy control systems

The fuzzification block translates each piece of input data into degrees of membership in one or several membership functions using tabulated data. Specifically, the fuzzification block matches the input data with the conditions of the rules to determine how well the condition of each rule matches that particular input. There is a degree of membership for each linguistic term that applies to each input variable. The knowledge base of the fuzzy controller consists of a data base (containing the definitions

of the scaling factors and the membership functions of the fuzzy sets that, together, specify the meaning of the linguistic terms) and a rule base (constituted by the collection of fuzzy rules, specified in an 'if-then' format). The inference engine is the driver program of the knowledge base. Depending on the inputs and the data in the data base, the inference engine operates on the knowledge in the knowledge base to solve problems and arrive at conclusions. The defuzzification block converts the resulting fuzzy set to a crisp number that can be sent to the controlled system as a control signal. There are several defuzzification methods, including the center of gravity, bisector of area, mean of maxima, and leftmost and rightmost maxima approaches [Kar04]. Finally, the postprocessor scales the output to engineering units, in cases where the output has been defined over a normalized range. The postprocessor often contains an output gain that can be tuned.

Genetic Algorithms: Evolutionary or genetic algorithms (GAs) are general-purpose search strategies that use principles inspired by biological evolution to solve optimization problems. Evolutionary strategies are very robust and can be used in problem domains where traditional optimization techniques fail. GAs are typically used in complex problem spaces that are difficult to understand or predict, since they are effective at exploring such spaces. The fundamental idea is to encode sets of system parameters in a population of chromosomes, each of which represents a candidate solution to the problem. The population of chromosomes is then evolved over time through competition among its members and controlled variation [Kar04]. Genetic algorithms consist of three operations: evaluation of the fitness of each individual chromosome, formation of a gene pool through the selection of chromosomes from the preceding generation, and recombination using the crossover and mutation operators.

A GA is initiated with a population of randomly generated chromosome, and discovers fitter chromosomes by applying genetic operators that are modelled after the genetic processes occurring in the nature. The population evolves by way of natural selection. During successive iterations, or so-called 'generations', the chromosomes in the population are evaluated for their adaptation as solutions. On the basis of these evaluations, a new population of chromosomes is formed using a selection mechanism and specific genetic operators, such as crossover and mutation. It is important to note that

a specific fitness function must be devised that describes the objective of the problem to be solved. Given a particular chromosome (i.e., a candidate solution), the fitness function returns a single numerical fitness value that is proportional to the utility or adaptation of the solution represented by that chromosome.

Whereas traditional optimization techniques, such as hill-climbing algorithms, search for global optima in a multi-dimensional space by iteratively refining a single solution vector, genetic algorithms operate on an entire population of candidate solutions in parallel. Therefore, GAs are less prone to becoming trapped by local optima. Local optima are regions of the search space that hold good solutions relative to their surrounding regions, but do not necessarily contain the best solutions in the entire problem space, which are described as global optima. Parallelism is one of the main strengths of GAs, since it helps to prevent premature convergence at local optima, and it reduces the importance of carefully selecting the initial conditions. Note that the mutation and crossover rates are among the most significant factors contributing to convergence and, therefore, must be selected carefully [Gol89]. Although the stochastic search used by genetic algorithms is exceptionally robust, its convergence is usually slower than that of traditional techniques. Moreover, due to the stochastic nature of genetic algorithms and the encoding of parameters into a finite number of genes, the solutions obtained by GAs are only approximations; they will only find an exact global optimum by chance.

Genetic Fuzzy System: Fuzzy logic and genetic algorithms have both been applied to a wide variety of problems. Still an active area of research, however, is the fusion of these techniques into a hybrid system that exploits their strengths while reducing the effects of their weaknesses. Two main hybrid approaches have been identified in this area: fuzzy evolutionary algorithms and genetic fuzzy systems. A fuzzy evolutionary algorithm is an evolutionary algorithm whose inherent parameters, such as its fitness function and stopping criterion, are fuzzified. The resulting hybrid system is capable of tolerating imprecision, which can reduce the computational resources required. Fuzzy inference systems can be used to adapt the parameters of an evolutionary algorithm, such as its mutation rate, crossover rate, and population size, or to adapt the genetic operators themselves. In the first case, the inputs to the fuzzy system would be the current control

parameters and performance measures, and the outputs would be the new control parameters subsequently used by the genetic algorithm [Her96, Vog98].

In the 1990s, despite the previous success of fuzzy logic systems, their inability to learn or adapt to their environment was found to severely limit their potential applications; genetic fuzzy systems address this limitation. A genetic fuzzy system is essentially a fuzzy system that is augmented by a learning process based on a genetic algorithm. The most popular type of genetic fuzzy system is the genetic fuzzy rule-based system, where an evolutionary algorithm is employed as a design method to learn or tune different components of a fuzzy knowledge base. The structure of a genetic fuzzy system is illustrated in Figure 4-5.

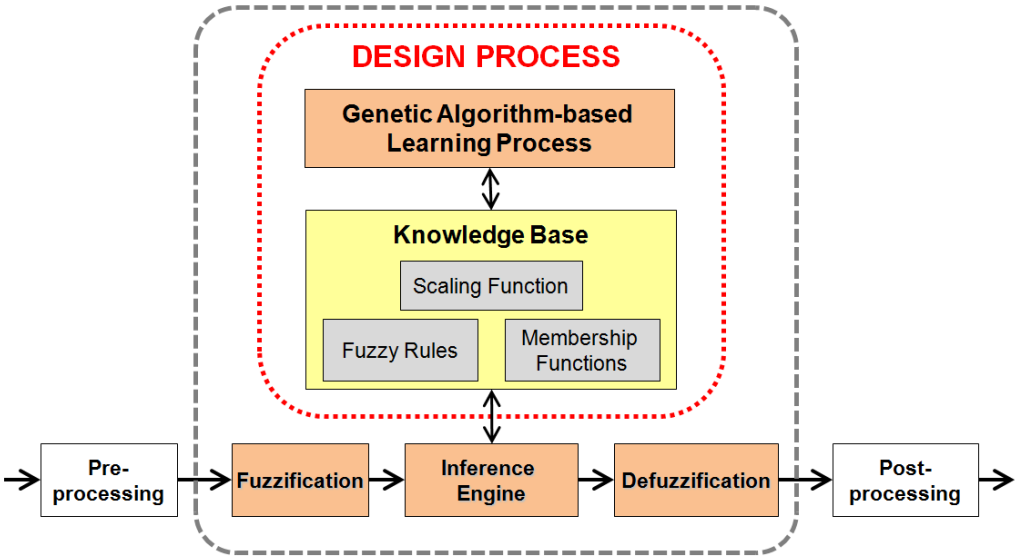

Figure 4-5: Block diagram of a genetic fuzzy control system

In order to use a genetic algorithm for optimizing a fuzzy knowledge base, the rules or membership functions must first be represented as a set of tunable parameters. It is also necessary to define an appropriate performance index, based on the optimization criterion, with which to evaluate the proposed knowledge bases. Finally, the knowledge base parameters must be transformed from the optimization space into a suitable genetic representation [Cor04]. A genetic process can then be used to evaluate, select, and evolve the genetically encoded candidate solutions. At this point, it is important to differentiate between tuning and learning problems. Tuning is concerned with the optimization of an existing fuzzy inference system having a predefined rule base. Learning, on the other hand, constitutes an automated design method for determining fuzzy rule sets from

scratch [Cor01]. In other words, learning processes do not require a predefined set of rules. The objective in the case of tuning is to find the best possible set of parameters for the data base of the fuzzy inference system. For instance, tuning can be applied to the scaling functions that normalize the domain of the input and output variables. Linear scaling functions can be parameterized by either a single scaling factor or by two parameters; nonlinear scaling functions generally use three or four parameters [Cor01]. Tuning can also be applied to the fuzzy membership functions. In this case, each chromosome encodes the parameterized membership functions associated with all the rules in the rule base. The rule base of a fuzzy inference system can also be tuned using a genetic algorithm, as described in [Yu02, Gur99].

4.3 Fuzzy yaw moment controller design

As mentioned earlier, fuzzy control systems are nonlinear control methods that can handle complicated nonlinear dynamic control problems and, as such, they are ideally suited for controlling the highly nonlinear behaviour inherent in vehicular dynamics. A fuzzy controller is described in vague linguistic terms, which suits the subjective nature of vehicle stability and handling, and allows one to encode expert knowledge directly in the rule base of the fuzzy controller [Kar04]. In addition, the idea of using a fuzzy logic controller as a high-level supervisory module that assigns tasks to low-level actuators and controllers appears to be an ideal method of addressing the complexities of integrated chassis control management. This approach allows the lower-level controllers to be designed simply as tracking controllers that attempt to match the state of their respective plants to the reference signals generated by the supervisory controller. In this work, a fuzzy YMC is developed for the AUTO21EV that determines the corrective yaw moment required to minimize the sideslip and yaw rate errors of the vehicle, comparing the actual values to those obtained using a reference model, with the ultimate objective of following the desired trajectory requested by the driver. The proposed controller requires two vehicle states, the yaw rate and vehicle sideslip angle, to calculate the required corrective yaw moment.

To date, yaw rate tracking algorithms have been used to improve the stability of a vehicle when driving near the handling limit [Man07]. A recurring problem found throughout the literature, however, is how to define the limits of handling and distinguish

between emergency and normal driving situations. The studies of yaw rate stability are dominated by the use of reference model feedback control, where the controller attempts to match the nonlinear behaviour of the vehicle with that of a reference bicycle model. As the vehicle approaches its performance limits, the actuation power required to reduce the tracking error becomes large and may exceed the capability of any active chassis subsystem. In general, information about the yaw rate alone is not always sufficient because, for instance, a vehicle may be undergoing an acceptable yaw rate while skidding sideways. Thus, many researchers claim that significantly more comprehensive control can be achieved given vehicle sideslip angle information [Man07]. The vehicle sideslip angle is defined as the angle between the longitudinal axis of the vehicle and the direction in which it is travelling. Human drivers are particularly sensitive to the sideslip motion of the vehicle, and tend to prefer small sideslip angles [Dix96]. This preference arises from the sensation of instability at larger angles, which is perhaps rooted in the real potential for the loss of control when the vehicle sideslip angle becomes too large. Thus, both sideslip and yaw rate are extremely important factors influencing the driver's perception of handling behaviour, especially when driving near the handling limit. As a result, the quality of the driving experience depends strongly on the quality of the feedback signals of these two states.

In order to calculate the desired yaw rate as the reference signal for the fuzzy yaw moment controller, a bicycle model is used, which is illustrated in Figure 4-6. In this model, the left and right tires on each axle are merged together, and the height of the center of mass of the vehicle is set to zero. In addition, the longitudinal tire forces and the variation of the vertical tire forces are not considered. The equations of motion of the bicycle model are linearized such that only small slip angles are considered, where $\sin(\alpha) \approx \alpha$ and $\cos(\alpha) \approx 1$, and linear tire behaviour is assumed, where the lateral tire stiffness (C_α) is a constant defining the linear relationship between the lateral force (F_y) and the slip angle (α) of a tire as follows:

$$C_\alpha = \frac{F_y}{\alpha} \tag{4.1}$$

Since the lateral inertial force acting on the center of mass of the vehicle is equal to the centrifugal force resulting from driving in a curve with a radius of R and a rotational speed of $\dot{\vartheta}$ (Figure 4-6), the following relationship can be assumed between the lateral

acceleration of the vehicle (a_y) and the speed (V), yaw rate ($\dot{\psi}$), and sideslip rate ($\dot{\beta}$) of the vehicle [Wal05]:

$$m_{CG} \cdot a_y = m_{CG} \cdot \frac{V^2}{R} = m_{CG} \cdot \frac{V}{R} \cdot (\dot{\vartheta} \cdot R) = m_{CG} \cdot V \cdot \left(\dot{\psi} - \dot{\beta}\right) \tag{4.2}$$

where m_{CG} is the total mass of the vehicle. Note that $V = \left|\vec{V}\right|$, $\dot{\psi} = \left|\dot{\vec{\psi}}\right|$, and $\dot{\beta} = \left|\dot{\vec{\beta}}\right|$ are the magnitudes of the velocity, yaw rate, and sideslip rate vectors of the vehicle, respectively, and $\dot{\vartheta} = \left|\dot{\vec{\vartheta}}\right|$ is the magnitude of the rotational velocity of the vehicle. Looking at Figure 4-6, the sideslip angle of the front (α_F) and rear (α_R) tires can be estimated as follows:

$$\alpha_F = \delta - \beta - \frac{a \cdot \dot{\psi}}{V} \tag{4.3}$$

$$\alpha_R = -\beta + \frac{b \cdot \dot{\psi}}{V} \tag{4.4}$$

where a and b are the distances of the front and rear axles from the vehicle center of mass and δ is the steering angle of the front wheel.

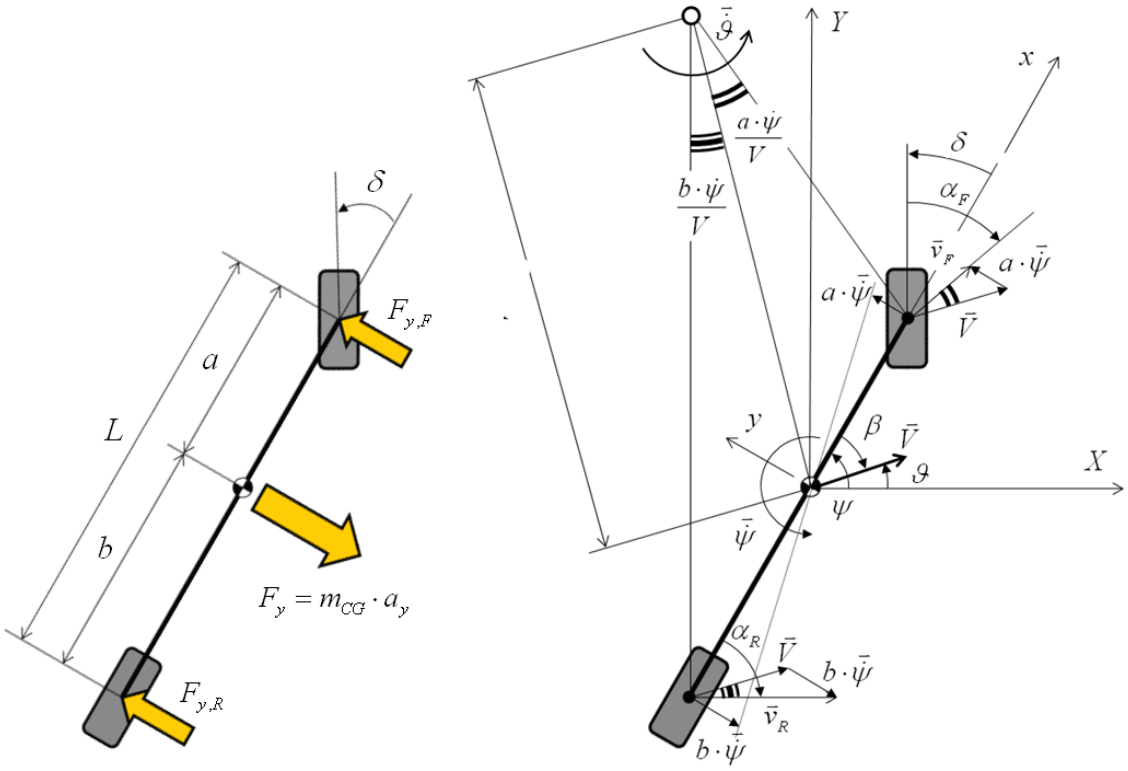

Figure 4-6: Linear bicycle model [Wal05]

As a vehicle travels through a circular path in a steady-state motion, the speed (*V*), yaw rate ($\dot{\psi}$), and sideslip angle (β) of the vehicle remain constant and, consequently, the longitudinal acceleration, yaw acceleration, and rate of change of the sideslip angle of the vehicle are zero ($a_x = 0,\ \ddot{\psi} = 0$, and $\dot{\beta} = 0$). Thus, in a steady-state circular motion, the following statements can be assumed from equation (4.2):

$$a_y = V \cdot \dot{\psi} \tag{4.5}$$

$$\frac{1}{R} = \frac{\dot{\psi}}{V} \tag{4.6}$$

Considering the sum of moments around the front and rear axles, the following equations can be derived:

$$F_{y,F} \cdot L = m_{CG} \cdot a_y \cdot b \tag{4.7}$$

$$F_{y,R} \cdot L = m_{CG} \cdot a_y \cdot a \tag{4.8}$$

where $F_{y,F}$ and $F_{y,R}$ are the lateral forces of the front and rear axles, respectively, and $L = a + b$ is the wheelbase of the vehicle. Substituting equations (4.1), (4.3), and (4.4) into equations (4.7) and (4.8), the following equations can be derived:

$$C_{\alpha F}\left(\delta - \beta - \frac{a \cdot \dot{\psi}}{V}\right) = m_{CG} \cdot a_y \cdot \frac{b}{L} \tag{4.9}$$

$$C_{\alpha R}\left(-\beta + \frac{b \cdot \dot{\psi}}{V}\right) = m_{CG} \cdot a_y \cdot \frac{a}{L} \tag{4.10}$$

where $C_{\alpha F}$ and $C_{\alpha R}$ are the total lateral stiffnesses of the front and rear tires, respectively. Calculating β from equation (4.9) and substituting it into equation (4.10), the following relationship between the steering angle and the lateral acceleration of the vehicle can be obtained:

$$\delta = \frac{L}{R} + \frac{m_{CG}}{L}\left(\frac{b}{C_{\alpha F}} - \frac{a}{C_{\alpha R}}\right) a_y \tag{4.11}$$

Substituting equations (4.5) and (4.6) into equation (4.11), the relationship between the vehicle yaw rate and the steering angle of the front wheel in a steady-state circular motion can be calculated as follows:

$$\dot{\psi} = \frac{V}{L + \frac{m_{CG}}{L}\left(\frac{b}{C_{\alpha F}} - \frac{a}{C_{\alpha R}}\right) V^2} \delta \tag{4.12}$$

Equation (4.12) is widely used to describe the desired yaw rate of the vehicle as a function of the steering angle by current stability controllers [Zan00]. In this work, a first-order lag element is also added to equation (4.12) to account for the lag between the steering input and the yaw rate response of the vehicle. Thus, the transfer function of the desired yaw rate ($\dot{\Psi}_{desired}(s)$) with respect to the steering angle ($\Delta(s)$) is defined in the linear s-domain as follows:

$$\frac{\dot{\Psi}_{desired}(s)}{\Delta(s)} = \frac{V(s)}{L + \frac{m_{CG}}{L}\left(\frac{b}{C_{\alpha F}} - \frac{a}{C_{\alpha R}}\right)V^2(s)} \frac{1}{1+Ts} \tag{4.13}$$

where the time constant of the lag element (T) is chosen to be 50 milliseconds. Note that this time constant is chosen to keep the reaction time of the maximum desired yaw rate in the range of 200 to 400 milliseconds, which is recommended for passenger cars [Wal05]. Furthermore, since the lateral acceleration of the vehicle is fundamentally limited by the friction coefficient of the tire-road contacts, the desired yaw rate must also be limited by a second value. Thus, from equation (4.2), the steady-state lateral acceleration of the vehicle is expressed either as a function of the radius of curvature (R) or as a function of the vehicle yaw rate ($\dot{\psi}$) as follows [Zan00]:

$$\left|a_y\right| = \left|\frac{V^2}{R}\right| = \left|V \cdot \dot{\psi}\right| \tag{4.14}$$

At the same time, the maximum lateral acceleration of the vehicle is theoretically limited by the friction coefficient of the tires:

$$\left|a_y\right| \leq \mu_{res} g \tag{4.15}$$

where μ_{res} is the resultant friction coefficient of the tires and g is the gravitational acceleration. Combining equations (4.14) and (4.15), the desired yaw rate is limited as follows [Zan00]:

$$\left|\dot{\psi}_{desired}\right| \leq \left|\frac{\mu_{res} g}{V}\right| \tag{4.16}$$

Since estimation of the friction coefficient is not always possible, the measured lateral acceleration can be used instead. This method is, in fact, used in the ESP system developed by Robert Bosch GmbH [Zan00]. Finally, note that, in this work, the desired sideslip angle is defined to be zero:

$$\beta_{desired} = 0 \tag{4.17}$$

and the actual sideslip angle is estimated using the neural network described in Chapter 3. Figure 4-7 illustrates the block diagram of the fuzzy YMC.

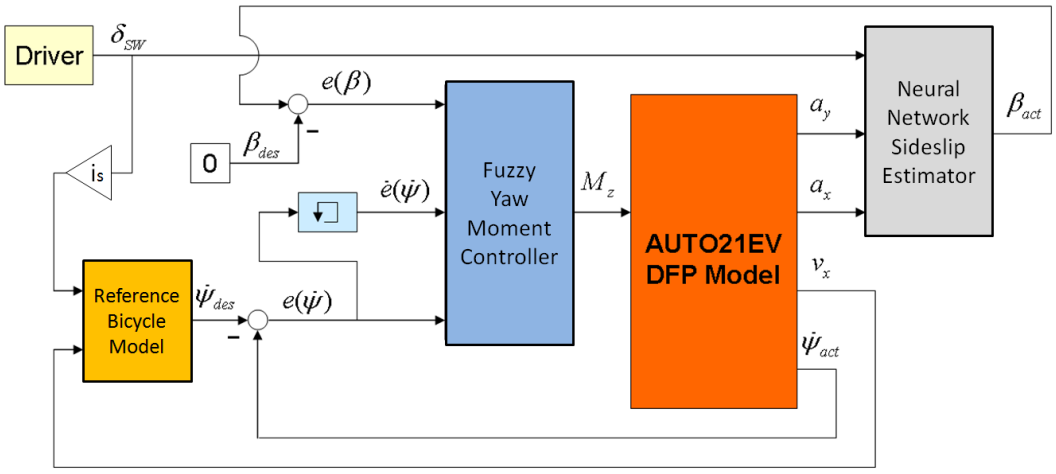

Figure 4-7: Block diagram of the fuzzy yaw moment controller

The rule base of the fuzzy controller was designed using the sideslip angle error $e(\beta)$, the yaw rate error $e(\dot{\psi})$, and the rate of change of the yaw rate error $\dot{e}(\dot{\psi})$ as the inputs; the required corrective yaw moment M_z is the output of the controller. Table 4-I lists the definitions of the input and output variables. The input variables are pre-processed to the range [-1, 1] before entering the fuzzy controller. The output variable is correspondingly post-processed to determine the required corrective yaw moment. Whereas the scaling factors used for pre-processing the input variables are chosen based on the actual vehicle states when driving through a severe maneuver, the scaling factor used for post-processing the output variable is determined based on the actuation potential of the in-wheel motors. In particular, the maximum allowable sideslip angle error, yaw rate error, and rate of change of yaw rate error when driving through a severe double-lane-change maneuver are assumed to be 10^o, 35^o/s, and 2000^o/s^2, respectively, which correspond well with the limits found in the literature for normal passenger cars [Kie05, Wal05]. Moreover, assuming that the maximum longitudinal tire force is about 3500 N by considering a nominal wheel load of 3800 N, the maximum possible yaw moment that can be generated by the in-wheel motors is created by generating a couple on the sides of the vehicle, applying negative torque to the wheels on one side and positive torque to those on the other side. By doing so, and knowing that the track width

of the AUTO21EV is 1.35 m, the maximum possible yaw moment is calculated as follows:

$$M_{z,\max} = 3500\ \mathrm{N} \cdot 2 \cdot 1.35\ \mathrm{m} = 9450\ \mathrm{Nm} \tag{4.18}$$

Variable	Definition
Input 1	$e(\beta) = \beta_{desired} - \beta_{actual}$
Input 2	$e(\dot{\psi}) = \dot{\psi}_{desired} - \dot{\psi}_{actual}$
Input 3	$\dot{e}(\dot{\psi}) = \dfrac{e(\dot{\psi})_k - e(\dot{\psi})_{k-1}}{\text{sample time}}$
Output	M_z

Table 4-I: Definition of the input and output variables of the fuzzy yaw moment controller

In order to provide enough rule coverage, five fuzzy sets are used for each of the yaw rate and sideslip error variables, and three fuzzy sets are used for the rate of change of the yaw rate error. Nine fuzzy sets are used to describe the output of the controller, which ranges from a very large positive (counterclockwise) moment to a very large negative (clockwise) moment. The fuzzy inference engine processes the list of rules in the knowledge base using the fuzzy inputs obtained from the previous time step of the simulation to create the fuzzy output for the current time step. A three-dimensional (3D) rule base table is developed for the proposed fuzzy YMC, as shown in Figure 4-8; the linguistic variables that have been used are listed in Table 4-II. These rules have been developed based on expert knowledge and intensive investigation. In other words, based on the possible sideslip angle error, the yaw rate error, and the rate of change of the yaw rate error, the vehicle state at each driving conditions is analyzed and the required corrective yaw moment at that specific condition is determined and translated into a specific rule in the rule base table. The fuzzy controller uses the Mamdani fuzzy inference method, which is characterized by the following fuzzy rule schema:

$$\text{IF } e(\beta) \text{ is } A \text{ AND } e(\dot{\psi}) \text{ is } B \text{ AND } \dot{e}(\dot{\psi}) \text{ is } C \text{ THEN } M_z \text{ is } D \tag{4.19}$$

where *A*, *B*, *C*, and *D* are fuzzy sets defined on the input and output domains. Given a certain vehicle sideslip error, yaw rate error, and rate of change of the yaw rate error, the 3D fuzzy rule base can determine the direction and relative magnitude of the required corrective yaw moment. The initial shape and distribution of the membership functions used for the input and output variables of the fuzzy controller are illustrated in Figure 4-9.

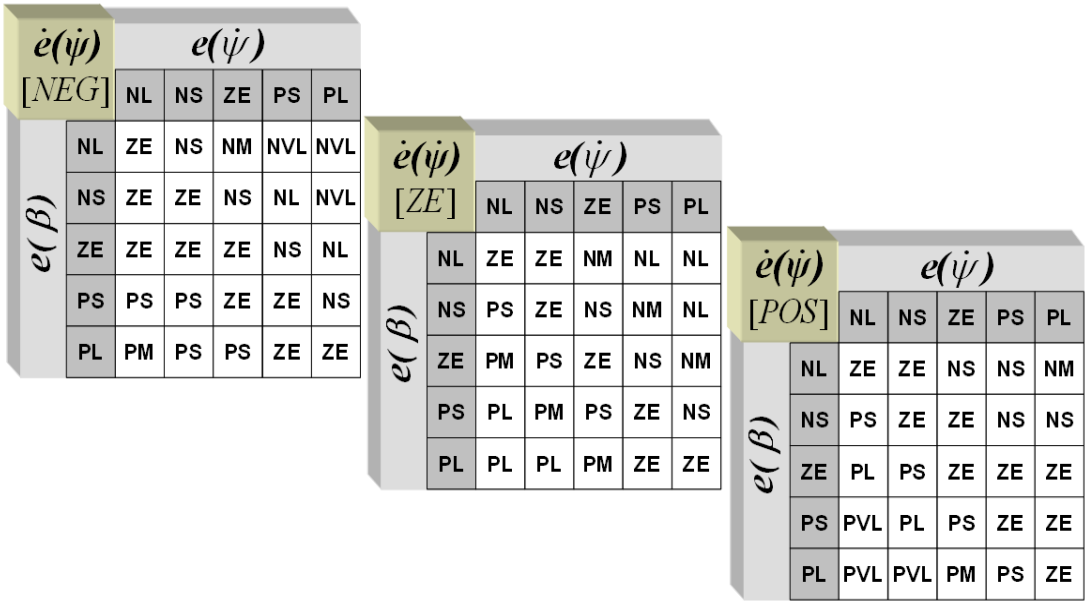

Figure 4-8: Three-dimensional rule base of the fuzzy YMC

Acronym	Linguistic Variable
NEG	Negative
NVL	Negative Very Large
NL	Negative Large
NM	Negative Medium
NS	Negative Small
ZE	Zero
PS	Positive Small
PM	Positive Medium
PL	Positive Large
PVL	Positive Very Large
POS	Positive

Table 4-II: Linguistic variables used in the fuzzy rules

Notice that, as is often the case, these fuzzy rules are formed using fuzzy variables whose membership functions are of unknown shapes, sizes, and relative positions. Since a fuzzy controller is unable to learn or adapt to its environment on its own, tuning the fuzzy membership functions must be done manually, which is an inefficient and time-consuming endeavour. Furthermore, looking at the corresponding control surfaces between the input and output variables of the fuzzy YMC shown in Figure 4-10, it is clear that the generated corrective yaw moment does not cover the entire output domain. In other words, although the maximum possible yaw moment is defined to be 9450 Nm, as

calculated in equation (4.18), according to the control surfaces in Figure 4-10, only 60% of the maximum yaw moment is achievable using the initial fuzzy membership functions.

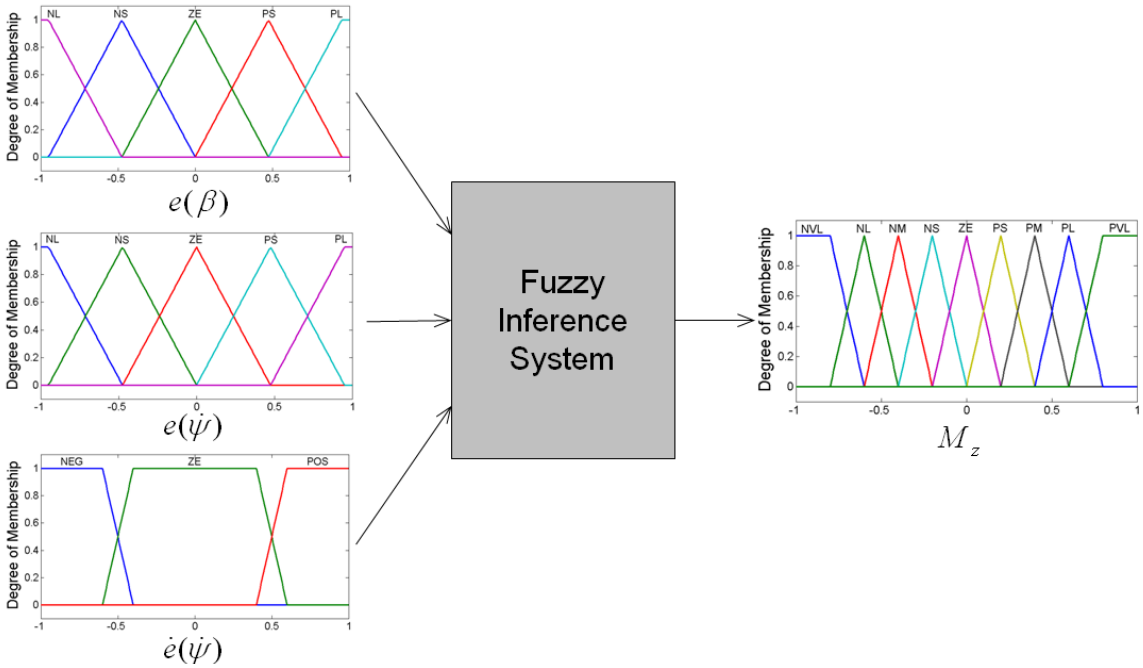

Figure 4-9: Initial shape and distribution of the membership functions for the input and output variables of the fuzzy YMC

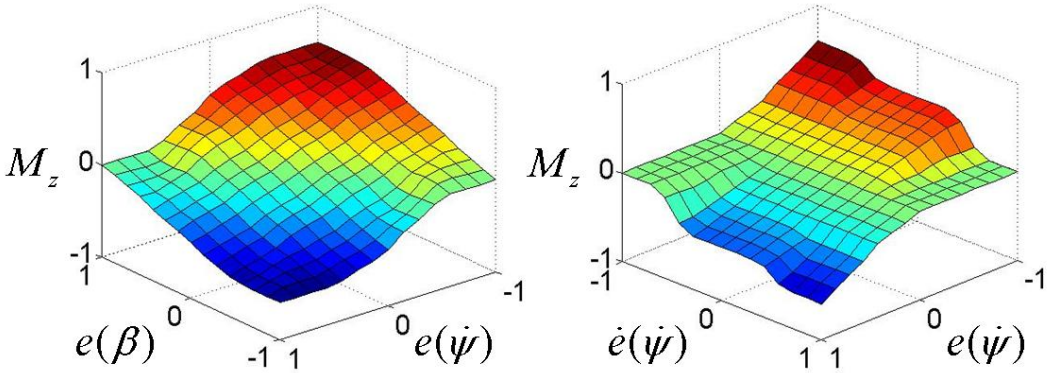

Figure 4-10: Control surfaces of the fuzzy YMC

4.4 Evaluation of the fuzzy yaw moment controller

In order to evaluate the performance of the fuzzy yaw moment controller, the AUTO21EV is driven through an ISO double-lane-change maneuver using the path-following driver model, whose characteristics are described in Chapter 2. An ISO double-lane-change maneuver is chosen because it can effectively demonstrate the cornering capability of a vehicle when driving near its handling limit. The AUTO21EV is driven through the double-lane-change maneuver with an initial speed of 75 km/h, both with and without using the fuzzy YMC. As can be seen in Figure 4-11, the driver model was not

able to negotiate the maneuver without using the fuzzy YMC, and three of the cones were struck along the way. In addition, a significant amount of effort was required, even counter-steering at some points, in order to control the vehicle through the maneuver. In comparison, the driver was able to negotiate the same maneuver much more easily and smoothly when the fuzzy YMC was active.

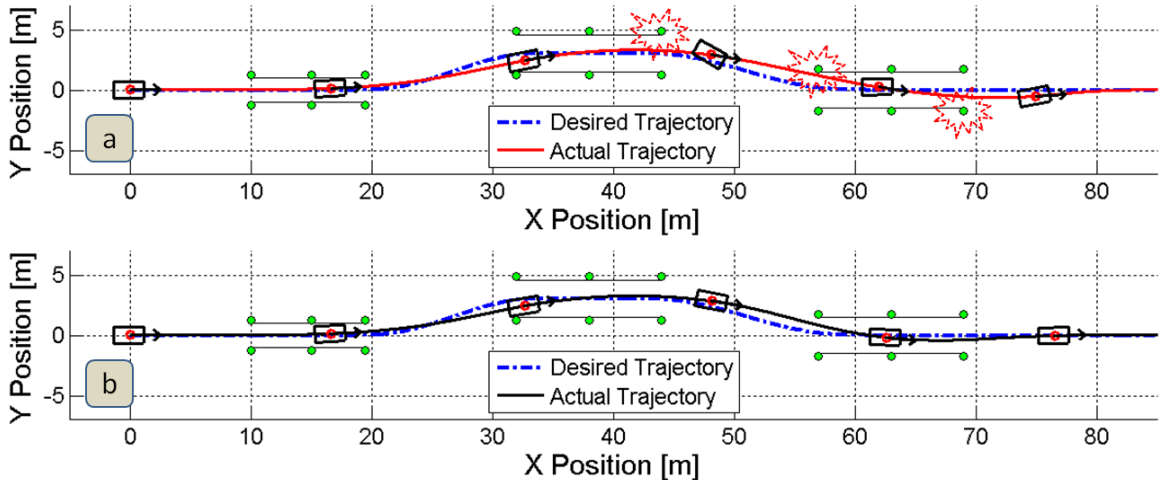

Figure 4-11: Desired and actual vehicle trajectories when driving through the double-lane-change maneuver with an initial speed of 75 km/h (a) using the driver model and (b) using the driver model with the fuzzy YMC

Figure 4-12 illustrates the vehicle yaw rate and sideslip angle for this maneuver, both of which are of a much smaller magnitude for the case when the fuzzy YMC is active. Although the fuzzy YMC is not able to control the vehicle such that it performs exactly like the desired reference bicycle model, it is able to reduce both the vehicle yaw rate and sideslip angle considerably, thereby allowing the driver to complete the maneuver with less effort. This performance is confirmed in Figure 4-13, which illustrates the lateral acceleration of the vehicle, the driver's steering input, and the vehicle forward speed as functions of time. The fact that the vehicle experiences a lateral acceleration of about 8 m/s^2 even when the fuzzy YMC is active confirms the severity of the double-lane-change maneuver, as well as the fact that the adhesion potentials on all tires are saturated widely in order to keep the vehicle on the desired path.

Looking at the plot of the driver's steering wheel angle (Figure 4-13-b), it is clear that the driver requires less steering effort when the fuzzy YMC is active, which indicates an easier and more comfortable drive. In addition, a reduction in the steering effort means that the vehicle loses less speed when driving through the maneuver (Figure 4-13-c). Figure 4-13-d, which illustrates the handling performance of the vehicle, clearly indicates

that the vehicle handling and agility have been significantly improved by the fuzzy YMC, as the hysteresis of the curve is considerably reduced. This plot indicates that the phase shift between the input and output signal of the controlled system (the vehicle) is reduced considerably. The generated corrective yaw moment is shown in Figure 4-14. Although the fuzzy YMC is not able to eliminate the vehicle yaw rate and sideslip angle errors during this severe double-lane-change maneuver (Figure 4-12), the maximum corrective yaw moment that is generated by the controller is only about one-third of its limit potential, as calculated in equation (4.18). This performance is due to the fact that the initial fuzzy membership functions, with arbitrary shape, size, and relative distribution, can only apply up to 60% of the maximum possible yaw moment.

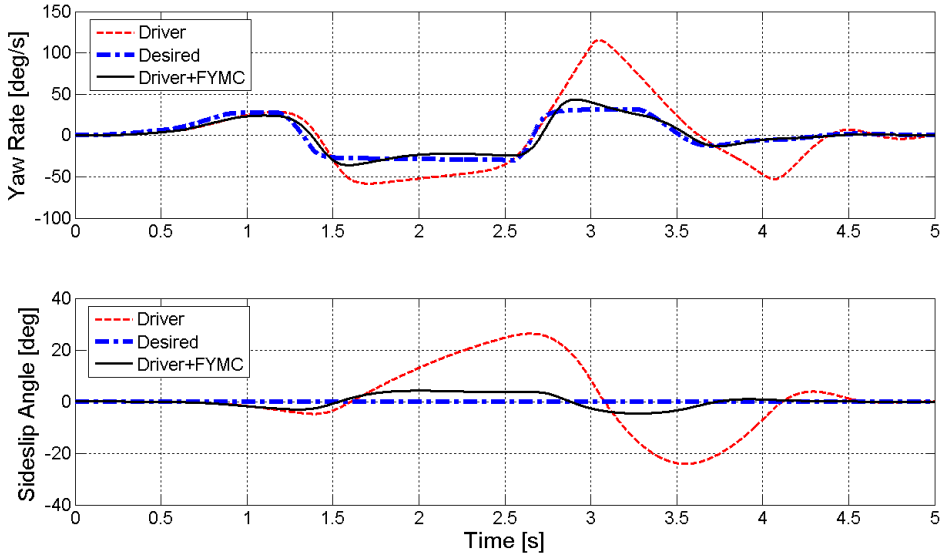

Figure 4-12: Desired and actual vehicle yaw rate (top) and sideslip angle (bottom) when driving through the double-lane-change maneuver using the driver model, with and without the fuzzy YMC (FYMC)

4.5 Genetic tuning of the fuzzy yaw moment controller

The rule base developed for the fuzzy YMC was determined based on expert knowledge and extensive investigation into the vehicle behaviour in different driving conditions. However, due to the arbitrary shape, size, and relative positions of the fuzzy membership functions, the performance of the resulting fuzzy YMC cannot be considered ideal. Since a fuzzy controller is unable to learn or adapt to its environment on its own, and instead of resorting to tuning the membership functions of the fuzzy controller manually, which is an inefficient, arduous, and time-consuming task, a multi-criteria genetic algorithm is used to tune the membership functions of the fuzzy YMC.

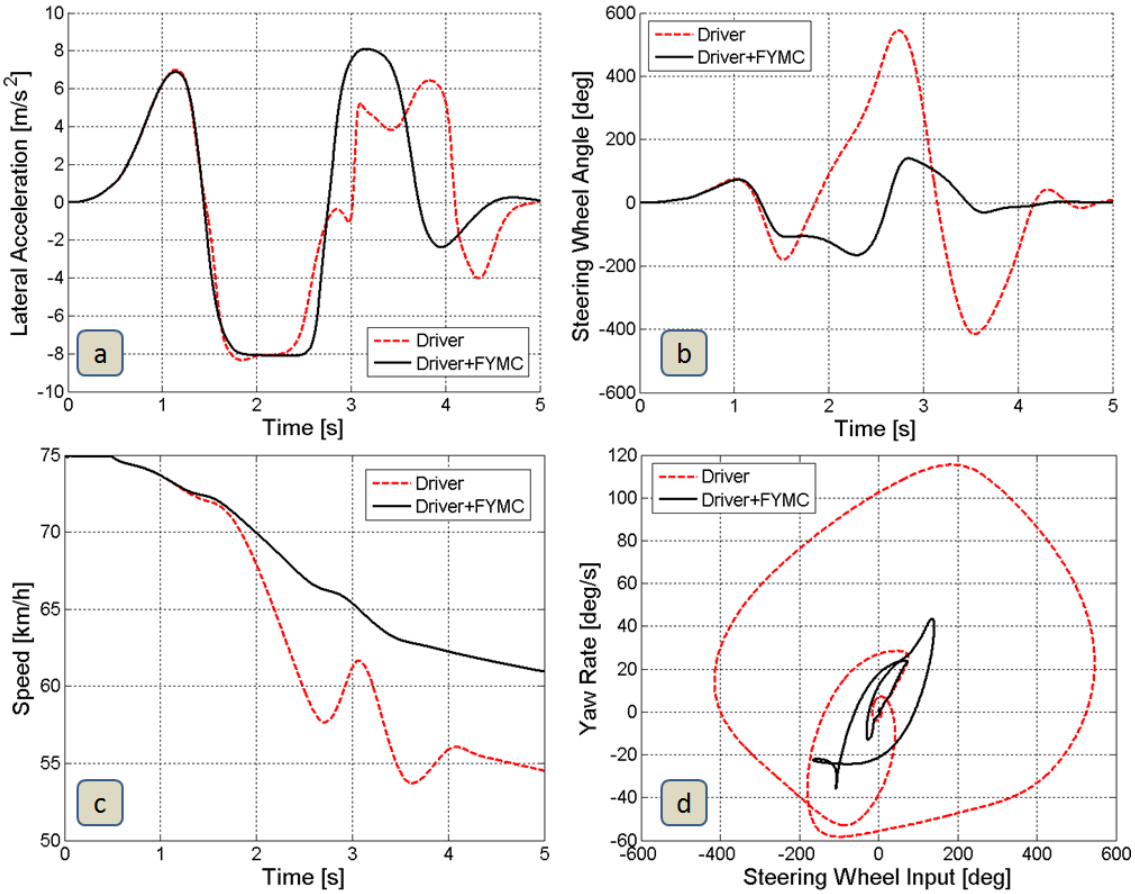

Figure 4-13: (a) Lateral acceleration, (b) steering wheel angle, and (c) vehicle speed as functions of time; and (d) vehicle yaw rate as a function of the steering wheel input when driving through the double-lane-change maneuver with and without the fuzzy YMC (FYMC)

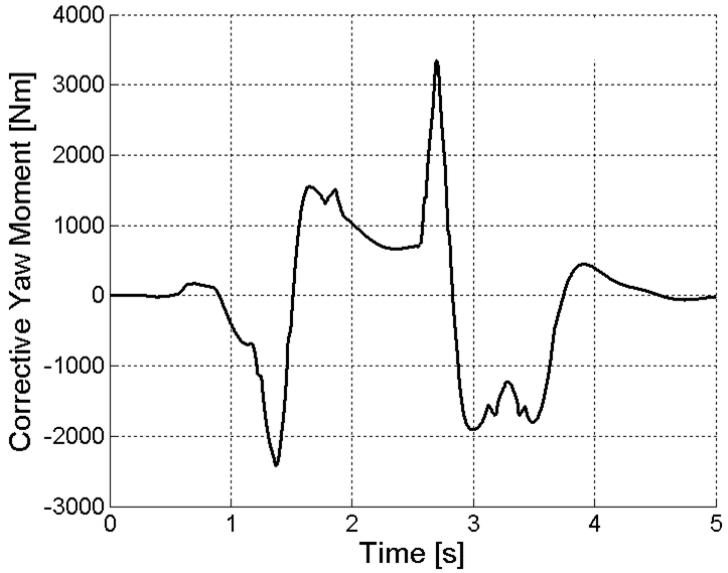

Figure 4-14: Corrective yaw moment generated by the fuzzy YMC

The ISO double-lane-change maneuver with obstacle avoidance was used to evaluate the effectiveness of each candidate controller in the genetic algorithm. As

mentioned earlier, such a severe maneuver effectively demonstrates the cornering capability of a vehicle when driving near its handling limit, which is why many car manufacturers and research institutions consider it to be a suitable test maneuver for assessing electronic stability controllers [Pai05]. The ISO double-lane-change maneuver is typically performed as a closed-loop driving test, and is used to adjust the dynamics of a vehicle based on the subjective evaluations of professional drivers. Due to the fact that the membership functions of the fuzzy controller must be tuned in a general sense, not based on a specific driver or driver model, the double-lane-change maneuver is considered to be an open-loop test for the sake of the optimization procedure. In this regard, the desired trajectory and the corresponding steering wheel input are determined for a 'neutral-steer' vehicle driving through the ISO double-lane-change test track at a low speed. This fixed steering wheel input, expressed as a function of forward displacement, is then considered to be the required steering input for driving through the double-lane-change maneuver even at higher speeds. Any deviations from the desired trajectory, yaw rate, or sideslip angle are considered to be stability errors that the fuzzy YMC should correct. The task of the multi-criteria genetic algorithm is to find the ideal shape and distribution for the membership functions of the fuzzy YMC such that the vehicle trajectory, yaw rate, and sideslip angle errors are minimized.

Looking at equation (4.11), the required steering angle for a 'neutral-steer' vehicle can be calculated as a function of the wheelbase of the vehicle (L) and the radius of curvature of the road (R) as follows:

$$\delta = \frac{L}{R} \tag{4.20}$$

The curvature of the road (κ), which is equal to the inverse of the radius of curvature, is defined as the derivative of the tangential angle (ϕ) with respect to the arc length (s) as follows [Cas96]:

$$\kappa = \frac{1}{R} = \frac{d\phi}{ds} \tag{4.21}$$

where the arc length (s) can be calculated using Cartesian parametric equations $x = x(t)$ and $y = y(t)$ as follows (Figure 4-15):

$$s = \sqrt{x^2 + y^2} \tag{4.22}$$

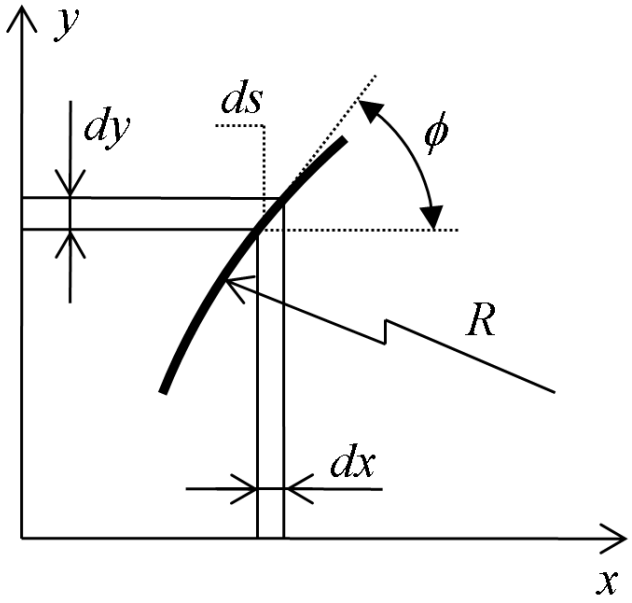

Figure 4-15: Curvature of the road in a two-dimensional plane using Cartesian coordinate system

Substituting equation (4.22) into equation (4.21), the following equation can be derived:

$$\kappa = \frac{1}{R} = \frac{d\phi}{ds} = \frac{\frac{d\phi}{dt}}{\frac{ds}{dt}} = \frac{\frac{d\phi}{dt}}{\sqrt{\dot{x}^2 + \dot{y}^2}} \tag{4.23}$$

Looking at Figure 4-15, the tangential angle ϕ can be calculated as follows:

$$\tan(\phi) = \frac{dy}{dx} = \frac{\frac{dy}{dt}}{\frac{dx}{dt}} = \frac{\dot{y}}{\dot{x}} \tag{4.24}$$

which can be differentiated to obtain an expression for $\dot{\phi}$:

$$\frac{d}{dt}\tan(\phi) = \left(1 + \tan^2(\phi)\right)\frac{d\phi}{dt} = \frac{\dot{x}\ddot{y} - \ddot{x}\dot{y}}{\dot{x}^2} \Rightarrow \frac{d\phi}{dt} = \frac{1}{1 + \frac{\dot{y}^2}{\dot{x}^2}}\frac{\dot{x}\ddot{y} - \ddot{x}\dot{y}}{\dot{x}^2} = \frac{\dot{x}\ddot{y} - \ddot{x}\dot{y}}{\dot{x}^2 + \dot{y}^2} \tag{4.25}$$

Substituting equation (4.25) into equation (4.23), the following expression can be derived for the curvature of the road:

$$\kappa = \frac{\dot{x}\ddot{y} - \ddot{x}\dot{y}}{\left(\dot{x}^2 + \dot{y}^2\right)^{3/2}} \tag{4.26}$$

For a two-dimensional curve written in the form $y = f(x)$, the equation of curvature takes the following form:

$$\kappa = \frac{\frac{d^2y}{dx^2}}{\left(1+\left(\frac{dy}{dx}\right)^2\right)^{3/2}} \tag{4.27}$$

Since the desired vehicle trajectory in a double-lane-change maneuver is defined as a function of forward displacement using equation (2.1) in Chapter 2, the required steering angle for a 'neutral-steer' vehicle can be calculated by substituting equations (4.21) and (4.27) into equation (4.20) as follows:

$$\delta = L \cdot \kappa = L \frac{\frac{d^2y}{dx^2}}{\left(1+\left(\frac{dy}{dx}\right)^2\right)^{3/2}} \tag{4.28}$$

Figure 4-16 illustrates the fixed steering wheel angle calculated for this maneuver using equation (4.28). Note that the amplitude and frequency associated with the first lane change are larger, as the first lane change is slightly more aggressive than the second one. Figure 4-17 illustrates the desired and actual vehicle trajectories, yaw rates, and sideslip angles when driving through the double-lane-change maneuver with an initial speed of 25 km/h using the calculated fixed steering wheel input. This figure demonstrates that the AUTO21EV is able to negotiate the maneuver with the calculated fixed steering wheel input at a low speed.

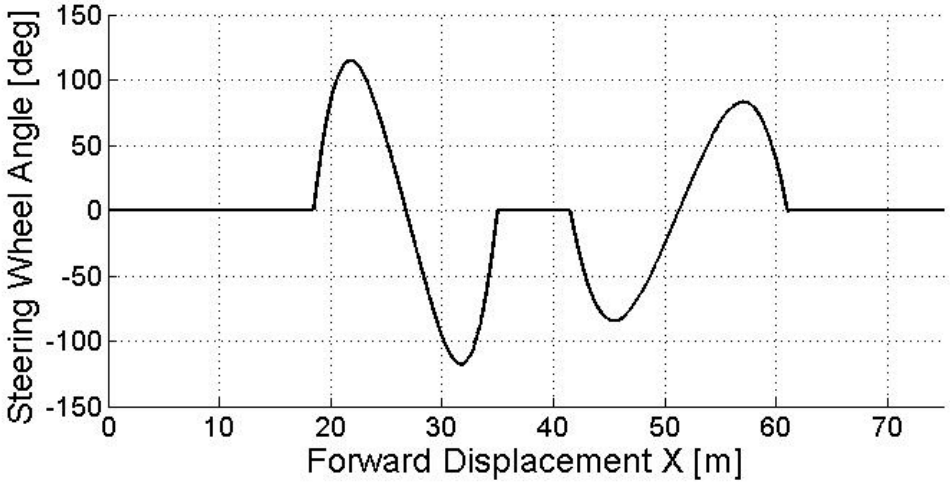

Figure 4-16: Desired fixed steering wheel input for driving through the double-lane-change maneuver

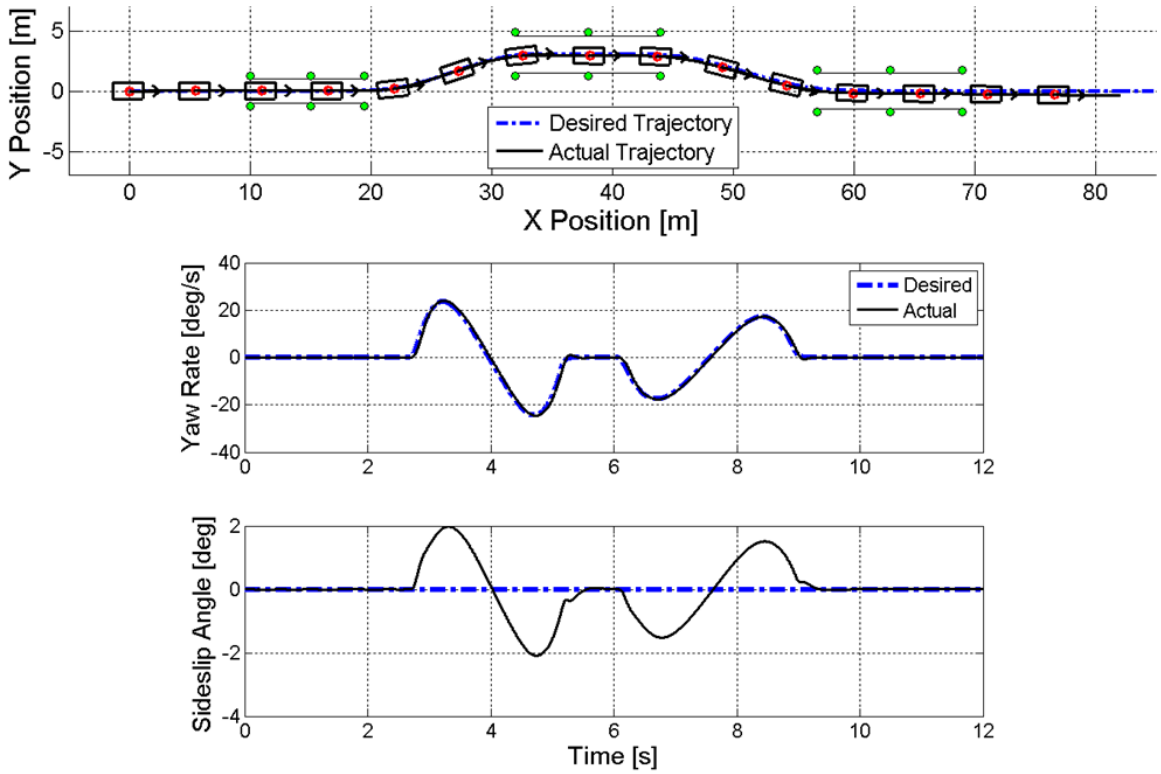

Figure 4-17: Desired and actual vehicle trajectories (top), and yaw rate and sideslip angle (bottom) when driving through the double-lane-change maneuver with a fixed steering wheel input

The scaling function technique is chosen for the genetic tuning of the fuzzy membership functions. Using scaling functions, the input and output variables are mapped into the range over which the fuzzy sets are defined. From a control engineering perspective, the scaling functions represent context information, while the membership functions describe the relative semantics of the linguistic variables, independent from the context. The scaling and membership functions together establish the absolute semantics of the linguistic variables. The context information represented by scaling functions can be related to the physical properties or dimensions of the controlled system, such as restrictions imposed due to the limitations of the actuators, or can represent information that affects the overall behaviour of the controlled system, such as conditioning the desired behaviour of the controlled system and not its physical limits [Cor01]. From a hierarchical point-of-view, modifying a rule consequence in the rule base of a fuzzy system has only a small effect, in that it can only affect one entry of the rule matrix. On the other hand, a single modified membership function has a somewhat greater effect, as it affects an entire column or row of the rule matrix. Scaling an input or output variable has a macroscopic impact, as it affects every rule in the rule base [Zhe92].

Two types of scaling functions can be found in the literature, namely linear and nonlinear scaling functions. Linear scaling uses a linear mapping, and is of the following form [Cor01]:

$$f(x) = \alpha x + \beta \tag{4.29}$$

where x defines the original space and $f(x)$ defines the scaled space. In addition, α is responsible for enlarging or reducing the operating range, which can, in turn, decrease or increase either the sensitivity of the controller with respect to an input variable, or the corresponding gain of an output variable; β shifts the operating range and plays the role of an offset to the corresponding variable (Figure 4-18). The main disadvantage of linear scaling is the fixed relative distribution of the membership functions. Nonlinear scaling can overcome this problem, as it modifies the relative distribution and changes the shape of the membership functions. Although many different nonlinear scaling functions have been proposed in the literature, only the family of scaling functions that produces the widest range of fuzzy partitions with the smallest number of parameters is considered in this work. A small number of parameters reduces the complexity of the search, while a wide range of possible fuzzy partitions increases the approximation accuracy of the fuzzy rule base system.

A common nonlinear scaling function used for a variable that is symmetric about the origin is of the following form [Cor01]:

$$f(x) = \text{sign}(x) \cdot |x|^{\alpha} \tag{4.30}$$

where $\alpha > 0$ is responsible for increasing (α > 1) or decreasing (α < 1) the relative sensitivity in the region around the origin, and has the opposite effect at the boundaries of the operating range. With a fixed set of normalized membership functions in which partitions are composed of regularly distributed isosceles triangles, a wide range of fuzzy partitions can be generated if an appropriate nonlinear scaling function is employed (Figure 4-18). As a result, the possible configurations of fuzzy partitions range from those with lower granularity for middle values of the variable to lower granularity for extreme values, including homogeneous granularity. Since the input and output variables of the fuzzy YMC are using a fixed set of normalized membership functions that are distributed symmetrically around the origin (Figure 4-9), four nonlinear scaling functions (one for each variable), similar to the one described in equation (4.30), are used to tune the fuzzy YMC. This method guarantees that the adjacency constraint is satisfied, which ensures

that the sum of all membership functions is equal to unity for every point in the domain; the final tuned membership functions are distributed symmetrically around the origin, and the genetic search examines a wide range of fuzzy partitions. At the same time, due to the fact that each of these nonlinear scaling functions uses only one parameter to affect the overall distribution and shape of the membership functions, encoding these parameters results in short chromosomes and, consequently, relatively fast computation times. Altogether, four scaling parameters are used for the input and output variables of the fuzzy YMC, and are concatenated to generate a chromosome for the genetic tuning process.

The genetic algorithm is particularly well suited for solving the multi-criteria optimization problem of tuning the input and output variables of the fuzzy YMC. The objective of the tuning process is to minimize the mean square error (MSE) of the vehicle trajectory, yaw rate, and sideslip angle, which are calculated as follows:

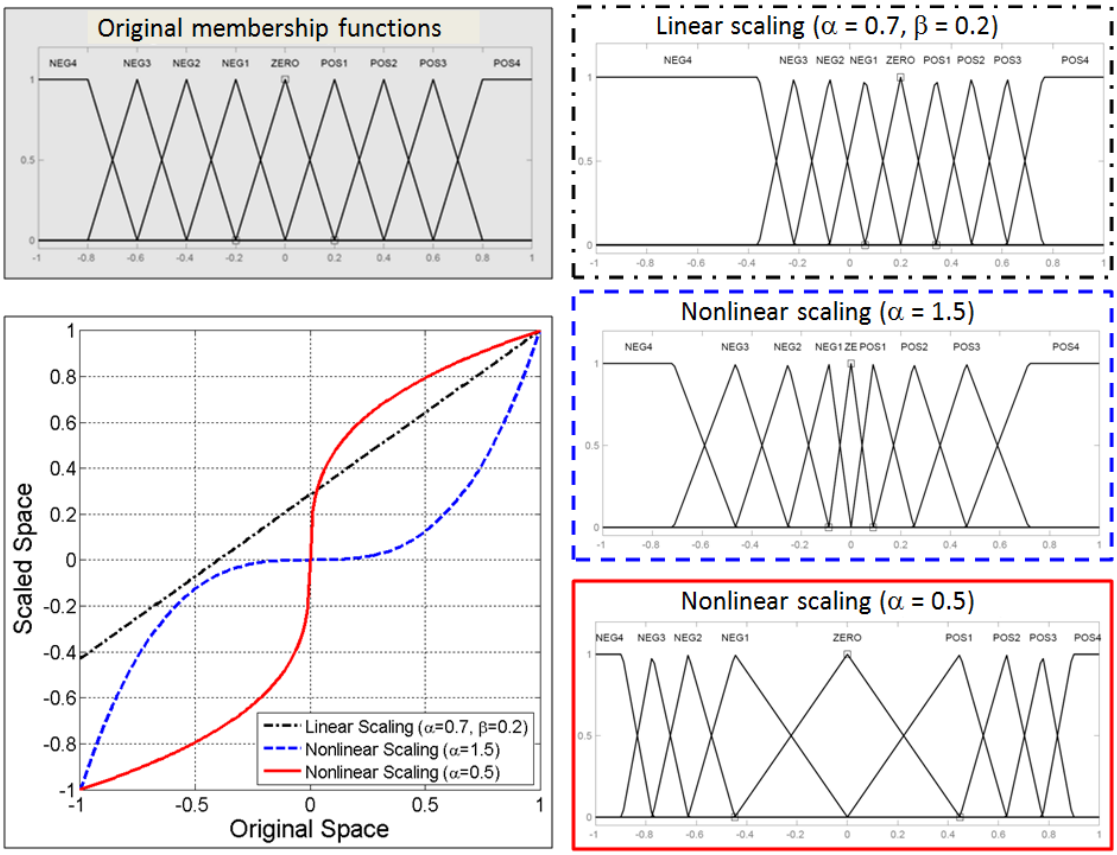

Figure 4-18: The effects of linear and nonlinear scaling functions on a fixed set of normalized membership functions

$$MSE_{Trajectory} = \frac{1}{N}\sum_{k=1}^{N}\left[y_{desired}(x_k) - y_{actual}(x_k)\right]^2 \tag{4.31}$$

$$MSE_{Yaw\ Rate} = \frac{1}{N}\sum_{k=1}^{N}\left[\dot{\psi}_{desired}(k) - \dot{\psi}_{actual}(k)\right]^2 \tag{4.32}$$

$$MSE_{Sideslip} = \frac{1}{N}\sum_{k=1}^{N}\left[\beta_{desired}(k) - \beta_{actual}(k)\right]^2 \tag{4.33}$$

where N is the number of sample points, $y_{desired}(x_k)$ and $y_{actual}(x_k)$ are the desired and actual lateral positions of the vehicle for a given forward position x_k, $\dot{\psi}_{desired}(k)$ and $\dot{\psi}_{actual}(k)$ are the desired and actual vehicle yaw rates, and $\beta_{desired}(k)$ and $\beta_{actual}(k)$ are the desired and actual vehicle sideslip angles at a given time step k, respectively. Since the objective of the multi-criteria genetic algorithm is to minimize these three errors, the fitness function associated with each chromosome is defined as the weighted sum of the inverses of the resulting vehicle trajectory, yaw rate, and sideslip angle mean square errors, as follows:

$$\text{Fitness Function} = \frac{w_1}{MSE_{Trajectory}} + \frac{w_2}{MSE_{Yaw\ Rate}} + \frac{w_3}{MSE_{Sideslip}} \tag{4.34}$$

where w_1, w_2, and w_3 are the weighting factors. The genetic algorithm was run for 50 generations, each of which had a population size of 500 chromosomes, a crossover rate of 95%, and a mutation rate of 15%. In addition, an elite selection rate of 2% was employed to ensure that the fittest chromosomes were retained unaltered from one generation to the next. Using the elite selection technique justifies the relatively high mutation rate and guarantees the thorough exploration of the search space without losing the fittest members of each generation. Convergence is assumed if the fittest chromosome survives for 10 consecutive generations, or 50 generations have elapsed. Figure 4-19 illustrates the maximum fitness function value for each generation and the convergence of the final results.

Figure 4-20 illustrates the entire optimization procedure. The optimization starts with a random set of chromosomes comprising the initial population, each of which encodes the parameters of the nonlinear scaling functions for the input and output variables of the fuzzy YMC. Next, the chromosomes are decoded into their corresponding scaling parameters, and the scaling functions are applied to the input and output variables of candidate fuzzy controllers. Subsequently, the AUTO21EV is driven through the double-lane-change maneuver using each of the tuned fuzzy YMCs. At the end of each simulation, the mean square error of the vehicle trajectory, yaw rate, and

sideslip angle are calculated, and the corresponding fitness function is evaluated. These steps are repeated for each chromosome in the current population.

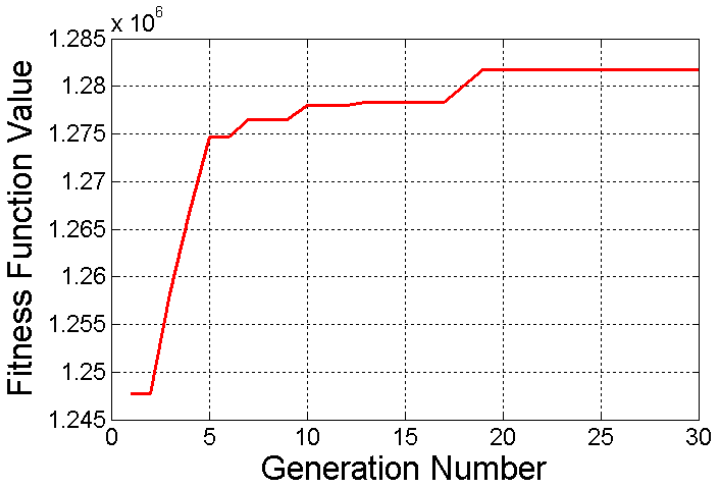

Figure 4-19: Maximum fitness function value for each generation of the multi-criteria genetic algorithm

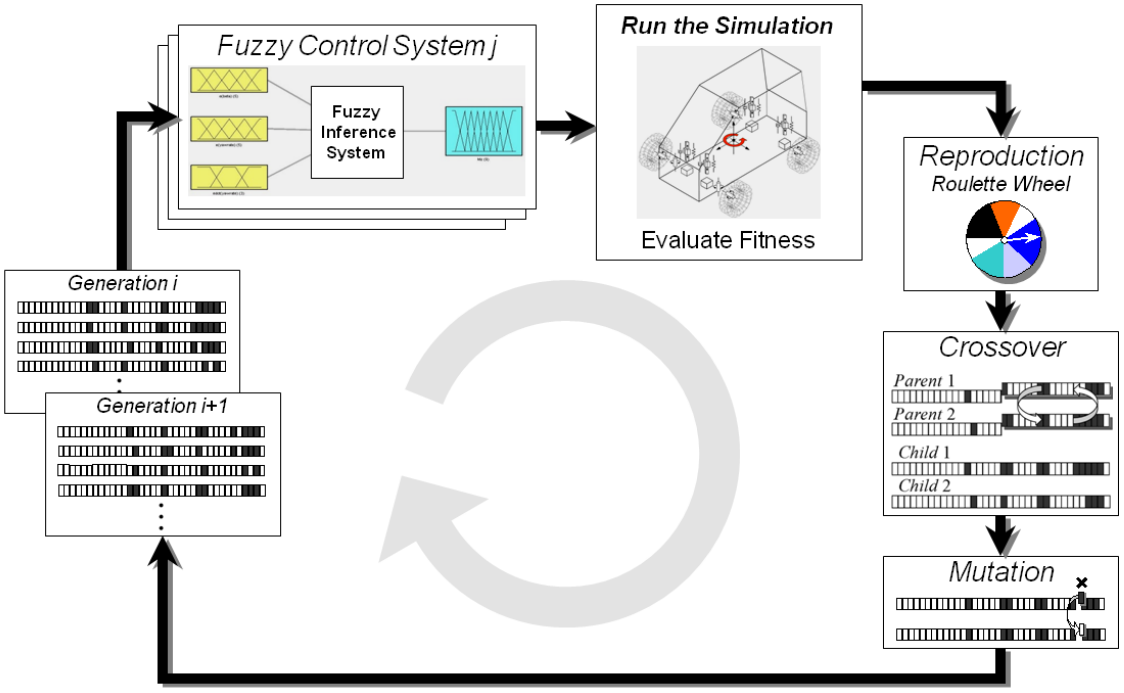

Figure 4-20: Block diagram of the multi-criteria genetic algorithm used for tuning the fuzzy YMC

Reproduction is the first genetic operation that is applied to the population. Each chromosome is duplicated with a probability that is proportional to its fitness using the Roulette wheel strategy; the fitter the chromosome, the more likely it is to be represented in the next generation. Following reproduction, crossover proceeds by randomly mating the members of the newly reproduced chromosomes. Each pair of mating chromosomes undergoes crossover as follows:

1. An integer position k along the chromosome is randomly selected between 1 and L-1, where L is the length of the chromosome.
2. Two new chromosomes are created by swapping all genes of the mated chromosomes between positions k+1 and L.

Although reproduction and crossover provide the majority of the processing power of genetic algorithms, they can occasionally lose some potentially useful genetic material. Whereas reproduction and crossover serve to explore variants of promising existing solutions while eliminating bad ones, mutation serves an essential role by introducing and reintroducing new genetic material, which can lead to even better solutions by exploring new areas of the search space [Kar04]. Mutation is performed by randomly altering the value of a gene in an individual chromosome. Once the genetic operations have been applied to the members of the population, a new generation of chromosomes will have been created, which will generally have better fitness values compared to their ancestors. This optimization procedure is continued until either convergence is achieved or the maximum number of generations is reached.

Figure 4-21 illustrates the resulting tuned membership functions for the input and output variables, and provides some insight into the relative importance of each error measure on the stability of the vehicle. As can be seen, the scaling functions have adjusted the shape, size, and relative distribution of the membership functions of the fuzzy YMC considerably. The new arrangement of the membership functions associated with the yaw rate error indicates that any amount of yaw rate error is highly undesirable. The scaling functions have forced the membership functions of the sideslip error and the rate of change of the yaw rate error to have a higher density for extreme values, whereas a high density is preferred in the middle of the yaw rate error domain. Furthermore, the membership functions associated with the corrective yaw moment have been redistributed to have higher density for extreme values. Comparing Figure 4-22, which illustrates the control surfaces of the tuned fuzzy YMC, to Figure 4-10, it is clear that the scaling functions have adjusted the membership functions of the fuzzy YMC such that the tuned control surfaces extend to the limits of the output domain and cover the entire control space.

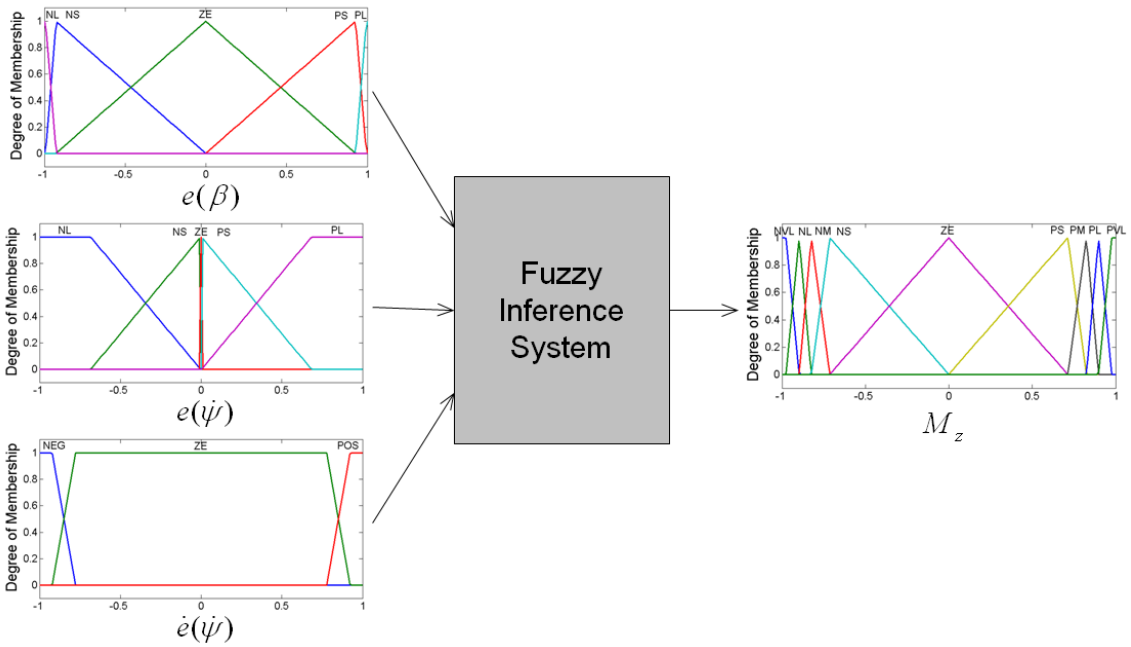

Figure 4-21: Shape and distribution of the genetically-tuned membership functions for the input and output variables of the fuzzy YMC

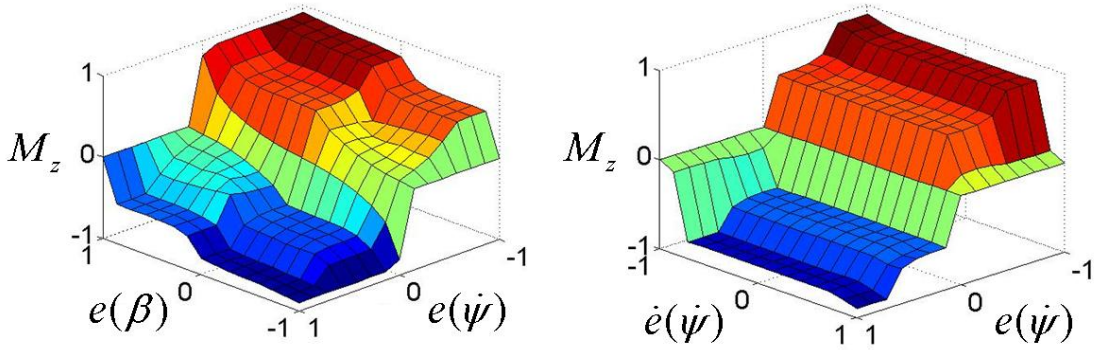

Figure 4-22: Control surfaces of the genetically-tuned fuzzy YMC

4.6 Evaluation of the genetic fuzzy yaw moment controller

In order to evaluate the performance of the genetic fuzzy YMC, the AUTO21EV is driven through a series of test maneuvers, which are described in Chapter 2.

4.6.1 ISO double-lane-change maneuver

The performance of the genetic fuzzy YMC is first compared to that of the untuned fuzzy YMC as the vehicle is driven through the double-lane-change maneuver with an initial speed of 75 km/h, using the path-following driver model. Figure 4-23 illustrates the vehicle trajectory and demonstrates that the driver is able to negotiate the maneuver more

easily and smoothly when the genetic fuzzy YMC is active, as compared to the case where no stability controller is used (Figure 4-11-a).

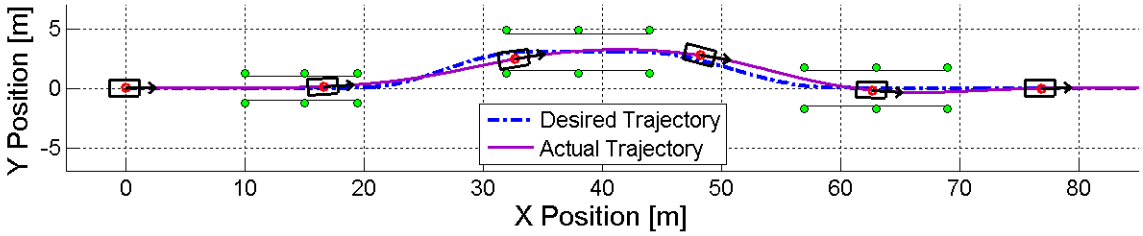

Figure 4-23: Desired and actual vehicle trajectories when driving through the double-lane-change maneuver with an initial speed of 75 km/h using the driver model and the genetic fuzzy YMC

Figure 4-24 illustrates the vehicle yaw rate and sideslip angle for this maneuver. Comparing this figure with Figure 4-12, it is clear that the genetically tuned fuzzy YMC is able to control the vehicle so that it performs more like the desired reference model than it did before undergoing the tuning process.

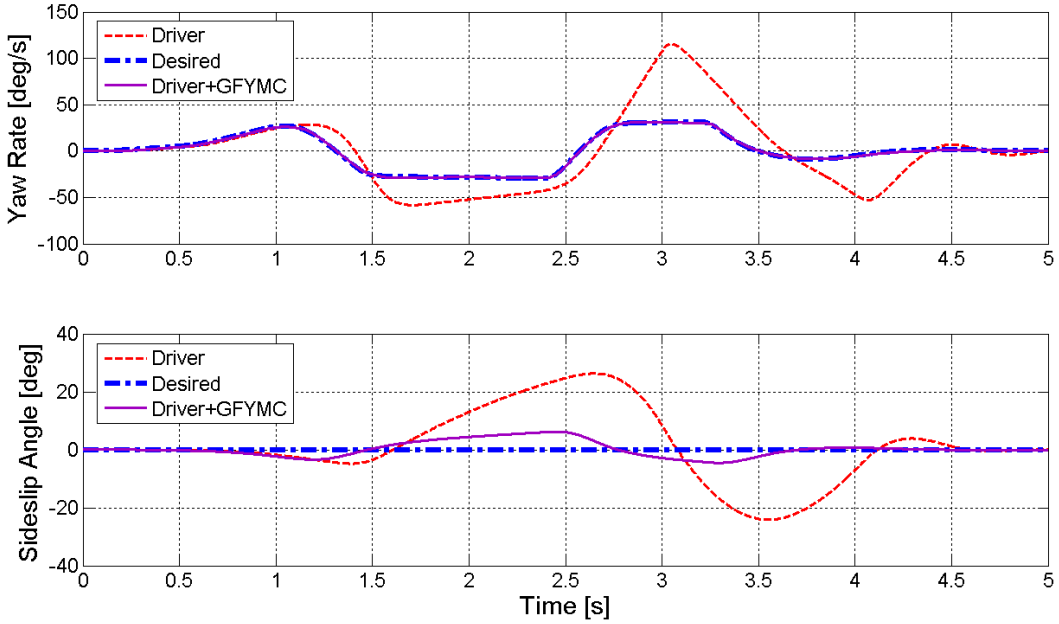

Figure 4-24: Desired and actual vehicle yaw rate (top) and sideslip angle (bottom) when driving through the double-lane-change maneuver using the driver model, with and without the genetic fuzzy YMC (GFYMC)

Figure 4-25 illustrates the lateral acceleration of the vehicle, the driver's steering input, and the vehicle forward speed as functions of time. As can be seen, the vehicle experiences a more harmonic lateral acceleration than it did when no stability controller was active. The maximum lateral acceleration is about 8.4 m/s^2, which indicates that the traction potentials on all tires are widely used to keep the vehicle on its desired path. Comparing the required steering wheel angles shown in Figure 4-25-b, it is clear that the driver requires the least steering effort when the genetic fuzzy YMC is active. As a result,

the vehicle loses even less speed with the genetic fuzzy YMC than it did with the untuned version of the controller. Figure 4-25-d illustrates the handling performance of the vehicle, and clearly indicates that the vehicle handling and agility have been significantly improved by the genetic fuzzy YMC. The hysteresis of this plot suggests an almost linear relationship between the steering wheel input and the vehicle yaw rate, which characterizes a vehicle with superior responsiveness. Note that, for clarity, the handling performance plot of the vehicle when no stability controller is active is not shown. The required corrective yaw moment shown in Figure 4-26 indicates that the genetic fuzzy YMC is able to generate larger corrective yaw moments than the untuned fuzzy YMC when the vehicle is driven through the same maneuver. Note that the generated corrective yaw moment is now large enough to eliminate the yaw rate error completely and minimize the sideslip angle error of the vehicle (Figure 4-24).

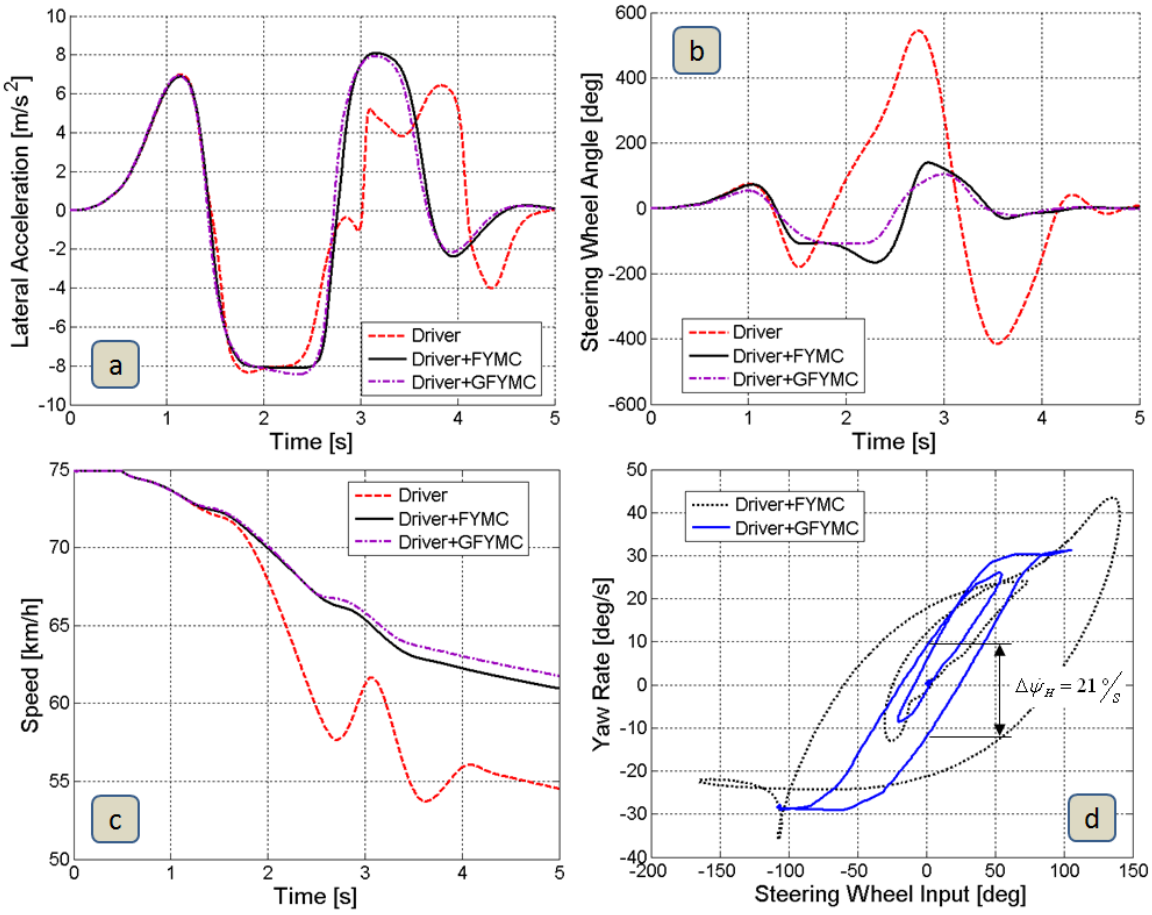

Figure 4-25: (a) Lateral acceleration, (b) steering wheel angle, and (c) vehicle speed as functions of time; and (d) vehicle yaw rate as a function of the steering wheel input when driving through the double-lane-change maneuver without a controller, with the fuzzy YMC (FYMC), and with the genetic fuzzy YMC (GFYMC)

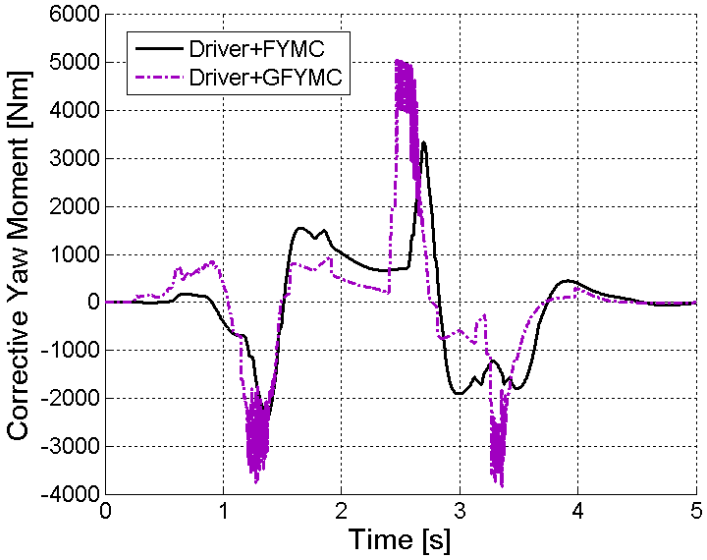

Figure 4-26: Comparison of the corrective yaw moment generated by the fuzzy and genetic fuzzy YMCs

Table 4-III summarizes the vehicle response during the double-lane-change maneuver when the genetic fuzzy YMC is active. Since the genetic fuzzy YMC demonstrates better performance in all aforementioned aspects than the untuned fuzzy YMC, only the genetic fuzzy YMC will be considered in the reminder of the evaluation process. Comparing different parameters of the vehicle response during the double-lane-change maneuver using the driver model with and without the genetic fuzzy YMC (Table 4-III), it can be seen that the genetic fuzzy YMC is very effective at improving all the decisive parameters that describe the handling, stability, and longitudinal dynamics of the vehicle (Figure 2-4). In particular, the genetic fuzzy YMC has reduced $|\beta|_{\max}$, $|\dot{\psi}|_{\max}$, $|\delta_{SW}|_{\max}$, and $\Delta\dot{\psi}_H$ significantly, and has increased $|a_y|_{\max}$ slightly, which together indicate that the vehicle handling has been improved considerably by the genetic fuzzy YMC. The reduction of $|\beta|_{\max}$ and $|\dot{\psi}|_{\max}$ implies, at the same time, that the stability of the vehicle has improved significantly. In addition, the fact that the vehicle loses less speed when the genetic fuzzy YMC is active indicates that the controller is very effective at improving the longitudinal dynamics of the vehicle.

Parameter	$\lvert\beta\rvert_{\max}$	$\lvert\dot{\psi}\rvert_{\max}$	$\lvert a_y\rvert_{\max}$	$\lvert\delta_{SW}\rvert_{\max}$	$\Delta\dot{\psi}_H$	v_{lost}
AUTO21EV	26.3^o	115.4^o/s	8.2 m/s^2	545^o	163.8^o/s	20.5 m/s
GFYMC	6.20^o	31.2^o/s	8.4 m/s^2	108^o	21^o/s	13.2 m/s

Table 4-III: Vehicle response during the double-lane-change maneuver using the driver model with and without the genetic fuzzy YMC (GFYMC)

4.6.2 Step-steer response maneuver

In order to evaluate the performance of the vehicle using the genetic fuzzy YMC in a step-steer response maneuver, the vehicle yaw rate, sideslip angle, and lateral acceleration response as functions of time are observed. Figure 4-27 illustrates the steering wheel step input and the lateral acceleration response of the vehicle. As can be seen, the vehicle reaches a lateral acceleration of about 4 m/s^2 with a steering wheel input of 18^o when no stability controller is activated. The rise time of the lateral acceleration response for the AUTO21EV model is about 0.66 seconds. This rise time is reduced to 0.51 seconds when the genetic fuzzy YMC is active, indicating an improvement in the responsiveness of the vehicle.

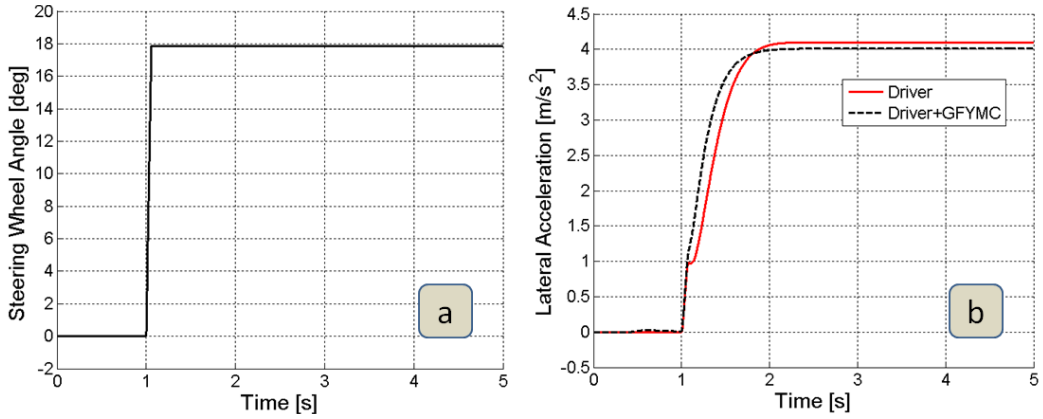

Figure 4-27: (a) Required steering wheel input and (b) lateral acceleration of the vehicle when driving through the step-steer maneuver

Figure 4-28 shows the yaw rate and sideslip angle of the vehicle with and without the genetic fuzzy YMC. Looking at the rise times of the yaw rate response with and without the controller, it is confirmed that the genetic fuzzy YMC improves the responsiveness of the vehicle considerably. Note that, due to the sharp steering input, the lateral forces on the front tires build up faster than those at the rear axle. Therefore, the vehicle experiences a positive sideslip angle for a short period of time (Figure 4-28), which diminishes and becomes negative once the lateral forces on the rear tires build up and get to the level that can create equilibrium around the center of mass of the vehicle. The short delay in the lateral acceleration plot, which occurs soon after the step input when driving through the maneuver without using a stability control system, is due to this phenomenon (Figure 4-27); however, the delay is suppressed when the genetic fuzzy YMC is active.

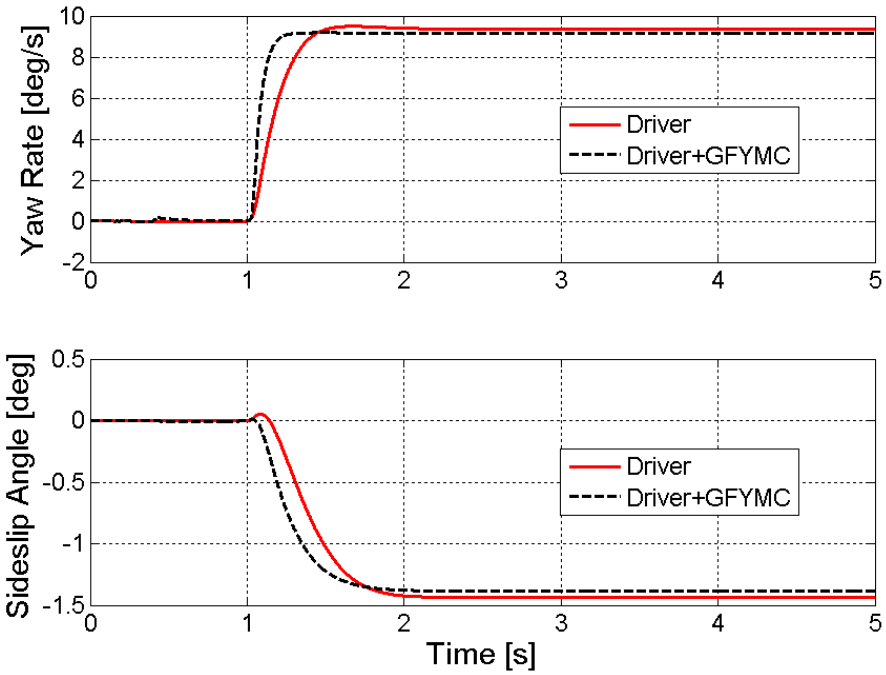

Figure 4-28: Yaw rate (top) and sideslip angle (bottom) of the vehicle when driving through the step-steer maneuver with and without the genetic fuzzy YMC (GFYMC)

Table 4-IV summarizes the vehicle response during the step-steer test maneuver. Comparing parameters of the vehicle response during the step-steer maneuver with and without the genetic fuzzy YMC, it can be recognized that the genetic fuzzy YMC is very effective at improving all the decisive parameters that describe the handling characteristics of the vehicle (Figure 2-4).

Parameter	$t_{\dot{\psi}}$	$\mathrm{PO}=\frac{\dot{\psi}_{\max}-\dot{\psi}_{ss}}{\dot{\psi}_{ss}}\times 100\%$	$\lvert\beta\rvert_{\max}$	t_{a_y}
AUTO21EV	0.34 s	1.30%	1.43^{o}	0.66 s
GFYMC	0.15 s	0.00%	1.38^{o}	0.51 s

Table 4-IV: Vehicle response during the step-steer maneuver using a fixed step-steer input with and without the genetic fuzzy YMC (GFYMC)

4.6.3 Brake-in-turn maneuver

Figure 4-29 illustrates the trajectory of the vehicle relative to the desired path during a brake-in-turn maneuver. As can be seen, the vehicle becomes unstable and leaves the predefined road when the YMC is not active; however, the driver is able to keep the vehicle on the predefined circular path while severely braking when using the genetic fuzzy YMC, and the lateral deviation of the vehicle from the desired path remains very small throughout the maneuver. Looking at the driver's steering wheel input as a function

of time, shown in Figure 4-30-a, it is clear that the driver model is not able to control the vehicle when the YMC is inactive even when very large steering wheel angles are applied. However, the driver model is able to control the vehicle when the genetic fuzzy YMC is active by applying a maximum steering wheel angle of only 45^{o}. In addition, the gradient of this plot indicates that it requires very little effort for the driver to control the vehicle when braking in a turn. Figure 4-30-b illustrates the lateral acceleration of the vehicle and confirms the stability of the vehicle when the genetic fuzzy YMC is active, even though it is being driven near its handling limit. Such a large lateral acceleration ($7.7\ m/s^2$) during a severe braking maneuver indicates that the traction potentials on all tires are widely used to hold the vehicle on its desired path.

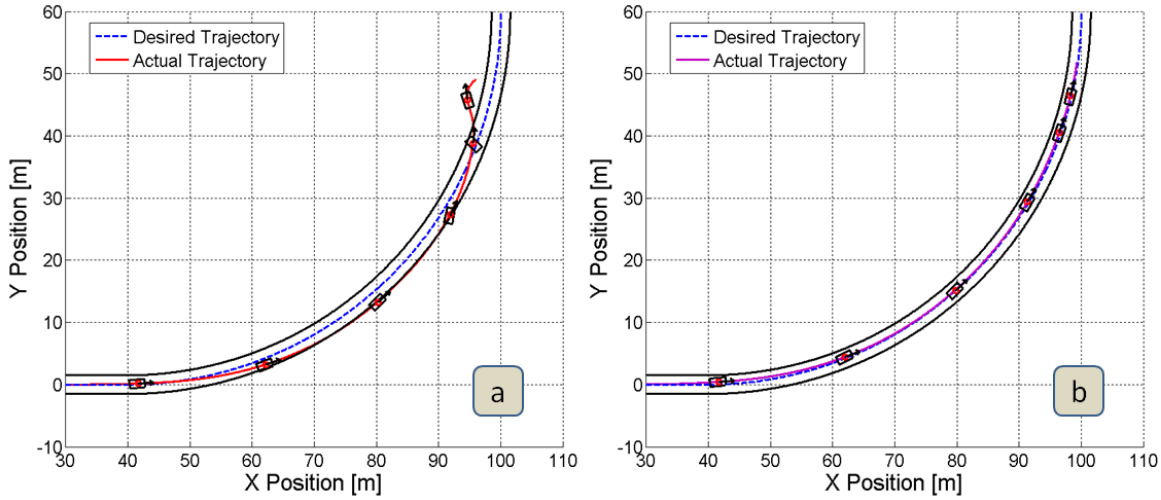

Figure 4-29: Desired and actual vehicle trajectories when braking in a turn using (a) the driver model only, and (b) using the driver model with the genetic fuzzy YMC (GFYMC)

Figure 4-31 compares the vehicle yaw rate and sideslip angle when driving through the brake-in-turn maneuver with and without the genetic fuzzy YMC. As can be seen, the vehicle behaves almost like the desired reference bicycle model when the genetic fuzzy YMC is active, and the driver is able to control the vehicle while braking in the curve. This figure also confirms the stability of the vehicle, as the yaw rate and sideslip angle both approach zero as the vehicle progresses toward larger deceleration rates. Figure 4-32 shows the vehicle speed as a function of time and the vehicle longitudinal acceleration as a function of vehicle speed. This figure confirms the performance of the speed controller and the severity of the braking component of this maneuver.

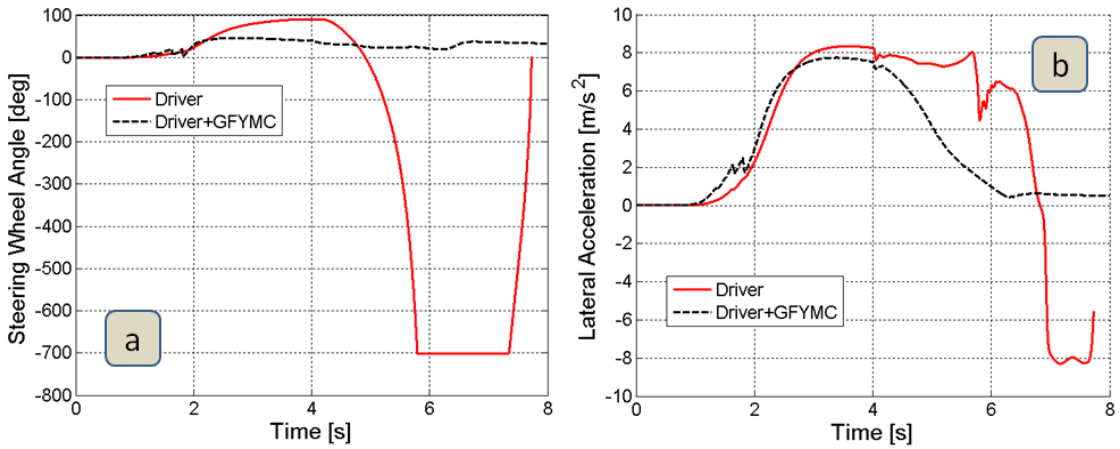

Figure 4-30: (a) Required steering wheel input and (b) lateral acceleration of the vehicle when braking in a turn with and without the genetic fuzzy YMC (GFYMC)

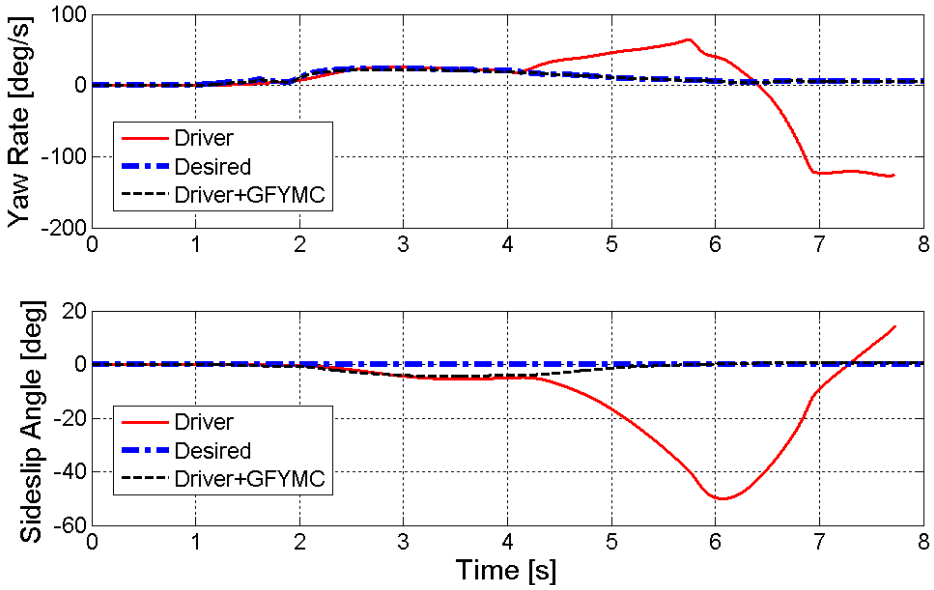

Figure 4-31: Desired and actual vehicle yaw rate (top) and sideslip angle (bottom) when braking in a turn using the driver model with and without the genetic fuzzy YMC (GFYMC)

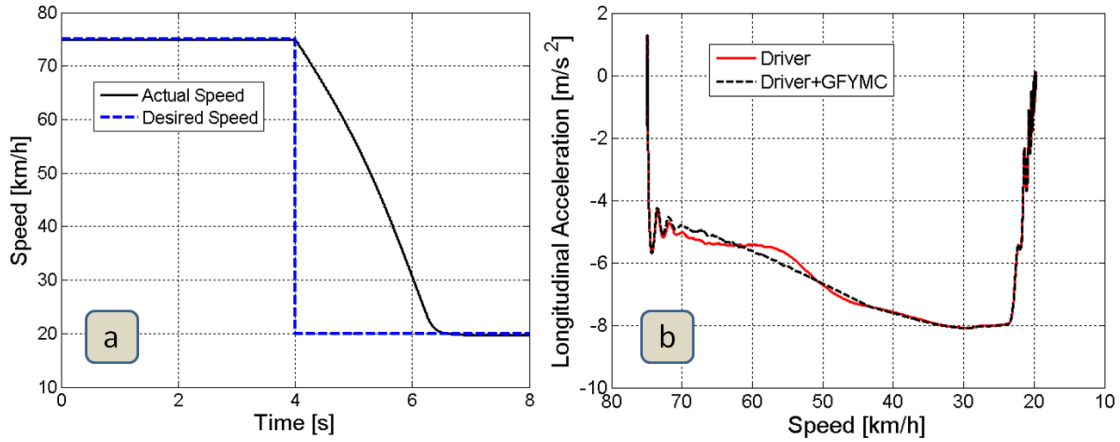

Figure 4-32: (a) Vehicle speed as a function of time and (b) longitudinal acceleration as a function of vehicle speed when braking in a turn using the driver model with and without the genetic fuzzy YMC

Table 4-V summarizes the vehicle response during the brake-in-turn maneuver. Comparing parameters of the vehicle response during the brake-in-turn maneuver using the driver model with and without the genetic fuzzy YMC, it can be seen that the genetic fuzzy YMC is very effective at improving all the decisive parameters that describe the handling, stability, and path-following capability of the vehicle (Figure 2-4). In particular, the genetic fuzzy YMC has reduced $|\beta|_{\max}$, $|\dot{\psi}|_{\max}$, and $|\delta_{SW}|_{\max}$ significantly, which indicates that this controller is very effective at enhancing the vehicle handling during this maneuver. In addition, a reduction of $|\beta|_{\max}$ and $|\dot{\psi}|_{\max}$ simultaneously indicates that the genetic fuzzy YMC is very effective at improving the vehicle stability. Finally, the fact that the maximum lateral deviation of the vehicle from the desired path remains very small confirms that the genetic fuzzy YMC is enhancing the path-following capability of the vehicle.

Parameter	$\|\dot{\psi}\|_{\max}$	$\|\beta\|_{\max}$	$\Delta y_{\max}$	$\|\delta_{SW}\|_{\max}$
AUTO21EV	126.5^{o}/s	50.1^{o}	3.67 m	700^{o}
GFYMC	22.60^{o}/s	4.36^{o}	0.18 m	46.4^{o}

Table 4-V: Vehicle response during the brake-in-turn maneuver using the driver model with and without the genetic fuzzy YMC (GFYMC)

4.6.4 Straight-line braking on a μ-split road

Braking on a μ-split road is a critical test maneuver, and can be used to confirm the performance and sensitivity of a vehicle and its stability control systems when subjected to external disturbances. During this test, due to the asymmetric braking forces generated on the left and right tires, the vehicle will be pushed to the side of the road that has a higher coefficient of friction. Figure 4-33 shows the vehicle trajectory for this maneuver and compares it to the case when the YMC is inactive. This comparison confirms that the genetic fuzzy YMC is able to correct the side-pushing effect of the vehicle while braking on a μ-split road, thereby preventing a dangerous instability situation. It is important to note that the braking distance of the vehicle is 44.5 meters when the genetic fuzzy YMC is active, which is an acceptable braking distance for this vehicle. Looking at the vehicle yaw rate and sideslip angle illustrated in Figure 4-34, it is clear that the genetic fuzzy YMC is able to limit and, later, diminish the yaw rate and sideslip angle of the vehicle while driving over the black ice patch. Figure 4-35 illustrates the required corrective yaw

moment that is applied by the genetic fuzzy YMC to compensate for the side-pushing effect.

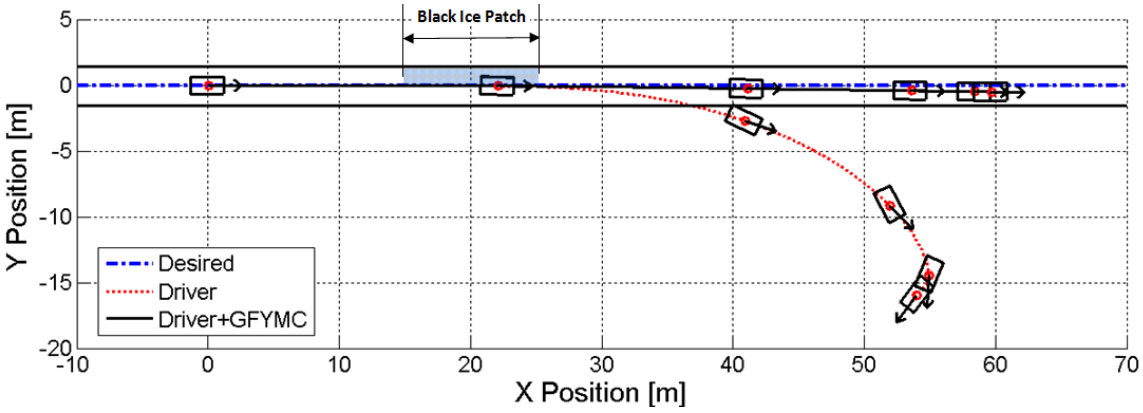

Figure 4-33: Desired and actual vehicle trajectories when braking on a μ-split road holding the steering wheel fixed with and without the genetic fuzzy YMC (GFYMC)

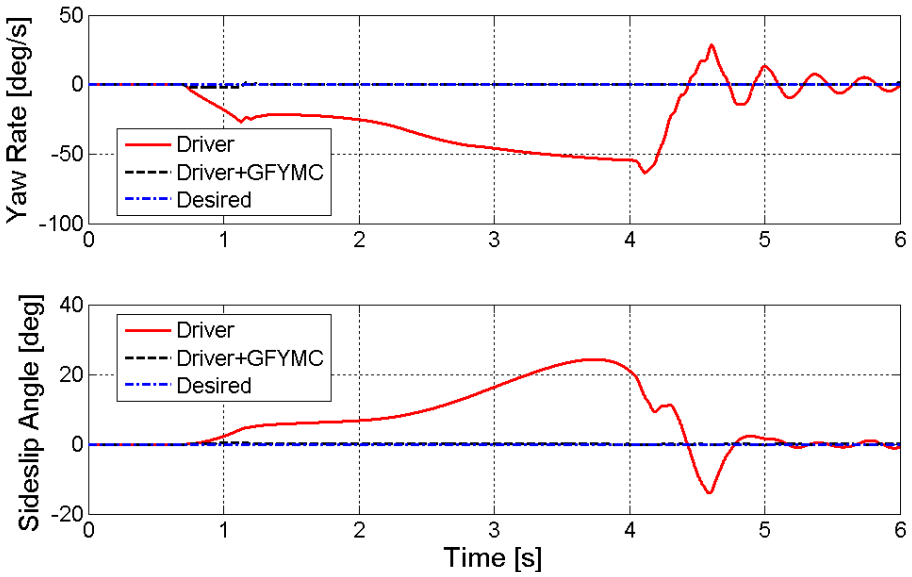

Figure 4-34: Desired and actual vehicle yaw rate (top) and sideslip angle (bottom) when braking on a μ-split road holding the steering wheel fixed with and without the genetic fuzzy YMC (GFYMC)

Table 4-VI summarizes the vehicle response during the straight-line braking maneuver performed on a μ-split road. Comparing parameters of the vehicle response while braking on a μ-split road, it can be seen that the genetic fuzzy YMC is very effective at improving all the decisive parameters that describe the stability, path-following capability, and braking performance of the vehicle. In particular, the genetic fuzzy YMC is able to reduce $|\beta|_{\max}$ and $|\dot{\psi}|_{\max}$ significantly, which indicates that the stability of the vehicle is greatly enhanced. Moreover, the braking distance of the vehicle has been reduced considerably when the genetic fuzzy YMC is active, indicating an

improvement in the longitudinal dynamics of the vehicle. The maximum lateral deviation of the vehicle is also reduced significantly, and the vehicle remains on the predefined road throughout the maneuver when the genetic fuzzy YMC is active.

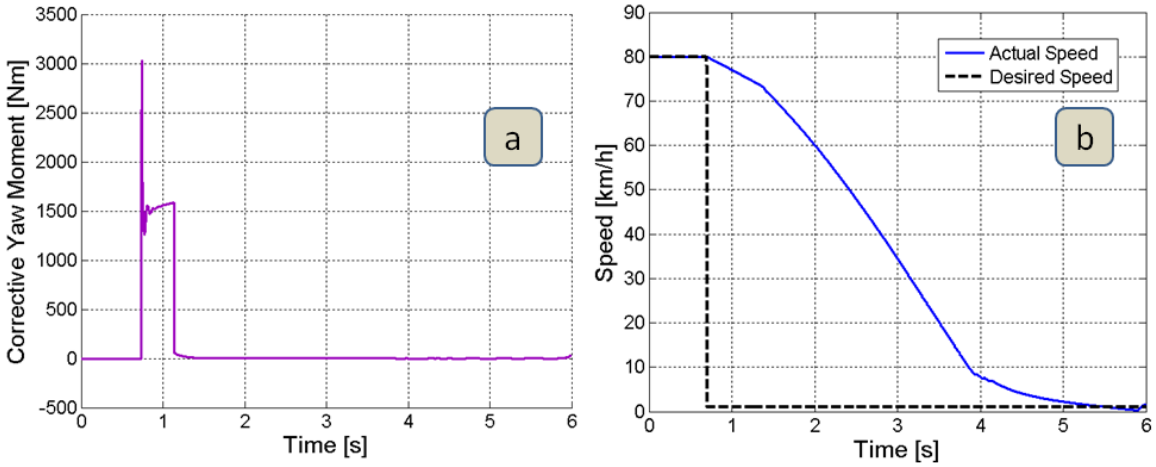

Figure 4-35: (a) Corrective yaw moment required to counteract the side-pushing effect of the vehicle and (b) vehicle speed while braking on a μ-split road holding the steering wheel fixed and using the genetic fuzzy YMC

Parameter	$\lvert\beta\rvert_{\max}$	$\lvert\dot{\psi}\rvert_{\max}$	$\Delta x_{braking}$	$\Delta y_{\max}$
AUTO21EV	24.2^{o}	63.4^{o}/s	48.4 m	15.9 m
GFYMC	0.40^{o}	1.85^{o}/s	44.5 m	0.46 m

Table 4-VI: Vehicle response during the straight-line braking on a μ-split road maneuver holding the steering wheel fixed with and without the genetic fuzzy YMC (GFYMC)

4.7 Chapter summary

In this chapter, a simple vehicle model is developed to allow for the testing of different control strategies, and for applying a genetic tuning algorithm to the development of the fuzzy yaw moment controller. The genetic tuning procedure is applied to the developed fuzzy YMC to improve its performance. A variety of maneuvers are simulated to demonstrate the effectiveness of the genetic fuzzy YMC. Table 4-VII provides a subjective evaluation of the effectiveness of the genetic fuzzy YMC based on different test maneuvers. In the next chapter, the issue of realistically generating the required corrective yaw moment using an advanced torque vectoring controller is addressed.

Characteristic / Maneuver	Handling	Stability	Path following	Longitudinal dynamics
Double-lane-change	3	3		2.5
Step-steer	3			
Brake-in-turn	3	3	3	
Straight-line braking on a μ-split road		3	2.5	3
Mean Value $\left(\bar{x} = \frac{1}{n}\sum_{i=1}^{n} x_i\right)$	3	3	2.75	2.75

Table 4-VII: Subjective evaluation of the effectiveness of the genetic fuzzy YMC based on different test maneuvers (3 = very effective, 2 = effective, 1 = effective to some extent, 0 = ineffective)

5 Advanced Torque Vectoring Controller

As mentioned previously, the AUTO21EV model with four direct-drive in-wheel motors is an exciting platform on which to apply advanced motion control techniques, such as advanced slip control and torque vectoring systems, since the motor torque and speed can be generated and controlled quickly, precisely, and independently at each wheel. An advanced slip control system is developed and tested in Chapter 3. In addition, a high-level genetic fuzzy yaw moment controller is developed in Chapter 4, the objective of which is to determine the corrective yaw moment required to minimize the vehicle yaw rate and sideslip errors. This genetically-tuned fuzzy yaw moment controller acts as a high-level supervisory module that assigns tasks to the lower-level controllers and actuators. In this section, an advanced torque vectoring controller is developed for the AUTO21EV that distributes the task of generating the calculated corrective yaw moment to the in-wheel motors. The developed advanced torque vectoring controller consists of left-to-right and front-to-rear torque vectoring components, which work together to distribute the calculated corrective yaw moment in an integrated approach.

5.1 Control method for left-to-right torque vectoring distribution

In this section, an advanced torque vectoring system is developed based on the previously developed genetic fuzzy yaw moment controller. The objective here is to distribute the calculated corrective yaw moment to the individual in-wheel motors in order to stabilize the vehicle driving dynamics. Assuming that M_z is the total required corrective yaw moment that is calculated by the genetic fuzzy yaw moment controller, the tire forces on each axle must be adjusted such that each axle generates a portion of the total corrective yaw moment, as follows:

$$M_z = M_{z,\,front} + M_{z,rear} = \theta_f \cdot M_z + \theta_r \cdot M_z \tag{5.1}$$

where $M_{z,\,front}$ and $M_{z,\,rear}$ are the portions of the required corrective yaw moment that must be generated at the front and rear axles, respectively. In other words, θ_f and θ_r are the percentages of the total required corrective yaw moment M_z that must be generated at the front and rear axles, such that $\theta_f + \theta_r = 100\%$. The relationship between θ_f and θ_r defines the front-to-rear torque vectoring distribution and will be discussed later.

Generating a couple (equal and opposite traction forces) on each axle is the best strategy for creating the required corrective yaw moment for two reasons: first, all tires participate in generating the required corrective yaw moment; secondly, the desired vehicle velocity will not be influenced by the activities of the torque vectoring system as they would in an ESP system, provided the forces on the sides of each axle can be generated without being restricted by the traction potential of the tires or the performance of the in-wheel motors. In addition, since all of the tires are involved in generating the corrective yaw moment, and since each tire can be accelerated or braked independently, this strategy has a better efficiency than conventional torque vectoring and ESP systems, in which only specific tires are involved to generate the corrective yaw moment. Figure 5-1 illustrates the proposed torque vectoring strategy, where a couple is generated on each axle. The generated yaw moment on each axle is calculated as follows:

$$\left.\begin{aligned} M_{z,\,front} &= F_{x,FR}\cdot\frac{t_f}{2}+F_{x,FL}\cdot\frac{t_f}{2} \\ F_{x,FR} &= F_{x,FL}=F_{x,F} \end{aligned}\right\} \Rightarrow M_{z,\,front}=F_{x,F}\cdot t_f \Rightarrow F_{x,F}=\frac{M_{z,\,front}}{t_f} \tag{5.2}$$

$$\left.\begin{aligned} M_{z,rear} &= F_{x,RR}\cdot\frac{t_r}{2}+F_{x,RL}\cdot\frac{t_r}{2} \\ F_{x,RR} &= F_{x,RL}=F_{x,R} \end{aligned}\right\} \Rightarrow M_{z,rear}=F_{x,R}\cdot t_r \Rightarrow F_{x,R}=\frac{M_{z,rear}}{t_r} \tag{5.3}$$

where $F_{x,FR}$, $F_{x,FL}$, $F_{x,RR}$, and $F_{x,RL}$ are the longitudinal tire forces of the front-right, front-left, rear-right, and rear-left wheels, respectively; t_f and t_r are the front and rear wheel tracks of the vehicle.

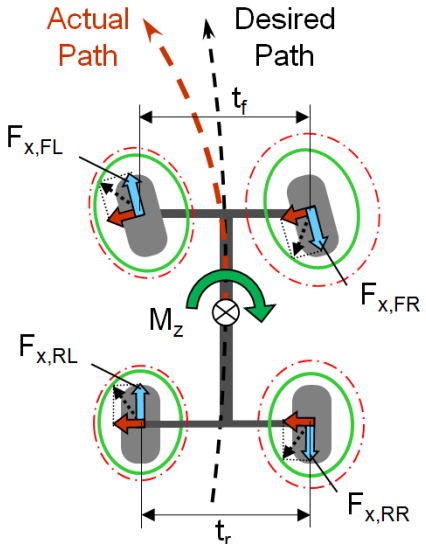

Figure 5-1: Advanced torque vectoring strategy using couple generation on each axle (the dash-dotted ellipse surrounding each tire indicates the adhesion potential of that tire; the solid ellipse indicates the actual friction ellipse)

In order to calculate the required motor torques, a torque balance is formed for each wheel. Figure 5-2 illustrates the model of a single wheel, where $I_{yy,w}$ denotes the moment of inertia of the wheel about its spin axis, T_m denotes the motor torque, r_{dyn} is the tire dynamic radius, ω_w is the angular velocity of the tire, F_z is the tire vertical force, and F_x is the tire longitudinal force. Note that the tire rolling resistance and the aerodynamic drag of the vehicle are neglected in this model for simplicity. By specifying the equation of motion of the wheel, the traction force at the tire-road contact patch can be estimated as follows:

$$T_m - F_x \cdot r_{dyn} = I_{yy,w} \cdot \dot{\omega}_w \Leftrightarrow F_x = \frac{1}{r_{dyn}} \cdot \left(T_m - I_{yy,w} \cdot \dot{\omega}_w \right) \tag{5.4}$$

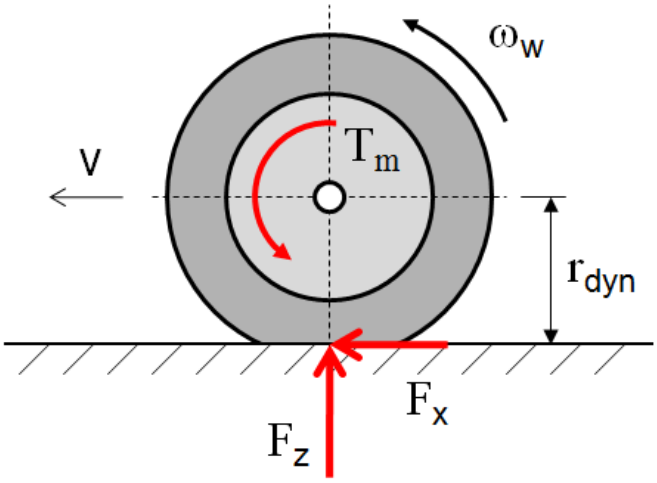

Figure 5-2: Torque balance at the tire-road contact patch

Substituting the traction force F_x from equation (5.4) into equations (5.2) and (5.3), the required motor torque at each wheel can be calculated as follows:

$$T_{m,i} = \frac{r_{dyn,i}}{t_f} \cdot M_{z,\,front} + I_{yy,w} \cdot \dot{\omega}_{w,i} \quad \text{where} \quad \mathrm{i} \in \{\mathrm{FR,\ FL}\} \tag{5.5}$$

$$T_{m,i} = \frac{r_{dyn,i}}{t_r} \cdot M_{z,rear} + I_{yy,w} \cdot \dot{\omega}_{w,i} \quad \text{where} \quad \mathrm{i} \in \{\mathrm{RR,\ RL}\} \tag{5.6}$$

Note that when the required corrective yaw moment is positive, the wheels on the right side of the vehicle must be driven and the wheels on the left side must be braked; when the required corrective yaw moment is negative, the wheels on the right side of the vehicle must be braked and those on the left side must be driven.

5.2 Calculation of tire adhesion potential

In order to prevent the tires from spinning out or locking up during the couple generation, the maximum possible traction force of each tire is estimated at each time step of the simulation and is used to limit the traction forces of the tires. In addition, the adhesion potential of each tire is calculated and used to define the extent to which the tire forces have been saturated. Estimating the adhesion potential requires information about the horizontal and vertical forces acting on the tire, as well as the friction coefficient between the tire and the road, the estimation of which is presented below.

The longitudinal and lateral tire forces are estimated using the well-known "Magic Tire Formula" [Pac02, Pac97]. This model is a semi-empirical set of curve fits that takes into account the coupling between the longitudinal and lateral tire forces through combined-slip characteristics, a limited tire adhesion potential, the variation in cornering stiffness with tire load, and the influence of the tire-road friction coefficient. The combined-slip horizontal tire forces are estimated using the following equations [Pac02]:

$$F_{x,i} = F_{xo,i} \cdot \cos\left(C \cdot \arctan\left(B \cdot \alpha - E \cdot \left(B \cdot \alpha - \arctan\left(B \cdot \alpha\right)\right)\right)\right) \tag{5.7}$$

$$F_{y,i} = F_{yo,i} \cdot \cos\left(C \cdot \arctan\left(B \cdot \lambda - E \cdot \left(B \cdot \lambda - \arctan\left(B \cdot \lambda\right)\right)\right)\right) \tag{5.8}$$

where $i \in \{\text{FL, FR, RL, RR}\}$. Note that these forces are calculated with respect to the wheel coordinate system. $F_{xo,i}$ and $F_{yo,i}$ represent the pure-slip tire forces in the longitudinal and lateral directions, respectively, and are calculated as follows [Pac02]:

$$F_{xo,i} = D \cdot \sin\left(C \cdot \arctan\left(B \cdot \lambda - E \cdot \left(B \cdot \lambda - \arctan\left(B \cdot \lambda\right)\right)\right)\right) \tag{5.9}$$

$$F_{yo,i} = D \cdot \sin\left(C \cdot \arctan\left(B \cdot \alpha - E \cdot \left(B \cdot \alpha - \arctan\left(B \cdot \alpha\right)\right)\right)\right) \tag{5.10}$$

In this tire model, the interdependence between the longitudinal and lateral tire forces is considered, where peak factors *D*, shape factors *C*, stiffness factors *B*, and curvature factors *E* are different for equations (5.7) to (5.10), and for the longitudinal and lateral directions [Pac02]. All the parameters required by this model are taken from the Pacejka 2002 tire data obtained for a 175/55 R15 tire. In addition, the slip ratio of each tire is calculated using equations (3.1) and (3.2) in Chapter 3, and the sideslip angle of each tire is approximated using a bicycle model, as indicated below [Wal05]:

$$\alpha_F = \delta + \beta - \frac{a \cdot \dot{\psi}}{v_x} \tag{5.11}$$

$$\alpha_R = \beta + \frac{b \cdot \dot{\psi}}{v_x} \tag{5.12}$$

where δ is the steering angle, β is the sideslip angle of the vehicle, a and b are the distances of the front and rear axles from the vehicle center of gravity, v_x is the vehicle forward speed, and $\dot{\psi}$ is the vehicle yaw rate.

Approximating the longitudinal and lateral tire forces using equations (5.7) and (5.8), the tire adhesion potential utilization η can be estimated using the following elliptic relation:

$$\eta_i = \sqrt{\left(\frac{F_{xi}}{F_{xi,\max}}\right)^2 + \left(\frac{F_{yi}}{F_{yi,\max}}\right)^2} \quad , \; 0 \le \eta_i \le 1 \;\text{ and }\; i \in \{\text{FL, FR, RL, RR}\} \tag{5.13}$$

where $F_{xi,\max}$ and $F_{yi,\max}$ represent the maximum possible forces in the longitudinal and lateral directions, respectively. With the nominal tire load F_{z0} and the tire-road friction coefficients μ_i, the maximum longitudinal and lateral tire forces can be approximated as follows [Pac97]:

$$F_{xi,\max} = \mu_i \cdot F_{zi} \cdot k_{x,i} \cdot \left(1 + l_x \cdot \frac{F_{zi} - F_{z0}}{F_{z0}}\right) \tag{5.14}$$

$$F_{yi,\max} = \mu_i \cdot F_{zi} \cdot k_{y,i} \cdot \left(1 + l_y \cdot \frac{F_{zi} - F_{z0}}{F_{z0}}\right) \tag{5.15}$$

where $k_{x,i}$ and $k_{y,i}$ depend on the actual tire camber angle, and parameters l_x and l_y, which define the degressive behaviour of the tire horizontal forces [Pac02], are set to 1. It is important to note that, due to the absence of the suspension kinematics in the DynaFlexPro model of the AUTO21EV (Figure 4-1), the camber angles are set to zero and do not vary during the simulation. For the sake of simplicity, the camber angles in the ADAMS model of the AUTO21EV are also assumed to be zero and constant throughout the simulation.

The actual vertical force applied to each tire (F_{zi}) is approximated by neglecting the coupling between the vehicle roll and pitch, and disregarding the suspension dynamics. To this end, two half-car models are used one for the longitudinal direction and one for the lateral direction. Figure 5-3-a illustrates a half-car model in the

longitudinal direction, where a_x indicates the longitudinal acceleration of the vehicle. The inertial force due to the longitudinal acceleration at the vehicle center of gravity (CG) causes a weight shift to the rear axle, which simultaneously reduces the front axle load and increases the rear axle load. Constructing the torque balance at the rear axle contact point yields the following expression for the front axle load ($F_{z,F}$) [Kie05]:

$$\sum M_y = 0 \Rightarrow (a+b)\cdot F_{z,F} - m_{CG}\cdot g\cdot b + m_{CG}\cdot a_x \cdot h_{CG} = 0 \Rightarrow$$
$$F_{z,F} = \frac{b}{a+b} m_{CG}\cdot g - \frac{h_{CG}}{a+b} m_{CG}\cdot a_x \tag{5.16}$$

where a and b are the distances of the front and rear axles from the vehicle center of gravity, m_{CG} is the total mass of the vehicle, h_{CG} is the height of the vehicle center of gravity, and g is the gravitational acceleration constant. a_x is the longitudinal acceleration of the vehicle, and can be measured using an accelerometer. Subtracting the front axle load ($F_{z,F}$) from the total vehicle weight, the rear axle load ($F_{z,R}$) is calculated as follows:

$$\sum F_z = 0 \Rightarrow F_{z,F} + F_{z,R} - m_{CG}\cdot g = 0 \Rightarrow F_{z,R} = \frac{a}{a+b} m_{CG}\cdot g + \frac{h_{CG}}{a+b} m_{CG}\cdot a_x \tag{5.17}$$

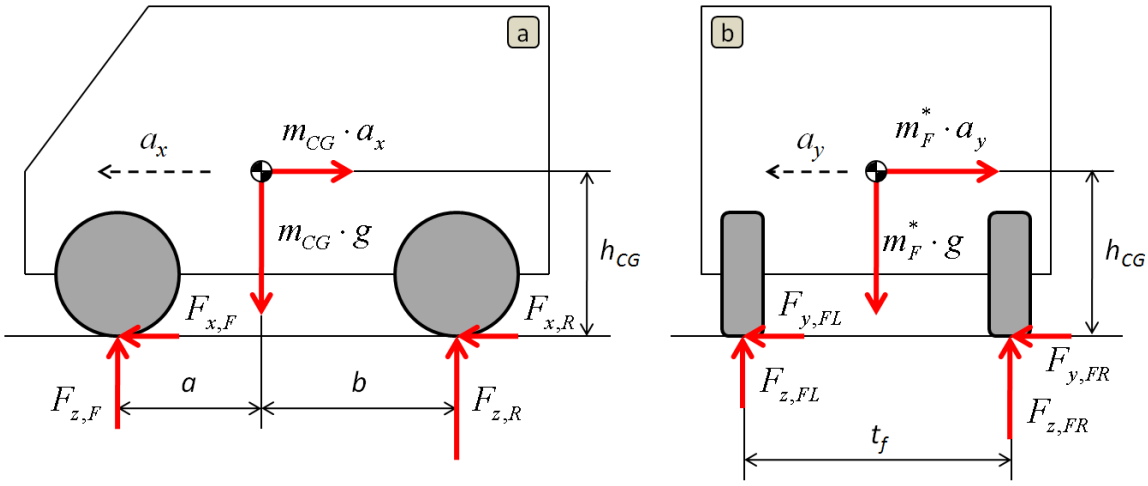

Figure 5-3: (a) Longitudinal weight shift during acceleration and (b) lateral weight shift during cornering

During cornering, the lateral acceleration causes a weight shift to one side of each axle, whose distribution between the front and rear axles depends on the axle loads. The two axles are considered to be decoupled from each other, and a half-car model is used to calculate the lateral weight shift on each axle. For instance, Figure 5-3-b illustrates the

half-car model for the front axle, where the virtual mass of the front axle m_F^* is calculated as follows:

$$m_F^* = \frac{F_{z,F}}{g} = \frac{F_{z,FL} + F_{z,FR}}{g} \tag{5.18}$$

Considering the torque balance equation at the point of contact between the ground and the front-left tire, the lateral weight shift at the front-right tire is calculated as follows:

$$\begin{aligned} &\sum M_x = 0 \;\Rightarrow\; F_{z,FR} \cdot t_f - m_F^* \cdot a_y \cdot h_{CG} - m_F^* \cdot g \cdot \frac{t_f}{2} = 0 \;\Rightarrow \\ &F_{z,FR} = \frac{m_F^*}{t_f}\left(a_y \cdot h_{CG} + \frac{t_f}{2} \right) \end{aligned} \tag{5.19}$$

Substituting into equation (5.19) the virtual mass of the front axle (m_F^*) from equation (5.18) and the front axle load ($F_{z,F}$) from equation (5.16), the front-right dynamic wheel load can be calculated as follows:

$$F_{z,FR} = m_{CG} \cdot \left(\frac{b}{a+b} g - \frac{h_{CG}}{a+b} a_x \right) \cdot \left[\frac{1}{2} + \frac{h_{CG} \cdot a_y}{t_f \cdot g} \right] \tag{5.20}$$

By analogy, the dynamic loads of the other three wheels can be computed as follows:

$$F_{z,FL} = m_{CG} \cdot \left(\frac{b}{a+b} g - \frac{h_{CG}}{a+b} a_x \right) \cdot \left[\frac{1}{2} - \frac{h_{CG} \cdot a_y}{t_f \cdot g} \right] \tag{5.21}$$

$$F_{z,RR} = m_{CG} \cdot \left(\frac{a}{a+b} g + \frac{h_{CG}}{a+b} a_x \right) \cdot \left[\frac{1}{2} + \frac{h_{CG} \cdot a_y}{t_r \cdot g} \right] \tag{5.22}$$

$$F_{z,RL} = m_{CG} \cdot \left(\frac{a}{a+b} g + \frac{h_{CG}}{a+b} a_x \right) \cdot \left[\frac{1}{2} - \frac{h_{CG} \cdot a_y}{t_r \cdot g} \right] \tag{5.23}$$

Note that the performance and accuracy of this method have been proven in [Kie05] by comparing data measured during a severe cornering maneuver with the wheel loads approximated by equations (5.20) to (5.23). Finally, substituting the traction force (F_x) from equation (5.4) into equation (5.14), the maximum motor torque at each wheel can be calculated as follows:

$$\begin{aligned} &\frac{1}{r_{dyn,i}} \cdot \left(T_{m,i_{\max}} - I_{yy,w_i} \cdot \dot{\omega}_{w_i} \right) = \mu_i \cdot F_{zi} \cdot k_{x,i} \cdot \left(1 + l_x \cdot \frac{F_{zi} - F_{z0}}{F_{z0}} \right) \Rightarrow \\ &T_{m,i_{\max}} = r_{dyn,i} \cdot \mu_i \cdot F_{zi} \cdot k_{x,i} \cdot \left(1 + l_x \cdot \frac{F_{zi} - F_{z0}}{F_{z0}} \right) + I_{yy,w_i} \cdot \dot{\omega}_{w_i} \end{aligned} \tag{5.24}$$

As can be seen, the maximum motor torque in equation (5.24) is a function of the tire-road friction coefficient (μ). This indicates that in the future a friction coefficient estimator must be implemented to the ATVC, such that the maximum possible motor torque can be calculated correctly on all road conditions. Equation (5.24) is used by the torque vectoring controller to limit the motor torque at each wheel when generating a couple.

In summary, by comparing equations (5.5) and (5.6) with equation (5.24), the motor torque at each wheel is limited as follows:

$$T_{m,i} = \min\left[\left(\frac{r_{dyn,i}}{t_f}\cdot M_{z,\,front} + I_{yy,w}\cdot\dot{\omega}_{w,i}\right), \left(r_{dyn,i}\cdot\mu_i\cdot F_{zi}\cdot k_{x,i}\cdot\left(1+l_x\cdot\frac{F_{zi}-F_{z0}}{F_{z0}}\right)+I_{yy,w_i}\cdot\dot{\omega}_{w_i}\right)\right] \quad (5.25)$$

where $i \in \{\text{FL, FR}\}$ and

$$T_{m,i} = \min\left[\left(\frac{r_{dyn,i}}{t_r}\cdot M_{z,rear} + I_{yy,w}\cdot\dot{\omega}_{w,i}\right), \left(r_{dyn,i}\cdot\mu_i\cdot F_{zi}\cdot k_{x,i}\cdot\left(1+l_x\cdot\frac{F_{zi}-F_{z0}}{F_{z0}}\right)+I_{yy,w_i}\cdot\dot{\omega}_{w_i}\right)\right] \quad (5.26)$$

where $i \in \{\text{RL, RR}\}$. As indicated in equation (5.1), $M_{z,\,front}$ and $M_{z,\,rear}$ are the portions of the required corrective yaw moment that must be generated at the front and rear axles, respectively. The relationship between these two moments defines the front-to-rear torque vectoring distribution, and will be defined in the next section.

5.3 Control method for front-to-rear torque vectoring distribution

As mentioned earlier, if a middle differential were used to distribute the driving torque between the front and rear axles, the fixed torque distribution could be established on the basis of the axle-load ratio, the design philosophy of the vehicle, or the desired handling characteristics of the vehicle. In the case of an active differential, however, this fixed ratio is adjusted according to the traction conditions or driving dynamics of the vehicle [Rei02]. Since no mechanical linkage exists between the wheels of the AUTO21EV, the front-to-rear torque distribution ratio must be set virtually and adjusted based on the vehicle driving dynamics or traction conditions. In normal driving conditions, a fixed 50:50 ratio has been chosen to split the required corrective yaw moment evenly between the front and rear axles. However, this ratio will be adjusted by a yaw rate feedback controller at high maneuvering speeds and in emergency situations in which the vehicle is operating near its handing limits. This approach uses the yaw rate error calculated for the

genetic fuzzy YMC (Table 4-I) and sets the front-to-rear distribution ratios, namely θ_f and θ_r, such that the deviation between the desired and actual yaw rate of the vehicle is minimized. This objective is accomplished by a PD controller as follows:

$$\theta_f = \theta_{f,\,fixed} + K_P \cdot e(\dot{\psi}) + K_D \cdot \frac{d}{dt} e(\dot{\psi}) \tag{5.27}$$

$$\theta_r = 100\% \; - \; \theta_f \tag{5.28}$$

where $\theta_{f,\,fixed}$ is the predefined fixed ratio of 50%, and K_P and K_D are the proportional and derivative feedback gains of the PD controller, respectively. Note that the controller gains are chosen manually using a trial-and-error approach. The performance and stability of this controller have been examined through numerous driving maneuvers in the simulation environment. Since the proposed PD controller is part of a digital control system, the derivative part of the controller is approximated as follows:

$$\frac{d}{dt} e(\dot{\psi}) \approx \frac{e(\dot{\psi})_k - e(\dot{\psi})_{k-1}}{\text{sample time}} \tag{5.29}$$

where $e(\dot{\psi})_k$ and $e(\dot{\psi})_{k-1}$ are the current and previous values of the yaw rate error, respectively.

5.4 Evaluation of the advanced torque vectoring controller

In order to evaluate the performance of the advanced torque vectoring controller (ATVC), the AUTO21EV is driven through a series of test maneuvers, as described in Chapter 2.

5.4.1 ISO double-lane-change maneuver

The performance of the ATVC is first evaluated by driving the AUTO21EV through the double-lane-change maneuver with an initial speed of 75 km/h and using the path-following driver model. Figure 5-4 illustrates the vehicle trajectory and demonstrates that the driver is able to negotiate the maneuver when the ATVC is active.

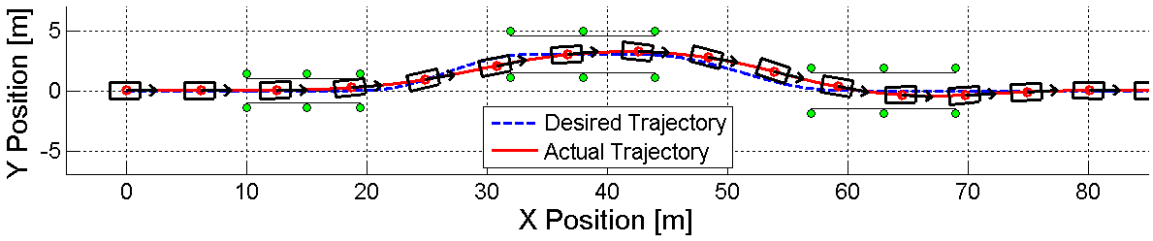

Figure 5-4: Desired and actual vehicle trajectories when driving through the double-lane-change maneuver with an initial speed of 75 km/h using the path-following driver model and the ATVC

Figure 5-5 illustrates the vehicle yaw rate and sideslip angle during this maneuver. As can be seen, the ATVC is not able to exactly match the actual vehicle yaw rate with the desired yaw rate calculated using the reference bicycle model. In addition, due to the actuation of the in-wheel motors, there are some oscillations in the actual vehicle yaw rate that might be perceived by the driver as being annoying. However, the sideslip angle of the vehicle is very close to that obtained when the genetic fuzzy YMC is active (see Figure 4-24).

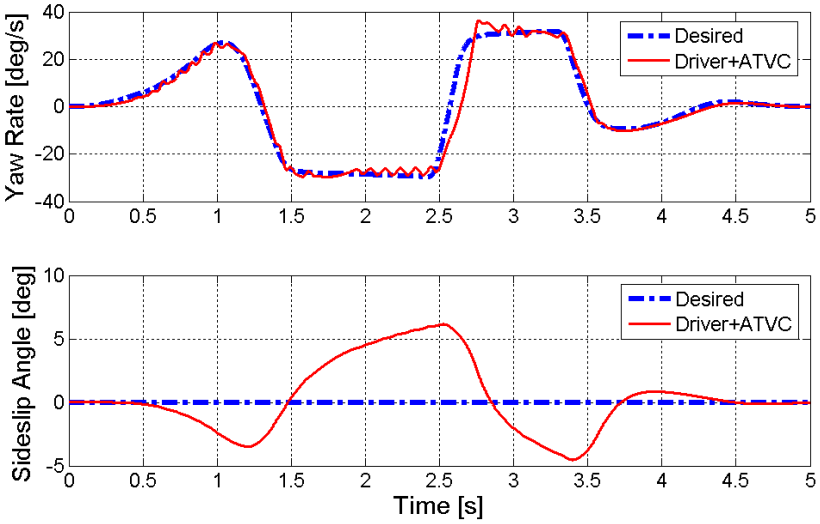

Figure 5-5: Desired and actual vehicle yaw rate (top) and sideslip angle (bottom) when driving through the double-lane-change maneuver using the driver model with and without the ATVC

Figure 5-6-a illustrates the vehicle lateral acceleration as a function of time. As can be seen, the results using the ATVC are very similar to those observed using the genetic fuzzy YMC except at the handling limits, where the activation of the in-wheel motors causes some oscillations in the lateral acceleration of the vehicle. As mentioned before, this type of oscillation might be perceived by the driver as being annoying, and should be avoided. Looking at Figure 5-6-b, it is confirmed that, except during the second lane-change, the driver requires about the same amount of steering wheel input as is the case when the genetic fuzzy YMC is active. Figure 5-6-c illustrates the vehicle speed during the double-lane-change maneuver, and confirms the advantage of the couple generation by the ATVC. Specifically, due to the couple generation at the front and rear axles, the speed reduction during this maneuver is much smoother and more linear than the case where no stability controller is active. As such, the vehicle loses almost the same amount of speed as is the case when the genetic fuzzy YMC is active. Figure 5-6-d illustrates the handling performance of the vehicle and indicates that the hysteresis of this

plot is twice as large as that of the analogous plot for the genetic fuzzy YMC. In other words, although the responsiveness and agility of the vehicle are considerably improved compared to the case where no stability controller is active, they are not as good as the case when the genetic fuzzy YMC is used to generate the corrective yaw moment.

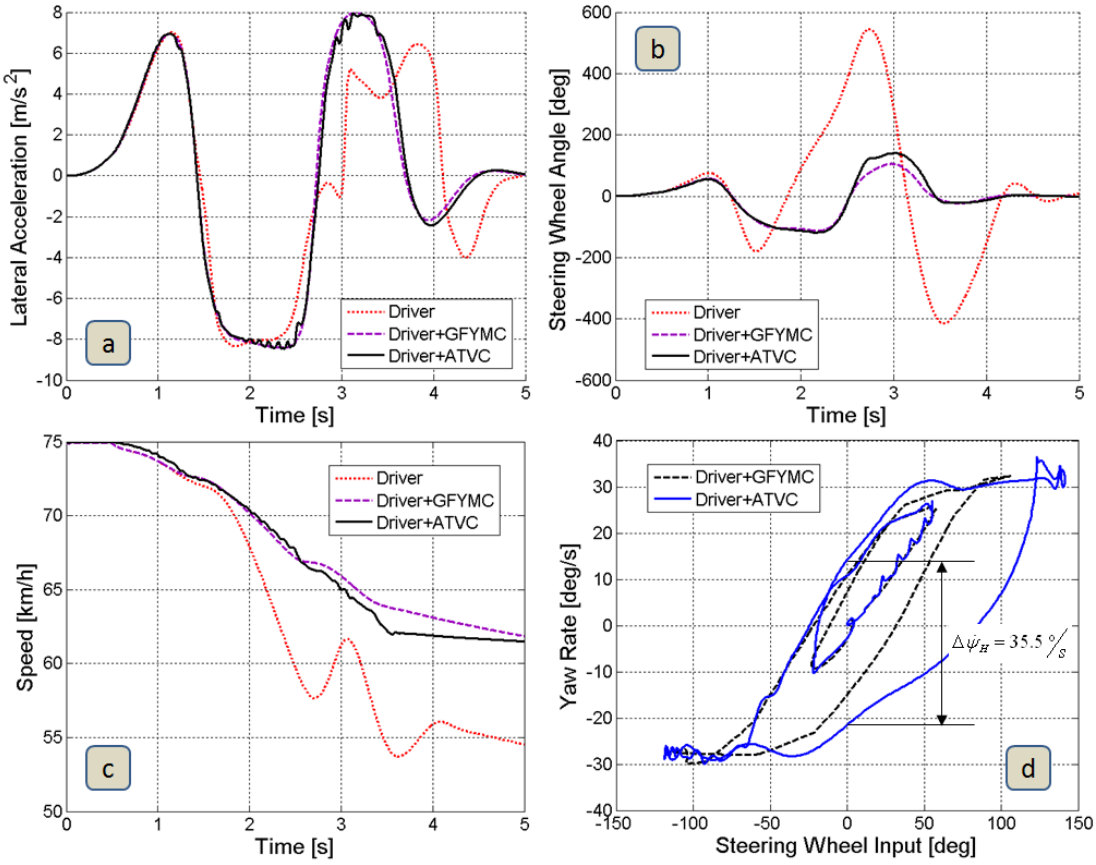

Figure 5-6: (a) Lateral acceleration, (b) steering wheel angle, and (c) vehicle speed as functions of time; and (d) vehicle yaw rate as a function of the steering wheel input when driving through the double-lane-change maneuver without a controller, with the genetic fuzzy YMC (GFYMC), and with the ATVC

Figure 5-7 illustrates the torque of each in-wheel motor during the double-lane-change maneuver. It is very important to notice that, at each wheel, the requested motor torque from the torque vectoring controller can be restricted by the maximum possible motor torque, which is calculated by equation (5.24), the slip controller that prevents the tires from locking up or spinning out, or by the power limitation of the in-wheel motor. As mentioned earlier, the performance of the in-wheel motors decreases the faster the motors rotate due to the inductive voltage losses. Looking at the motor torque plots, it can be seen that, although the ATVC has always requested couple forces on the sides of both axles, the requested motor torques could not always be generated due to one of the aforementioned limitations. For instance, between 1.2 and 1.45 seconds of the simulation,

the actual motor torques generated at the front wheels and the rear-right wheel are less than the requested torques because, at a speed of 72 km/h, the motors are not powerful enough to generate the requested torques. At the rear-left tire, however, the requested motor torque is restricted by the maximum allowable torque. Another interesting region to observe is between 2.45 and 3.1 seconds of the simulation, during which time the transition between the minimum and maximum lateral accelerations occurs (Figure 5-6-b). As can be seen, the left-to-right torque vectoring controller has first ordered the left wheels to brake and the right wheels to accelerate in order to correct an oversteering situation, where the actual yaw rate is larger than the desired one (Figure 5-5). At 2.73 seconds of the simulation, however, as the transition from a negative lateral acceleration to a positive one occurs and the yaw rate error becomes zero, the left-to-right torque vectoring controller changes its request by ordering the left wheels to accelerate and the right wheels to brake, which is again done to correct an oversteering situation.

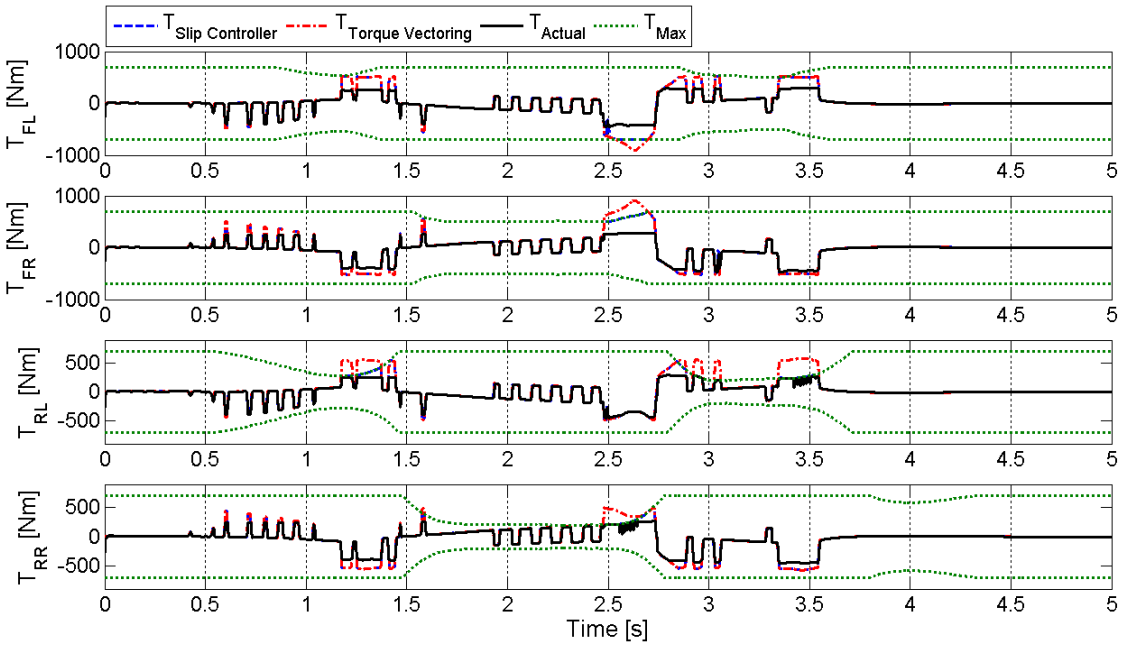

Figure 5-7: Requested and actual motor torque at each wheel when driving through the double-lane-change maneuver using the driver model with the ATVC

Looking at the activation plot of the front-to-rear torque vectoring controller in Figure 5-8, it can be confirmed that the actions of the left-to-rear torque vectoring controller have been supported by the front-to-rear torque vectoring controller. In particular, the front-to-rear torque vectoring controller has requested the front motors to generate up to 72% of the total required corrective yaw moment between 2.45 and 2.73 seconds and, later, it changes its request by asking for more torque from the rear motors

between 2.73 and 3.1 seconds of the simulation. Note that generating more torque at the front motors rather than the rear ones reduces the lateral force potential at the front axle and increases that at the rear axle. The asymmetric lateral force potentials on the front and rear axles is used to generate the required corrective yaw moment. The effect of the front-to-rear torque vectoring controller can also be seen in Figure 5-7. For instance, between 2.45 and 2.73 seconds, the front-to-rear torque vectoring controller has requested the front-left motor to generate up to 900 Nm of braking torque and the front-right motor to generate up to 900 Nm of driving torque while, at the same time, the controller has requested up to 350 Nm of braking and driving torques from the rear-left and rear-right motors, respectively. Note that, although the controller has requested the front motors to generate large motor torques, the motors are not powerful enough to generate the requested torques when the vehicle is travelling at a speed of 66 km/h. The effects seen in Figure 5-7 can also be confirmed by looking at the tire traction potentials and tire slip ratios shown in Figures 5-9 and 5-10, respectively. For instance, the maximum traction potential of the rear-left tire has been exceeded once at 1.2 seconds and then between 3.37 and 3.56 seconds of the simulation (Figure 5-9). Looking at Figures 5-7 and 5-10, it can be confirmed that the requested motor torque on the rear-left wheel is first restricted by the maximum torque limiter (at 1.2 seconds) and then by the slip controller (between 3.37 and 3.56 seconds) in order to prevent tire spin-out. This observation suggests that the excess of the traction potential of the rear-left tire is due to the fact that the lateral force of the tire has exceeded its limit.

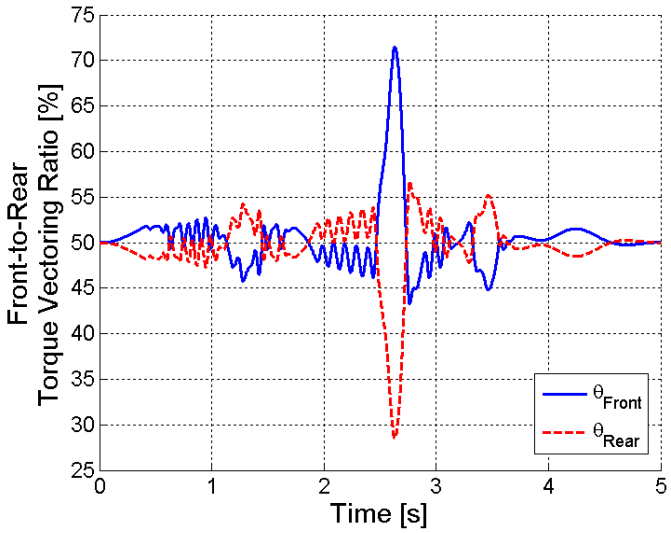

Figure 5-8: Front-to-rear torque vectoring ratios when driving through the double-lane-change maneuver using the driver model with the ATVC

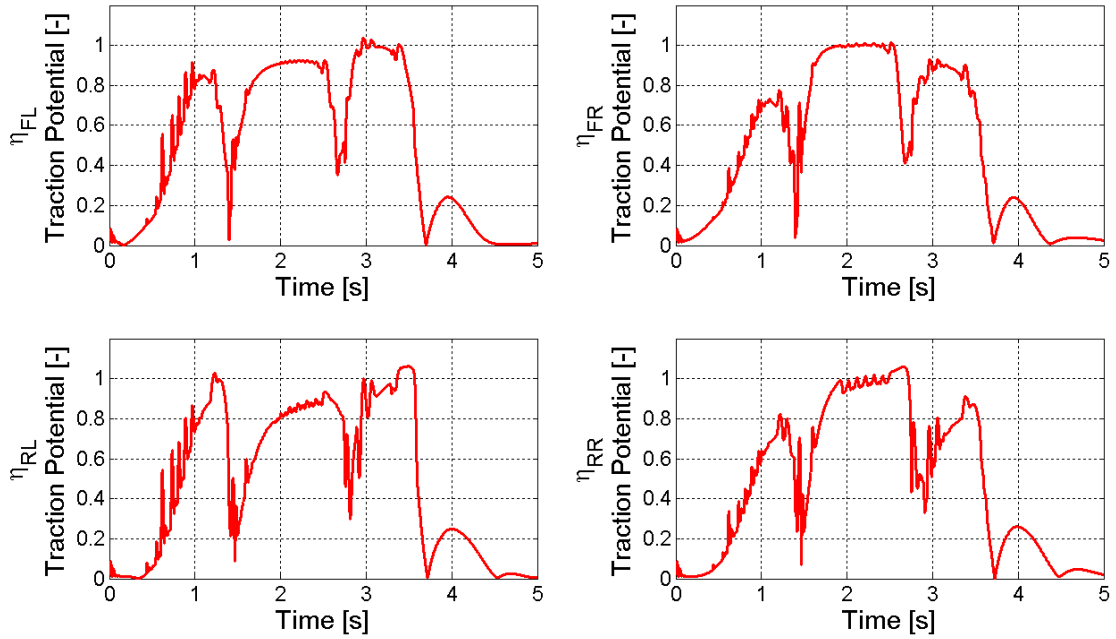

Figure 5-9: Traction potential of each tire when driving through the double-lane-change maneuver using the driver model with the ATVC

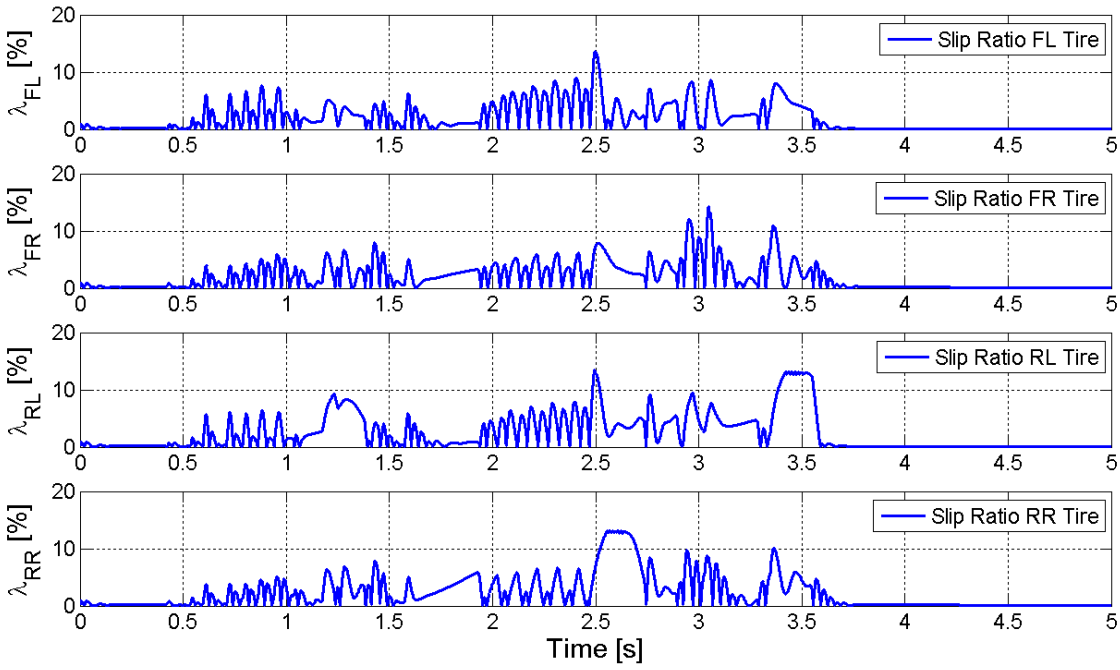

Figure 5-10: Tire slip ratios when driving through the double-lane-change maneuver using the driver model with the ATVC

Table 5-I summarizes the vehicle response during the double-lane-change maneuver using the driver model when the advanced torque vectoring controller is active, and compares it to the results obtained when no stability controller is active and when the genetic fuzzy YMC is active. Comparing different parameters of the vehicle response during the double-lane-change maneuver, it can be seen that, although the ATVC has

improved all the decisive parameters that describe the handling, stability, and longitudinal dynamics of the vehicle, it cannot be considered as effective as the genetic fuzzy YMC, which represents the ideal case but is not directly realizable. With respect to the handling of the vehicle, the ATVC has reduced $|\beta|_{\max}$ and $|\dot{\psi}|_{\max}$ by about the same amount as the genetic fuzzy YMC. The maximum lateral acceleration of the vehicle, $|a_y|_{\max}$, has increased the same amount as it did when the genetic fuzzy YMC was active; however, when the ATVC is active, the driver requires a larger maximum steering wheel angle to negotiate the maneuver. In addition, the hysteresis of the performance plot ($\Delta\dot{\psi}_H$) is about 1.7 times larger than it is when the genetic fuzzy YMC is active. Altogether, the ATVC is considered to be an effective controller for improving the handling characteristics of the vehicle. Since the ATVC has reduced $|\beta|_{\max}$ and $|\dot{\psi}|_{\max}$ by about the same amount as the genetic fuzzy YMC, it is considered to be as effective at improving the stability of the vehicle. The speed lost during the maneuver is about the same as that observed when the genetic fuzzy YMC is used and, therefore, the ATVC is also considered to be a very effective controller for improving the longitudinal dynamics of the vehicle.

Parameter	$\lvert\beta\rvert_{\max}$	$\lvert\dot{\psi}\rvert_{\max}$	$\lvert a_y\rvert_{\max}$	$\lvert\delta_{SW}\rvert_{\max}$	$\Delta\dot{\psi}_H$	v_{lost}
AUTO21EV	26.3^o	115.4^o/s	8.2m/s^2	545^o	163.8^o/s	20.5m/s
GFYMC	6.2^o	31.2^o/s	8.4m/s^2	108^o	21^o/s	13.2m/s
ATVC	6.1^o	36.4^o/s	8.4m/s^2	140^o	35.5^o/s	13.5m/s

Table 5-I: Vehicle response during the double-lane-change maneuver using the driver model without a controller, with the genetic fuzzy YMC (GFYMC), and with the ATVC

5.4.2 Step-steer response maneuver

In order to evaluate the performance of the vehicle using the ATVC in a step-steer response maneuver, the vehicle yaw rate, sideslip angle, and lateral acceleration as functions of time are observed. Figure 5-11 illustrates the steering wheel input and the lateral acceleration of the vehicle. As can be seen, the lateral acceleration when using the ATVC is similar to that obtained when using the genetic fuzzy YMC; however, due to the actuation of the in-wheel motors, some small oscillations can be observed in the lateral acceleration plot. The rise time of the lateral acceleration response is about 0.47 seconds when using the ATVC. Figure 5-12 shows the yaw rate and sideslip angle of the vehicle

during this maneuver. A severe oscillation can be observed in the yaw rate response when using the ATVC, which would be perceived by the driver as being annoying, and should be avoided. Therefore, in practice, the ATVC should only be activated when the yaw rate error exceeds a particular threshold and should not be used to correct small yaw rate errors. Although the rise time of the yaw rate response is similar to that obtained when using the genetic fuzzy YMC, an overshoot is clearly visible when using the ATVC. The sideslip angle of the vehicle is slightly less than that observed when using the genetic fuzzy YMC but, again, some oscillations can be seen in the response.

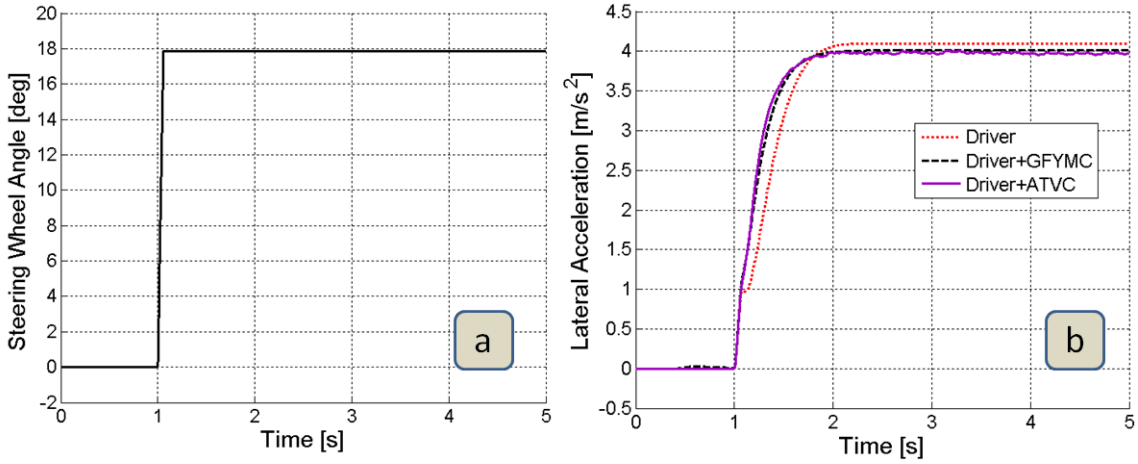

Figure 5-11: (a) Required steering wheel input and (b) lateral acceleration of the vehicle when driving through the step-steer maneuver using the ATVC

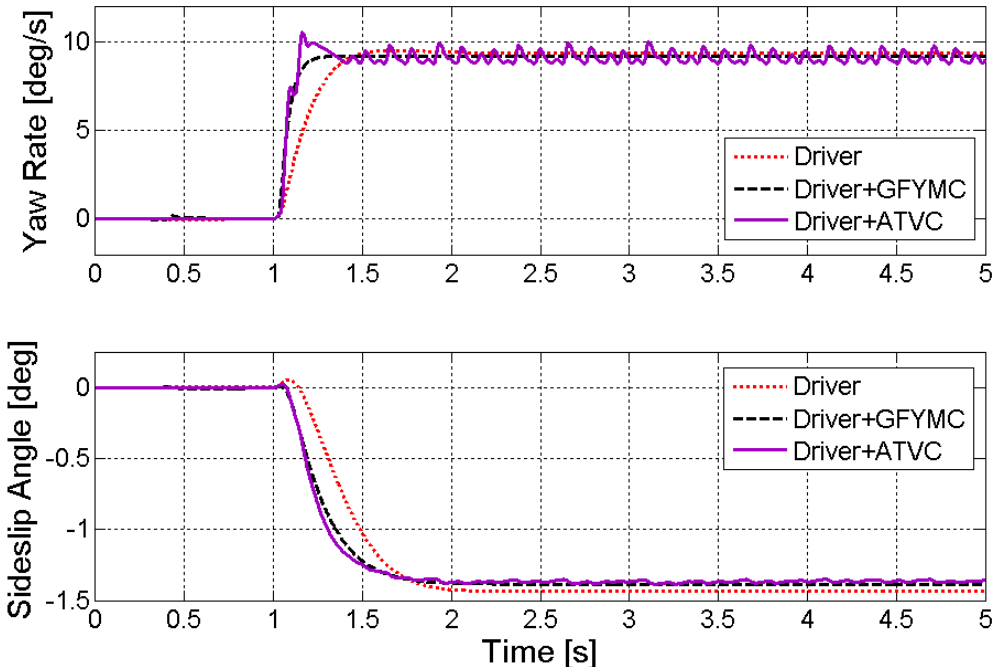

Figure 5-12: Yaw rate (top) and sideslip angle (bottom) of the vehicle when driving through the step-steer maneuver using the ATVC

Table 5-II summarizes the vehicle response during the step-steer test maneuver. Comparing different parameters of the vehicle response with and without the ATVC, it can be recognized that the ATVC is effective at improving all the decisive performance parameters of the vehicle which, for this maneuver, describe the vehicle handling characteristics. However, two problems must be addressed: the severe oscillation in the yaw rate response of the vehicle and the overshooting effect of the yaw rate response.

Parameter	$t_{\dot{\psi}}$	$\mathrm{PO} = \frac{\dot{\psi}_{\max} - \dot{\psi}_{ss}}{\dot{\psi}_{ss}} \times 100\%$	$\lvert\beta\rvert_{\max}$	t_{a_y}
AUTO21EV	0.34s	1.30%	1.43^{o}	0.66s
GFYMC	0.15s	0.00%	1.38^{o}	0.51s
ATVC	0.15s	16.1%	1.36^{o}	0.47s

Table 5-II: Vehicle response during the step-steer maneuver using the driver model without a controller, with the genetic fuzzy YMC (GFYMC), and with the ATVC

5.4.3 Brake-in-turn maneuver

Figure 5-13-a illustrates the trajectory of the uncontrolled vehicle relative to the desired path during a brake-in-turn maneuver and compares it to the case when the ATVC is active (Figure 5-13-b). As can be seen, the vehicle becomes unstable and leaves the predefined road when no stability controller is active. However, the driver model is able to keep the vehicle very close to the predefined circular path while severely braking when the ATVC is active, and the lateral deviation of the vehicle from the desired path remains very small throughout the maneuver. Looking at the driver's steering wheel input as a function of time, shown in Figure 5-14-a, it is clear that the driver model is able to control the vehicle when the ATVC is active by applying a maximum steering wheel angle of only 48^{o}. In addition, the gradient of this plot indicates that it is very easy for the driver to control the vehicle when braking in a turn. Figure 5-14-b illustrates the lateral acceleration of the vehicle and confirms that the vehicle remains stable when the ATVC is active, even though it is being driven near its handling limit. As can be seen, the lateral acceleration of the vehicle when using the ATVC is very similar to that obtained when the genetic fuzzy YMC is active, but contains some oscillations at higher lateral accelerations.

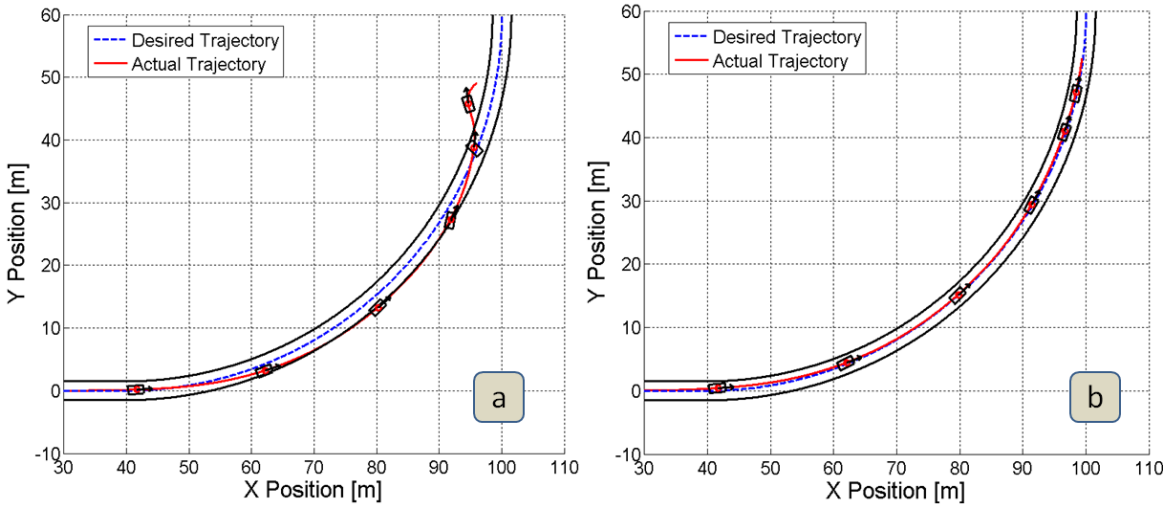

Figure 5-13: Desired and actual vehicle trajectories when braking in a turn using (a) the driver model only and (b) the driver model with the advanced torque vectoring controller (ATVC)

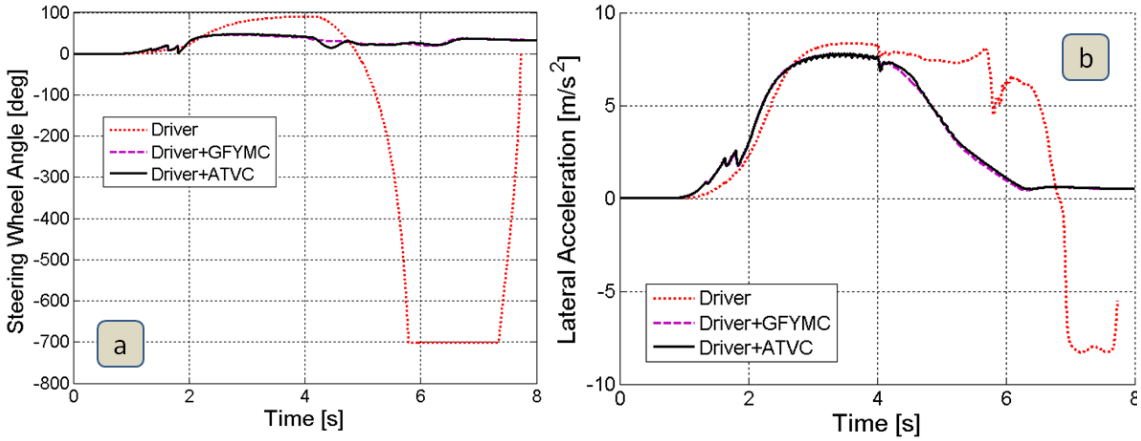

Figure 5-14: (a) Required steering wheel input and (b) lateral acceleration of the vehicle when braking in a turn using the driver model without a controller, with the genetic fuzzy YMC (GFYMC), and with the ATVC

Figure 5-15 illustrates the vehicle yaw rate and sideslip angle when driving through the brake-in-turn maneuver using the genetic fuzzy YMC and the ATVC. Note that, for clarity, the yaw rate and sideslip angle of the vehicle are not shown for the case where no stability controller is active. As can be seen, the vehicle yaw rate follows the desired reference model, but it is superimposed with oscillations. In addition, for a short time after the braking starts (between the fourth and fifth seconds of the simulation), the ATVC is not able to minimize the yaw rate error. However, the driver is still able to control the vehicle while braking in the curve. This figure also confirms the stability of the vehicle, since the yaw rate and sideslip angle both approach zero as the vehicle progresses towards larger deceleration rates. Figure 5-16 shows the vehicle speed as a function of time and the vehicle longitudinal acceleration as a function of vehicle speed.

These plots confirm the performance of the speed controller as well as the severity of the braking component of this maneuver.

Table 5-III summarizes the vehicle response during the brake-in-turn maneuver using the driver model. Comparing different parameters of the response when this maneuver is performed without a controller, with the genetic fuzzy YMC, and with the ATVC, it can be seen that the ATVC is as effective as the genetic fuzzy YMC at improving all the decisive parameters that describe the handling, stability, and path-following capability of the vehicle during a brake-in-turn maneuver. In particular, the ATVC has reduced $|\beta|_{\max}$, $|\dot{\psi}|_{\max}$, and $|\delta_{SW}|_{\max}$ significantly, which indicates that this controller is very effective at enhancing the handling capabilities of the vehicle. It is important to notice that, due to the severe oscillations in the yaw rate response of the vehicle (Figure 5-15), the driver would perceive the activation of the ATVC as being disruptive. A reduction of $|\beta|_{\max}$ and $|\dot{\psi}|_{\max}$ by the ATVC indicates that it is also very effective at improving the stability of the vehicle. Since the maximum lateral deviation of the vehicle from the desired path remains very small throughout the maneuver, the ATVC is also very effective at enhancing the path-following capability of the vehicle.

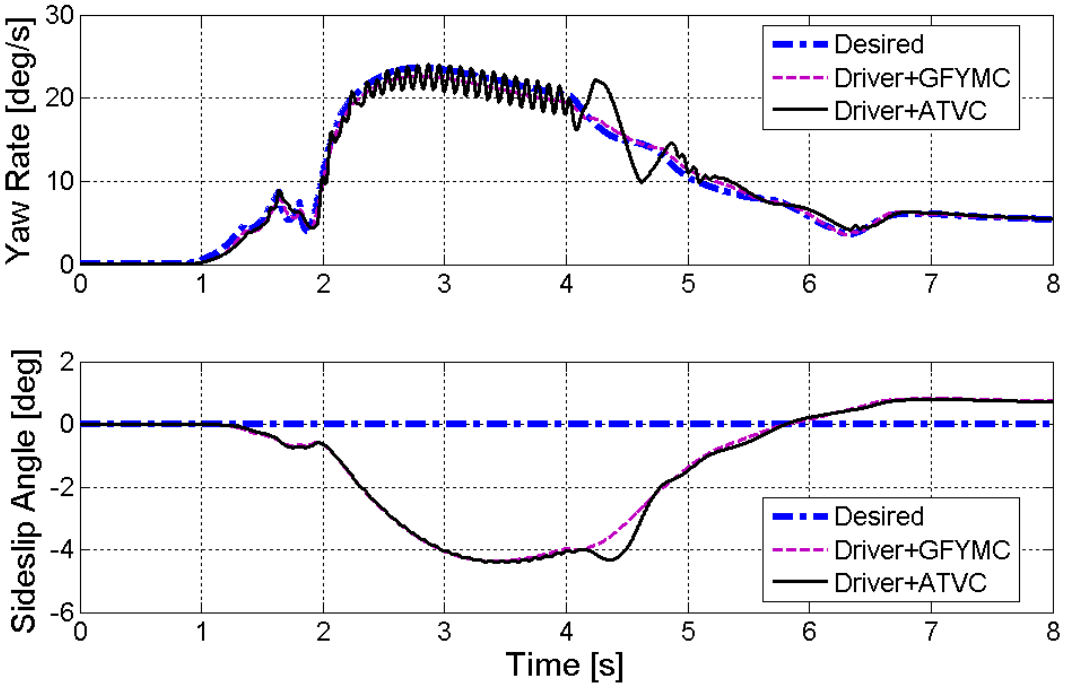

Figure 5-15: Desired and actual vehicle yaw rate (top) and sideslip angle (bottom) when braking in a turn using the driver model without a controller, with the genetic fuzzy YMC (GFYMC), and with the ATVC

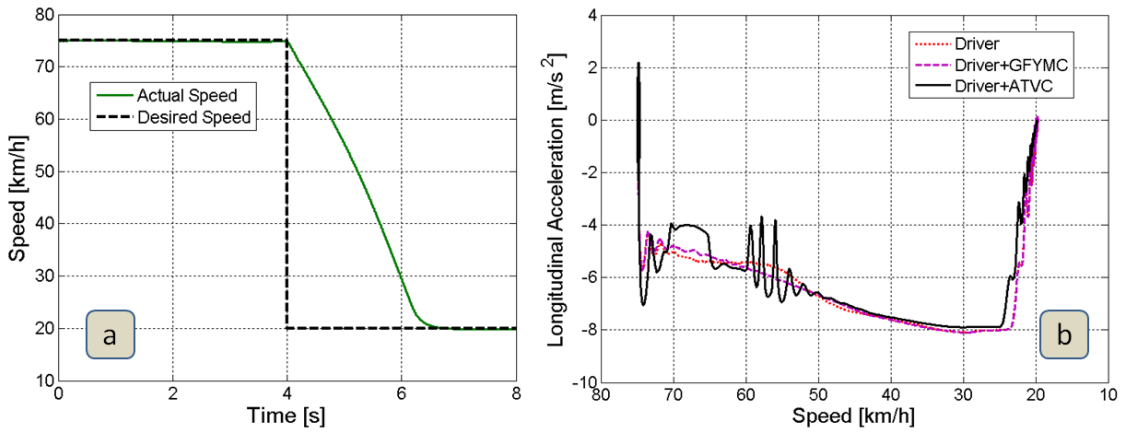

Figure 5-16: (a) Vehicle speed as a function of time using the driver model with the ATVC and (b) longitudinal acceleration as a function of vehicle speed when braking in a turn using the driver model without a controller, with the genetic fuzzy YMC (GFYMC), and with the ATVC

Parameter	$\lvert\dot{\psi}\rvert_{max}$	$\lvert\beta\rvert_{max}$	Δy_{max}	$\lvert\delta_{SW}\rvert_{max}$
AUTO21EV	126.5^{o}/s	50.1^{o}	3.67m	700^{o}
GFYMC	22.60^{o}/s	4.36^{o}	0.18m	46.4^{o}
ATVC	24.00^{o}/s	4.40^{o}	0.18m	48.0^{o}

Table 5-III: Vehicle response during the brake-in-turn maneuver using the driver model without a controller, with the genetic fuzzy YMC (GFYMC), and with the ATVC

5.4.4 Straight-line braking on a μ-split road

As mentioned before, braking on a μ-split road can be used to confirm the performance and sensitivity of a vehicle and its stability control systems when subjected to external disturbances. Figure 5-17 shows the vehicle trajectory for this maneuver when no stability controller is active and compares it to the case when the ATVC is active. This comparison confirms that the ATVC is able to reduce the side-pushing effect of the vehicle while braking on a μ-split road, but the vehicle still leaves the predefined road, which is considered to be a dangerous situation. The braking distance of the vehicle is reduced to about 47.3 meters when the ATVC is active. Looking at Figure 5-18, it is clear that the ATVC is able to limit and, later, diminish the yaw rate and sideslip angle of the vehicle while driving over the black ice patch, but does not prevent the vehicle from leaving the predefined road.

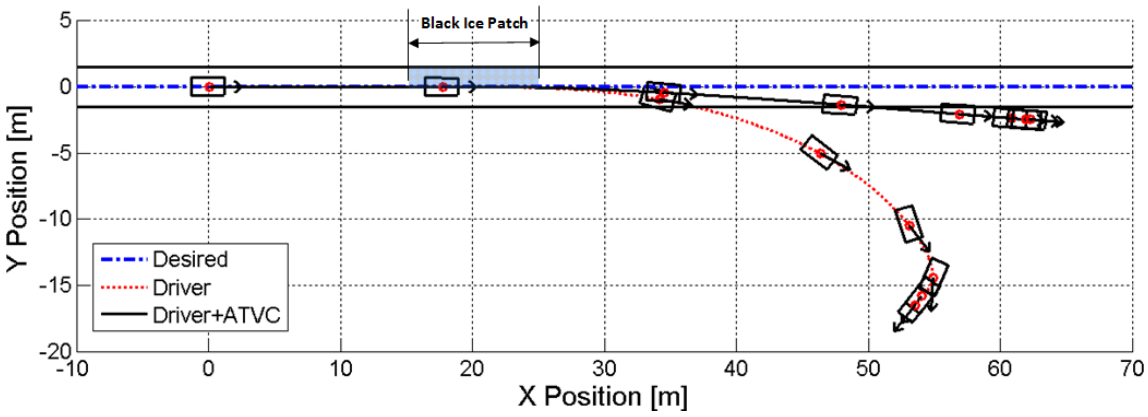

Figure 5-17: Desired and actual vehicle trajectories when braking on a μ-split road holding the steering wheel fixed with and without the ATVC

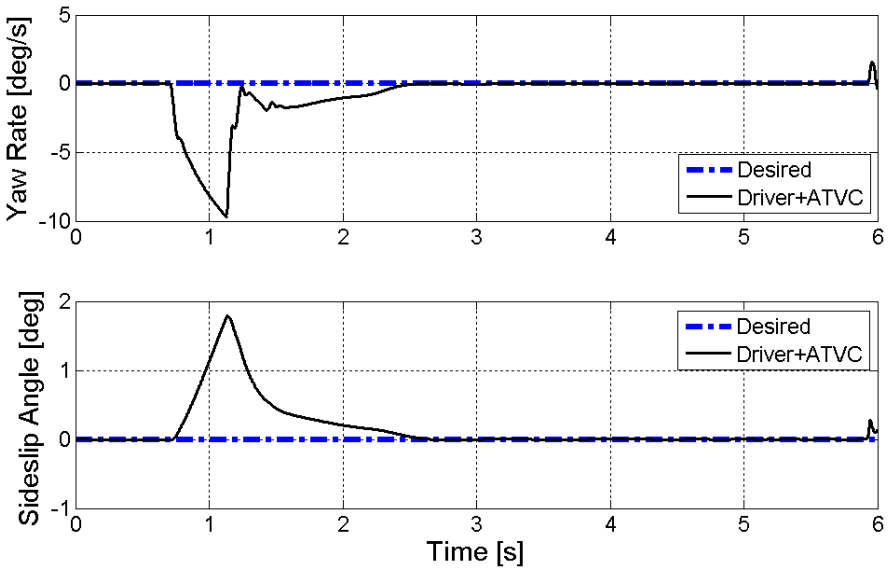

Figure 5-18: Desired and actual vehicle yaw rate (top) and sideslip angle (bottom) when braking on a μ-split road holding the steering wheel fixed with and without the ATVC

Figure 5-19 illustrates the tire slip ratios while braking on a μ-split road and indicates that the slip controllers on the left wheels have limited the motor torques between 0.7 and 1.15 seconds of the simulation in order to prevent the tires from locking up while, at the same time, ensuring the maximum possible braking force is being applied when braking on the black ice patch. Later in the simulation, due to the weight shift to the front axle, the slip controllers on the rear axle have limited the motor torques to prevent tire lock-up at higher deceleration rates. Looking at Figure 5-20, which illustrates the motor torques for all four wheels, it is apparent that the slip controllers on the left wheels have limited the braking torques to 20 Nm (between 0.7 and 1.15 seconds) in order to prevent tire lock-up when braking on the black ice patch. As mentioned earlier, as a result of the asymmetric braking forces generated on the left and right wheels, the vehicle is

pushed to the right side of the road. In order to prevent this side-pushing effect, the left-to-right torque vectoring controller has requested larger braking forces on the left wheels, which are restricted by the slip controllers, and has reduced the braking forces on the right wheels.

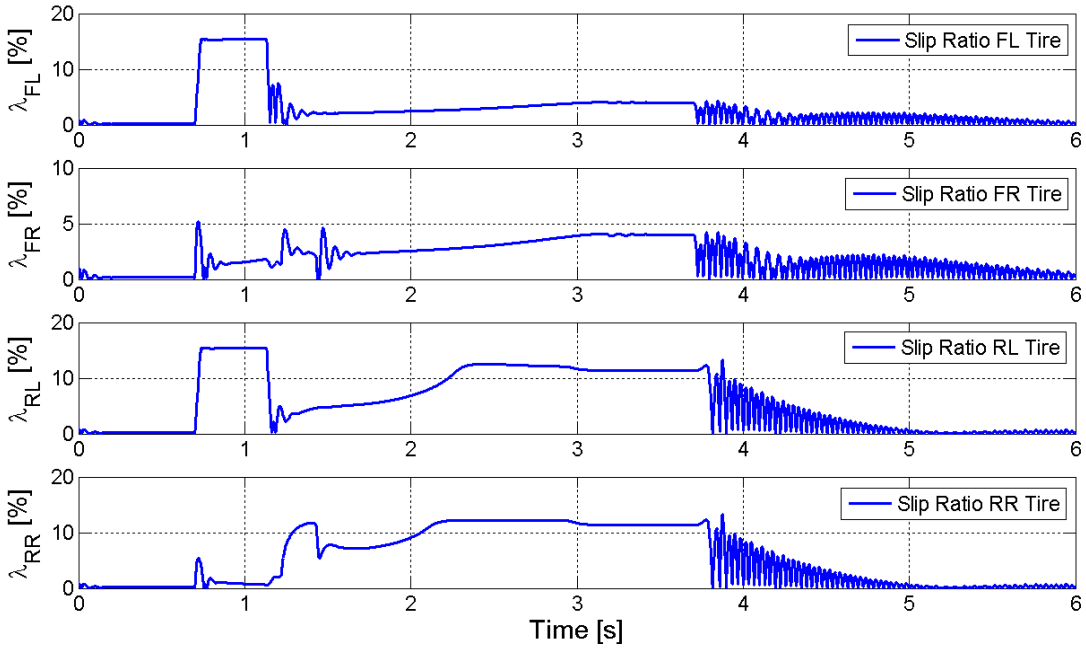

Figure 5-19: Tire slip ratios when braking on a μ-split road holding the steering wheel fixed and using the ATVC

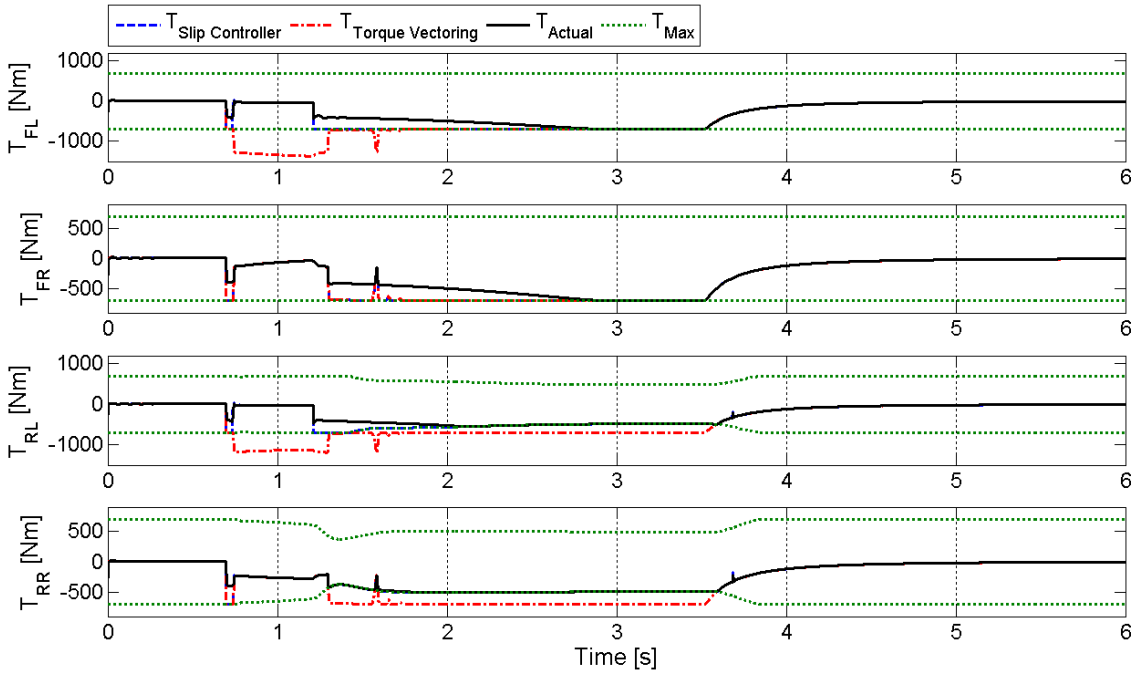

Figure 5-20: Requested and actual motor torque at each wheel when braking on a μ-split road holding the steering wheel fixed and using the ATVC

Figure 5-21 illustrates the torque distribution requested by the front-to-rear torque vectoring controller. As can be seen, the front-to-rear torque vectoring controller has requested the front motors to generate up to 60% of the required corrective yaw moment in order to correct the undesirable side-pushing effect when driving over the black ice patch. Requesting more torque from the front motors reduces the lateral force potential of the front axle and increases that of the rear axle. The asymmetric lateral force potentials on the front and rear axles helps to generate the required corrective yaw moment.

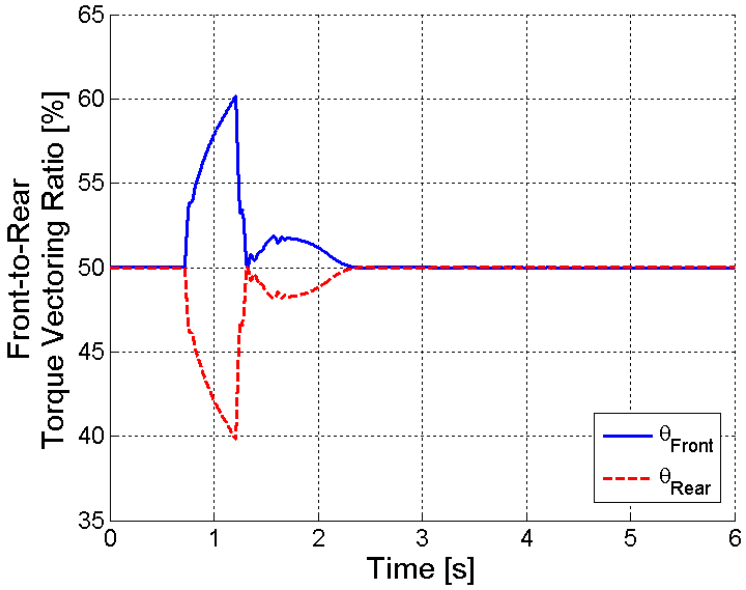

Figure 5-21: Front-to-rear torque vectoring activation when braking on a μ-split road holding the steering wheel fixed and using the ATVC

Table 5-IV summarizes the vehicle response during the straight-line braking on a μ-split road maneuver when using the ATVC. Comparing different parameters of the vehicle response during this maneuver, it can be seen that the effectiveness of the ATVC at improving the stability, path-following capability, and braking performance of the vehicle is limited. Although the ATVC has reduced the $|\beta|_{max}$ and $|\dot{\psi}|_{max}$ values in comparison to those obtained when no stability controller was active and has avoided instability, its intervention was not large enough to prevent the vehicle from leaving the predefined road. Moreover, when the ATVC is active, the braking distance of the vehicle is longer than that observed when the genetic fuzzy YMC is active. Finally, the ATVC could not keep the vehicle on the predefined road, which indicates that the ATVC cannot be considered an effective controller for enhancing the path-following capability of the vehicle when braking on a μ-split road.

Parameter	$\lvert\beta\rvert_{max}$	$\lvert\dot{\psi}\rvert_{max}$	$\Delta x_{braking}$	Δy_{max}
AUTO21EV	24.2^o	63.4^o/s	48.4m	15.9m
GFYMC	0.40^o	1.85^o/s	44.5m	0.46m
ATVC	1.70^o	9.70^o/s	47.3m	2.70m

Table 5-IV: Vehicle response during the straight-line braking on a μ-split road maneuver holding the steering wheel fixed without a controller, with the genetic fuzzy YMC (GFYMC), and with the ATVC

5.5 Chapter summary

In this chapter, an advanced torque vectoring controller is developed based on the previously developed genetic fuzzy yaw moment controller. The objective of the advanced torque vectoring controller is to distribute the calculated corrective yaw moment to the individual in-wheel motors in order to stabilize the vehicle driving dynamics. A novel algorithm is developed for the left-to-right torque vectoring on each axle, and a PD controller is introduced for the front-to-rear torque vectoring distribution action. A variety of maneuvers are simulated to demonstrate the performance and effectiveness of the ATVC. Table 5-V provides a subjective evaluation of the effectiveness of the ATVC based on different test maneuvers. In the next chapter, a genetic fuzzy active steering controller is developed, which is considered to be an alternative stability controller to the ATVC presented in this section.

Characteristic / Maneuver	Handling	Stability	Path following	Longitudinal dynamics
Double-lane-change	2	2.5		2.5
Step-steer	2			
Brake-in-turn	2.5	3	3	
Straight-line braking on a μ-split road		2.5	1	1
Mean Value $\left(\bar{x} = \frac{1}{n}\sum_{i=1}^{n} x_i\right)$	2.17	2.67	2	1.75

Table 5-V: Subjective evaluation of the effectiveness of the ATVC based on different test maneuvers (3 = very effective, 2 = effective, 1 = effective to some extent, 0 = ineffective)

6 Genetic Fuzzy Active Steering Controller

Active steering fills the gap between conventional steering systems and steer-by-wire technology. Although an active steering system provides the capability of applying driver-independent steering intervention, the mechanical linkage between the steering wheel and the rack-and-pinion system remains in place, acting as a fail-safe mechanism. An active steering system facilitates two major functions: a variable steering ratio, and maintaining vehicle stability and maneuverability during emergency maneuvers or when driving conditions call for a change in the steering response. In this chapter, however, we shall limit our focus to the vehicle stabilization capability of an active steering system.

As mentioned earlier in Chapter 1, it is advantageous to employ steering intervention rather than braking intervention to generate a corrective yaw moment when controlling a vehicle on slippery surfaces, where the limits of adhesion are easily reached. In general, steering intervention has a faster response than braking individual wheels, as is done by an ESP system, since the later requires a certain period of time to build up hydraulic brake pressure. Furthermore, modifying the reaction of the vehicle using steering intervention is a more continuous process and, therefore, is not noticeable or, at least, is not perceived as being annoying [Koe04]. In addition, active steering is highly effective when driving on a μ-split road, and is able to correct the side-pushing effect that occurs due to the different traction forces on the two sides of the vehicle. However, the range of effectiveness of an active steering system is severely restricted by the actuator range limit. For instance, the active steering system designed by BMW is only able to manipulate the steering angle of the front wheels by up to 3° [Koe04], which is equivalent to a driver steering wheel input of about 54°, when assuming a steering ratio of 1:18.

A complete steering system has been developed for the AUTO21EV in the ADAMS/View environment [Bod06], where the kinematics and dynamics of the steering system have been analyzed. This steering system has a 55% Ackermann behaviour in order to provide smaller turning radii and a higher lateral force capacity on the front tires when turning at higher speeds. The nonlinear characteristics of the steering system have been implemented in the DynaFlexPro model of the AUTO21EV (Figure 4-1) using look-up tables and independent motion drivers for the front-left and front-right wheels. A

genetic fuzzy active steering controller is developed based on this steering system, which can generate the required corrective yaw moment by manipulating the steering angle of the front tires, augmenting the steering input provided by the driver.

6.1 Fuzzy active steering controller design

Almost every active steering system available on the market today is based on the classical PID control system [Koe04, Yih05, Mam02, Kno99, Ack98, Rei04]. In general, tuning the gains of such a PID controller requires extensive and rigorous field tests that are conducted by vehicle experts in a car manufacturing company. In this work, however, a novel fuzzy active steering controller (ASC) and a reliable method by which its membership functions can be tuned in an optimized way are developed, which may make most of the expensive field testing unnecessary.

As mentioned in Chapter 4, fuzzy control systems are well suited for tackling the highly nonlinear behaviour inherent in vehicle dynamics. In addition, the rule base of the fuzzy ASC can be described in vague linguistic terms using expert knowledge, which suits the subjective nature of vehicle stability and handling. Although many researchers argue that more comprehensive control can be achieved by simultaneously considering the vehicle yaw rate and sideslip angle [Man07], an active steering system is not expected to be of significant help when driving a vehicle near its handling limit due to the limited range of effectiveness caused by actuator restrictions. In other words, in cases where a high sideslip angle is likely, an active steering system would not be considered the primary control system for stabilizing the vehicle; rather, it is a complementary system that can help to stabilize the vehicle in collaboration with other active chassis subsystems [Gor03, And06]. With this in mind, the inputs to the fuzzy ASC are defined to be the yaw rate error $e(\dot{\psi})$ and the rate of change of the yaw rate error $\dot{e}(\dot{\psi})$, and the output of the controller is the corrective steering angle that will augment the driver's steering input in order to stabilize the vehicle. The desired yaw rate to which the controller attempts to match the nonlinear behaviour of the vehicle is calculated using the linear bicycle model that is introduced in Chapter 4. Figure 6-1 illustrates the block diagram of the fuzzy ASC.

Table 6-I lists the definitions of the input and output variables of the fuzzy ASC. The input variables are pre-processed to the range [-1, 1] before entering the fuzzy controller, and the output variable of the controller is post-processed to determine the

required corrective steering angle. Note that the fuzzy ASC uses the same input variables and corresponding scaling factors that were defined for the genetic fuzzy yaw moment controller in Chapter 4; thus, it is unnecessary to calculate them again. The scaling functions for the yaw rate error and the rate of change of the yaw rate error are, again, assumed to be 35^{o}/s and 2000^{o}/s^2, respectively. Note that the scaling factor used for post-processing the output variable of the fuzzy ASC is determined based on the active steering actuator range limit. In order for the simulation to be as realistic as possible, the actuator range limit of the active steering controller developed by BMW is adopted, which only allows a steering angle manipulation of up to 3° [Koe04].

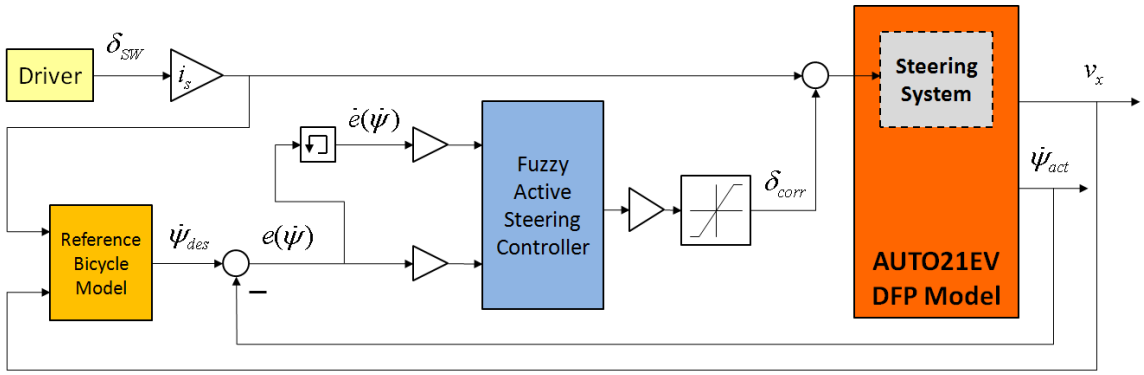

Figure 6-1: Block diagram of the fuzzy active steering controller

Variable	Definition
Input 1	$e(\dot{\psi}) = \dot{\psi}_{desired} - \dot{\psi}_{actual}$
Input 2	$\dot{e}(\dot{\psi}) = \dfrac{e(\dot{\psi})_k - e(\dot{\psi})_{k-1}}{\text{sample time}}$
Output	δ_{corr}

Table 6-I: Definition of the input and output variables of the fuzzy active steering controller

In order to provide enough rule coverage, five fuzzy sets are used for the yaw rate error and the rate of change of the yaw rate error; nine fuzzy sets are used to describe the output of the controller, which is the required corrective steering angle. A Mamdani fuzzy inference system processes the input variables through the list of rules in the knowledge base and calculates the output based on the following fuzzy rule schema:

IF e($\dot{\psi}$) is *A* AND $\dot{e}(\dot{\psi})$ is *B* THEN δ_{corr} is *C* (6.1)

where *A*, *B*, and *C* are fuzzy sets defined on the input and output domains. The initial shape and distribution of the membership functions used for the input and output variables of the fuzzy ASC are illustrated in Figure 6-2.

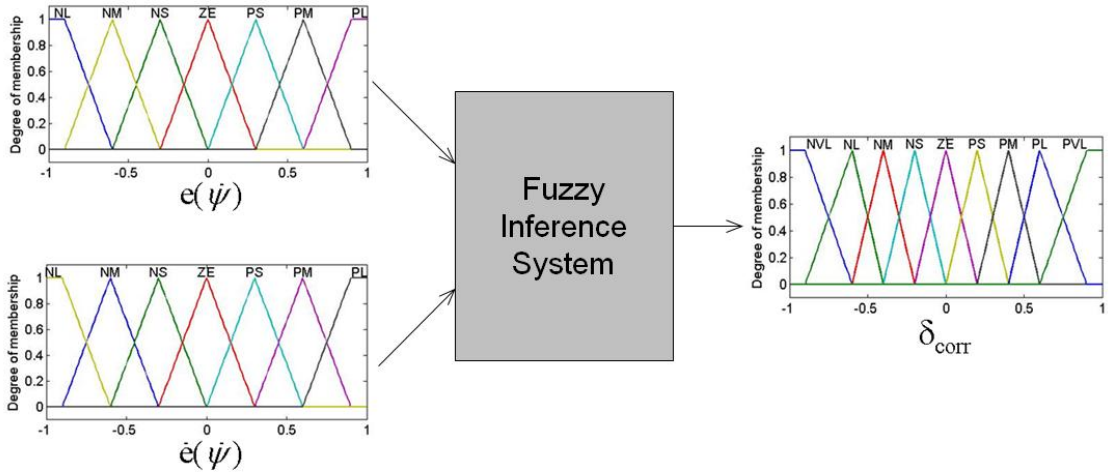

Figure 6-2: Initial shape and distribution of the membership functions for the input and output variables of the fuzzy ASC

A two-dimensional (2D) rule base table is developed for the fuzzy ASC, whose rules are determined based on expert knowledge and extensive investigation into the dynamic behaviour of the vehicle in different driving conditions. Figure 6-3 illustrates the 2D fuzzy rule base and the corresponding control surface of the fuzzy ASC using the initial untuned fuzzy membership functions. The linguistic terms that have been used in the rule base table are defined in Table 4-II. Note that these fuzzy rules are formed using fuzzy variables whose membership functions are of unknown shapes, sizes, and relative positions. As a result, the generated corrective steering angle of the fuzzy ASC can only cover up to 75% of the output domain, as is evident from the control surface shown in Figure 6-3.

Control Rule Base		$e(\dot{\psi})$						
		NL	**NM**	**NS**	**ZE**	**PS**	**PM**	**PL**
$\dot{e}(\dot{\psi})$	**NL**	NVL	NVL	NL	NM	NS	ZE	ZE
	NM	NVL	NL	NM	NS	ZE	ZE	PS
	NS	NL	NM	NS	ZE	ZE	PS	PM
	ZE	NL	NM	NS	ZE	PS	PM	PL
	PS	NM	NS	ZE	ZE	PS	PM	PL
	PM	NS	ZE	ZE	PS	PM	PL	PVL
	PL	ZE	ZE	PS	PM	PL	PVL	PVL

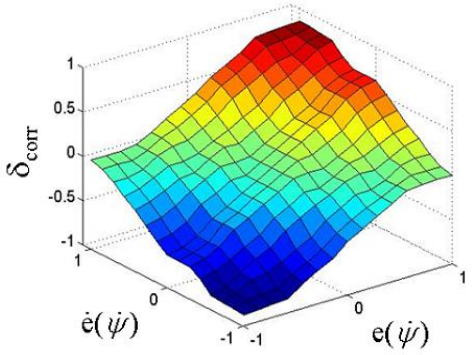

Figure 6-3: Rule base (left) and control surface (right) of the proposed fuzzy active steering controller

6.2 Evaluation of the fuzzy active steering controller

The performance of the fuzzy ASC is evaluated by driving the AUTO21EV through the ISO double-lane-change maneuver using the path-following driver model, whose characteristics are described in Chapter 2. Since the effective range of the fuzzy ASC is limited, the initial speed for this maneuver is chosen to be 60 km/h. Figure 6-4 illustrates the desired and actual vehicle trajectories when driving through the double-lane-change maneuver using the path-following driver model with and without the fuzzy ASC. The driver model is able to negotiate the maneuver even without using the fuzzy ASC.

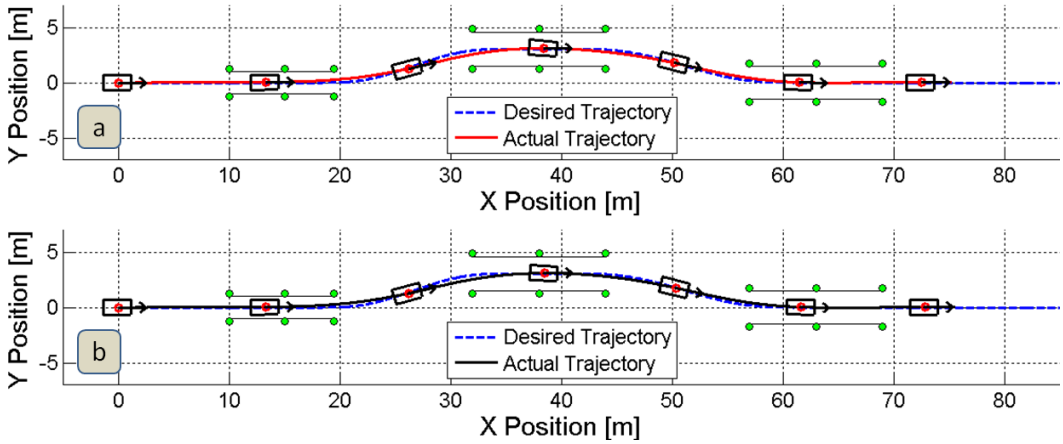

Figure 6-4: Desired and actual vehicle trajectories when driving through the double-lane-change maneuver with an initial speed of 60 km/h (a) using the driver model and (b) using the driver model with the fuzzy ASC

The performance of the fuzzy ASC becomes clear when looking at the vehicle yaw rate and sideslip angle for this maneuver, which are shown in Figure 6-5. Although the fuzzy ASC is not able to control the vehicle such that it performs exactly like the desired reference model, it is able to reduce the magnitudes of both the maximum yaw rate and the maximum sideslip angle of the vehicle. The performance of the fuzzy ASC is confirmed in Figure 6-6, which illustrates the lateral acceleration of the vehicle, the driver's steering wheel input, and the vehicle forward speed as functions of time. The vehicle experiences a lateral acceleration of about 7 m/s^2, which indicates that the vehicle is undergoing a severe maneuver. Looking at Figure 6-6-b, which illustrates the driver's steering wheel input and the equivalent corrective steering wheel input that the fuzzy ASC has added to the driver's steering request, it is clear that the driver requires less steering effort when the fuzzy ASC is active. Note that the generated corrective steering angle is not large enough to eliminate the yaw rate error of the vehicle entirely (Figure 6-

5). A reduction in the final steering angle also means that the vehicle loses less speed when driving through this maneuver (Figure 6-6-c). The handling performance of the vehicle is illustrated in Figure 6-6-d, which clearly indicates that the vehicle handling is improved by the fuzzy ASC, as the hysteresis of the plot has been reduced.

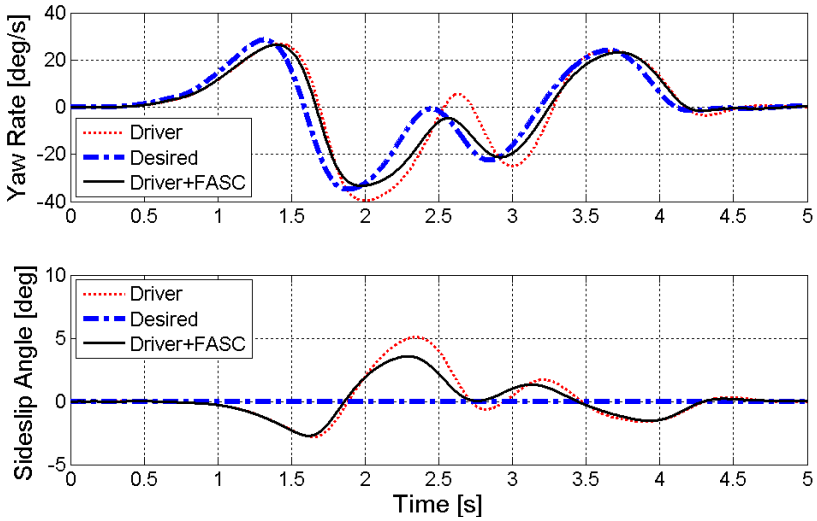

Figure 6-5: Desired and actual vehicle yaw rate (top) and sideslip angle (bottom) when driving through the double-lane-change maneuver using the driver model with and without the fuzzy ASC (FASC)

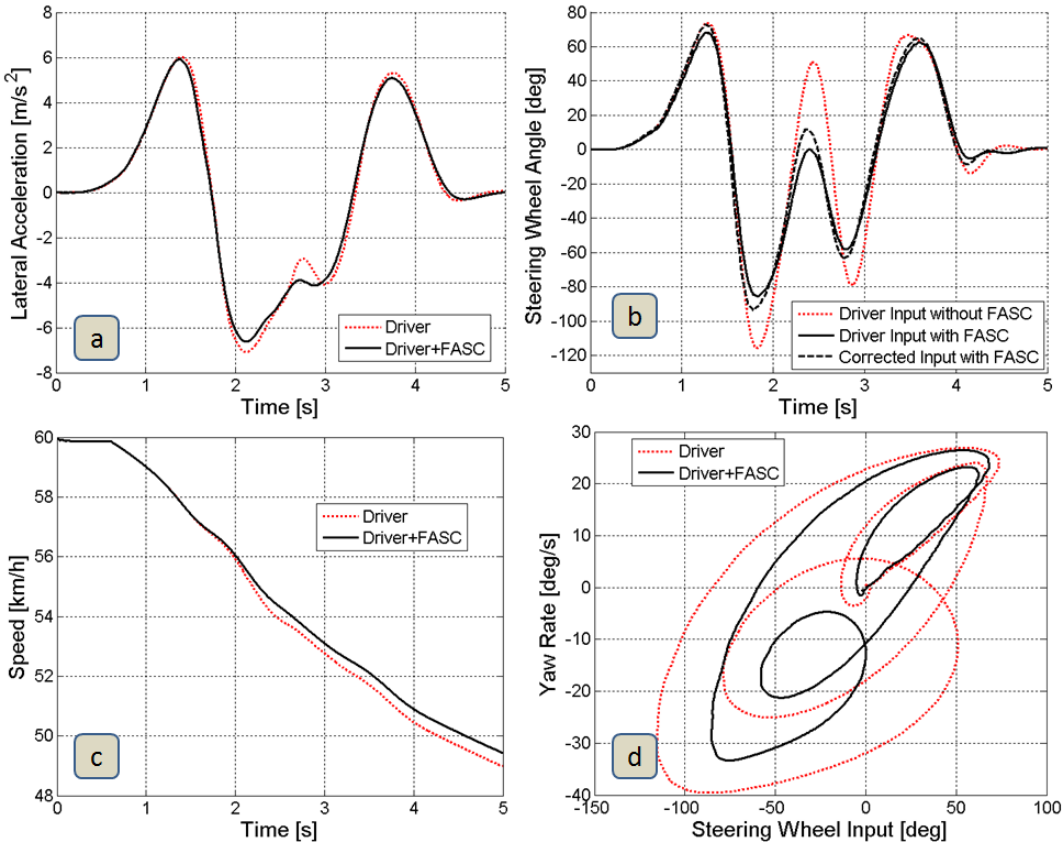

Figure 6-6: (a) Lateral acceleration, (b) steering wheel angle, and (c) vehicle speed as functions of time; and (d) vehicle yaw rate as a function of the steering wheel input when driving through the double-lane-change maneuver with and without the fuzzy ASC (FASC)

6.3 Genetic tuning of the fuzzy active steering controller

As mentioned above, due to the arbitrary shape, size, and distribution of the fuzzy membership functions, the performance of the resulting fuzzy ASC cannot be considered optimal. Since the fuzzy ASC is unable to learn or adapt to its environment on its own, and instead of resorting to the tedious task of tuning the membership functions manually, a multi-criteria genetic algorithm is used to adjust the membership functions and achieve better controller performance. A procedure similar to that used for tuning the membership functions of the input and output variables of the fuzzy YMC, described in Chapter 4, is used for genetically tuning the membership functions of the fuzzy ASC. The ISO double-lane-change maneuver with obstacle avoidance is used to evaluate the effectiveness of each candidate controller in the genetic algorithm. Once again, due to the fact that the membership functions of the fuzzy ASC must be tuned in a general sense, not based on a specific driver or driver model, the double-lane-change maneuver is treated as an open-loop test, in which a predefined fixed steering input is used to drive the AUTO21EV through the maneuver. Details about the fixed steering input can be found in Chapter 4. Using this fixed steering input, any deviations from the desired vehicle trajectory, yaw rate, and sideslip angle are considered to be stability errors that the fuzzy ASC should correct. The goal of the multi-criteria genetic algorithm is to identify the ideal shape, size, and distribution of the membership functions so as to minimize the vehicle trajectory, yaw rate, and sideslip angle errors.

The scaling function technique is chosen for the genetic tuning of the fuzzy membership functions. Since the input and output variables of the fuzzy ASC are initially described using a set of normalized membership functions that are distributed symmetrically around the origin (Figure 6-2), three nonlinear scaling functions, similar to that described in equation (4.12) of Chapter 4, are again used to tune the membership functions of the input and output variables. Since each of these nonlinear scaling functions uses only one parameter to affect the overall distribution and shape of the membership functions, only three scaling parameters are required, which are concatenated to form a chromosome for the genetic tuning process. This method of tuning also guarantees that the adjacency constraint is satisfied, which ensures that the sum of all membership functions is equal to unity for every point in the domain, the final

tuned membership functions are distributed symmetrically around the origin, and the genetic search examines a wide range of fuzzy partitions.

The objective of the multi-criteria genetic algorithm is to tune the input and output variables of the fuzzy ASC such that the mean square errors (MSE) of the vehicle trajectory, yaw rate, and sideslip angle are minimized when driving through the double-lane-change maneuver. These mean square errors are calculated as follows:

$$MSE_{Trajectory} = \frac{1}{N}\sum_{k=1}^{N}\left[y_{desired}(x_k) - y_{actual}(x_k)\right]^2 \tag{6.2}$$

$$MSE_{Yaw\ Rate} = \frac{1}{N}\sum_{k=1}^{N}\left[\dot{\psi}_{desired}(k) - \dot{\psi}_{actual}(k)\right]^2 \tag{6.3}$$

$$MSE_{Sideslip} = \frac{1}{N}\sum_{k=1}^{N}\left[\beta_{desired}(k) - \beta_{actual}(k)\right]^2 \tag{6.4}$$

where N is the number of sample points, $y_{desired}(x_k)$ and $y_{actual}(x_k)$ are the desired and actual lateral positions of the vehicle for a given forward position x_k, $\dot{\psi}_{desired}(k)$ and $\dot{\psi}_{actual}(k)$ are the desired and actual vehicle yaw rates, and $\beta_{desired}(k)$ and $\beta_{actual}(k)$ are the desired and actual vehicle sideslip angles at a given time step k, respectively. Since the objective of the multi-criteria genetic algorithm is to minimize these three errors, the fitness function associated with each chromosome is defined as the weighted sum of the inverses of the resulting vehicle trajectory, yaw rate, and sideslip angle mean square errors as follows:

$$\text{Fitness Function} = \frac{w_1}{MSE_{Trajectory}} + \frac{w_2}{MSE_{Yaw\ Rate}} + \frac{w_3}{MSE_{Sideslip}} \tag{6.5}$$

where w_1, w_2, and w_3 are the weighting factors. The genetic algorithm was run for 50 generations, each of which had a population size of 200 chromosomes, a crossover rate of 95%, and a mutation rate of 15%. In addition, an elite selection rate of 2% was employed to ensure that the fittest chromosomes were retained unaltered from one generation to the next. Using the elite selection technique justifies the relatively high mutation rate, which facilitates the thorough exploration of the search space without losing the fittest members of each generation. Convergence is assumed if the fittest chromosome in a given generation survives for 10 consecutive generations, or after 50 generations have elapsed.

Figure 6-7 illustrates the maximum fitness function value for each generation, and the convergence of the final results.

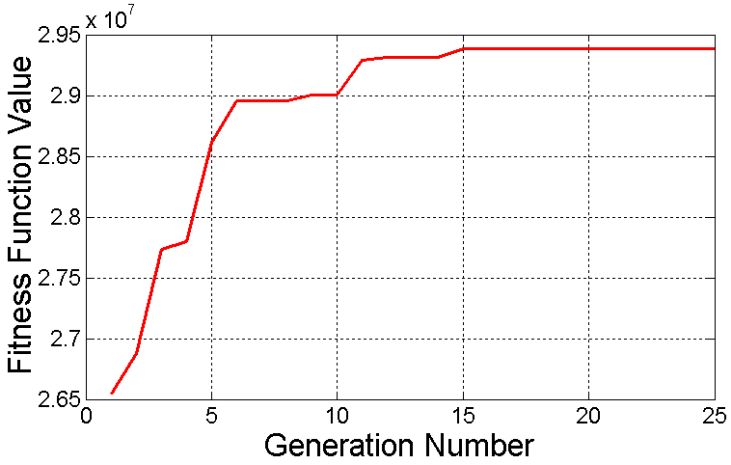

Figure 6-7: Maximum fitness function value for each generation of the multi-criteria genetic algorithm

Comparing Figure 6-8, which illustrates the control surface of the tuned fuzzy ASC, with Figure 6-3, it is clear that the scaling functions have adjusted the membership functions of the output variable of the fuzzy controller such that the control surface reaches the limits of the output domain, thereby covering the entire control space. Figure 6-9 illustrates the resulting tuned membership functions for the input and output variables of the genetic fuzzy ASC. As can be seen, the scaling functions have adjusted the shape, size, and distribution of the membership functions of the fuzzy ASC considerably (see Figure 6-2). The new distribution of the membership functions associated with the yaw rate error indicates that the controller does not tolerate small yaw rate errors. The tuning process has had the opposite effect on the membership functions for the rate of change of the yaw rate error, essentially reducing the relative severity of having small errors associated with this performance metric.

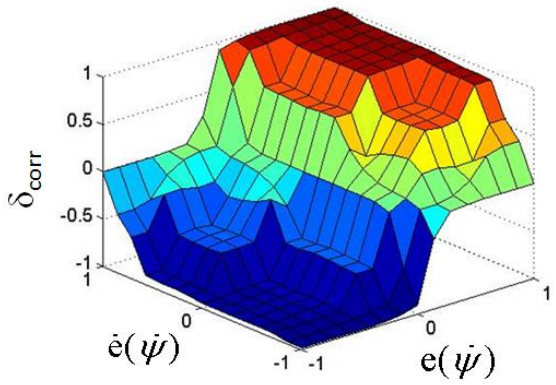

Figure 6-8: Control surface of the genetically-tuned fuzzy ASC

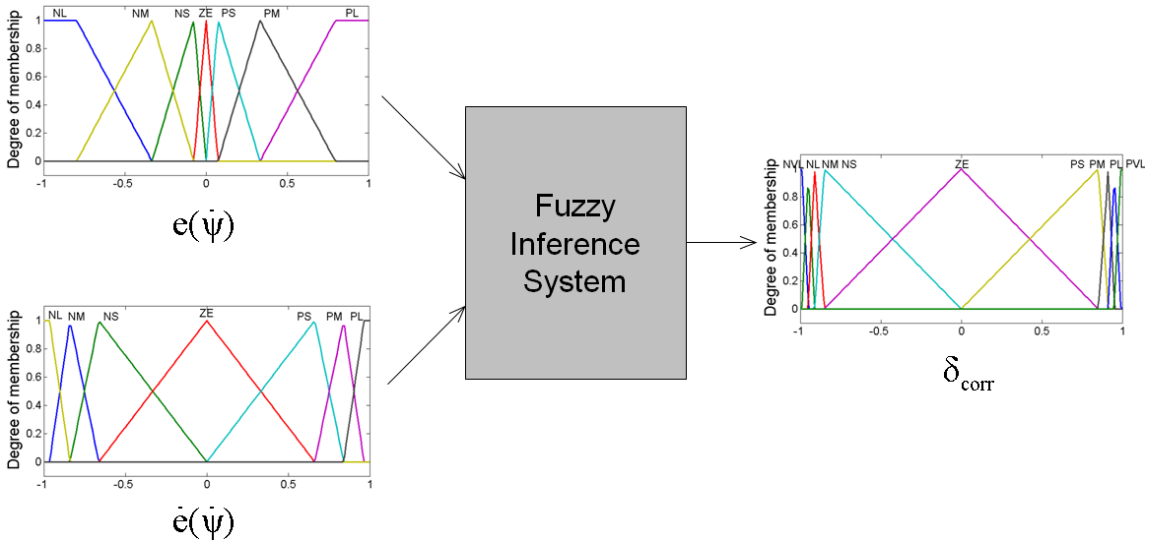

Figure 6-9: Shape and distribution of the genetically-tuned membership functions for the input and output variables of the fuzzy ASC

6.4 Evaluation of the genetic fuzzy active steering controller

In order to evaluate the performance of the genetic fuzzy ASC, the AUTO21EV is driven through a series of test maneuvers, which are described in Chapter 2.

6.4.1 ISO double-lane-change maneuver

The performance of the genetic fuzzy ASC is first compared to that of the untuned fuzzy ASC as the vehicle is driven through the double-lane-change maneuver with an initial speed of 60 km/h using the path-following driver model. Figure 6-10 illustrates the vehicle trajectory and demonstrates that the driver model is able to negotiate the maneuver when the genetic fuzzy ASC is active. Figure 6-11 illustrates the vehicle yaw rate and sideslip angle for this maneuver. Comparing this figure with Figure 6-5, it is clear that the genetically-tuned fuzzy ASC is better able to control the vehicle yaw rate such that it tracks that of the reference bicycle model. The sideslip angle of the vehicle is also less than it was prior to the tuning process.

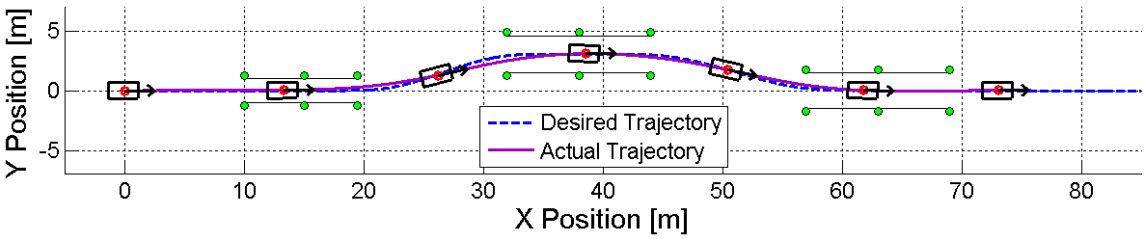

Figure 6-10: Desired and actual vehicle trajectories when driving through the double-lane-change maneuver with an initial speed of 60 km/h using the driver model and the genetic fuzzy ASC

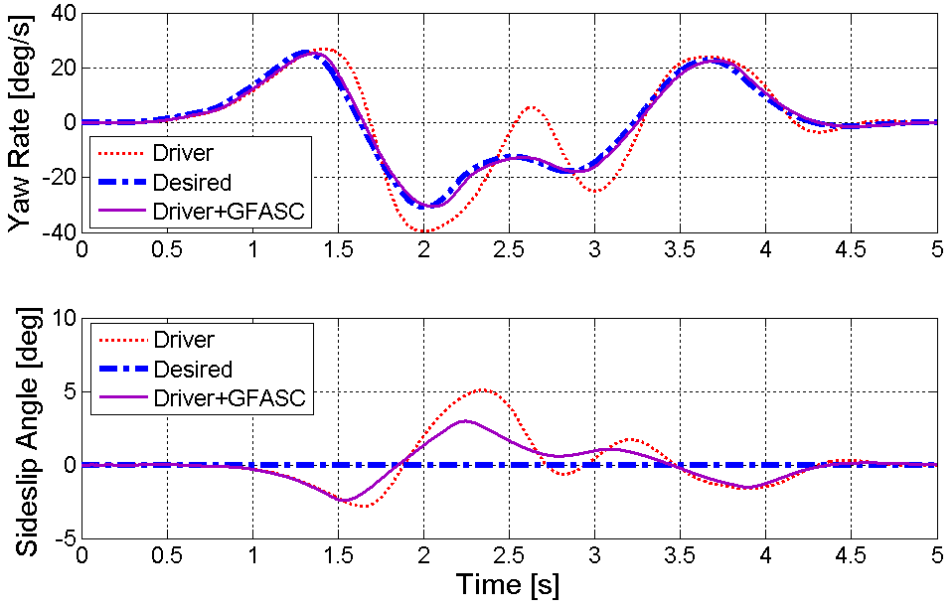

Figure 6-11: Desired and actual vehicle yaw rate (top) and sideslip angle (bottom) when driving through the double-lane-change maneuver with an initial speed of 60 km/h using the driver model, with and without the genetic fuzzy ASC (GFASC)

Figure 6-12 illustrates the lateral acceleration of the vehicle, the driver's steering input, and the vehicle forward speed as functions of time. As can be seen, the vehicle experiences less lateral acceleration than it did when either no stability controller or the fuzzy ASC was active. This result can be attributed to the fact that the vehicle is more stable when the genetic fuzzy ASC is active, so less steering effort is required to negotiate the maneuver. Comparing the steering wheel angles applied by the driver, as shown in Figure 6-12-b, it is clear that the driver requires the least steering effort when the genetic fuzzy ASC is active. In addition, note that the generated corrective steering angle is much larger than that observed when using the untuned fuzzy ASC. As a result of using less total steering angle, the vehicle loses even less speed with the genetic fuzzy ASC than it did with the untuned controller. Figure 6-12-d illustrates the handling performance of the vehicle, and clearly indicates that the vehicle handling and agility have been significantly improved by the genetic fuzzy ASC. The hysteresis of the performance plot is the least when the genetic fuzzy ASC is active, which characterizes a vehicle with superior responsiveness.

Since the genetic fuzzy ASC demonstrates better performance in all aforementioned aspects when compared to the untuned fuzzy ASC, only the genetic fuzzy ASC will be considered in the reminder of the evaluation process. Moreover, since the performance of the genetic fuzzy ASC must be compared to that of the other stability

controllers (namely, the genetic fuzzy YMC and the advanced torque vectoring controller) using the same test maneuvers, the double-lane-change maneuver is repeated using an initial speed of 75 km/h.

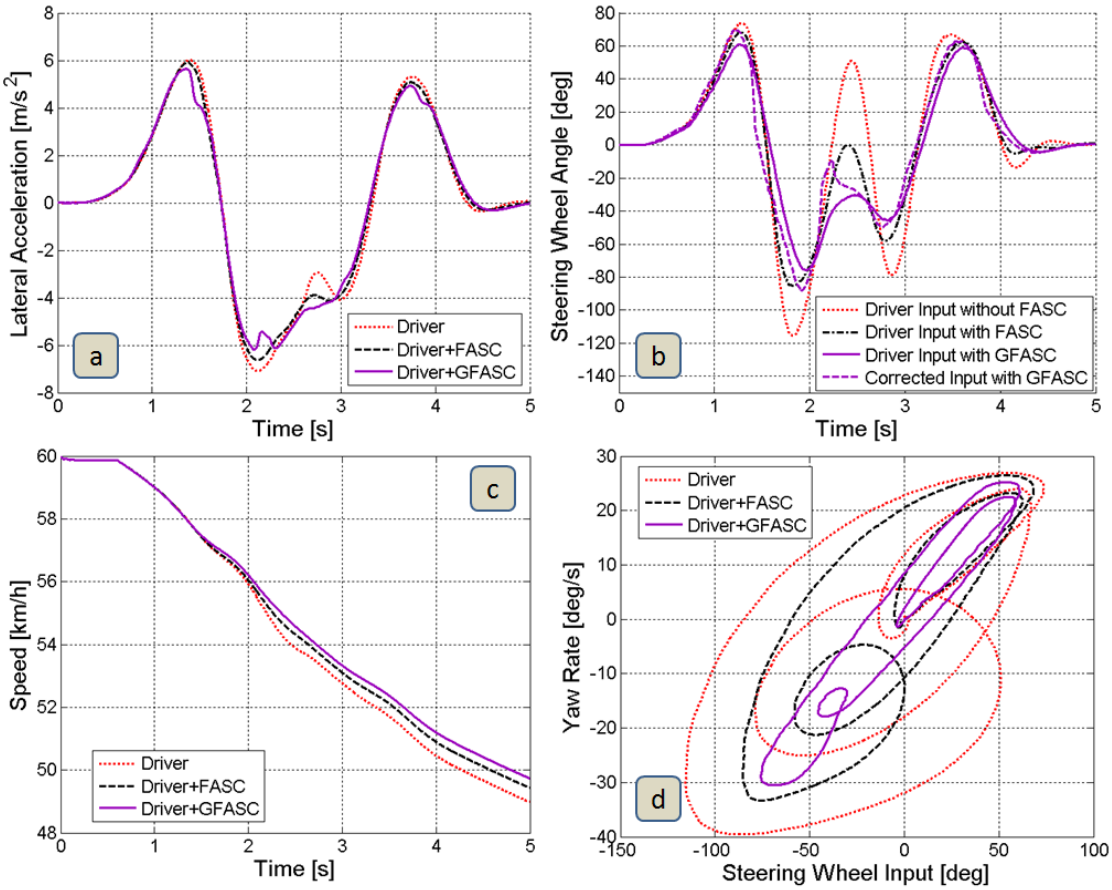

Figure 6-12: (a) Lateral acceleration, (b) steering wheel angle, and (c) vehicle speed as functions of time; and (d) vehicle yaw rate as a function of the steering wheel input when driving through the double-lane-change maneuver with an initial speed of 60 km/h without a controller, with the fuzzy ASC (FASC), and with the genetic fuzzy ASC (GFASC)

Figure 6-13 illustrates the vehicle trajectory when driving through the double-lane-change maneuver with an initial speed of 75 km/h when using the genetic fuzzy ASC. As can be seen, at higher speeds, the genetic fuzzy ASC is not powerful enough to help the driver negotiate the maneuver without hitting the cones. This performance is confirmed by looking at the vehicle yaw rate and sideslip angle shown in Figure 6-14. Due to the actuator range limit of the active steering system, the genetic fuzzy ASC is not able to control the behaviour of the vehicle such that it performs like the desired reference bicycle model when driving through this maneuver. Nevertheless, the genetic fuzzy ASC is able to reduce the maximum vehicle yaw rate and sideslip angle by more than half when compared to the case when no stability controller is active.

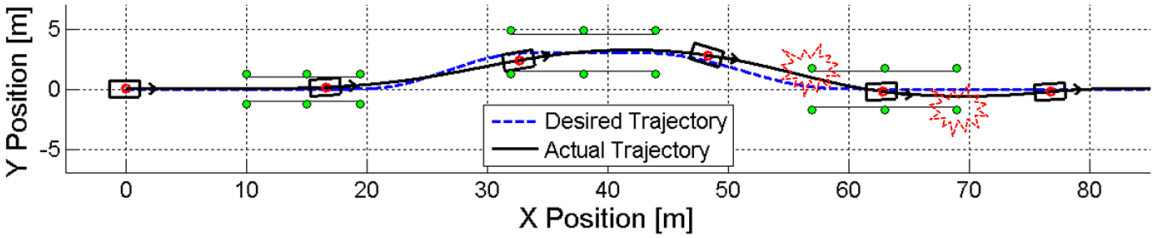

Figure 6-13: Desired and actual vehicle trajectories when driving through the double-lane-change maneuver with an initial speed of 75 km/h using the driver model and the genetic fuzzy ASC

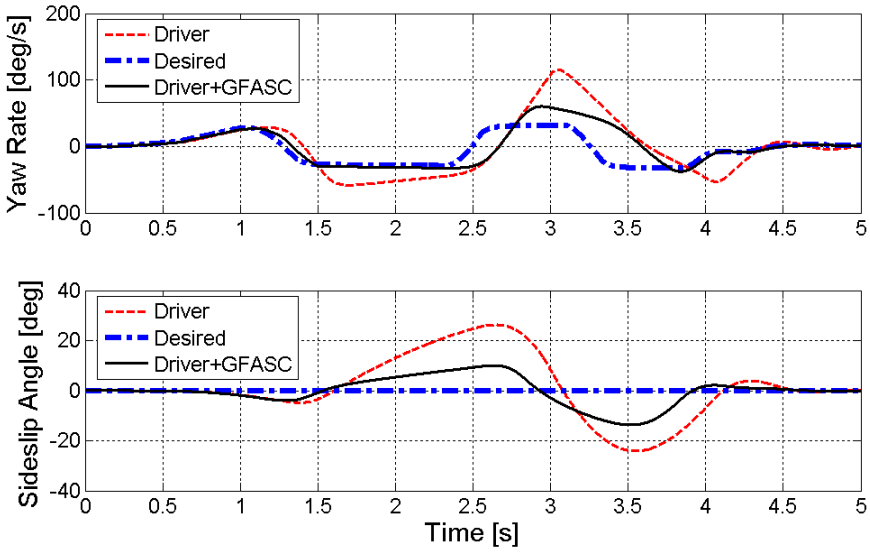

Figure 6-14: Desired and actual vehicle yaw rate (top) and sideslip angle (bottom) when driving through the double-lane-change maneuver with an initial speed of 75 km/h using the driver model, with and without the genetic fuzzy ASC (GFASC)

Figure 6-15 illustrates the lateral acceleration of the vehicle, the driver's steering input, and the vehicle forward speed as functions of time. As can be seen, the maximum lateral acceleration that the vehicle experiences is about 8.4 m/s^2, which indicates the severity of this maneuver. Comparing the required steering wheel angles shown in Figure 6-15-b, it is clear that the driver requires more steering effort when the genetic fuzzy ASC is used than when either the genetic fuzzy YMC or the ATVC is used. Although the fuzzy ASC augmentes the driver's steering input, its intervention is not sufficient to eliminate the vehicle yaw rate and sideslip errors completely and, thus, is unable to fully stabilize the vehicle. Since the driver requires more steering effort when the genetic fuzzy ASC is active than when the other stability controllers are active, the vehicle loses more speed in this case (Figure 6-15-c). The handling performance curve of the vehicle, illustrated in Figure 6-15-d, clearly indicates that the genetic fuzzy ASC is not as effective at improving the vehicle handling and agility as are the other stability controllers.

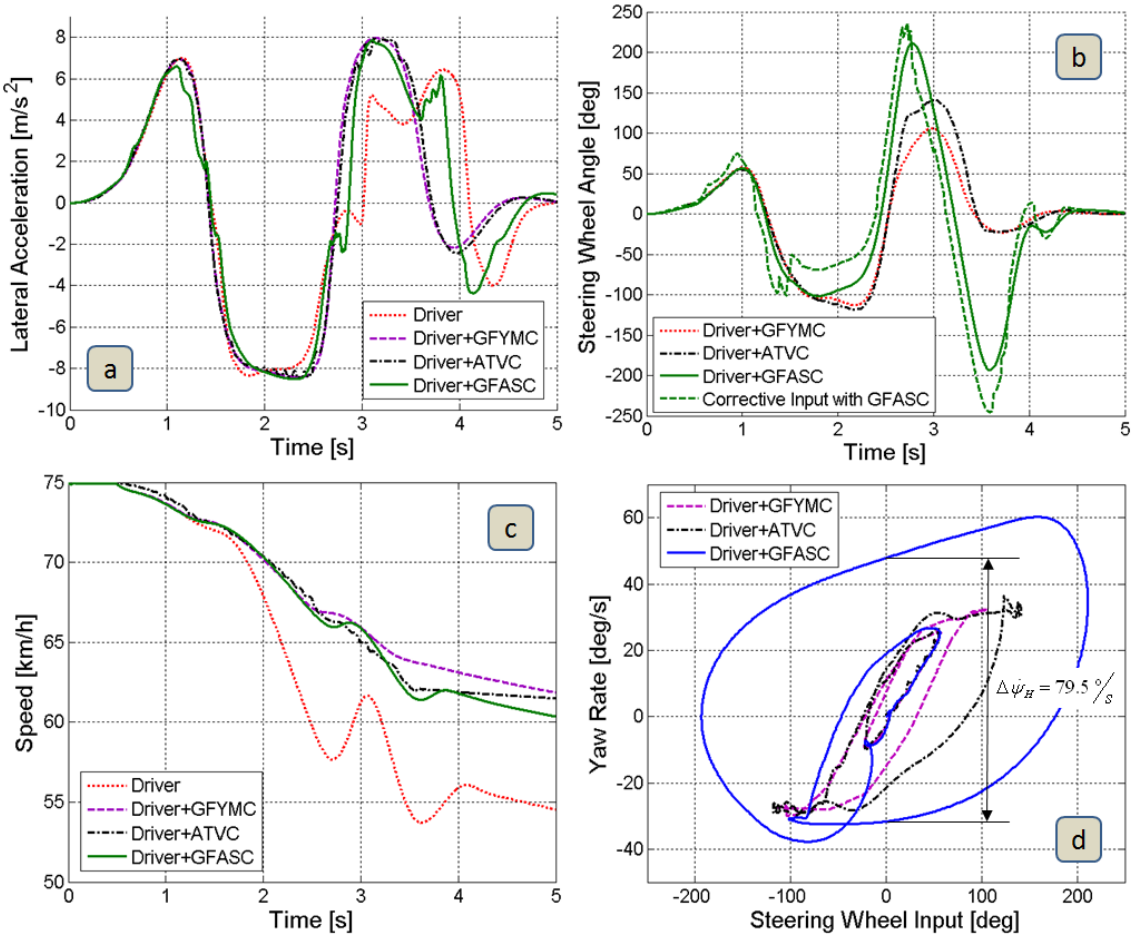

Figure 6-15: (a) Lateral acceleration, (b) steering wheel angle, and (c) vehicle speed as functions of time; and (d) vehicle yaw rate as a function of the steering wheel input when driving through the double-lane-change maneuver with an initial speed of 75 km/h without a controller, with the genetic fuzzy YMC (GFYMC), with the ATVC, and with the genetic fuzzy ASC (GFASC)

Table 6-II summarizes the vehicle response during the double-lane-change maneuver when the driver model is used with the genetic fuzzy ASC, and compares it to the performance observed when the driver model is used with no stability controller, with the genetic fuzzy YMC, and with the ATVC. Comparing different parameters of the vehicle response during this maneuver, it can be seen that the genetic fuzzy ASC has improved all the decisive parameters that describe the handling, stability, and longitudinal dynamics of the vehicle when compared to the case in which no stability controller is active; however, it is not as effective as the genetic fuzzy YMC or the ATVC. With respect to the handling characteristic of the vehicle, $|\beta|_{\max}$, $|\dot{\psi}|_{\max}$, and $|\delta_{SW}|_{\max}$ are about twice as large when the genetic fuzzy ASC is active than they are when the genetic fuzzy YMC is active. In addition, the hysteresis of the performance plot ($\Delta\dot{\psi}_H$) is about four times larger than that observed when the genetic fuzzy YMC is active. Note that the

driver was not able to negotiate the maneuver at a high speed without hitting the cones. Therefore, the genetic fuzzy ASC is considered to be a controller that can improve the handling characteristics of the vehicle to some extent, but it is not considered to be as effective as the genetic fuzzy YMC or the ATVC. The genetic fuzzy ASC is considered to be an effective stability controller because it has reduced $|\beta|_{\max}$ and $|\dot{\psi}|_{\max}$ by more than half when compared to the case where no stability controller is used. The genetic fuzzy ASC is also considered to be an effective controller for improving the longitudinal dynamics of the vehicle.

Parameter	$\|\beta\|_{\max}$	$\|\dot{\psi}\|_{\max}$	$\|a_y\|_{\max}$	$\|\delta_{SW}\|_{\max}$	$\Delta\dot{\psi}_H$	v_{lost}
AUTO21EV	26.3^o	115.4^o/s	8.2m/s^2	545^o	163.8^o/s	20.5m/s
GFYMC	6.2^o	31.2^o/s	8.4m/s^2	108^o	21^o/s	13.2m/s
ATVC	6.1^o	36.4^o/s	8.4m/s^2	140^o	35.5^o/s	13.5m/s
GFASC	13.6^o	60.1^o/s	8.4m/s^2	211^o	79.5^o/s	14.6m/s

Table 6-II: Vehicle response during the double-lane-change maneuver using the driver model without a controller, with the genetic fuzzy YMC (GFYMC), with the ATVC, and with the genetic fuzzy ASC (GFASC)

6.4.2 Step-steer response maneuver

In order to evaluate the performance of the vehicle using the genetic fuzzy ASC in a step-steer response maneuver, the vehicle yaw rate, sideslip angle, and lateral acceleration as functions of time are observed. Figure 6-16-a illustrates the fixed step-steer input and the equivalent corrective steering input generated by the genetic fuzzy ASC. As can be seen, the genetic fuzzy ASC has applied a large steering correction at the beginning of the step-steer input in order to match the behaviour of the vehicle to that of the desired bicycle model. Due to the augmented steering input, the vehicle experiences a lateral acceleration of 4.3 m/s^2, which is larger than that obtained when using the other stability control systems and when no stability controller is active (Figure 6-16-b). The rise time of the lateral acceleration response is about 0.53 seconds when the genetic fuzzy ASC is active, which indicates an improvement in the responsiveness of the vehicle when compared to the case where no stability controller is active. Figure 6-17 illustrates the vehicle yaw rate and sideslip angle when the genetic fuzzy ASC is active, and compares the response to that obtained when no stability controller is active, when the genetic fuzzy YMC is active, and when the ATVC is used. As can be seen, the vehicle experiences the largest

sideslip angle when the genetic fuzzy ASC is active, which is due to the fact that the genetic fuzzy ASC applies a larger steering angle than is applied in the other cases.

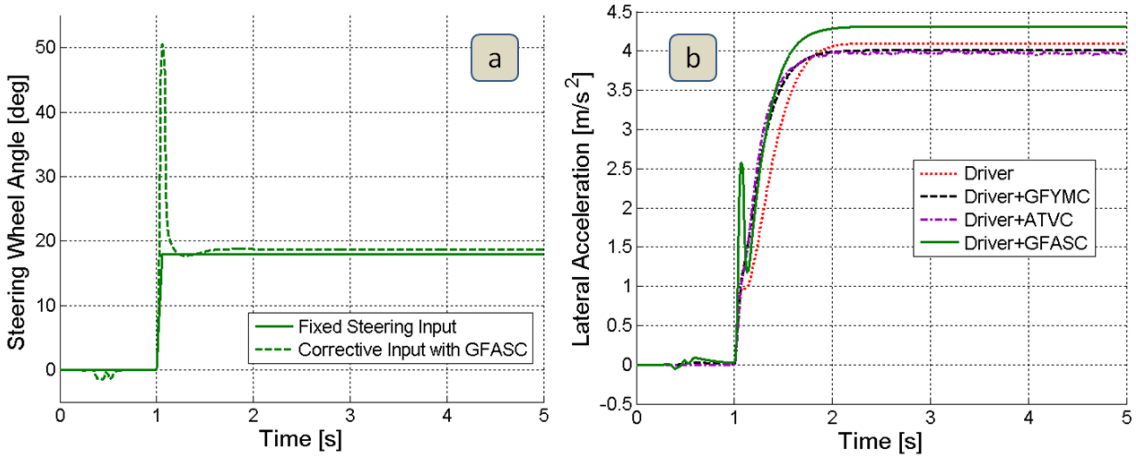

Figure 6-16: (a) Required steering wheel input and (b) lateral acceleration of the vehicle when driving through the step-steer maneuver using the genetic fuzzy ASC (GFASC)

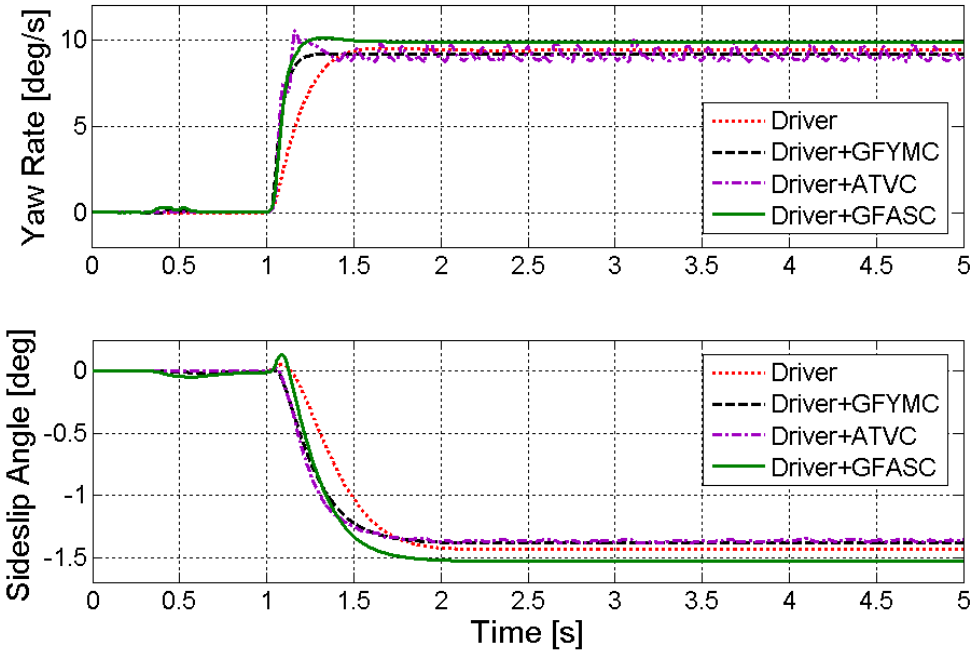

Figure 6-17: Yaw rate (top) and sideslip angle (bottom) of the vehicle when driving through the step-steer maneuver using the genetic fuzzy ASC (GFASC)

Table 6-III summarizes the vehicle response during the step-steer test maneuver. Comparing different parameters of the vehicle response during this maneuver when it is performed with and without the genetic fuzzy ASC, this controller can be considered very effective at improving all the decisive parameters of the vehicle that describe its handling characteristics.

Parameter	$t_{\dot{\psi}}$	$\mathrm{PO}=\frac{\dot{\psi}_{\max}-\dot{\psi}_{ss}}{\dot{\psi}_{ss}}\times 100\%$	$\lvert\beta\rvert_{\max}$	t_{a_y}
AUTO21EV	0.34s	1.30%	1.43^{o}	0.66s
GFYMC	0.15s	0.00%	1.38^{o}	0.51s
ATVC	0.15s	16.1%	1.36^{o}	0.47s
GFASC	0.15s	2.20%	1.53^{o}	0.53s

Table 6-III: Vehicle response during the step-steer maneuver using the driver model without a controller, with the genetic fuzzy YMC (GFYMC), with the ATVC, and with the genetic fuzzy ASC (GFASC)

6.4.3 Brake-in-turn maneuver

Figure 6-18 illustrates the vehicle trajectory relative to the desired circular path during a brake-in-turn maneuver using the driver model with and without the genetic fuzzy ASC. As can be seen, the driver model is not able to control the vehicle during this maneuver when no stability controller is active. However, the driver model is able to keep the vehicle on the predefined circular path while severely braking when the genetic fuzzy ASC is active, and the lateral deviation of the vehicle from the desired path remains negligible throughout the maneuver.

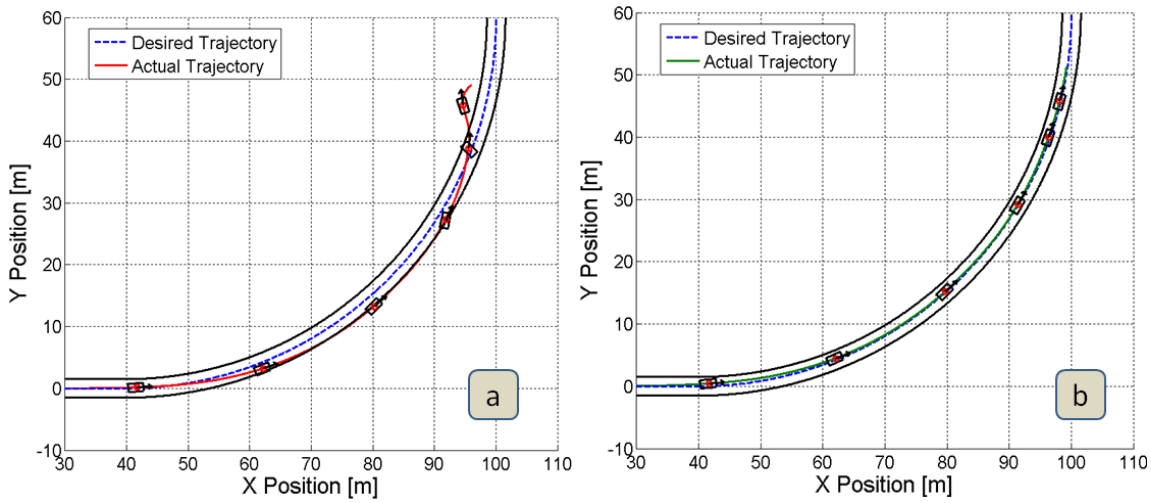

Figure 6-18: Desired and actual vehicle trajectories when braking in a turn using (a) the driver model only and (b) the driver model with the genetic fuzzy ASC

Figure 6-19-a illustrates the driver's steering wheel input as a function of time, and indicates that the driver model is able to control the vehicle very smoothly and with little steering effort when the genetic fuzzy ASC is active. This figure also shows the activity of the active steering controller as it augments the driver's steering wheel input at each time step. Figure 6-19-b illustrates the lateral acceleration of the vehicle and

confirms that the vehicle remains stable when the genetic fuzzy ASC is active. Note that, for clarity, the driver's steering input and the lateral acceleration of the vehicle when no stability controller is active have not been illustrated in Figure 6-19.

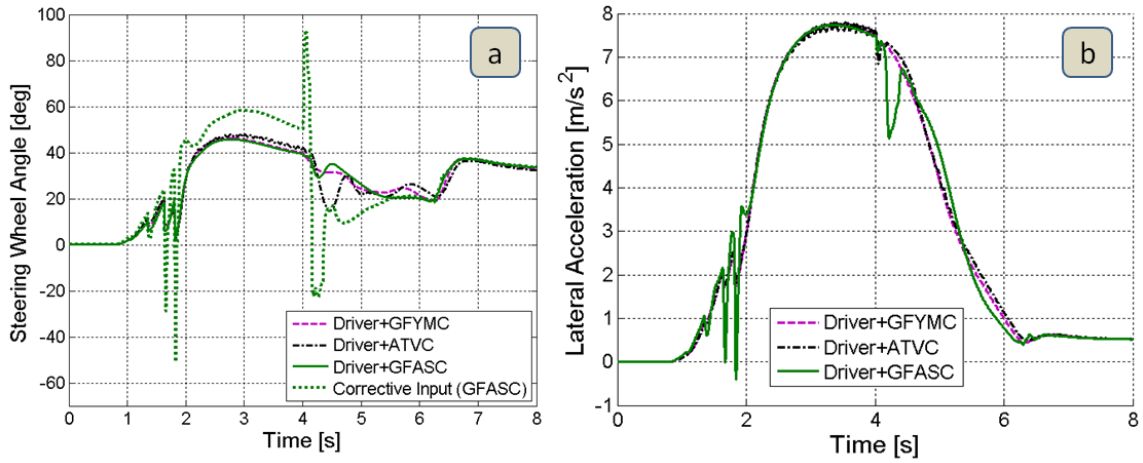

Figure 6-19: (a) Required steering wheel input and (b) lateral acceleration of the vehicle when braking in a turn using the driver model with the genetic fuzzy YMC (GFYMC), with the ATVC, and with the genetic fuzzy ASC (GFASC)

Figure 6-20 compares the vehicle yaw rate and sideslip angle when driving through the brake-in-turn maneuver using the driver model with the genetic fuzzy YMC, with the ATVC, and with the genetic fuzzy ASC. Again, for clarity, the yaw rate and sideslip angle of the vehicle when no stability controller is active are not illustrated. When the genetic fuzzy ASC is active, the vehicle behaves almost like the desired reference model until the braking begins. After the start of braking, the genetic fuzzy ASC attempts to minimize the yaw rate error by augmenting the driver's steering input (Figure 6-19-a). As can be seen in Figure 6-20, the genetic fuzzy ASC is more effective at minimizing the yaw rate error of the vehicle than the ATVC, and it does not cause the severe oscillations that the ATVC causes. Figure 6-20 also confirms that the genetic fuzzy ASC is able to stabilize the vehicle when braking in a turn, since the yaw rate and sideslip angle both approach zero as the vehicle progresses toward larger deceleration rates. Figure 6-21-a illustrates the vehicle speed as a function of time and confirms the performance of the speed controller. Figure 6-21-b illustrates the vehicle longitudinal acceleration as a function of vehicle speed, and confirms the severity of the braking action in this maneuver.

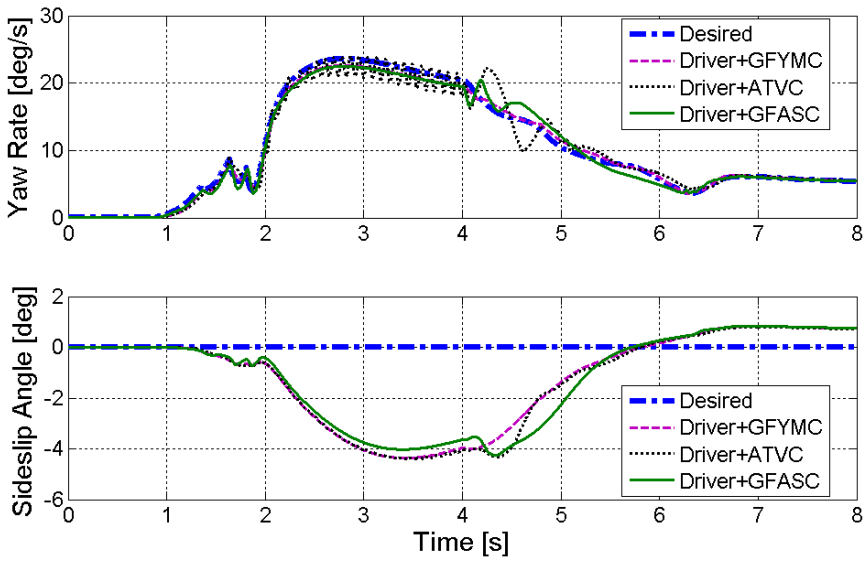

Figure 6-20: Desired and actual vehicle yaw rate (top) and sideslip angle (bottom) when braking in a turn using the driver model with the genetic fuzzy YMC (GFYMC), with the ATVC, and with the genetic fuzzy ASC (GFASC)

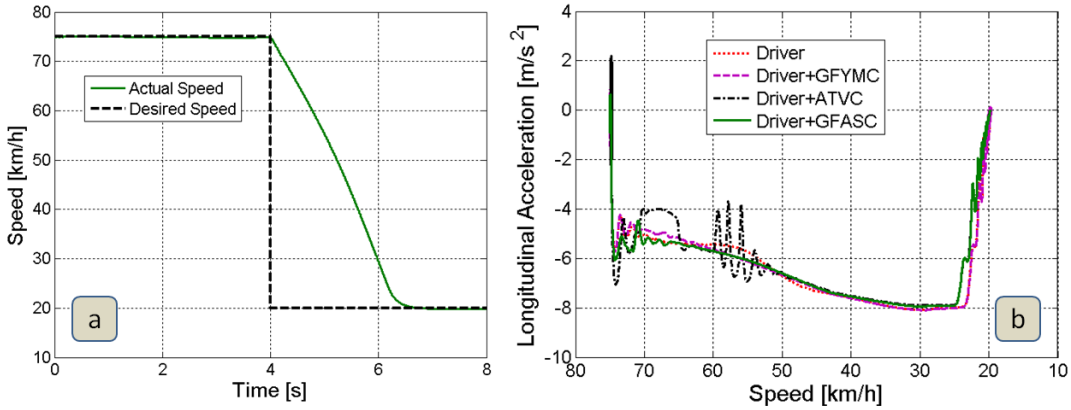

Figure 6-21: (a) Vehicle speed as a function of time when braking in a turn using the driver model with the genetic fuzzy ASC, and (b) longitudinal acceleration as a function of vehicle speed when braking in a turn using the driver model without a controller, with the genetic fuzzy YMC (GFYMC), with the ATVC, and with the genetic fuzzy ASC (GFASC)

Table 6-IV summarizes the vehicle response during the brake-in-turn maneuver when the genetic fuzzy ASC is active, and compares it with the performance observed when no stability controller is used, when the genetic fuzzy YMC is used, and when the ATVC is used. Comparing different parameters of the vehicle response during this maneuver, it can be seen that the genetic fuzzy ASC is very effective at improving all the decisive parameters that describe the handling, stability, and path-following capabilities of the vehicle. The genetic fuzzy ASC is able to reduce $|\beta|_{\max}$, $|\dot{\psi}|_{\max}$, and $|\delta_{SW}|_{\max}$ significantly, which indicates that this controller is very effective at enhancing the vehicle handling during this maneuver. Simultaneously, a reduction of $|\beta|_{\max}$ and $|\dot{\psi}|_{\max}$ by the

genetic fuzzy ASC indicates that it is also very effective at improving the vehicle stability. Finally, the fact that the maximum lateral deviation of the vehicle from the desired path remains very small throughout the maneuver confirms that the genetic fuzzy ASC enhances the path-following capability of the vehicle as well.

Parameter	$\lvert\dot{\psi}\rvert_{max}$	$\lvert\beta\rvert_{max}$	Δy_{max}	$\lvert\delta_{SW}\rvert_{max}$
AUTO21EV	126.5^o/s	50.1^o	3.67m	700^o
GFYMC	22.60^o/s	4.36^o	0.18m	46.4^o
ATVC	24.00^o/s	4.40^o	0.18m	48.0^o
GFASC	22.45^o/s	4.25^o	0.16m	45.7^o

Table 6-IV: Vehicle response during the brake-in-turn maneuver using the driver model without a controller, with the genetic fuzzy YMC (GFYMC), with the ATVC, and with the genetic fuzzy ASC (GFASC)

6.4.4 Straight-line braking on a μ-split road

As the final test, the AUTO21EV is driven on a μ-split road and the driver model attempts to stop the vehicle in an emergency braking situation. Figure 6-22 illustrates the vehicle trajectory for this maneuver when no stability controller is active and compares it to the case when the genetic fuzzy ASC is active. As can be seen, the genetic fuzzy ASC is able to correct the side-pushing effect of the vehicle while braking on a μ-split road, and prevents the vehicle from leaving the predefined road. The braking distance of the vehicle is about 45.7 meters. Looking at Figure 6-23, it is clear that the genetic fuzzy ASC is able to limit and, later, diminish the yaw rate and sideslip angle of the vehicle while driving over the black ice patch, which indicates that the vehicle remains stable during this maneuver. Note that, for clarity, the yaw rate and sideslip angle of the vehicle observed when no controller is active are not illustrated here.

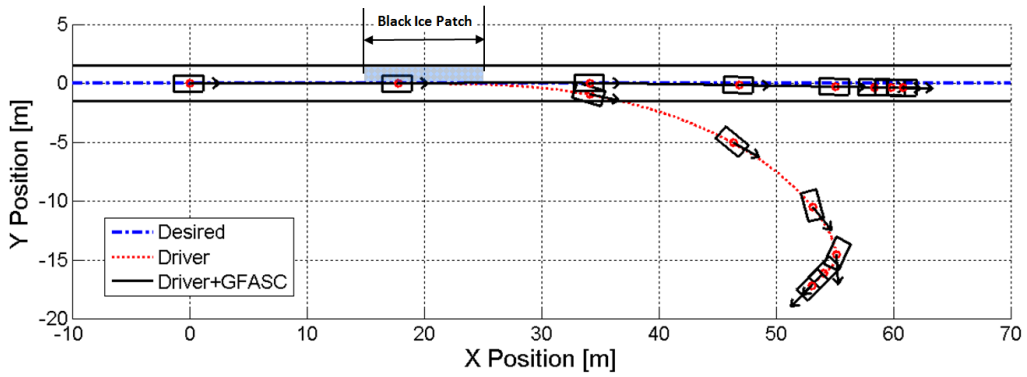

Figure 6-22: Desired and actual vehicle trajectories when braking on a μ-split road while holding the steering wheel fixed, with and without the genetic fuzzy ASC (GFASC)

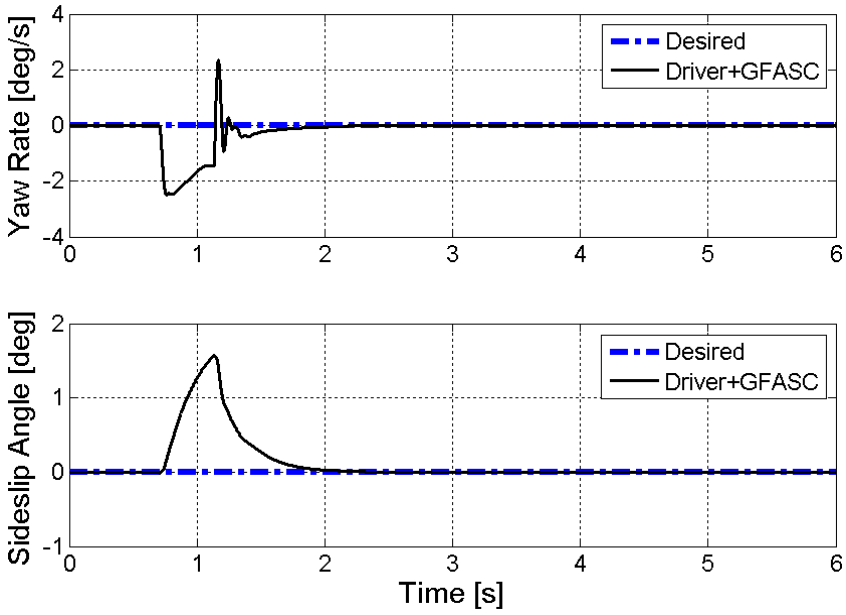

Figure 6-23: Desired and actual vehicle yaw rate (top) and sideslip angle (bottom) when braking on a μ-split road while holding the steering wheel fixed and using the genetic fuzzy ASC (GFASC)

Figure 6-24 illustrates the fixed steering wheel input and the equivalent corrective steering wheel angle that is generated by the genetic fuzzy ASC to counteract the side-pushing effect of the vehicle. As can be seen, the active steering controller has applied up to 54^{o} of equivalent steering wheel angle in order to correct the side-pushing effect of the vehicle. Figure 6-25 illustrates the tire slip ratios while braking on the μ-split road, and indicates that the slip controllers on the left wheels have limited the motor torques between 0.7 and 1.15 seconds of the simulation in order to prevent tire lock-up while ensuring the maximum possible braking force is applied when braking on the black ice patch. Later in the simulation, due to the weight shift to the front axle, the slip controllers on the rear axle have limited the motor torques to prevent tire lock-up at higher deceleration rates. The activation of the slip controllers is confirmed in Figure 6-26, which illustrates the motor torques for all four wheels.

Table 6-V summarizes the vehicle response during the straight-line braking on a μ-split road maneuver when holding the steering wheel fixed and using the genetic fuzzy ASC. Comparing different parameters of the vehicle response during this maneuver, it can be seen that the genetic fuzzy ASC is very effective at improving all the decisive parameters that describe the stability, path-following capability, and braking performance of the vehicle. In particular, the genetic fuzzy ASC has reduced the $|\beta|_{\max}$ and $|\dot{\psi}|_{\max}$ values significantly, which indicates an enhancement in the stability of the vehicle.

Moreover, the braking distance of the vehicle has been reduced considerably by the genetic fuzzy ASC, indicating an improvement in the longitudinal dynamics of the vehicle. The genetic fuzzy ASC also reduces the maximum lateral deviation of the vehicle such that the vehicle remains on the predefined road throughout the maneuver.

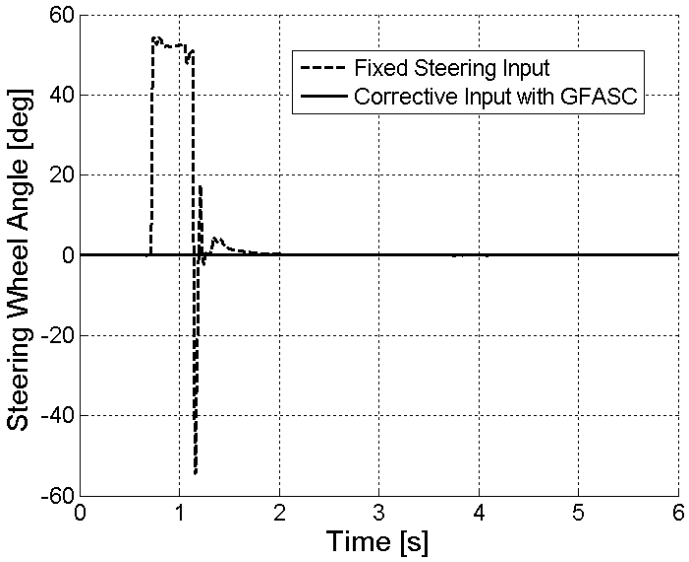

Figure 6-24: Equivalent corrective steering wheel input applied by the genetic fuzzy ASC (GFASC), augmenting the fixed steering input of the driver in order to correct the side-pushing effect of the vehicle when braking on a μ-split road

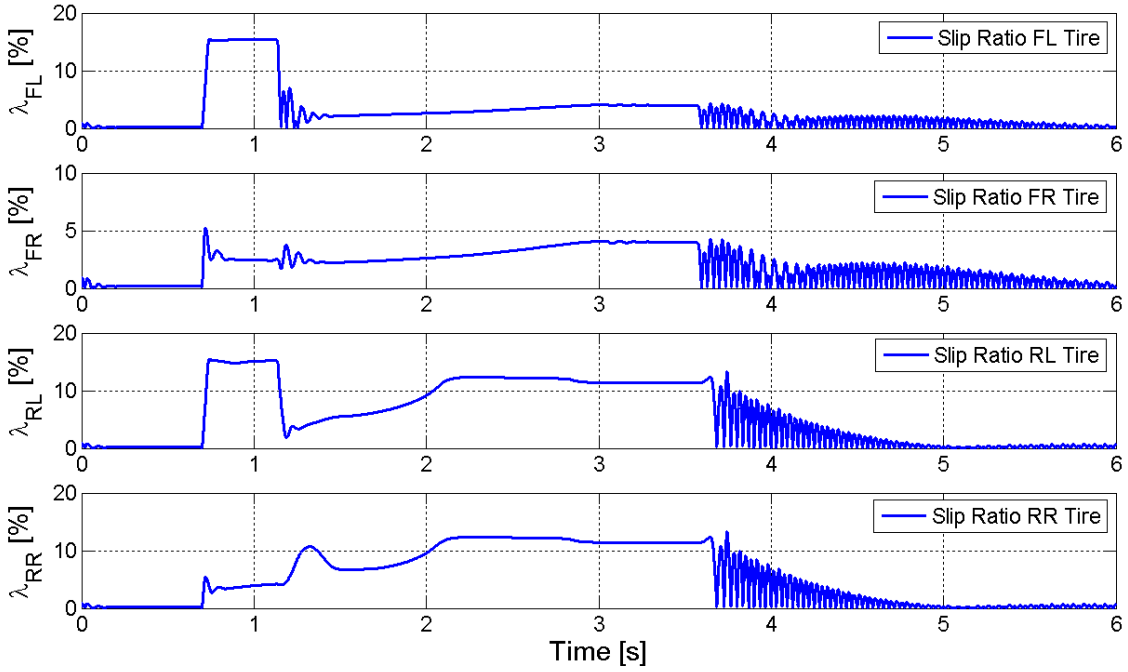

Figure 6-25: Tire slip ratios when braking on a μ-split road while holding the steering wheel fixed and using the genetic fuzzy ASC (GFASC)

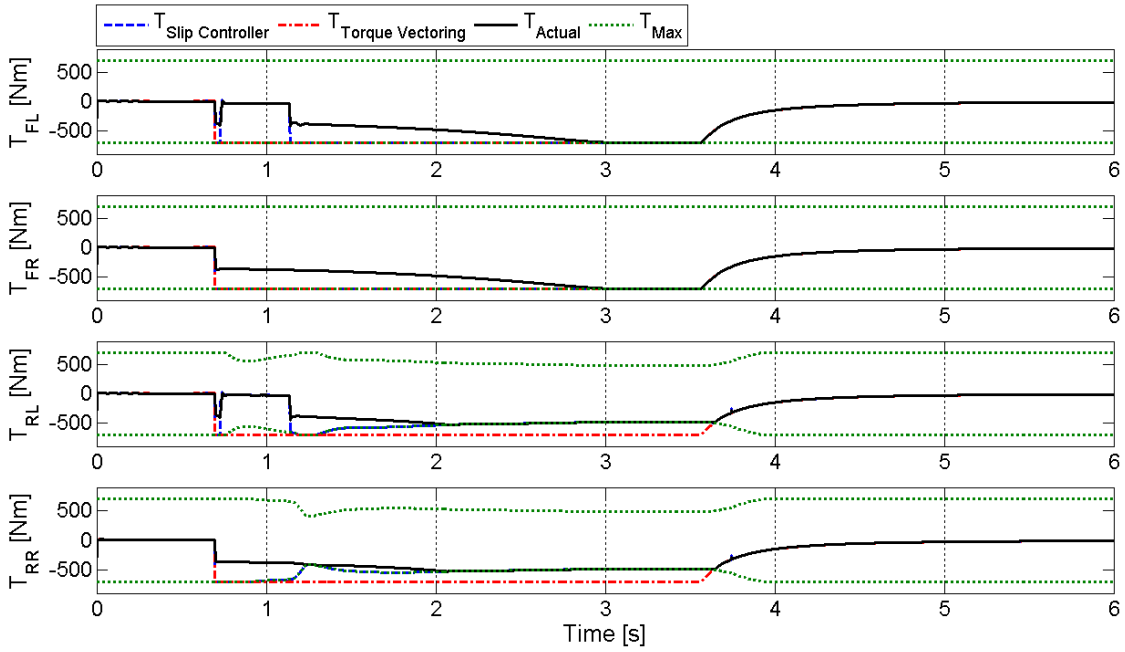

Figure 6-26: Requested and actual motor torque at each wheel when braking on a μ-split road while holding the steering wheel fixed and using the genetic fuzzy ASC (GFASC)

Parameter	$\lvert\beta\rvert_{max}$	$\lvert\dot{\psi}\rvert_{max}$	$\Delta x_{braking}$	Δy_{max}
AUTO21EV	24.2^{o}	63.4^{o}/s	48.4m	15.9m
GFYMC	0.40^{o}	1.85^{o}/s	44.5m	0.46m
ATVC	1.7^{o}	9.70^{o}/s	47.3m	2.70m
GFASC	1.6^{o}	2.50^{o}/s	45.7m	0.36m

Table 6-V: Vehicle response during the straight-line braking on a μ-split road maneuver without a controller, with the genetic fuzzy YMC (GFYMC), with the ATVC, and with the genetic fuzzy ASC (GFASC)

6.5 Chapter summary

In this chapter, the simplified 14-DOF vehicle model introduced in Chapter 4 is used to develop an active steering controller. Use of this simplified vehicle model facilitates the testing of different control strategies and the application of a genetic algorithm procedure to the development of the fuzzy active steering controller. A genetic tuning procedure is applied to the developed fuzzy ASC to improve its performance. A variety of maneuvers are simulated to demonstrate the performance and effectiveness of the genetic fuzzy ASC. Table 6-VI provides a subjective evaluation of the effectiveness of the genetic fuzzy ASC based on different test maneuvers.

Characteristic / Maneuver	Handling	Stability	Path following	Longitudinal dynamics
Double-lane-change	1	1		2
Step-steer	3			
Brake-in-turn	3	3	3	
Straight-line braking on a μ-split road		3	2.5	2.5
Mean Value $\left(\bar{x} = \frac{1}{n}\sum_{i=1}^{n} x_i\right)$	2.33	2.33	2.75	2.25

Table 6-VI: Subjective evaluation of the effectiveness of the genetic fuzzy ASC based on different test maneuvers (3 = very effective, 2 = effective, 1 = effective to some extent, 0 = ineffective)

7 Integration of the Advanced Torque Vectoring and Genetic Fuzzy Active Steering Controller

As mentioned earlier in Chapter 1, the optimum driving dynamics can only be achieved when the tire forces on all wheels in all three coordinate directions are monitored and controlled precisely. This advanced level of control is only possible when the vehicle is equipped with various active chassis control systems that are networked together in an integrated fashion. Taking advantage of the strengths of each active chassis subsystem, the ideal traction and stability performance of the vehicle can be obtained by activating the subsystem or subsystems that will be most effective given the required and actual behaviour of the vehicle. In the previous chapters, the performance and effectiveness of each stability control system, namely the advanced torque vectoring controller (ATVC) and the genetic fuzzy active steering controller (GFASC), were studied and evaluated individually. In this chapter, we investigate whether the integration of these stability control systems enhances the performance of the vehicle in terms of handling, stability, path-following, and longitudinal dynamics. An integrated approach is introduced that distributes the required control effort between the in-wheel motors and the active steering system.

7.1 Integration of chassis control systems using an activation function

As mentioned in Chapter 6, superimposing the steering input provided by the driver with a correction generated by the GFASC is considered to be a continuous process, and is not perceived by the driver as being annoying. It is also advantageous to employ steering intervention rather than braking or driving individual wheels when controlling the vehicle on slippery surfaces, since steering intervention requires less frictional force between the tire and the road to generate a corrective yaw moment. However, the GFASC is not of significant help when the vehicle is driven near its handling limits due to its limited range of effectiveness (caused by actuator restrictions). In Chapter 5, on the other hand, it has been confirmed that the ATVC is very effective at improving the vehicle stability and handling, even when driving the vehicle near its handling limits. It has also been observed, however, that the activation of the in-wheel motors to generate a corrective

yaw moment can cause some oscillations in the vehicle states, which might be perceived by the driver as being disruptive and annoying.

Figure 7-1 compares the performance and effectiveness of the genetic fuzzy yaw moment controller (GFYMC), ATVC, and GFASC based on different test maneuvers, which are listed in Tables 4-VII, 5-V, and 6-VI, respectively. Recall that the GFYMC is considered to be the ideal stability controller against which the performance and effectiveness of all other controllers are compared. As can be seen, neither the ATVC nor the GFASC can match the performance and effectiveness of the GFYMC in all four categories. Moreover, although the ATVC demonstrates better performance in the stability category when compared to the GFASC, the performance and effectiveness of the GFASC is superior in the other three categories (namely, vehicle handling, path-following, and longitudinal dynamics). Therefore, it makes sense to integrate these two controllers such that their individual strengths can be exploited, the effects of their weaknesses can be reduced, and the overlapping of their functionalities can be avoided.

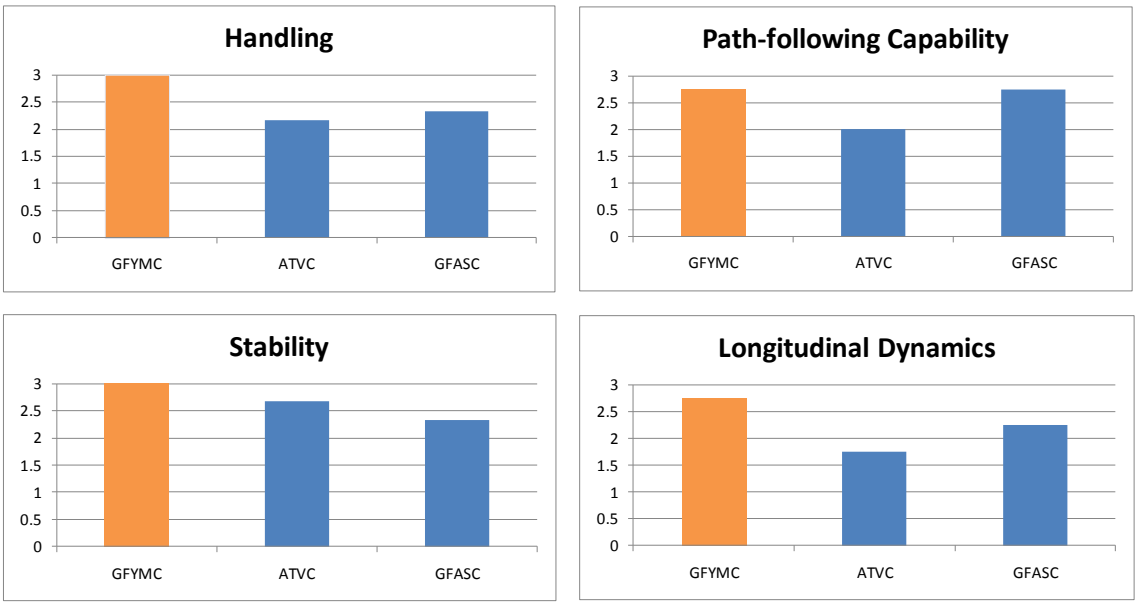

Figure 7-1: Subjective evaluation of the performance and effectiveness of the GFYMC, ATVC, and GFASC based on different test maneuvers (3 = very effective, 2 = effective, 1 = effective to some extent, 0 = ineffective)

In this work, the integration of the ATVC and GFASC is realized by using the activation function illustrated in Figure 7-2. This activation function is a standard Gaussian curve generated using the following exponential function:

$$\chi_{ATVC}\left(\delta_{corr}\right)=\begin{cases}\exp\left[\dfrac{-\left(\delta_{corr}-\delta_{corr_{\max}}\right)^2}{2\sigma^2}\right]\cdot 100\% & ,\ \left|\delta_{corr}\right|\le 3^{\circ}\\ 100\% & ,\ \left|\delta_{corr}\right|>3^{\circ}\end{cases} \tag{7.1}$$

where $\chi_{ATVC}\left(\delta_{corr}\right)$ is the ATVC activation function, which is defined as a function of the corrective steering angle (δ_{corr}); $\delta_{corr_{\max}}$ is the actuator range limit of the active steering controller, which is set at 3^{o}; and σ is the standard deviation, which is set at 0.7 in order to form the bell curve shown in Figure 7-2. Note that the shape of this activation function is designed such that the contribution of the ATVC is introduced gradually rather than abruptly. In other words, depending on the driving conditions and the difference between the desired and actual behaviour of the vehicle, the GFASC first attempts to stabilize the vehicle without receiving any support from the ATVC. As the required corrective steering angle increases, the activation function gradually activates the ATVC to support the GFASC in its effort to stabilize the vehicle. If the required corrective steering angle is larger than 3^{o}, thus exceeding the actuator range limit of the active steering controller, the activation function fully activates the ATVC such that both controllers are fully deployed to help stabilize the vehicle.

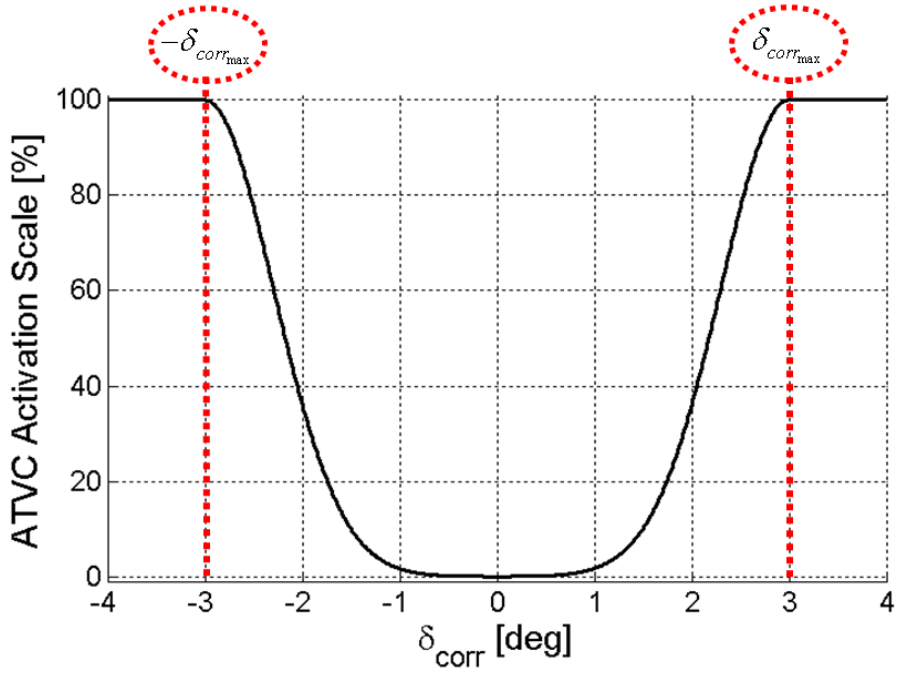

Figure 7-2: Activation function used for the integration of the ATVC and GFASC

7.2 Evaluation of the integrated control of the advanced torque vectoring and genetic fuzzy active steering

In order to evaluate the performance and effectiveness of the integrated control of the ATVC and GFASC, the AUTO21EV is driven through a series of test maneuvers, as described in Chapter 2.

7.2.1 ISO double-lane-change maneuver

The performance of the integrated control system consisting of the ATVC and the GFASC is first evaluated by driving the AUTO21EV through the double-lane-change maneuver with an initial speed of 75 km/h and using the path-following driver model. Figure 7-3 illustrates the vehicle trajectory and demonstrates that the driver is able to negotiate the maneuver without hitting the cones when the integrated control strategy is used. Note that the path-following driver model is not able to negotiate this maneuver at higher speeds without hitting the cones when only the GFASC is active (see Figure 4-11).

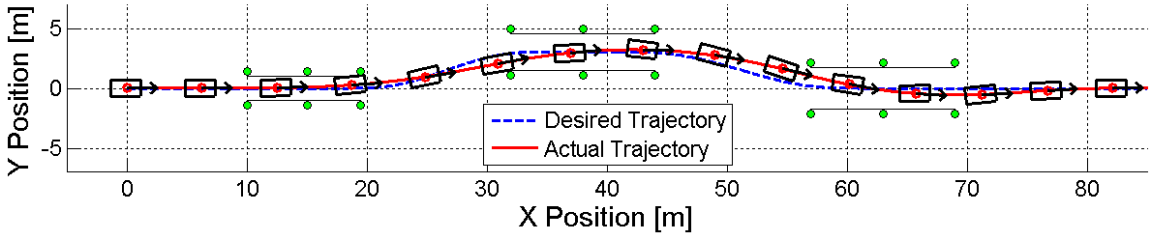

Figure 7-3: Desired and actual vehicle trajectories when driving through the double-lane-change maneuver with an initial speed of 75 km/h using the path-following driver model and the integrated control of the ATVC and GFASC

Figure 7-4 illustrates the vehicle yaw rate and sideslip angle during this maneuver. In contrast to the individual performance of the ATVC and GFASC (Figures 5-6 and 6-15), the integrated control scheme using both the ATVC and GFASC is able to match the actual vehicle yaw rate with the desired yaw rate that is calculated using the reference bicycle model. Note that the oscillations in the actual vehicle yaw rate that were observed when the ATVC was used on its own are not present when the integrated control approach is used. In addition, the maximum yaw rate and sideslip angle of the vehicle are almost the same as those obtained when the GFYMC was active (Figure 7-25). Figure 7-5-a illustrates the vehicle lateral acceleration as a function of time. As can be seen, the lateral acceleration when using the integrated control approach is, in some regions,

similar to that observed when using the GFASC and, in other regions, is similar to that observed when using the ATVC. At the handling limits, oscillations can be seen in the lateral acceleration of the vehicle, which are caused by the activation of the in-wheel motors, but they are mostly damped out. Figure 7-5-b confirms that, except during the second lane-change, the driver requires about the same amount of steering wheel input as is the case when only the ATVC is used. Figure 7-5-c illustrates the vehicle speed during the double-lane-change maneuver, and confirms that the vehicle loses the least amount of speed when the integrated control approach is used. This lack of deceleration can be attributed to the fact that only relatively small steering angles are needed to negotiate the maneuver (Figure 7-5-b) and the fact that the couples generated at the front and rear axles do not slow the vehicle down. As a result, the speed reduction during this maneuver when using the integrated control approach is even less than that observed when the GFYMC is active. Figure 7-5-d illustrates the handling performance of the vehicle and indicates that the hysteresis of this plot is less than that of the analogous plots for the GFASC and the ATVC. In other words, the responsiveness and agility of the vehicle are considerably improved compared to the cases where only individual controllers (namely, the GFASC and the ATVC) are active. However, the responsiveness and agility of the vehicle are not as good as they are when the GFYMC is used to generate the required corrective yaw moment.

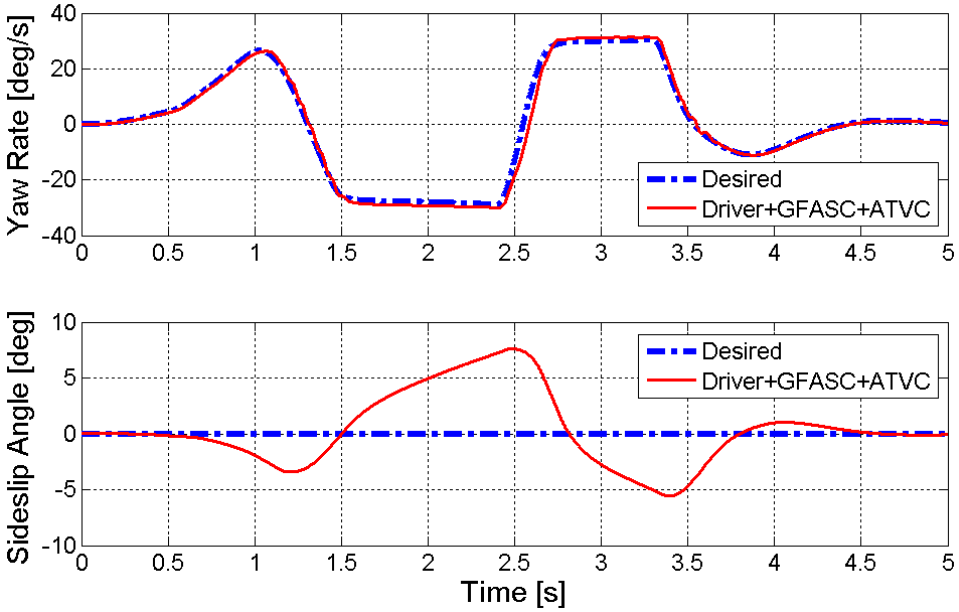

Figure 7-4: Desired and actual vehicle yaw rate (top) and sideslip angle (bottom) when driving through the double-lane-change maneuver with an initial speed of 75 km/h using the driver model and the integrated control of the ATVC and the GFASC

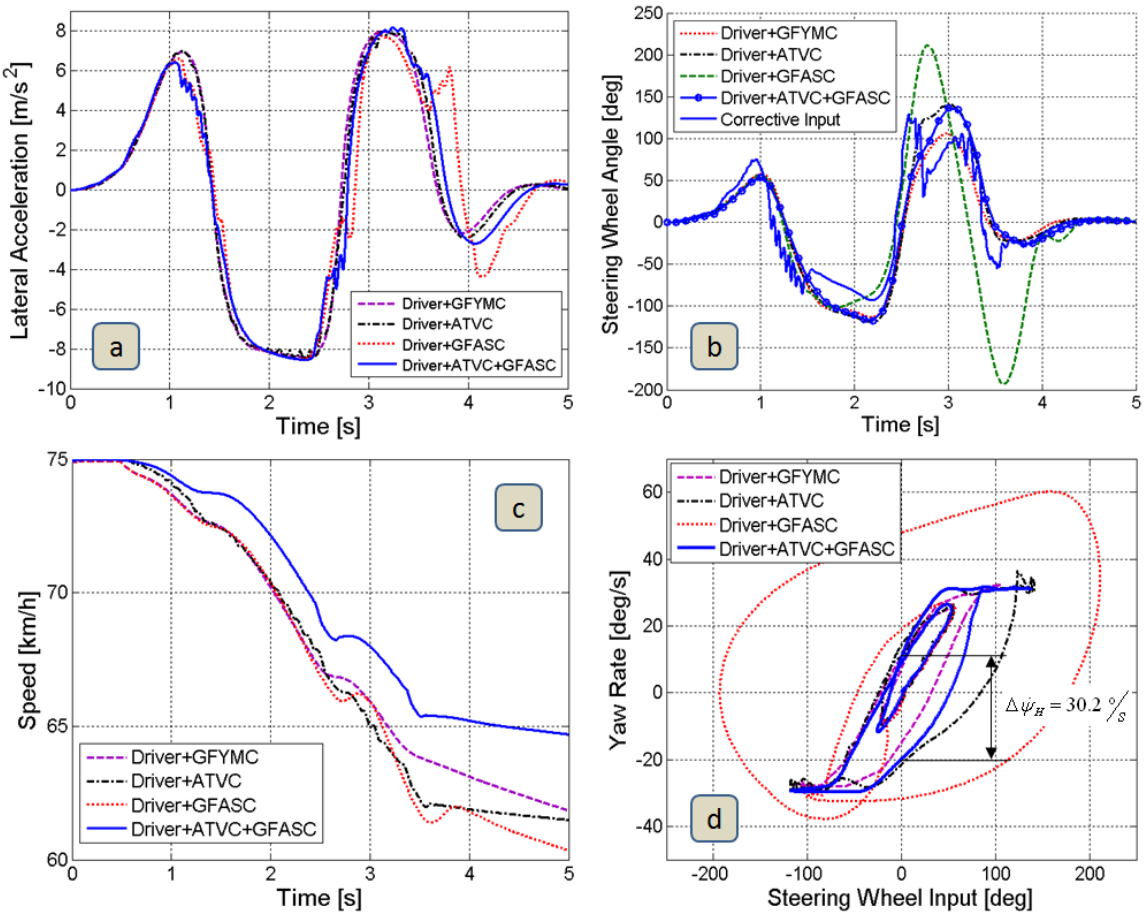

Figure 7-5: (a) Lateral acceleration, (b) steering wheel angle, and (c) vehicle speed as functions of time; and (d) vehicle yaw rate as a function of the steering wheel input when driving through the double-lane-change maneuver with the GFYMC, the ATVC, the GFASC, and the integrated control of the ATVC and GFASC

Figure 7-6 illustrates the torque of each in-wheel motor during the double-lane-change maneuver. Comparing this figure to Figure 5-7, it is clear that the use of the ATVC is reduced to a minimum by the activation function. In other words, the ATVC is only activated when the GFASC is unable to stabilize the vehicle on its own, which generally only happens when the vehicle is driven near its handling limits. Looking at the motor torque plots, it can be seen that the GFASC is able to stabilize the vehicle most of the time, and the ATVC is only activated at three time periods. For instance, between 2.4 and 2.65 seconds of the simulation, during which time the vehicle experiences the maximum lateral acceleration of 8.5 m/s^2 (Figure 7-5-a), the left-to-right torque vectoring controller has ordered the left wheels to brake and the right wheels to accelerate, thereby generating a positive corrective yaw moment to compensate for an oversteering situation, where the actual yaw rate is larger than the desired one (Figure 7-4). Looking at the torque vectoring ratios shown in Figure 7-7, it can be confirmed that the front-to-rear

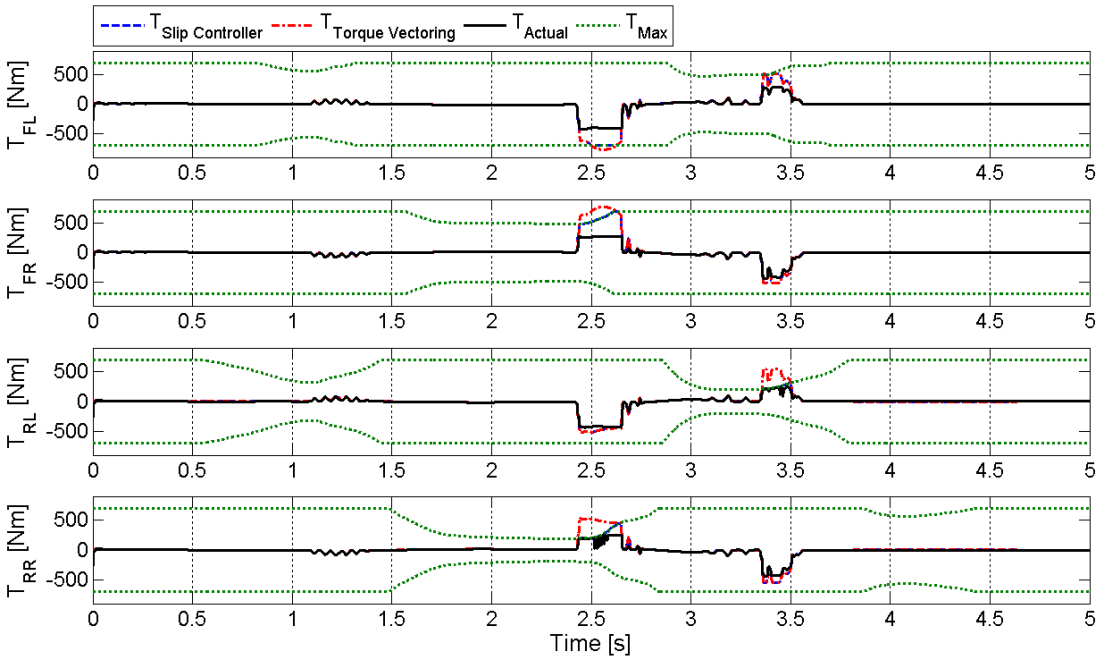

Figure 7-6: Requested and actual motor torque at each wheel when driving through the double-lane-change maneuver using the driver model with the integrated control of the ATVC and GFASC

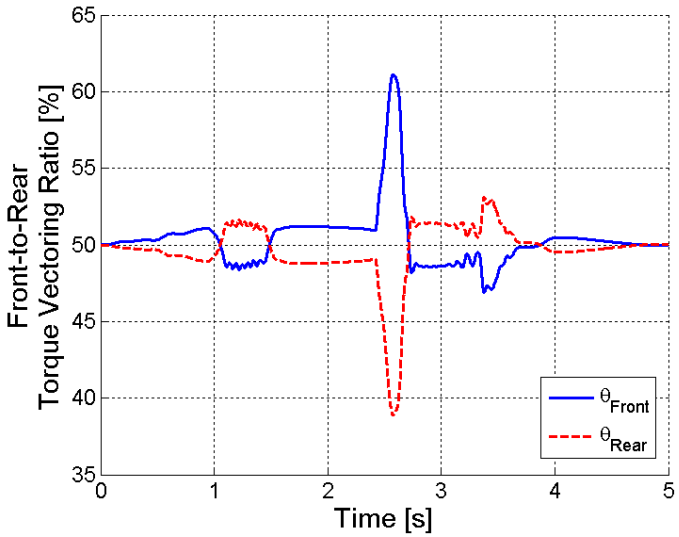

Figure 7-7: Front-to-rear torque vectoring ratios when driving through the double-lane-change maneuver using the driver model with the integrated control of the ATVC and GFASC

torque vectoring controller supports both the GFASC and the left-to-right torque vectoring controller in a coordinated effort to stabilize the vehicle. For instance, between 2.4 and 2.65 seconds, the front-to-rear torque vectoring controller has requested that the front motors generate up to 61% of the total required corrective yaw moment. Note that generating more torque with the front motors and less with the rear ones reduces the lateral force potential at the front axle and increases that at the rear axle, and vice versa. The asymmetric lateral force potentials on the front and rear axles help to generate the

required corrective yaw moment. The activation of the front-to-rear torque vectoring controller can also be confirmed in Figure 7-6. For instance, between 2.4 and 2.65 seconds, the front-to-rear torque vectoring controller has requested the front-left motor to generate up to 770 Nm of braking torque and the front-right motor to generate up to 770 Nm of driving torque while, at the same time, the controller has requested up to 510 Nm of braking and driving torques from the rear-left and rear-right motors, respectively. Note that, although the controller has requested large motor torques from the front motors, the motors are not powerful enough to generate the requested torques at a speed of 68 km/h. The effects seen in Figure 7-6 can also be confirmed by looking at the tire traction potentials and tire slip ratios shown in Figures 7-8 and 7-9, respectively. For instance, the maximum traction potential of the rear-left tire is only exceeded once, at 3.35 seconds (Figure 7-8). Looking at Figures 7-6 and 7-9, it can be confirmed that the requested motor torque at the rear-left wheel is restricted by the slip controller during this time period in order to prevent tire spin-out. Thus, the plot of the traction potential of the rear-left tire exceeds 1 due to the fact that the lateral force of the tire has exceeded its limit. The same explanation is valid for the rear-right tire when its traction potential is exceeded at 2.45 seconds.

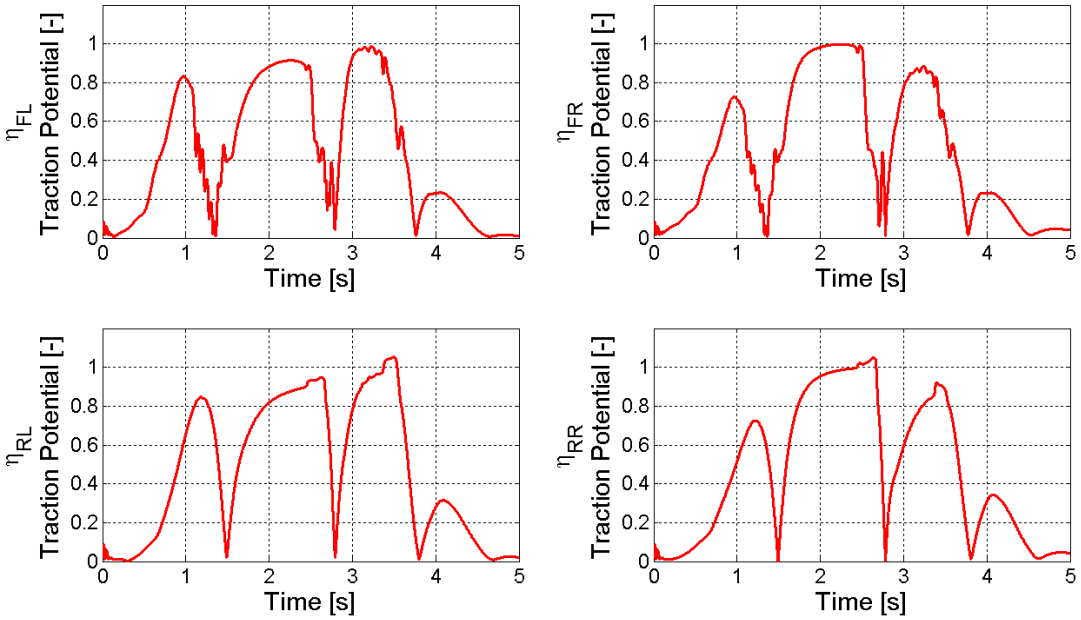

Figure 7-8: Traction potential of each tire when driving through the double-lane-change maneuver using the driver model with the integrated control of the ATVC and GFASC

Table 7-I summarizes the vehicle response during the double-lane-change maneuver when the driver model is used with the integrated control of the ATVC and

GFASC. The vehicle response is compared to the cases where the driver model is used with no stability controller, with the GFYMC, with the ATVC, and with the GFASC. Comparing different parameters of the vehicle response during the double-lane-change maneuver, it can be seen that the performance of the integrated controller – in all the decisive parameters that describe the handling, stability, and longitudinal dynamics of the vehicle – is better than that of either of the individual controllers (namely, the ATVC and the GFASC). Moreover, with respect to the handling of the vehicle, the integrated control approach has reduced $|\beta|_{\max}$ and $|\dot{\psi}|_{\max}$ by about the same amount as the GFYMC. The maximum lateral acceleration of the vehicle ($|a_y|_{\max}$) is also about the same as it is when the GFYMC is active; however, when the integrated control system is active, the driver requires a larger maximum steering wheel angle to negotiate the maneuver. In addition, the hysteresis of the performance plot ($\Delta\dot{\psi}_H$) is about 1.4 times larger than that observed when the GFYMC is active. However, the speed lost during the maneuver is less than that lost when the GFYMC is active. Altogether, the integrated control approach is considered to be very effective at improving the handling and stability characteristics of the vehicle. Since the least amount of speed is lost during the maneuver when the integrated control approach is used, it is considered to be the most effective controller for improving the longitudinal dynamics of the vehicle.

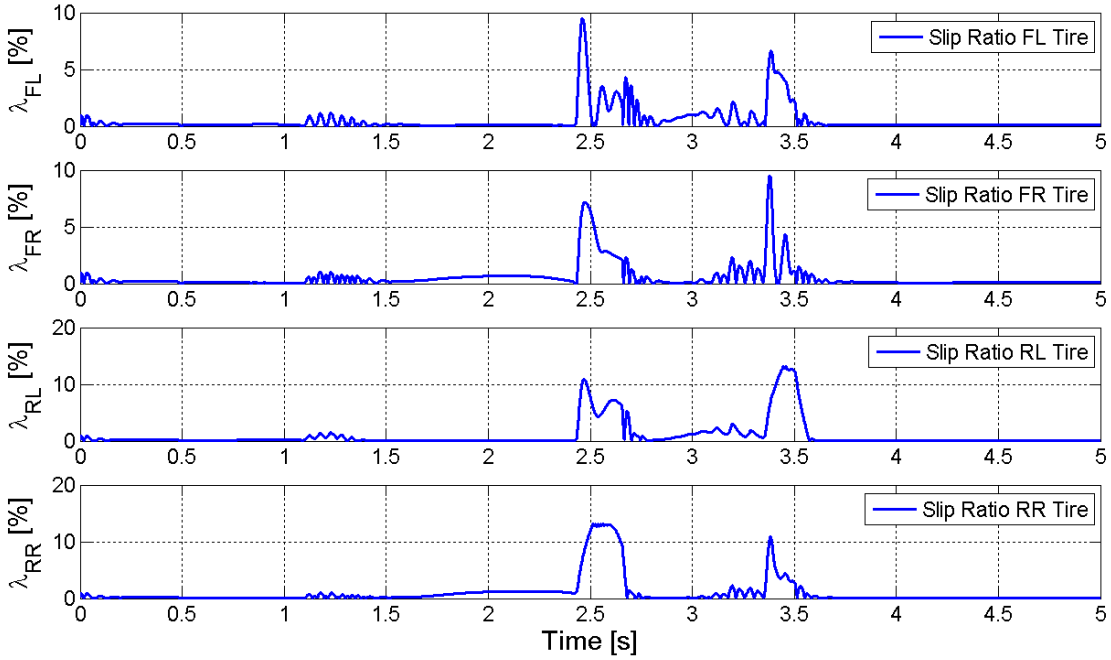

Figure 7-9: Tire slip ratios when driving through the double-lane-change maneuver using the driver model with the integrated control of the ATVC and GFASC

Parameter	$\lvert\beta\rvert_{max}$	$\lvert\dot{\psi}\rvert_{max}$	$\lvert a_y\rvert_{max}$	$\lvert\delta_{SW}\rvert_{max}$	$\Delta\dot{\psi}_H$	v_{lost}
AUTO21EV	26.3°	115.4°/s	8.2m/s^2	545°	163.8°/s	20.5m/s
GFYMC	6.2°	31.2°/s	8.4m/s^2	108°	21.0°/s	13.2m/s
ATVC	6.1°	36.4°/s	8.4m/s^2	140°	35.5°/s	13.5m/s
GFASC	13.6°	60.1°/s	8.4m/s^2	211°	79.5°/s	14.6m/s
ATVC+GFASC	7.5°	31.5°/s	8.5m/s^2	136°	30.2 °/s	10.3m/s

Table 7-I: Vehicle response during the double-lane-change maneuver using the driver model without a controller, with the GFYMC, with the ATVC, with the GFASC, and with the integrated control of the ATVC and GFASC

7.2.2 Step-steer response maneuver

In order to evaluate the performance of the vehicle using the integrated control of the ATVC and GFASC in a step-steer response maneuver, the vehicle yaw rate, sideslip angle, and lateral acceleration as functions of time are observed. Figure 7-10-a illustrates the fixed step-steer input and the equivalent corrective steering input generated by the GFASC. As can be seen, the intervention of the GFASC is almost the same as that observed when the GFASC is used on its own (Figure 6-16-a). In other words, the GFASC is able to match the behaviour of the vehicle to that of the desired bicycle model without requiring a significant amount of support from the ATVC. As a result, the vehicle experiences a lateral acceleration of 4.3 m/s^2, which is similar to that obtained when the GFASC is used on its own (Figure 7-10-b).

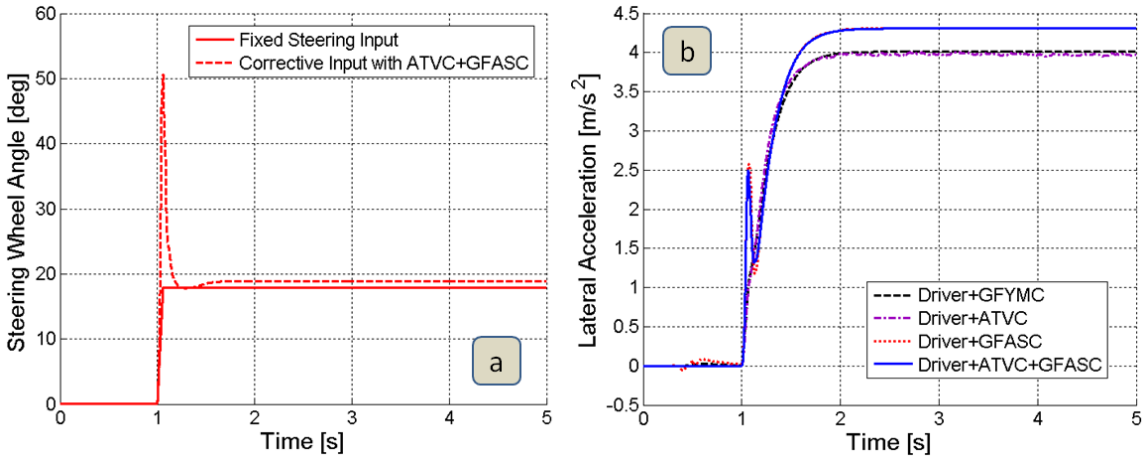

Figure 7-10: (a) Required steering wheel input and (b) lateral acceleration of the vehicle when driving through the step-steer maneuver using the integrated control of the ATVC and GFASC

Figure 7-11 illustrates the vehicle yaw rate and sideslip angle when the integrated control of the ATVC and GFASC is used, and compares the response to that obtained

when no stability controller is used, and when the GFYMC, ATVC, and GFASC are used. As can be seen, the yaw rate and sideslip angle of the vehicle are similar to the results obtained when the GFASC is active. Table 7-II summarizes the vehicle response during the step-steer test maneuver. By comparing different parameters of the vehicle response during this maneuver when it is performed with and without the integrated control of the ATVC and GFASC, we can conclude that the integrated control approach is very effective at improving all the decisive parameters of the vehicle that describe its handling characteristics.

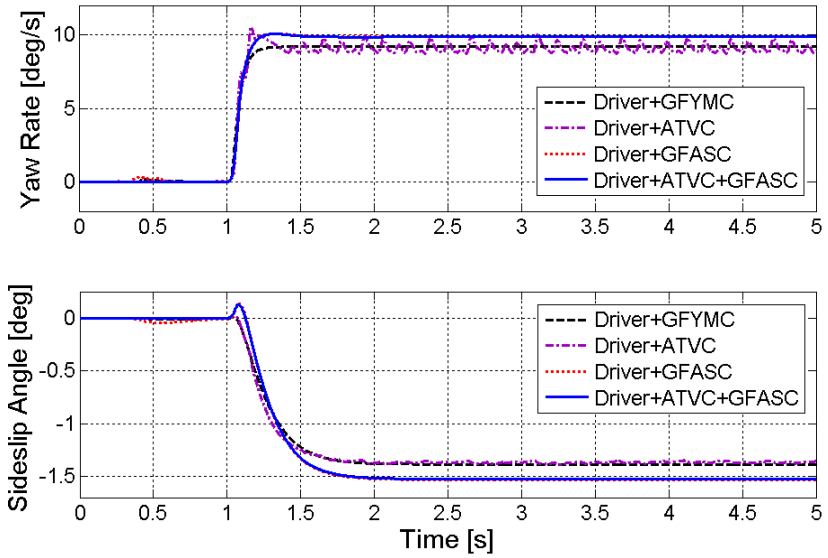

Figure 7-11: Yaw rate (top) and sideslip angle (bottom) of the vehicle when driving through the step-steer maneuver using the integrated control of the ATVC and GFASC

Parameter	$t_{\dot{\psi}}$	$\text{PO} = \frac{\dot{\psi}_{\max} - \dot{\psi}_{ss}}{\dot{\psi}_{ss}} \times 100\%$	$\lvert\beta\rvert_{\max}$	t_{a_y}
AUTO21EV	0.34s	1.30%	1.43^{o}	0.66s
GFYMC	0.15s	0.00%	1.38^{o}	0.51s
ATVC	0.15s	16.1%	1.36^{o}	0.47s
GFASC	0.15s	2.20%	1.53^{o}	0.53s
ATVC+GFASC	0.15s	2.20%	1.53^{o}	0.53s

Table 7-II: Vehicle response during the step-steer maneuver using the driver model without a controller, with the GFYMC, with the ATVC, with the GFASC, and with the integrated control of the ATVC and GFASC

7.2.3 Brake-in-turn maneuver

Figure 7-12 illustrates the vehicle trajectory relative to the desired circular path during a brake-in-turn maneuver, using the driver model with and without the integrated control of

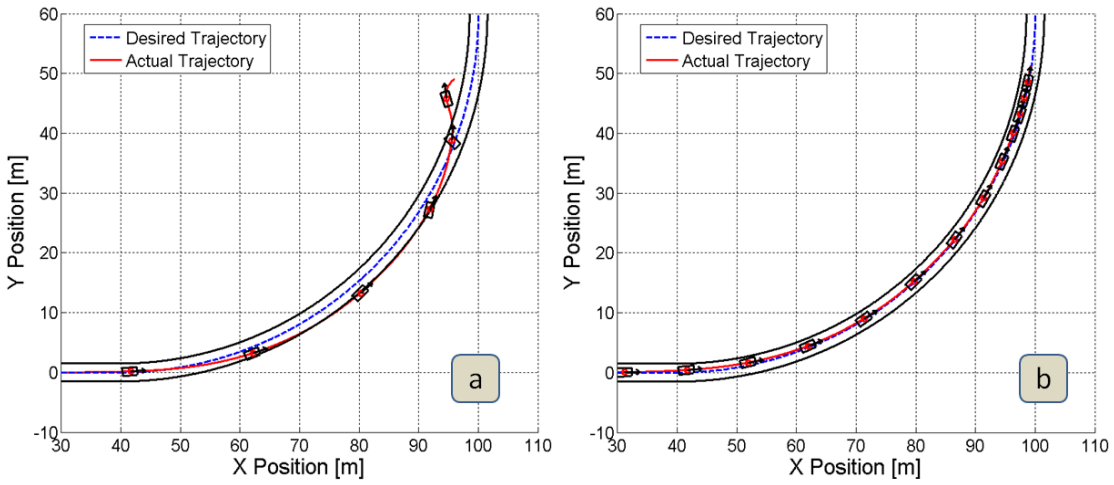

Figure 7-12: Desired and actual vehicle trajectories when braking in a turn using (a) the driver model only and (b) the driver model with the integrated control of the ATVC and GFASC

the ATVC and GFASC. As can be seen, the driver model is able to keep the vehicle on the predefined circular path while severely braking when the integrated controller is active, and the lateral deviation of the vehicle from the desired path remains negligible throughout the maneuver. Figure 7-13-a illustrates the driver's steering wheel input as a function of time, and indicates that the driver model is able to control the vehicle very smoothly and with little steering effort when the integrated controller is used. This figure also shows the activity of the active steering controller when using the integrated control approach as it superimposes a corrective signal atop the driver's steering wheel input at each time step. Comparing this figure to Figure 6-19-a, it can be confirmed that the integrated control approach requires a smaller corrective steering angle than the GFASC, which can be attributed to the fact that the ATVC also helps to stabilize the vehicle. Figure 7-13-b illustrates the lateral acceleration of the vehicle and confirms that the vehicle remains stable when the integrated control approach is used. This figure also confirms that the vehicle does not experience any high oscillations at higher lateral accelerations, as is the case when the ATVC is used on its own. Note that, for clarity, the driver's steering input and the lateral acceleration of the vehicle when no stability controller is active are not illustrated in Figure 7-13.

Figure 7-14 compares the vehicle yaw rate and sideslip angle when driving through the brake-in-turn maneuver using the driver model with the GFYMC, the ATVC, the GFASC, and the integrated control of the ATVC and GFASC. Note that, for clarity, the yaw rate and sideslip angle of the vehicle when no stability controller is active are not illustrated. When the integrated control approach is used, the vehicle behaves almost like

the desired reference model until the braking action begins, using primarily the GFASC because the required corrective steering angle remains below 1^{o}. However, once the braking begins, both the GFASC and the ATVC contribute to minimizing the yaw rate error. As can be seen in Figure 7-13-a, the GFASC superimposes the driver's steering input with a steering angle of up to 2.7^{o} at 4.3 seconds of the simulation, which is equivalent to a steering wheel angle of about 48^{o}, assuming a steering ratio of 1:18. In other words, the activation function engages the ATVC up to 90% of its full potential at 4.3 seconds in order to support the GFASC as it attempts to stabilize the vehicle.

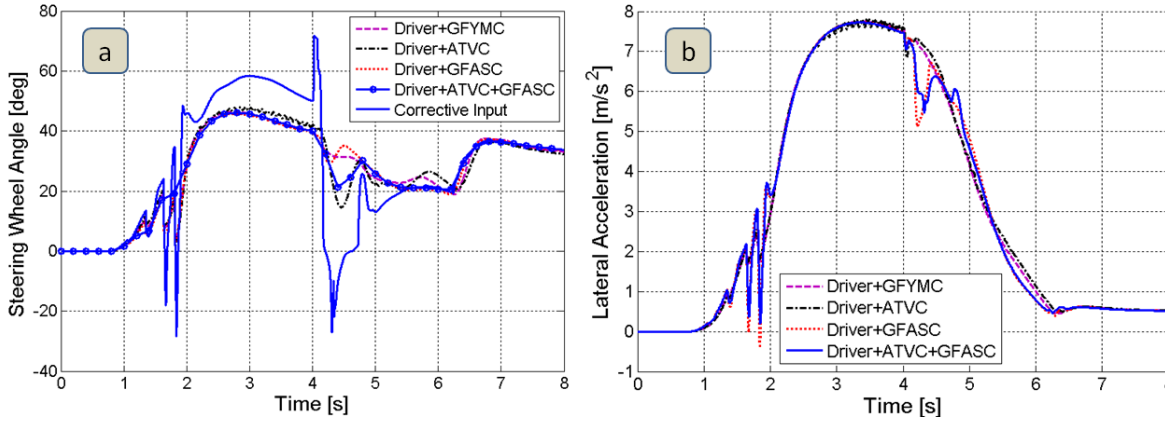

Figure 7-13: (a) Required steering wheel input and (b) lateral acceleration of the vehicle when braking in a turn using the driver model with the GFYMC, the ATVC, the GFASC, and the integrated control of the ATVC and GFASC

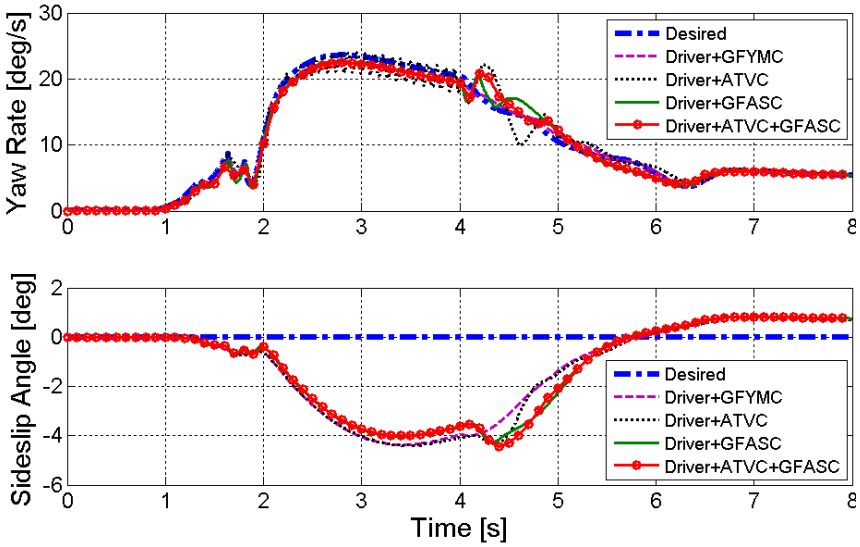

Figure 7-14: Desired and actual vehicle yaw rate (top) and sideslip angle (bottom) when braking in a turn using the driver model with the GFYMC, the ATVC, the GFASC, and the integrated control of the ATVC and GFASC

Figure 7-15 illustrates the torque of each in-wheel motor during this maneuver. Until the braking begins, the speed-control driver model requests up to 63 Nm of drive

torque from all four motors to keep the vehicle speed constant. When the braking begins, the ATVC increases the braking torque request on the right wheels and reduces that on the left wheels; however, at a speed of 70 km/h, the motors are not powerful enough to provide the motor torques requested by the ATVC. Braking the vehicle in a curve causes a weight shift to the front and, in this case, right side of the vehicle that considerably reduces the traction potential of the left tires. Therefore, the slip controllers limit the braking torque of the front-left wheel between 4 and 4.1 seconds, and that of the rear-left wheel between 4.1 and 5.3 seconds, in order to avoid wheel lock-up. The slip controller for the rear-right wheel limits its braking torque between 5.5 and 5.9 seconds in order to avoid a lock-up situation caused by the high available braking torque and the weight shift to the front axle. The activation of the slip controllers can be confirmed in Figure 7-16, which illustrates the slip ratio of each tire. Figure 7-17 shows the traction potential at each tire and clearly indicates that the traction potentials of the left tires have exceeded their limits. In other words, although the slip controllers have limited the braking torques on the left wheels, the high lateral acceleration of the vehicle has caused the resultant tire forces on the left wheels to exceed their traction potentials. Figure 7-18 illustrates the front-to-rear torque vectoring ratios and indicates that this controller also supports the driver in stabilizing the vehicle while braking in a turn, requesting more braking torque from the rear wheels than the front wheels, thereby reducing the lateral force potential at the rear axle and increasing that at the front axle. Figure 7-19-a illustrates the vehicle speed as a function of time and confirms the performance of the speed controller. Figure 7-19-b illustrates the vehicle longitudinal acceleration as a function of vehicle speed, and confirms the severity of the braking action in this maneuver.

Table 7-III summarizes the vehicle response during the brake-in-turn maneuver when the integrated control approach is used, and compares it with the performance observed when no stability controller is used, and when the GFYMC, ATVC, and GFASC are used. Comparing different parameters of the vehicle response during this maneuver, it can be seen that the integrated control approach is very effective at improving all the decisive parameters that describe the handling, stability, and path-following capabilities of the vehicle. The integrated control of the ATVC and GFASC is able to reduce $|\beta|_{\max}$, $|\dot{\psi}|_{\max}$, and $|\delta_{SW}|_{\max}$ significantly in comparison to those obtained when no stability controller is used, which indicates that the integrated control approach

is very effective at enhancing the vehicle handling during this maneuver. Simultaneously, a reduction of $|\beta|_{max}$ and $|\dot{\psi}|_{max}$ indicates that the integrated control approach is also very effective at improving the vehicle stability. Finally, the fact that the maximum lateral deviation of the vehicle from the desired path remains very small throughout the maneuver confirms that the integrated control approach enhances the path-following capability of the vehicle as well.

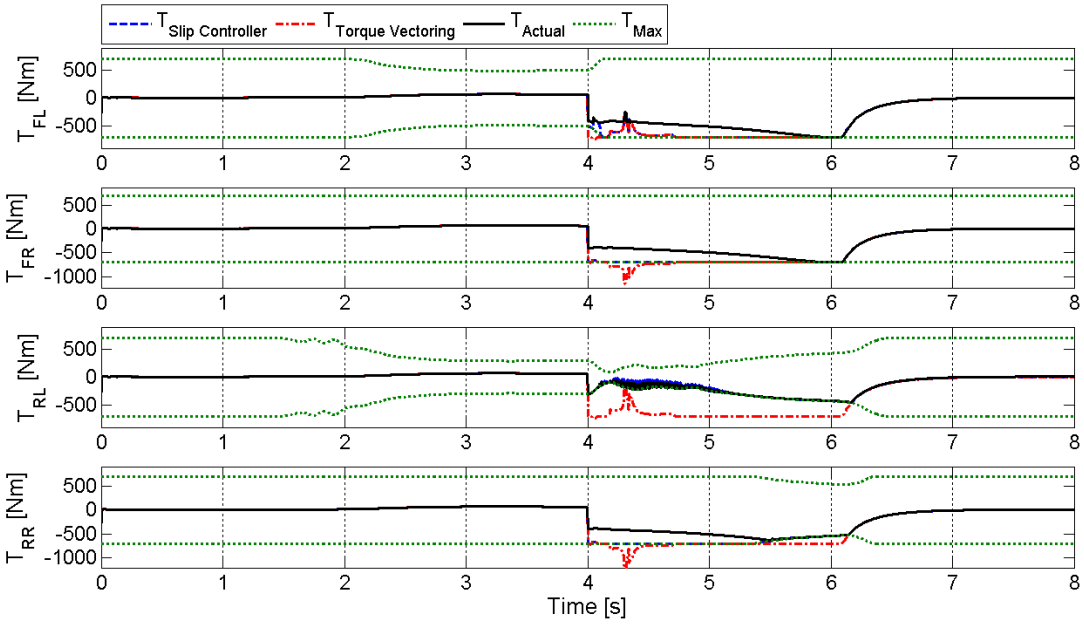

Figure 7-15: Requested and actual motor torque at each wheel when braking in a turn using the driver model with the integrated control of the ATVC and GFASC

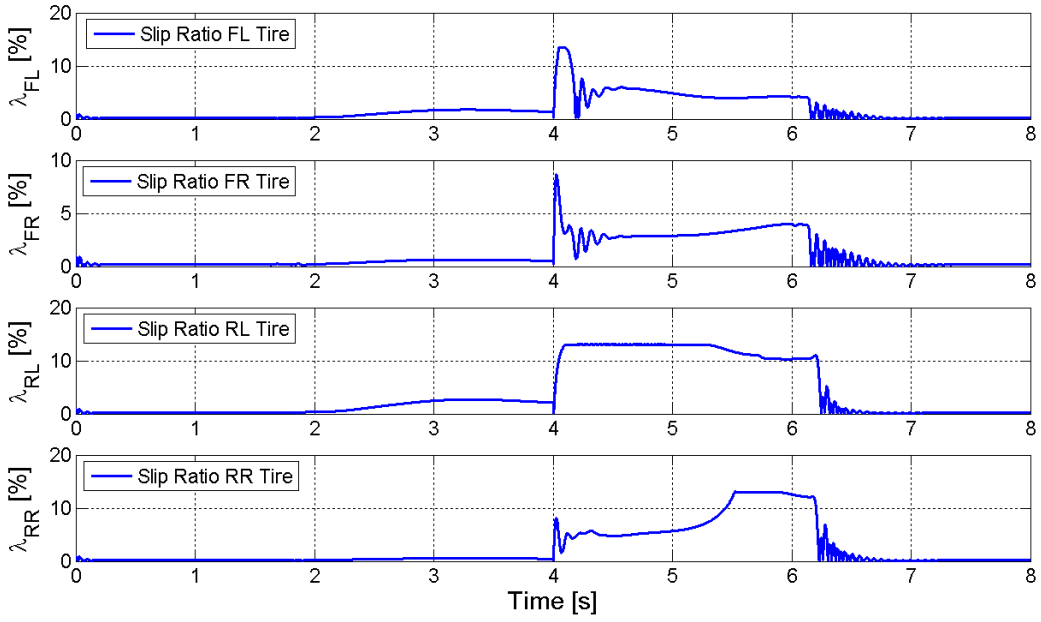

Figure 7-16: Tire slip ratios when braking in a turn using the driver model with the integrated control of the ATVC and GFASC

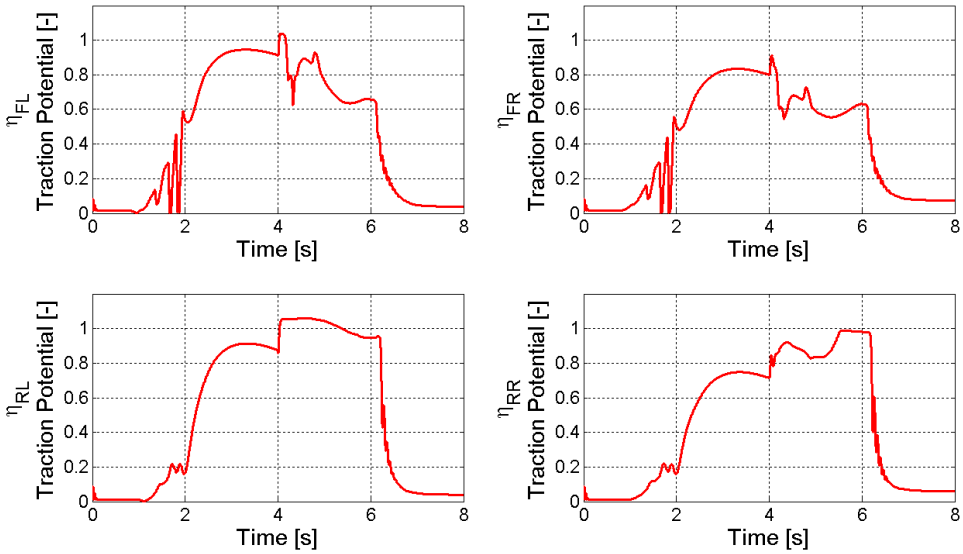

Figure 7-17: Traction potential of each tire when braking in a turn using the driver model with the integrated control of the ATVC and GFASC

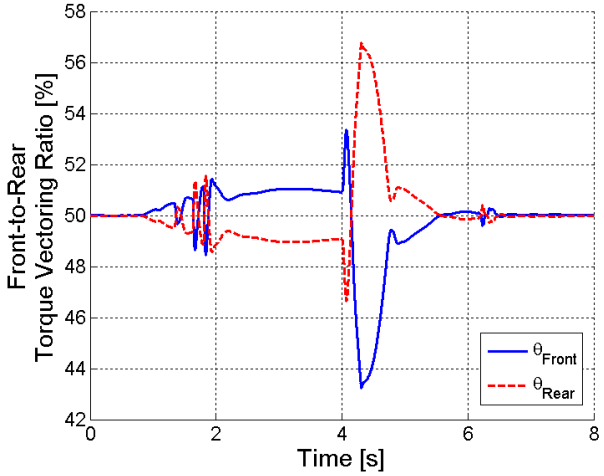

Figure 7-18: Front-to-rear torque vectoring ratios when braking in a turn using the driver model with the integrated control of the ATVC and GFASC

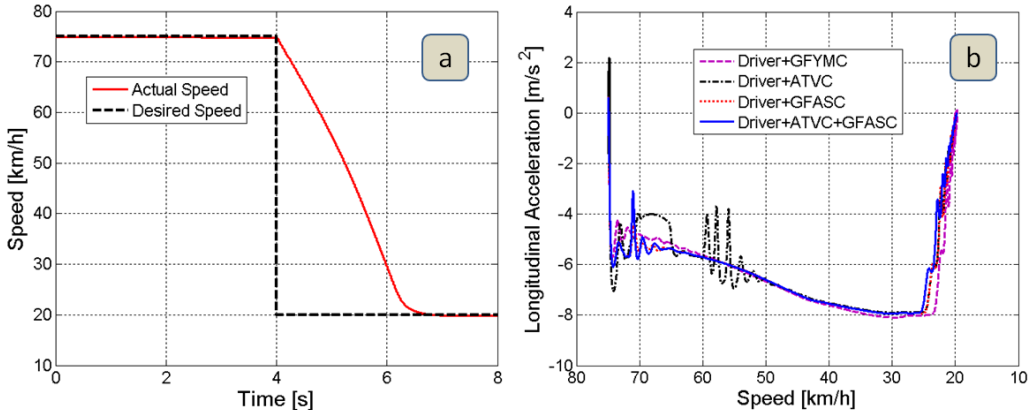

Figure 7-19: (a) Vehicle speed as a function of time when braking in a turn using the driver model with the integrated control of the ATVC and GFASC, and (b) longitudinal acceleration as a function of vehicle speed when braking in a turn using the driver model with the GFYMC, the ATVC, the GFASC, and the integrated control of the ATVC and GFASC

Parameter	$\lvert\dot{\psi}\rvert_{max}$	$\lvert\beta\rvert_{max}$	Δy_{max}	$\lvert\delta_{SW}\rvert_{max}$
AUTO21EV	126.5°/s	50.1°	3.67m	700°
GFYMC	22.60°/s	4.36°	0.18m	46.4°
ATVC	24.00°/s	4.40°	0.18m	48.0°
GFASC	22.45°/s	4.25°	0.16m	45.7°
ATVC+GFASC	22.45°/s	4.45°	0.17m	46.1°

Table 7-III: Vehicle response during the brake-in-turn maneuver using the driver model without a controller, with the GFYMC, with the ATVC, with the GFASC, and with the integrated control of the ATVC and GFASC

7.2.4 Straight-line braking on a μ-split road

As a final test, the AUTO21EV is driven on a μ-split road and the driver model attempts to stop the vehicle in an emergency braking situation. Figure 7-20 illustrates the vehicle trajectory for this maneuver when no stability controller is active and compares it to the case when the integrated control of the ATVC and GFASC is used. As can be seen, the integrated control approach is able to correct the side-pushing effect of the vehicle while braking on a μ-split road, and prevents the vehicle from leaving the predefined road. The braking distance of the vehicle remains the same as it was when the GFASC was used alone. Looking at Figure 7-21, it is clear that the integrated control approach is able to limit and, later, diminish the yaw rate and sideslip angle of the vehicle while driving over the black ice patch, which indicates that the vehicle remains stable during this maneuver. Note that the yaw rate and sideslip angle of the vehicle when no controller is active have been omitted from Figure 7-21 for clarity.

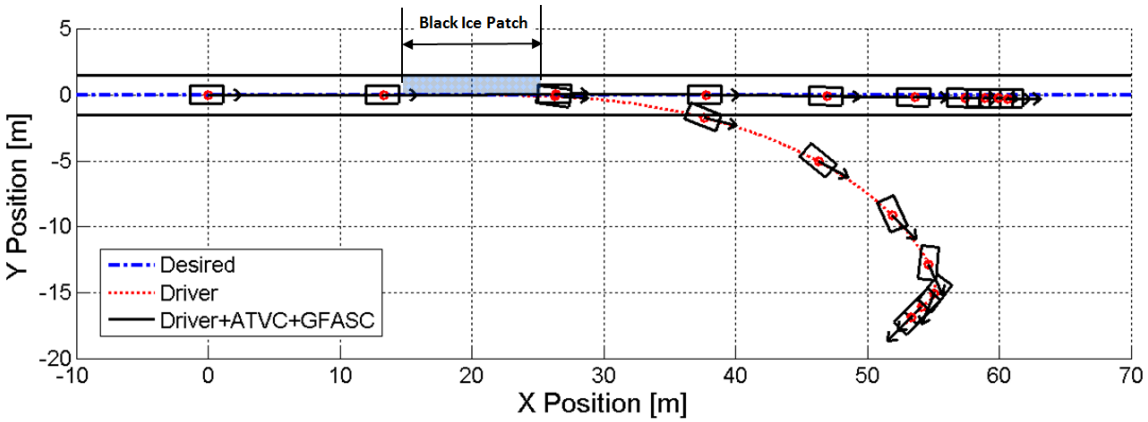

Figure 7-20: Desired and actual vehicle trajectories when braking on a μ-split road while holding the steering wheel fixed, with and without using the integrated control of the ATVC and GFASC

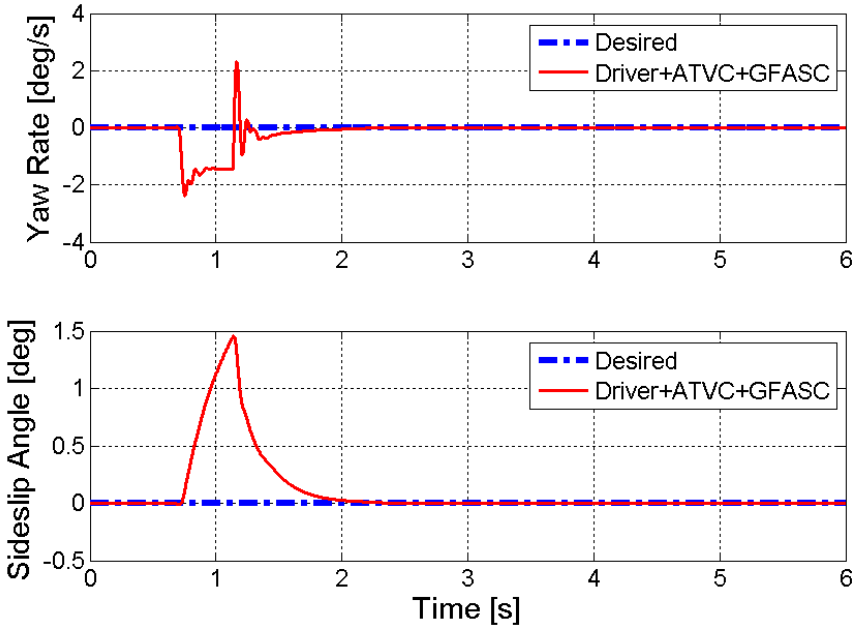

Figure 7-21: Desired and actual vehicle yaw rate (top) and sideslip angle (bottom) when braking on a μ-split road while holding the steering wheel fixed, using the integrated control of the ATVC and GFASC

Figure 7-22 illustrates the fixed steering wheel input and the equivalent corrective steering wheel angle required to counteract the side-pushing effect of the vehicle, which is generated by the GFASC. As can be seen, the active steering controller has applied up to 3^o of corrective steering angle, which is equivalent to 54^o of steering wheel angle, in order to correct the side-pushing effect of the vehicle. Thus, the activation function has engaged the ATVC up to 100% of its full potential in order to support the driver in stabilizing the vehicle. This level of activation can be confirmed by looking at Figure 7-23, which illustrates the motor torques for all four wheels. As can be seen, between 0.7 and 0.9 seconds of the simulation, the left-to-right torque vectoring controller has requested more braking torque from the left motors than the right motors in order to counteract the side-pushing effect of the vehicle. Note that the left motors are not able to generate the high braking torques requested by the ATVC due to their performance limits at high speeds, but the braking torques on the right motors are adjusted accordingly. The opposite situation occurs at 1.15 seconds, when a corrective steering angle of up to -3^o is generated by the GFASC. In this case, the ATVC requests more braking torque from the right motors than the left ones which are, once again, unable to meet the demands of the ATVC.

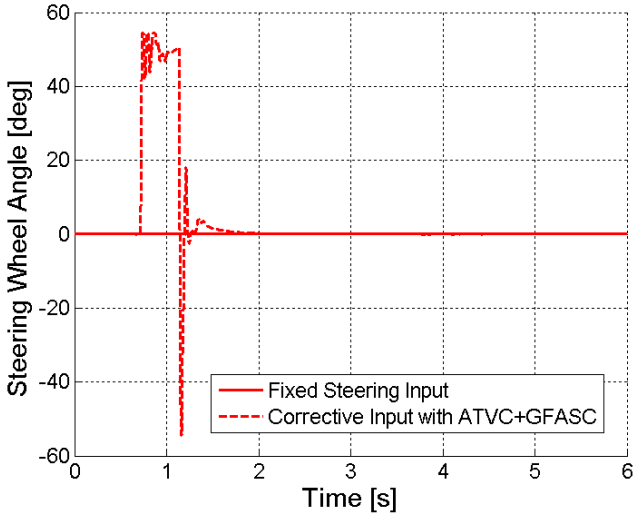

Figure 7-22: Equivalent corrective steering wheel input applied by the GFASC when using the integrated control of the ATVC and GFASC, augmenting the fixed steering input in order to correct the side-pushing effect of the vehicle when braking on a μ-split road

Comparing Figures 7-23 and 5-20, it can be confirmed that, when using the integrated control approach, the ATVC only becomes activated when the GFASC reaches its actuator range limits. Looking at Figure 7-23, it is also apparent that the slip controllers on the left wheels have limited the braking torques to 20 Nm (between 0.7 and 1.15 seconds) in order to prevent wheel lock-up while, at the same time, ensuring the maximum possible braking force is being applied when braking on the black ice patch. The activation of the slip controllers is confirmed in Figure 7-24, which illustrates the tire slip ratios while braking on the μ-split road. Note that, later in the simulation, due to the weight shift to the front axle, the motor torques at the rear axle are limited by the maximum possible motor torques (calculated by equation (5.24) in Chapter 5) to prevent wheel lock-up at higher deceleration rates. This observation is confirmed in Figure 7-25, which illustrates the traction potential for each tire. As can be seen, the traction potentials of the rear tires are restricted and do not exceed their limits. Figure 7-26 illustrates the torque distribution applied by the front-to-rear torque vectoring controller. As can be seen, this controller has requested that the front motors generate up to 52.5% of the required corrective yaw moment in order to correct the undesirable side-pushing effect when driving over the black ice patch. Requesting more torque from the front motors reduces the lateral force potential on the front axle and increases that on the rear axle. The asymmetric lateral force potentials on the front and rear axles also help to generate the required corrective yaw moment around the vertical axis of the vehicle.

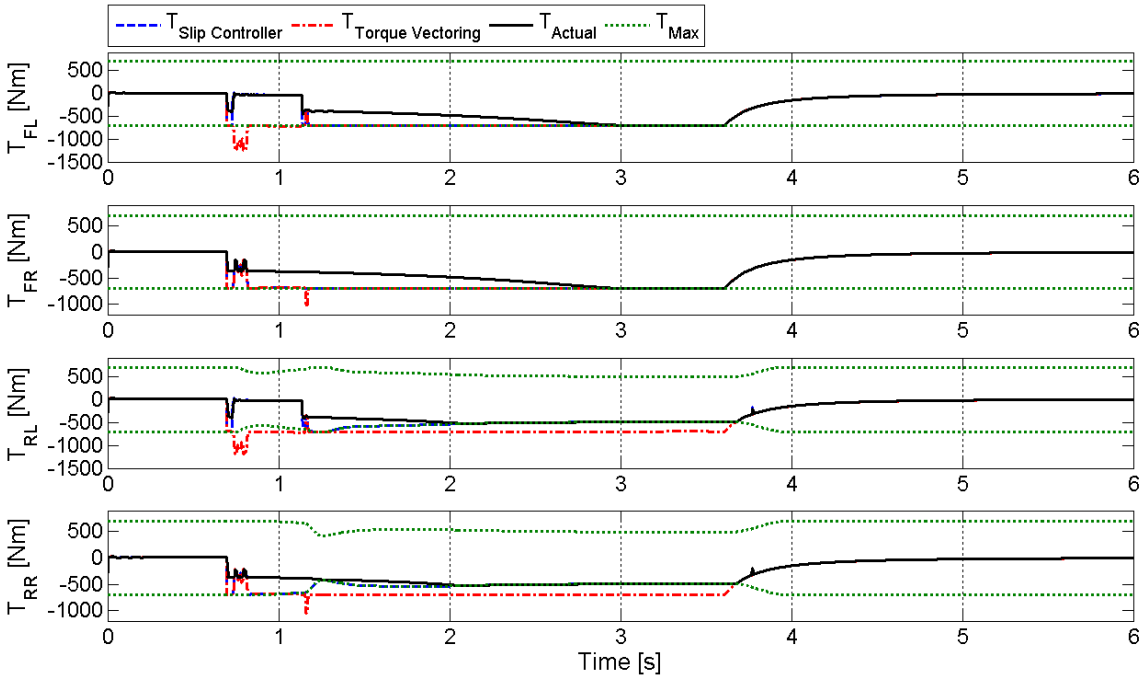

Figure 7-23: Requested and actual motor torque at each wheel when braking on a μ-split road while holding the steering wheel fixed, using the integrated control of the ATVC and GFASC

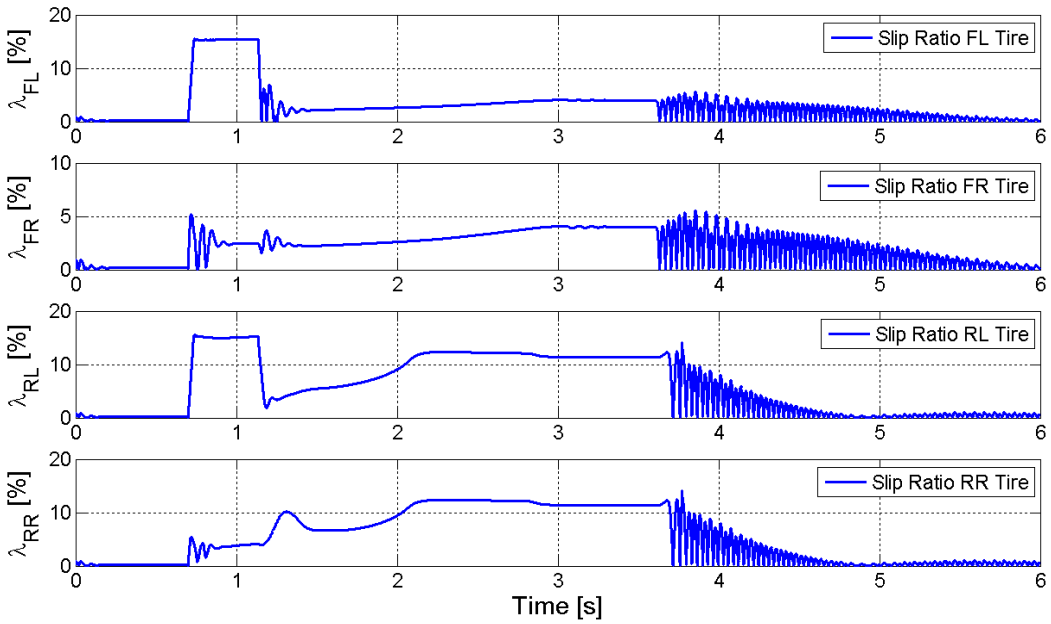

Figure 7-24: Tire slip ratios when braking on a μ-split road while holding the steering wheel fixed, using the integrated control of the ATVC and GFASC

Table 7-IV summarizes the vehicle response during the straight-line braking on a μ-split road maneuver when holding the steering wheel fixed and using the integrated control of the ATVC and GFASC. Comparing different parameters of the vehicle response during this maneuver, it can be seen that the integrated control approach is very effective at improving all the decisive parameters that describe the stability, path-

following, and braking performance of the vehicle. In particular, the integrated control approach has reduced the $|\beta|_{max}$ and $|\dot{\psi}|_{max}$ values significantly, which indicates an enhancement in the stability of the vehicle. The braking distance of the vehicle has also been reduced considerably by the integrated control approach, indicating an improvement in the longitudinal dynamics of the vehicle. The integrated control approach reduces the maximum lateral deviation of the vehicle as well, and prevents the vehicle from leaving the predefined road throughout the maneuver.

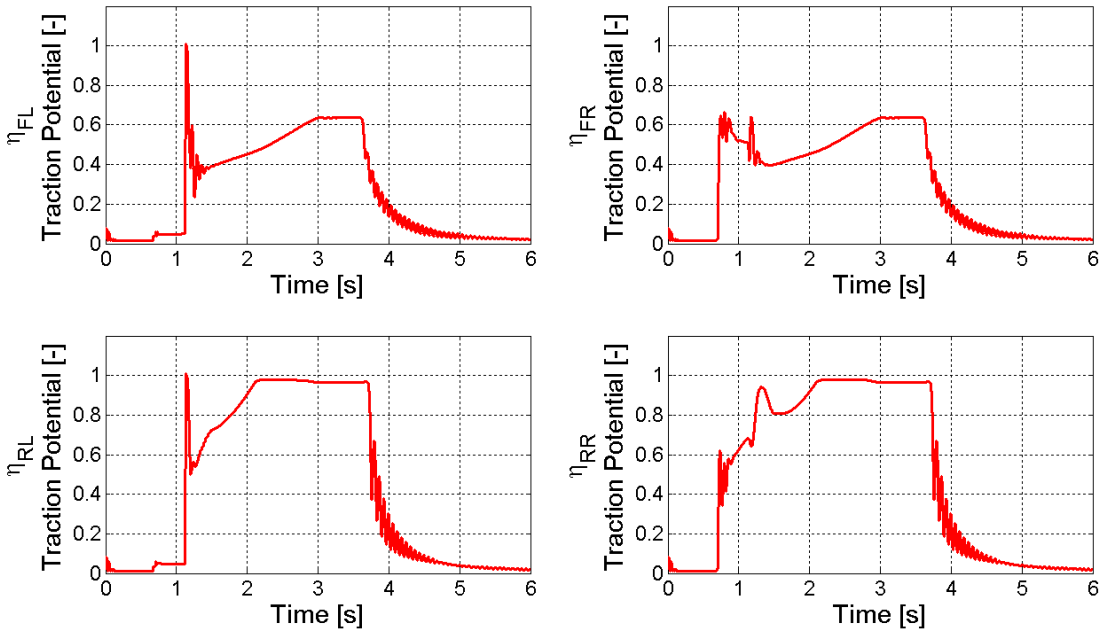

Figure 7-25: Traction potential of each tire when braking on a μ-split road while holding the steering wheel fixed, using the integrated control of the ATVC and GFASC

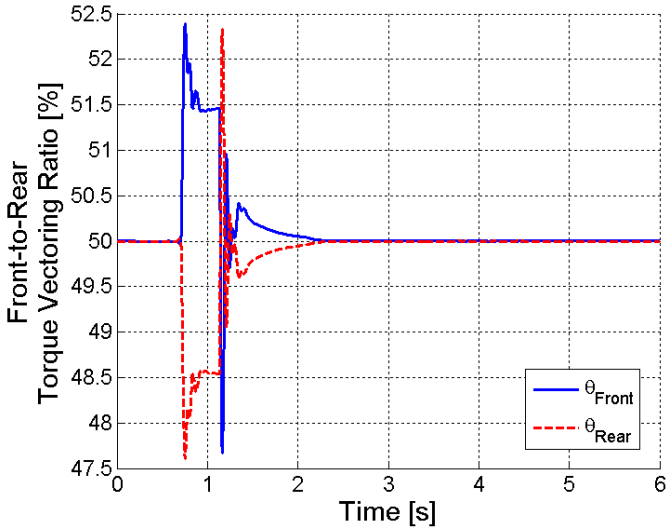

Figure 7-26: Front-to-rear torque vectoring ratios when braking on a μ-split road while holding the steering wheel fixed, using the integrated control of the ATVC and GFASC

Parameter	$\lvert\beta\rvert_{\max}$	$\lvert\dot{\psi}\rvert_{\max}$	$\Delta x_{braking}$	$\Delta y_{\max}$
AUTO21EV	24.2^{o}	63.4^{o}/s	48.4m	15.9m
GFYMC	0.40^{o}	1.85^{o}/s	44.5m	0.46m
ATVC	1.70^{o}	9.70^{o}/s	47.3m	2.70m
GFASC	1.60^{o}	2.50^{o}/s	45.7m	0.36m
ATVC+GFASC	1.45^{o}	2.35^{o}/s	45.6m	0.27m

Table 7-IV: Vehicle response during the straight-line braking on a μ-split road maneuver while holding the steering wheel fixed without a controller, with the GFYMC, with the ATVC, with the GFASC, and with the integrated control of the ATVC and GFASC

7.3. Chapter summary

In this chapter, an activation function is introduced that integrates the control efforts of the ATVC and the GFASC. A variety of test maneuvers are simulated to demonstrate the performance and effectiveness of this integrated control approach. Table 7-V provides a subjective evaluation of the effectiveness of the integrated control of the ATVC and GFASC based on different test maneuvers.

Characteristic / Maneuver	Handling	Stability	Path following	Longitudinal dynamics
Double-lane-change	2.5	3		3
Step-steer	3			
Brake-in-turn	3	3	3	
Straight-line braking on a μ-split road		3	3	2.5
Mean Value $\left(\bar{x} = \frac{1}{n}\sum_{i=1}^{n} x_i\right)$	2.83	3	3	2.75

Table 7-V: Subjective evaluation of the effectiveness of the integrated control of the ATVC and GFASC based on different test maneuvers (3 = very effective, 2 = effective, 1 = effective to some extent, 0 = ineffective)

Figure 7-27 compares the performance and effectiveness of the GFYMC, ATVC, GFASC, and the integrated control of the ATVC and GFASC based on different test maneuvers (as listed in Tables 4-VII, 5-V, 6-VI, and 7-V, respectively). Note that the GFYMC is considered to be the ideal stability controller against which the performance and effectiveness of all other controllers are compared. As can be seen, the performance and effectiveness of the integrated control approach exceeds that of the individual control

systems in all four categories. In addition, the integrated control of the ATVC and GFASC demonstrates the same performance as the GFYMC in the stability and longitudinal dynamics categories. Although the performance of the integrated control approach in the handling category cannot match that of the GFYMC, the integrated controller demonstrates better performance in the path-following category.

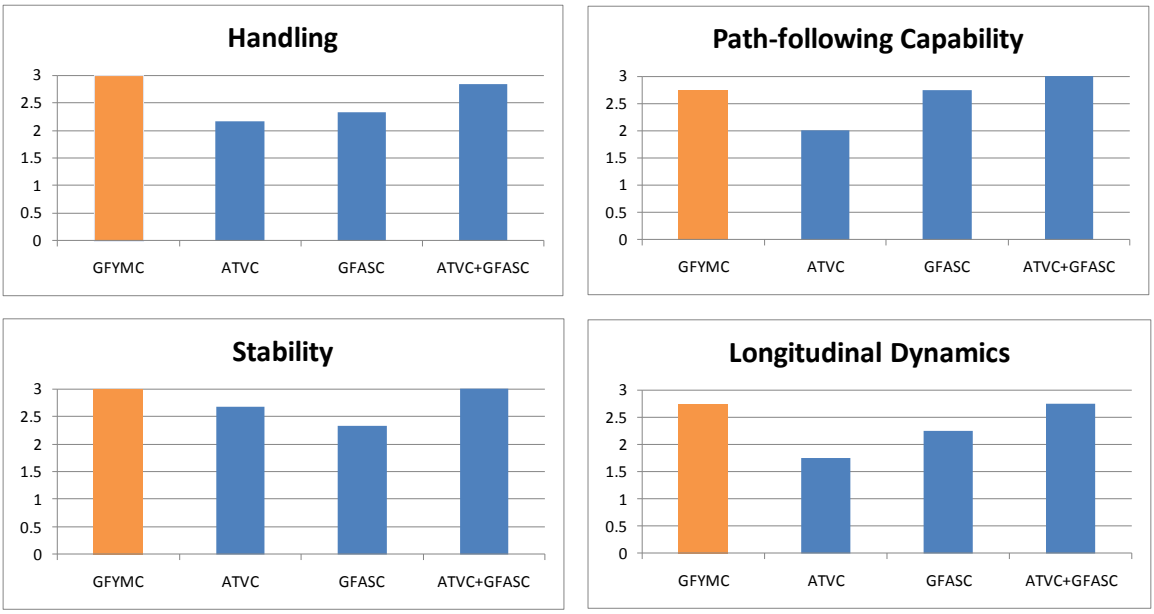

Figure 7-27: Subjective evaluation of the performance and effectiveness of the GFYMC, ATVC, GFASC, and integrated control of the ATVC and GFASC based on different test maneuvers (3 = very effective, 2 = effective, 1 = effective to some extent, 0 = ineffective)

8 Conclusions and Future Work

The vision for the future automotive chassis is to interconnect the lateral, longitudinal, and vertical dynamics by controlling the driving, braking, steering, and damping actions of each wheel separately. Drive-by-wire technology is currently being used in concept vehicles for the electronic control and actuation of braking, steering, suspension, and drive systems. These technologies attract strong interest from the automotive industry but, for the most part, are not yet commercially available.

The chassis control systems developed today are distinguished by the way the individual subsystems work in order to provide vehicle stability and control. Since the influences of individual subsystems are interconnected and coupled through the tire-road characteristics, each individual subsystem often influences two of the three vehicle dynamics domains (namely, the longitudinal, lateral, or vertical dynamics). Therefore, by installing more than one chassis control system into a vehicle, it must be ensured that the systems function together properly and do not interfere with each other. This level of cooperation requires that the individual chassis control systems are integrated and networked together using a high-level supervisory control system that can monitor and coordinate the behaviour of the individual subsystems, assigning appropriate tasks to each of them depending on the driving maneuver and road conditions. Ultimately, the optimum driving dynamics can only be achieved when the tire forces on all wheels and in all three directions can be influenced and controlled precisely. Only in this way can the highest level of active safety, ride quality, and driving pleasure be achieved in every possible driving situation, up to the limits of adhesion.

Recently, mostly due to global warming concerns and high oil prices, electric vehicles have attracted a great deal of interest as an elegant solution to environmental and energy problems. In fact, we are likely to see more changes in automotive powertrains in the next five years than we have seen in the last 100 years. Many car companies have already revealed their plans to bring plug-in hybrid and battery electric vehicles to the commercial market in the next five years [Adc10]. In addition to the fact that electric vehicles have no tailpipe emissions and are more efficient than internal combustion engine vehicles, they represent an exciting platform on which to apply advanced motion

control techniques, since the torque of an electric motor can be generated and controlled quickly and precisely in an efficient way.

The prime focus of this thesis is to develop effective control strategies to improve driving dynamics and safety based on the philosophy of individually monitoring and controlling the tire forces on each wheel. In this regard, an electric vehicle with four direct-drive in-wheel motors and an active steering system is designed and modelled in the ADAMS/View environment. This platform represents a two-passenger electric all-wheel-drive urban vehicle (AUTO21EV) that has a similar configuration to the commercially-available Smart *fortwo*. The front and rear suspension systems of the AUTO21EV are designed, analyzed, and tuned to have a high amount of flexibility in their kinematic layouts, providing self-steering behaviour, Ackermann steering, anti-squat mechanism, and maintaining the maximum lateral force potential on the tires when cornering. The dynamic characteristics of the suspension systems are also analyzed and optimized to minimize the effects of the large sprung mass and the vibrations and dynamic loads that are transmitted to the chassis and suspension components. The full kinematic model of the AUTO21EV is later transformed into a dynamic model in ADAMS/View by equipping the vehicle with Pacejka tire models and introducing a road model. The results of these analyses are presented in Appendix A.

In Chapter 2, a number of different open-loop and closed-loop test maneuvers are identified that can provide important information about different aspects of the dynamic behaviour of the vehicle and the performance and effectiveness of individual chassis control systems. These test maneuvers are chosen such that all aspects of the vehicle dynamics are addressed. In addition, a comprehensive evaluation method is presented that combines the results of different test maneuvers and evaluates them as a whole to identify the advantages of each control method. Since closed-loop test maneuvers are used in this work, two driver models are developed and implemented in the simulation environment for providing the driver inputs required to successfully negotiate the maneuvers. In this regard, a multiple-preview-point path-following driver model is developed that can look ahead and adjust the steering wheel angle based on the lateral offset between predefined preview points on the optical lever of the driver and the desired path. Moreover, a gain scheduling PID controller is developed for the speed-control driver model, which can adjust the speed of the vehicle to that requested by the driver by controlling the torques of

the in-wheel motors. The performance and effectiveness of the driver models are evaluated and confirmed using some standard test maneuvers. It has been confirmed that both the path-following and speed-control driver models are able to negotiate complex test maneuvers, such as the ISO double-lane-change maneuver and brake-in-turn maneuver, very well.

In Chapter 3, an advanced fuzzy slip controller is developed for the AUTO21EV that combines the functionalities of an ABS, a TCS, and the brake system of the vehicle. This slip controller is designed based on the idea of limiting the maximum possible tire slip ratio to a fixed, predefined amount in order to generate the maximum possible braking or traction force while decelerating or accelerating, respectively, on different road conditions. The performance and functionalities of the developed fuzzy slip control system are evaluated using several standard test maneuvers. It has been confirmed that the fuzzy slip controller is able to fulfill the functionalities of the ABS and conventional hydraulic brake systems by outperforming the regulations on braking systems for passenger vehicles. It has been also confirmed that the fuzzy slip controller is able to maximize the traction potential of each tire when accelerating.

In Chapter 4, a 14-degree-of-freedom vehicle model is developed to allow for the testing of different control strategies, and for applying a genetic tuning algorithm to the development of the fuzzy yaw moment controller. Based on this simplified vehicle model, a fuzzy yaw moment controller is developed for the AUTO21EV that determines the corrective yaw moment required to minimize the sideslip and yaw rate errors of the vehicle, comparing the actual values to those obtained using a reference model, with the ultimate objective of following the desired trajectory requested by the driver. The fuzzy yaw moment controller is designed as a high-level supervisory module that assigns tasks to low-level actuators and controllers, employing an integrated chassis control management philosophy. However, at this stage of development, the calculated corrective yaw moment is applied directly to a torque driver that is positioned at the center of mass and around the vertical axis of the vehicle. Although this torque driver symbolizes an unrealistic control system, the fuzzy yaw moment controller represents the ideal stability control system, in which any corrective yaw moment can be generated without being restricted by the actuator range limits or performance. In addition, a novel hybrid genetic-fuzzy tuning technique is developed to optimize the shape and distribution of the

membership functions of the fuzzy controller. By combining a multi-criteria genetic algorithm with the fuzzy yaw moment controller, a more powerful genetic fuzzy yaw moment controller is produced that provides better performance. The effectiveness and performance of the genetic fuzzy yaw moment controller is evaluated using a variety of test maneuvers. In particular, it has been confirmed through several maneuvers that the genetic fuzzy yaw moment improves the handling, stability, path-following, and longitudinal dynamics of the vehicle considerably in comparison to those obtained when no stability controller is active.

Chapter 5 describes the development of an advanced low-level torque vectoring controller that receives tasks from the previously developed high-level genetic fuzzy yaw moment controller. The objective of the advanced torque vectoring controller is to generate the required corrective yaw moment through the torque intervention of the individual in-wheel motors to stabilize the vehicle during normal and emergency driving maneuvers. A novel algorithm is developed for the left-to-right torque vectoring control on each axle, and a PD controller is introduced for the front-to-rear torque vectoring distribution action. Again, the effectiveness and performance of the advanced torque vectoring controller is evaluated using several test maneuvers. It has been confirmed that, although the advanced torque vectoring controller has improved all the decisive parameters that describe the handling, stability, path-following, and longitudinal dynamics of the vehicle in comparison to the results obtained when no stability controller is active, it cannot be considered as effective as the genetic fuzzy yaw moment controller, which represents the ideal case but is not directly realizable. In addition, it has been observed that the actuation of the in-wheel motors when stabilizing the vehicle near its handling limits would cause severe oscillation in the yaw rate response, which would be perceived by the driver as being disruptive and annoying. Therefore, in practice, the advanced torque vectoring controller should not be used for correcting small yaw rate errors.

In Chapter 6, a novel fuzzy active steering controller is developed, and a reliable method to tune its membership functions in an optimized way is presented, which can make it unnecessary to perform much of the expensive field testing that would otherwise be used to tune a stability control system. Fuzzy logic is chosen for the active steering controller because it represents a robust and flexible inference method that is well suited

for tackling the highly nonlinear behaviour inherent in vehicle dynamics. The rule base of the fuzzy active steering controller is described in vague linguistic terms using expert knowledge, which suits the nonlinear behaviour of vehicle dynamics. A novel multi-criteria genetic algorithm, which is similar to the one introduced in Chapter 4, is presented to optimize the distribution of the fuzzy membership functions of the input and output variables in order to improve the performance of the fuzzy active steering controller. Again, the performance and effectiveness of the genetic fuzzy active steering controller are evaluated using several test maneuvers. It has been confirmed that the genetic fuzzy active steering controller can improve all the decisive parameters that describe the handling, stability, path-following, and longitudinal dynamics of the vehicle when compared to the case in which no stability controller is active; however, it is not as effective as the genetic fuzzy yaw moment controller. In addition, it has been confirmed that the performance and effectiveness of the genetic fuzzy active steering controller is superior in the vehicle handling, path-following, and longitudinal dynamics when compared to the results obtained using the advanced torque vectoring controller. However, due to the actuator rage limits of the genetic fuzzy active steering controller, the advanced torque vectoring controller demonstrates better performance in the stability category.

Chapter 7 addresses the integration of the developed advanced torque vectoring controller and genetic fuzzy active steering controller. Comparing the performance and effectiveness of the individual control systems, it has been found that the intervention of the genetic fuzzy active steering controller is considered to be a continuous process, and is not perceived by the driver as being annoying. It is also advantageous to employ steering intervention rather than braking or driving individual wheels when controlling the vehicle on slippery surfaces, since steering intervention requires less frictional force between the tire and the road to generate a corrective yaw moment. However, the genetic fuzzy active steering controller suffers from its limited range of effectiveness (caused by actuator restrictions). The advanced torque vectoring controller, on the other hand, is found to be very effective at improving the vehicle stability and handling, even when the vehicle is driven near its handling limits. However, it has also been observed that the actuation of the in-wheel motors to generate a corrective yaw moment can cause some oscillations in the vehicle states, which might be perceived by the driver as being

disruptive. To overcome the shortcomings of each of these control systems, a novel activation function is introduced that takes advantage of the strengths of each chassis control system and distributes the required control effort between the in-wheel motors and the active steering system based on the difference between the desired and actual behaviour of the vehicle. The performance and effectiveness of the integrated approach are evaluated using several maneuvers. It is confirmed that the integrated control approach has superior performance over the individual control systems in all chosen test maneuvers. The integrated control of the advanced torque vectoring and genetic fuzzy active steering controller has demonstrated the same performance as the genetic fuzzy yaw moment controller in the stability and longitudinal dynamics categories. Moreover, although the performance of the integrated control approach in the handling category cannot match that of the genetic fuzzy yaw moment controller, the integrated controller demonstrates better performance in the path-following category.

Although all of the control strategies developed in this work have demonstrated a good performance and effectiveness at increasing the vehicle stability, handling, path-following, and longitudinal dynamics, further effort has been invested into discovering an optimal method of generating the required corrective yaw moment using the available actuators and controllers. In this regard, a more elegant approach can be found in the aerospace and marine vessel industries, which deal with over-actuated systems, and is called the ‘control allocation’ technique [Hae03, Dur93, And07, Ore06]. In this method, the control effort is determined in two separate steps: in the first step, conventional control laws are used to determine the total control effort that must be produced; in the second step, a control allocator is used to map the total control demand onto individual actuator settings, taking into account various actuator constraints. Therefore, a logical future extension of this work should involve the use of an optimization-based control allocation method that can allocate the required corrective yaw moment generated by the genetic fuzzy yaw moment controller between the in-wheel motors and the active steering controller in an optimal way. It would be very interesting to compare the performance and effectiveness of the control allocation method with the results obtained using the integrated control approach developed in this work. In this way, the effectiveness of each control system can be compared against an optimization based control allocation method

and better conclusions can be made about the operation and effectiveness of the developed controllers in this work.

It is also very important to examine the robustness of the developed control systems against internal and external disturbances. This should be done both in the simulation environment and, later, through various field testing of a physical prototype of the AUTO21EV. In this regard, a parameter sensitivity analysis should be performed to understand the most important model parameters and the sensitivity of the different control systems with respect to these parameters. Note that the sensitivity of the control systems against the various parameters of the Magic Tire Formula should contain the major part of this analysis. Moreover, the sensitivity of the control systems to different sampling times has to be analyzed.

As mentioned earlier, there is also an immediate need for a friction coefficient estimator, since the bicycle model and the maximum torque estimator of the advanced torque vectoring controller require knowledge of the current friction coefficient between the tire and the road in order to adequately adapt to various road conditions.

Although the performance of the advanced fuzzy slip controller and the genetic fuzzy active steering controller have been confirmed in a driving simulator set up, the performance of the advanced torque vectoring controller and the integrated control approach of the genetic fuzzy active steering controller and the advanced torque vectoring controller have to be confirmed in the driving simulator environment as well. Ultimately, the performance and effectiveness of all of the developed control systems have to be examined, analyzed, and confirmed on a physical prototype of the AUTO21EV using a human driver. In this regard, the human driver can subjectively evaluate the effectiveness of each candidate controller in real driving conditions and compare his evaluations with those performed using a driver model in this work.

References

[Ack98] Ackermann, J.: “Active steering for better safety, handling, and comfort”, Conference on Advances in Vehicle Control and Safety, Amiens, France, 1998.

[Ack99] Ackermann, J., Odenthal, D., and Bünte, T.: “Advantages of active steering for vehicle dynamics control”, 32nd International Symposium on Automotive Technology and Automation, Vienna, pp. 263-270, 1999.

[ADA02] ADAMS/Tire manual: “Using ADAMS/Tire”, Mechanical Dynamics, Part Nr. 120TIRG-01, 2002.

[Adc10] Adcock, I., Bailey, S., and Simanaitis, D.: “Propulsion Prognostications: Who’s coming out with what – and when?”, Road & Track magazine, Vol. 61, No. 7, March 2010.

[Aga03] Aga, M. and Okada, A.: “Analysis of Vehicle Stability Control (VSC)’s effectiveness from accident data”, Paper Number 541, Proceedings of the 18th International Technical Conference on the Enhanced Safety of Vehicle, National Highway Traffic Safety Administration, Washington DC, 2003.

[Aks06] Akshay, S.: Special ADAMS/Car Training for Universities, MSC Software, 2006.

[Alb96] Alberti, V. and Babbel, E.: “Improved driving stability by active braking of the individual wheels”, Proceedings of the International Symposium on Advanced Vehicle Control, Aachen, pp. 717-732, 1996.

[And06] Andreasson, J., Knobel, C., and Bünte, T.: “On road vehicle motion control – striving towards synergy”, Proceedings of the 8th International Symposium on Advanced Vehicle Control, AVEC060209, Taiwan, 2006.

[And07] Andreasson, J.: On Generic Road Vehicle Motion Modelling and Control, Ph.D. Dissertation, Royal Institute of Technology, Stockholm, Sweden, 2007.

[ATZ06] ATZ magazine: “Automobiltechnische Zeitschrift”, ISSN 0001-2785-10810, May, 2006.

[Bau99] Bauer, H. et al.: Driving-safety Systems, Society of Automotive Engineers and Robert Bosch GmbH, 2nd edition, Warrendale, 1999.

[Bei00] Beiker, S.: Improving the Vehicle Dynamics Behaviour through Integrated Control Systems, (“Verbesserungsmoeglichkeiten des Fahrverhaltens von Pkw durch

zusammenwirkende Regelsysteme"), Ph.D. Dissertation, Technical University of Braunschweig, Germany, 2000.

[Bix95] Bixel, R., Heydinger, G.J., Durisek, N. J., and Guenther, D.A.: "Developments in vehicle center of gravity and inertial parameter estimation and measurement", SAE World Congress, 950356, 1995.

[Blu04] Blundell, M. and Harty, D.: The Multibody Systems Approach to Vehicle Dynamics, Society of Automotive Engineers, 2004.

[Bod06] Bode, K.H.: Preliminary Suspension Design and Stability Control Strategies for an Electric Vehicle with Four Independently Driven In-Wheel Motors, Project Thesis, University of Waterloo, 2006.

[Bol95] Bolton, W.: Mechatronics – Electronic Control Systems in Mechanical Engineering, Longman Scientific and Technical, 1995.

[Bos07] Bosch Automotive Handbook, 7th edition, Robert Bosch GmbH, Plochingen, 2007.

[Bow93] Bowman, J.E. and Law, E.H.: "A feasibility study of an automotive slip control braking system", SAE World Congress, 930762, Detroit, 1993.

[Bra94] Brandt, B.: Build Your Own Electric Car, TAB Books, 1994.

[Bur04] Burton, D., Delaney, A., Newstead, S., Logan, D., and Fildes, B.: "Effectiveness of ABS and vehicle stability control systems", Royal Automobile Club of Victoria (RACV) Ltd., Report Number 04/01, April 2004.

[Bur93] Burckhardt, M.: Chassis and Suspension Design: Slip Control Systems (Fahrwerktechnik: Radschlupfregelsysteme), Vogelverlag, Wuerzburg, 1993.

[Cas96] Casey, J.: Exploring Curvature, Friedrich Vieweg and Sohn Verlag, Wiesbaden, Germany, 1996.

[Cor01] Cordon, O., Herrera, F., Hoffmann, F., and Magdalena, L.: Genetic Fuzzy Systems: Evolutionary Tuning and Learning of Fuzzy Knowledge Bases (Advances in Fuzzy Systems - Applications and Theory), 19, World Scientific Publishing, 2001.

[Cor04] Cordon, O., Gomide, F., Hoffmann, F., and Magdalena, L.: "Ten years of genetic fuzzy systems: current framework and new trends", Fuzzy Sets and Systems, 141, pp. 5-31, 2004.

[Cun89] Cundy, H. and Rollett, A.: "Lissajous figures", Section 5.5.3 in Mathematical Models, 3rd edition, Tarquin Publication, Stradbroke, England, pp. 242-244, 1989.

[Dan04] Dang, J.: Preliminary Results Analyzing Effectiveness of Electronic Stability Control (ESC) Systems, DOT HS 809 790, 2004.

[Dix96] Dixon, J.C.: Tires, Suspension, and Handling, Society of Automotive Engineers, 2nd edition, 1996.

[Don95] Donges, E.: "Supporting drivers by chassis control systems", in Smart Vehicles, J.P. Pauwelussen, H.B. Pacejka (eds.), pp. 276-296, Delft, 1995.

[Dur03] Durali, M. and Bahramzadeh, Y.: "Vehicle stability improvement using fuzzy controller and neural-network slip angle observer", SAE World Congress, 2003-01-2883, Detroit, 2003.

[Dur93] Durham, W.C.: "Constrained control allocation", Journal of Guidance, Control, and Dynamics, 16(4), pp. 717-725, 1993.

[Elb04] Elbers, C., Ersoy, M., and Fecht, N.: Automotive Chassis Technology – Fundamentals, concepts, processes and trends, ZF Lemfoerder Fahrwerktechnik, printed by the Verlag Moderne Inductrie, 2004.

[Far04] Farmer, C.: "Effect of electronic stability control on automobile crash risk", Traffic Injury Prevention, 5, pp. 317-325, 2004.

[FMV07] FMVSS No. 126, Electronic Stability Control Systems; Controls and Displays, Docket No. NHTSA–200727662, 2007.

[Gil92] Gillespie, T.D.: Fundamentals of Vehicle Dynamics, Society of Automotive Engineers, 1992.

[Gol89] Goldenberg, D.E.: Genetic Algorithms in Search, Optimization, and Machine Learning, Addison-Wesley, 1989.

[Gor03] Gordon, T.: "Integrated control methodology for road vehicles", Vehicle System Dynamics, 40(1-3), pp. 157-190, 2003.

[Gre06] Green, P. and Woodrooffe, J.: The Effect of Electronic Stability Control on Motor Vehicle Crash Prevention, UMTRI200612, Transportation Research Institute, University of Michigan, 2006.

[Gri98] Gribben, C.: Debunking the Myth of EVs and Smokestacks, Electric Vehicle Association of Greater Washington, D.C., 1998.

[Guo82] Guo, K.H.: "A statistical analysis of vehicle vibration and dynamic loads, and selection of suspension design parameters", Technical Report UM-MEAM-82-15, Dep. of Mech. Eng., University of Michigan, Ann Arbor, 1982.

[Guo93] Guo, K. and Guan, H.: "Modeling of driver/vehicle directional control system", Vehicle System Dynamics, 22(3-4), pp. 141-184, 1993.

[Gur99] Gurocak, H.B.: "A genetic-algorithm-based method for tuning fuzzy logic controllers", Fuzzy Sets and Systems, 108(1), pp. 39-47, 1999.

[Hae03] Haerkegrad, O.: Backstepping and Control Allocation with Applications to Flight Control, Ph.D. Thesis, University of Linkoping, 2003.

[Ham03] Hammett R.C. and Babcock, P.S.: "Achieving 10^{-9} dependability with drive-by-wire systems" SAE World Congress, 2003-01-1290, Detroit, 2003.

[Han94] Hanselman, D.C.: Brushless Permanent Magnet Motor Design, McGraw-Hill, New York, 1994.

[Her96] Herrera, F. and Lozano, M.: "Adaptation of genetic algorithm parameters based on fuzzy logic controllers", in Genetic Algorithms and Soft Computing, F. Herrera and J.L. Verdegay (eds.), Physica-Verlag, pp. 95-125, 1996.

[Hor04] Hori, Y.: "Future vehicle driven by electricity and control – research on four wheel motored UOT Electric March II", IEEE Transactions on Industrial Electronics, 51(5), pp. 954-962, 2004.

[Hro81] Hrovat, D. and Hubbard, M.: "Optimum vehicle suspensions minimizing RMS rattle space, sprung-mass acceleration and jerk", Journal of Dynamic Systems Measurement and Control, ASME, 103(3), pp. 228-236, 1981.

[Ise02] Isermann, R., Schwarz, R., and Stölzl, S.: "Fault-tolerant drive-by-wire systems", IEEE Control Systems Magazine, 2002.

[ISO82] ISO 4138: Passenger cars – Steady-state Circular Test Procedure, 1982.

[ISO85] ISO 7975: Passenger cars – Braking in a Turn: Open-loop Test Procedure, 1985.

[Jal04] Jalali, K.: The Concept and Development of an Optimized Actuator for the Clutch of a Transfer Case, Diploma Thesis, RWTH Aachen, 2004.

[Jal05] Jalali, K.: "Design, Optimization, and Kinematics Analysis of a Front Double-Wishbone Suspension Using ADAMS/View", ME752 course project report, University of Waterloo, 2005.

[Jal07] Jalali, K., Lambert, S., and McPhee, J.: "Optimization of a vehicle suspension using a genetic algorithm method", 21st Canadian Congress of Applied Mechanics, CANCAM, 2007.

[Jal10] Jalali, K., Uchida, T., Lambert, S., and McPhee, J.: "Development of an advanced slip controller and an active steering system for an electric vehicle with in-wheel motors using soft computing techniques", awaiting publication, 2010.

[Jan98] Jantzen, J.: "Design of fuzzy controllers", Technical University of Denmark, Department of Automation, Tech. Report Number 98-E 864 (design), 19 August, 1998.

[JB04] JB: "Drive-by-Wire Pininfarina Autosicura – White Paper", Pi Technology, UK, 2004.

[Jur06] Jurgen, R.K.: Electronic Braking, Traction, and Stability Control, Volume 2, SAE International, 2006.

[Kar04] Karray, F.O. and de Silva, C.: Soft Computing and Intelligent Systems Design, Pearson Education Limited, 2004.

[Kie05] Kiencke, U. and Nielsen, L.: Automotive Control Systems for Engine, Driveline, and Vehicle, 2nd edition, Springer, 2005.

[Kno99] Knoop, M., Leimbach, K.D., and Schroeder, W.: "Increased driving comfort and safety by electric active steering", Active Safety TOPTEC, Wien, September, 1999.

[Koe04] Koehn, P. and Echrich, M.: "Active steering – The BMW approach towards modern steering technology", SAE World Congress, 2004-01-1105, Detroit, 2004.

[Koe06] Koehn, P., Eckrich, M., Smakman, H., and Schaffert, A.: "Integrated chassis management: Introduction into BMW's approach to ICM", SAE World Congress, 2006-01-1219, Detroit, 2006.

[Lib05] Liebemann, E.K., Meder, K., Schuh, J., and Nenninger, G.: "Safety and performance enhancement: The Bosch Electronic Stability Control (ESP)", Paper Number 05-0471, International Technical Conference of the Enhanced Safety of Vehicles (ESV), Washington, DC, 2005.

[Lie05] Lie A., Tingvall, C., Krafft, M., and Kullgren, A.: "The effectiveness of ESC (Electronic Stability Control) in reducing real life crashes and injuries", Paper Number 050135, Proceedings of the 19th International Technical Conference on the Enhanced Safety of Vehicle, National Highway Traffic Safety Administration, Washington DC, 2005.

[Mac96] MacAdam, C.C. and Johnson, G.F.: "Application of elementary neural networks and preview sensors for representing driver steering control behavior", Vehicle System Dynamics, 25(1), pp. 3-30, 1996.

[Mam02] Mammar, S. and König, D.: "Vehicle handling improvement by active steering", Vehicle System Dynamics, 38(3), pp. 211-242, 2002.

[Man07] Manning, W.J. and Crolla, D.A.: "A review of yaw rate and sideslip controllers for passenger vehicles", Transactions of the Institute of Measurement and Control, 29(2), pp. 117-135, 2007.

[Mar02-a] Marshek, K., Cuderman II, J., and Johnson, M.: "Performance of anti-lock braking system equipped passenger vehicles - Part I: Braking as a function of brake pedal application force", SAE World Congress, 2002-01-0304, Detroit, 2002.

[Mar02-b] Marshek, K., Cuderman II, J., and Johnson, M.: "Performance of anti-lock braking system equipped passenger vehicles - Part II: Braking as a function of initial vehicle speed in braking maneuver", SAE World Congress, 2002-01-0307, Detroit, 2002.

[Maz01] Mazzae, E.N., Garrott, W.R., Barickman, F., Ranney, T.A., and Snyder, A.: "NHTSA light vehicle anti-lock brake system research program-Task 7.1: Examination of ABS-related behavioral adaptation - License plate study", DOT HS 809 430, November 2001.

[McP05] McPhee, J.: Unified Modeling Theories for the Dynamics of Multidisciplinary Multibody Systems, in Advances in Computational Multibody Systems, J. Ambrosio (ed.), Springer-Verlag, pp. 129-158, 2005

[Mil02] Milliken W.F. and Milliken, D.L.: Chassis Design: Principles and Analysis – Based on Unpublished Technical Notes by Maurice Olley, Society of Automotive Engineers, 2002.

[Mil95] Milliken, W.F. and Milliken, D.L.: Race Car Vehicle Dynamics, Society of Automotive Engineers, Warrendale, 1995.

[Mit82] Mitschke, M.: Dynamic der Kraftfahrzeuge, Band A, Springer Verlag, 1982.

[MMG10] L-3 Communications Magnet-Motor GmbH, Starnberg, Germany, http://www.magnet-motor.de, 2010.

[Oez95] Oezguener, O., Uenyelioglu, K.A., and Hatipoglu, C.: "An analytical study of vehicle steering control", Proceedings of the 4th IEEE Conference on Control Applications, pp. 125-130, 1995.

[Ore06] Orend, R.: Integrierte Fahrdynamikregelung mit Einzelradaktorik – Ein Konzept zur Darstellung des fahrdynamischen Optimums, Ph.D. Dissertation, University of Erlangen-Nuernberg, Erlangen, 2006.

[Pac02] Pacejka, H.B.: Tire and Vehicle Dynamics, SAE International, Warrendale, 2002.

[Pac97] Pacejka, H.B. and Besselink, I.J.M.: "Magic formula tire model with transient properties", Vehicle System Dynamics, 27 (Suppl.), pp. 234-249, 1997.

[Pai05] Paine, M.: "Electronic stability control: Review of research and regulations", Vehicle Design and Research Pty Limited, Report Number G248, June, 2005.

[Pel05] Pelchen, C., Zdych, R., Baasch, D., and Kubalczyk, R.: "Improvement of vehicle agility and safety by means of wheel torque based driving dynamics", 14th Aachen Colloquium, Automobile and Engine Technology, 2005.

[Pen96] Peng, H. and Hu, J.S.: "Traction/braking force distribution for optimal longitudinal motion during curve following", Vehicle System Dynamics, 26, pp. 301-320, 1996.

[Pet05] Petersen, W.: "Development of a tool for rapid design and analysis of trailing and semi-trailing arm suspensions", Project Thesis, University of Waterloo, 2005.

[Pil89] Pillay, P. and Krishnan, R.: "Modeling, simulation, and analysis of permanent magnet motor drives, Part I: The permanent-magnet synchronous motor drive", IEEE Transactions on Industry Applications, 25(2), pp. 265-273, 1989.

[Rah85] Rahman, M.A. and Slemon, G.R.: "Promising applications of neodymium boron iron magnets in electrical machines", IEEE Transactions on Magnetics, MAG-21(5), pp. 1712-1716, 1985.

[Rei02] Reimpell, J., Stoll, H., and Betzler, W.: The Automotive Chassis: Engineering Principles, Society of Automotive Engineering, 2nd edition, 2002.

[Rei04] Reinelt, W., Klier, W., Reimann, G., Schuster, W., and Grossheim, R.: "Active front steering (Part 2): safety and functionality", SAE World Congress, 2004-01-1101, Detroit, 2004.

[Rey03] Reynolds, B. and Wheals, J.: "Torque vectoring driveline: Design, simulations, capabilities and control", 12th Aachen Colloquium, Automobile and Engine Technology, pp. 1497-1523, 2003.

[Rie05] Rieger, G., Scheef, J., Becker, H., Stanzel, M., and Zobel, R.: "Active safety systems change accident environment of vehicles significantly – A challenge for vehicle design", Paper Number 050052, Proceedings of the 19th International Technical

Conference on the Enhanced Safety of Vehicle, National Highway Traffic Safety Administration, Washington DC, 2005.

[Rie99] Rieth, P.: "Electronic driver assistance" (in German), in VDA-Technischer Kongress, pp. 119-136, Frankfurt, 1999.

[Roe77] Roenitz, R., Braess, H.H., and Zomotor, A.: "Methods and criterions for evaluation of the behaviour of the passenger vehicle – Part I", ("Verfahren und Kriterien zur Bewertung des Fahrverhaltens von Personenkraftwagen – Stand und Problematik, Teil 1"), ATZ Automobiltechnische Zeitschrift, 1/77 and 3/77, pp. 29-38 and 39-46, 1977.

[Roe98] Roenitz, R., Braess, H.H., and Zomotor, A.: "Methods and criterions for evaluation of the behaviour of the passenger vehicle – Part II", ("Verfahren und Kriterien zur Bewertung des Fahrverhaltens von Personenkraftwagen – Ein Rueckblick auf die letzten 20 Jahre, Teil 2"), ATZ Automobiltechnische Zeitschrift, 99/100, pp. 780-786, 1998.

[San05] Sanna, L.: "Driving the solution: The plug-in hybrid vehicle", EPRI Journal, 2005.

[Say96] Sayers, M.W. and Han, D.: "A generic multibody vehicle model for simulating handling and braking", Vehicle System Dynamics, 25(Suppl.), pp. 599-613, 1996.

[Sch04] Schmitke, C.: Modelling Multibody Multi-domain Systems using Subsystems and Linear Graph Theory, Ph.D. Thesis, University of Waterloo, 2004.

[Sch08] Schmitke, C., Morency, K., and McPhee, J.: "Using graph theory and symbolic computing to generate efficient models for multi-body vehicle dynamics", Journal of Multibody Dynamics, 222(K4), pp. 339-352, 2008.

[Sem06] Semmler, S.J., Reith, P.E., and Linkenbach, S.J.: "Global chassis control – The networked chassis", SAE World Congress, 2006-01-1954, Detroit, 2006.

[Sha00] Sharp, R.S., Casanova, D., and Symonds, P.: "A mathematical model for driver steering control, with design, tuning and performance results", Vehicle System Dynamics, 33, pp. 289-326, 2000.

[Sma10] Smart Canada, fortwo coupé specifications, http://www.thesmart.ca, 2010.

[Ter97] Terashima, M., Ashikaga, T., Mizuno, T., Natori, K., Fujiwara, N., and Yada, M.: "Novel motors and controller for high-performance electric vehicle with four in-wheel motors", IEEE transactions on industry electronics, 44(1), February, 1997.

[TM410] TM4 Inc., Quebec, Canada, http://www.tm4.com/home.aspx, 2010.

[Vel01] Veloso, F. and Fixson, F.: "Make-buy decisions in the auto industry: New perspectives on the role of the supplier as an innovator", Technological Forecasting and Social Change, 67, pp. 239-257, 2001.

[Vog07] Vogt, H.: Real Time Dynamics Simulation of an Electric Vehicle with In-Wheel Motors, Project Thesis, University of Waterloo, 2007.

[Vog09] Vogt, H., Schmitke, C., Jalali, K., and McPhee, J.: "Unified modelling and real-time simulation of an electric vehicle", International Journal of Vehicle Autonomous Systems, 6(3-4), pp. 288-307, 2009.

[Vog98] Voget, S. and Kolonko, M.: "Multidimensional optimization with a fuzzy genetic algorithm", Journal of Heuristics, 4(3), pp. 221-244, 1998.

[Wal05] Wallentowitz, H.: Vertical and Lateral Dynamics of Passenger Vehicles, Automotive Technology II, ("Vertical- und Querdynamik von Kraftfahrzeugen, Voerlesungsumdruck Fahrzeugtechnik II"), course notes, Institute of Automotive Engineering, Aachen University of Technology, Germany, 2005.

[Wal06] Wallentowitz, H. and Reif, K.: Handbuch Kraftfahrzeugelektronik: Grundlagen, Komponenten, Systeme, Anwendungen, ATZ/MTZ-Fachbuch, Friedr. Vieweg & Sohn Verlag, 2006.

[Whe02] Wheals, J.C.: "Torque vectoring center differential for AWD: Design and integration", Innovative Fahrzeug-Getriebe Symposium, IIR Deutschland GmbH, 2002.

[Whe05] Wheals, J.C., Baker, H., Ramsey, K., and Turner, W.: "Torque vectoring driveline: SUV-based demonstrator and practical actuation technologies", SAE World Congress, 2005-01-0553, Detroit, 2005.

[Wun05] Wunschelmeier, U. and Huchtkoetter, H.: "Traction and stability enhancement using active limited-slip differentials", 14th Aachen Colloquium, Automobile and Engine Technology, 2005.

[Yam91] Yamamoto, M.: "Active control strategy for improved handling and stability", SAE World Congress, 911902, pp. 1638-1648, Detroit, 1991.

[Yih05] Yih, P.: Steer-by-Wire: Implications for Vehicle Handling and Safety, Ph.D. Dissertation, Department of Mechanical Engineering, Stanford University, January 2005.

[Yu02] Yu, Y., Zeng, B., Zhong, G., and Peng, H.: "A real-time method to tune rule base of fuzzy control system", Proceedings of the 2002 IEEE International Conference on Fuzzy Systems, pp. 425-430, 2002.

[Zan00] van Zanten, A.T.: "Bosch ESP systems: 5 years of experience", SAE World Congress, 2000-01-1633, Detroit, 2000.

[Zhe92] Zheng, L.: "A practical guide to tune of proportional and integral (PI) like fuzzy controllers", IEEE International Conference on Fuzzy Systems, pp. 633-640, 1992.

[Zie42] Ziegler, J.G. and Nichols, N.B.: "Optimum setting for automatic controllers", Transactions of the ASME, 65, pp. 756-765, 1942.

Appendices

A Design and Modelling of the AUTO21EV

Many controller designs have been proposed for the control of individual vehicles. The combination and coordination of these active systems, however, has not been fully addressed, even though some of them have similar or complementary objectives. Since the translational and rotational degrees-of-freedom of a vehicle are coupled, one chassis control system may adversely affect the operation of other systems. As such, it is evident that the appropriate integration of chassis control systems could be used to improve vehicle stability, safety, and comfort simultaneously. Hence, the integration of various control systems has the potential to optimize the dynamic behaviour of the vehicle independently of the driving maneuver by controlling the allocation of the horizontal and vertical forces at each individual wheel.

The objective of this research is to develop effective control strategies to improve vehicle dynamics, based on the philosophy of individually monitoring and controlling the tire-road forces on each wheel. In this regard, a full vehicle with four in-wheel motors and an active steering system has been modelled in the ADAMS/View environment in order to investigate advanced vehicle stability and traction control strategies. This platform represents a two-passenger electric all-wheel-drive urban vehicle (AUTO21EV) that has a similar configuration to the commercially-available *Smart fortwo* (Figure A-1). An electric vehicle with four direct-drive in-wheel motors is the most exciting platform on which to apply advanced motion control techniques, since the motor torque and speed can be generated and controlled quickly and precisely. In fact, the torque response of an electric motor is on the order of a few milliseconds and, therefore, responds 10 to 100 times faster than the internal combustion engines and hydraulic braking systems in use today [Hor04]. The use of small but powerful direct-drive in-wheel motors allows for the implementation of the most advanced torque vectoring system possible, in which any desired torque distribution between the four wheels can be realized. Such a platform also represents the most advanced all-wheel-drive (AWD) system, generating the optimal amount of traction by controlling the slip ratio of each tire. In addition, steer-by-wire

technology on the front axle facilitates the inclusion of an active steering system, which helps maintain vehicle stability by electronically augmenting the driver's steering input.

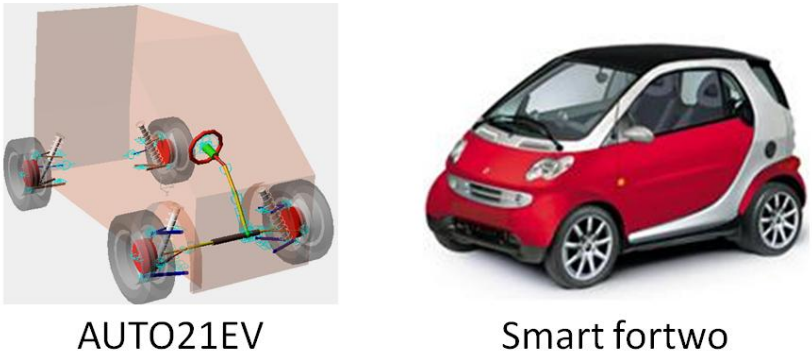

Figure A-1: AUTO21EV concept car (left) and the commercially-available Smart fortwo [Sma10] (right)

A.1 Preliminary vehicle design

As a first step in the design of the AUTO21EV, the vehicle dynamics in the longitudinal, lateral, and vertical directions are examined.

A.1.1 Longitudinal dynamics

The initial design stage involves a comprehensive acceleration analysis to determine the power and traction force demands of the vehicle. Various sizes of electric in-wheel motors are considered, and the vehicle performance is assessed to ensure that the vehicle is able to bend safely with ordinary city traffic and drive up a regulated maximum slope. Figure A-2 illustrates the acceleration performance of the selected direct-drive in-wheel motors. Here, $F_{resist\_0\%}$ to $F_{resist\_30\%}$ indicate the total stationary resistive forces as a function of vehicle speed on different upward slopes, and $F_{traction\_total}$ indicates the total available traction force as a function of speed. The available traction effort results in a fairly high acceleration potential even at higher speeds. For example, an acceleration potential of about 5 m/s^2 at the vehicle's maximum speed of 90 km/h allows the vehicle to maneuver easily in urban traffic. In addition, due to the high motor torques available, the vehicle experiences its maximum acceleration of about 8.3 m/s^2 at zero speed when driving on a dry flat road. Note that, due to the high acceleration rate at low speeds and, consequently, a weight transfer to the rear axle, the front tires will spin out if their respective motor torques are not controlled by a slip controller.

The traction effort and power characteristics of the vehicle are used to size an appropriate electric motor for the AUTO21EV. Although the in-wheel motors currently

on the market are generally designed as direct-drive permanent magnet synchronous machines (PMSM), in this stage of the design process, permanent magnet direct current (PMDC) motors are used in order to simplify the modelling process. Direct-drive electric motors use no gear reduction between the motor and the drive shaft, thereby reducing the weight and size of the system, but they require the speed-torque characteristics of the motor to directly meet the requirements of the vehicle. These machines are characterized by containing permanent magnets in their rotor, usually rare-earth magnets to increase the power density, where the rotor can be attached to the rim of the tire. Furthermore, these motors are brushless and, therefore, are very robust and reliable. PMSMs have the advantage that the magnetization loss in the field of the motors can be eliminated, which not only improves the efficiency, but also prevents overheating of the tires by the outer rotor [Ter97]. Figure A-3 illustrates the run-up characteristics of the chosen PMDC motor, where the motor voltage, torque, and power are shown as functions of motor speed.

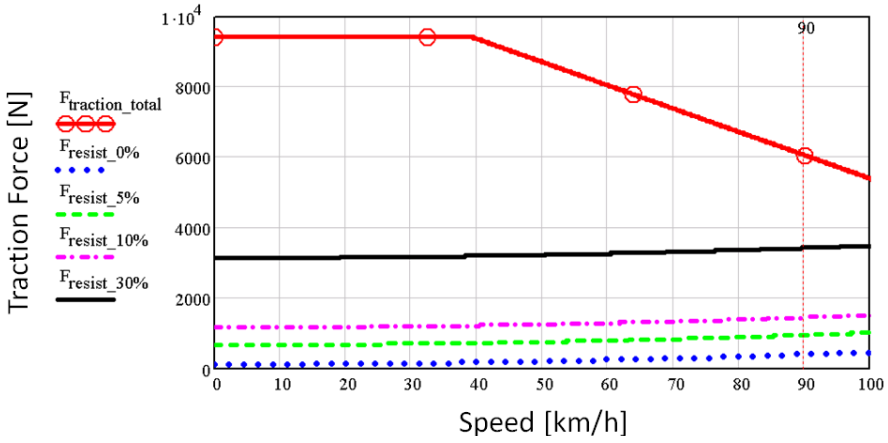

Figure A-2: AUTO21EV longitudinal traction effort characteristics

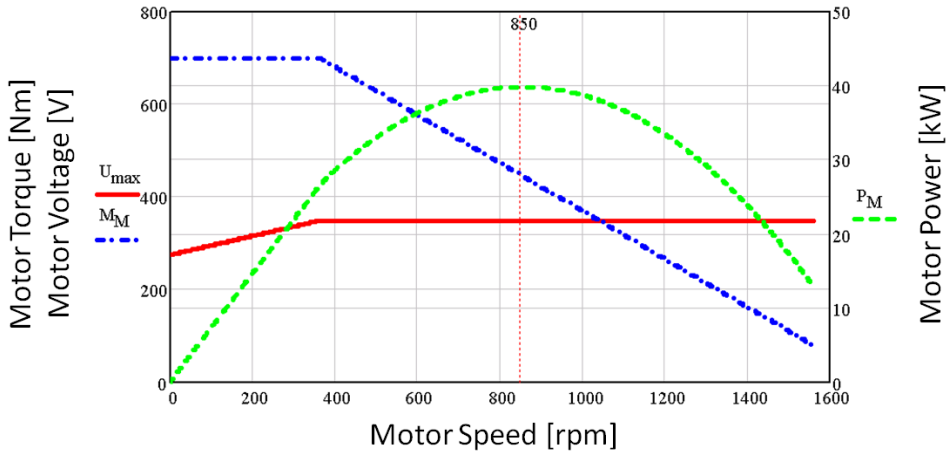

Figure A-3: Direct-drive PMDC in-wheel motor run-up characteristics

Table A-I illustrates the specifications of the chosen PMDC motor. Based on these characteristics, the vehicle power system characteristics are defined, as illustrated in Figure A-4. Here, $P_{required\_0\%}$ to $P_{required\_30\%}$ illustrate the power required to overcome the stationary resistive forces on different road gradients as a function of vehicle speed, and $P_{available}$ indicates the total available power as a function of speed. It is confirmed that the chosen drivetrain is powerful enough to offer sufficient acceleration potential throughout the entire speed range, and enables the vehicle to drive up the maximum slope of 30 percent gradient. Note that the power characteristics curve of the vehicle must be greater than the maximum power required to drive up the maximum slope of 30 percent gradient.

Specification	Value	Unit
Peak Power	40	kW
Peak Torque	700	Nm
Maximum Speed	1650	rpm
Maximum Voltage	350	V
Maximum Current	311	A
Total Mass	30	kg
Rotor Mass	11.2	kg
Internal Resistance	0.768	Ω
Motor Constant	1.95	mH
Current Restriction Factor	3.25	-

Table A-I: PMDC motor characteristics

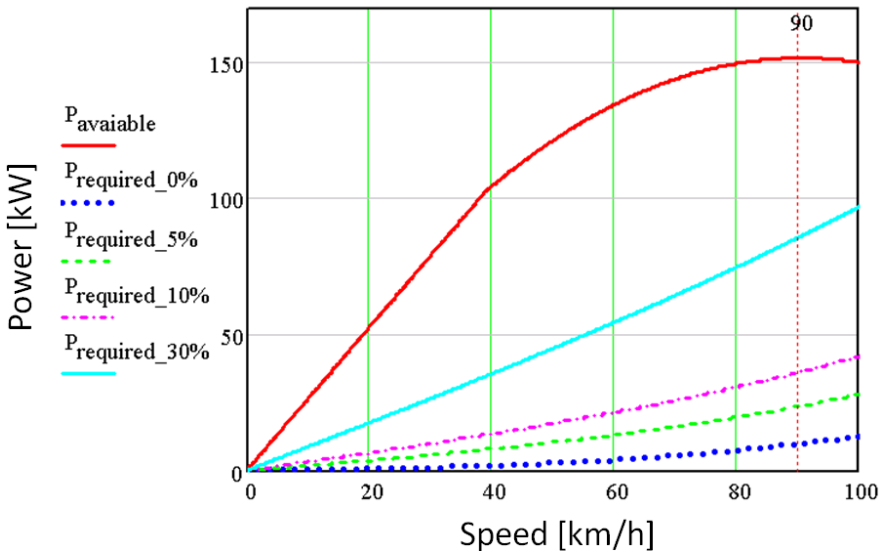

Figure A-4: AUTO21EV power requirements

The brakes of the AUTO21EV are designed to ensure that the rear brakes do not lock before those on the front axle, which would result in vehicle instability. The relationship between the front and rear braking force distribution is illustrated in Figure A-5, where each axis describes the braking force at each axle relative to the total weight of the vehicle. The ideal braking force ratio represents the optimal braking force ratio on the front and rear axles for every possible adhesion situation and, thus, every possible braking condition. The optimal braking force distribution depends on various parameters, such as the vehicle's center of gravity, speed, and payload. In order to ensure that the front wheels consistently lock earlier than the rear wheels, the constant braking ratio must remain below the ideal braking ratio for all adhesion coefficients. Based on legislative braking guidelines, a constant braking ratio is only allowed to exceed the ideal braking distribution curve after an adhesion coefficient of 0.8 has been reached [Wal05].

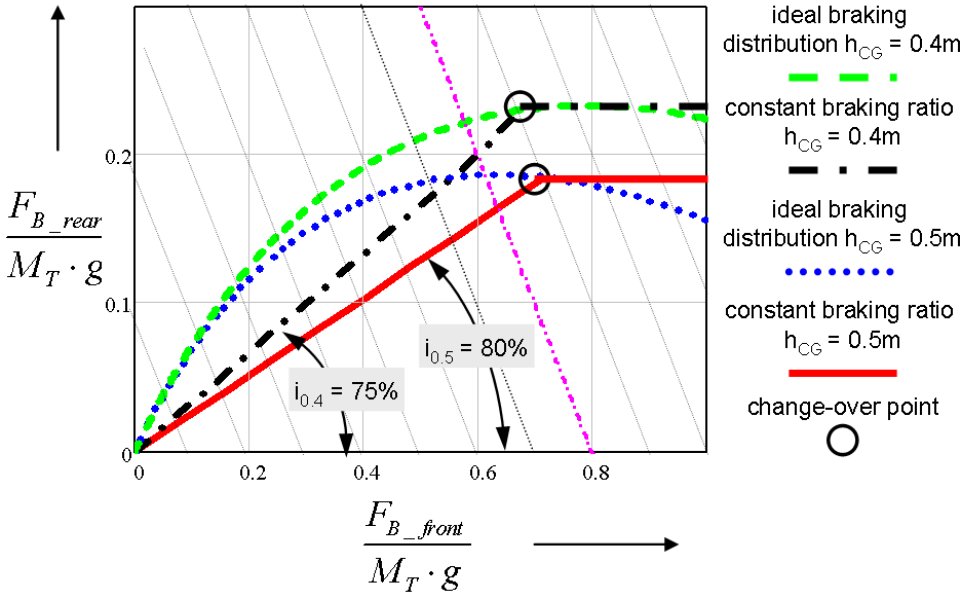

Figure A-5: Ideal braking force distribution and a braking force limiter technique for different CG heights

It is the job of the proportioning valve to adjust the braking force balance and achieve a close approximation to the ideal distribution, as illustrated by the parabolic curves in Figure A-5. These curves represent the ideal braking force distributions for vehicles with center of gravity heights of 0.4 m and 0.5 m. This figure confirms that the lower the location of the vehicle's center of mass, the lower the braking ratio required. If no braking force proportioning valve is installed, then the distribution of the braking force forms a straight line whose slope is the ratio of the braking force at the front and rear axles. The point at which the front wheels lock is found at the intersection of the base

distribution and the lines representing the respective coefficients of friction (the dotted lines with slope -1 in Figure A-5). However, a braking force limit proportioning valve is usually installed to actuate after the braking distribution line reaches the ideal braking force distribution, so that the rear axle braking force does not increase further.

An extensive braking system analysis is performed to examine different vehicle center of mass locations and braking ratios. Based on these calculations, the vehicle's center of gravity position is chosen to be located at 0.4 m above the ground and at 0.82 m behind the front axle for the curb weight plus driver. Moreover, a constant base braking ratio of 75 percent to the front axle and 25 percent to the rear axle is selected, which stops the vehicle from its top speed of 90 km/h in about 3 seconds, requiring a braking distance of 36 m.

A.1.2 Lateral dynamics

A bicycle model is used to investigate the effects of front and rear tire cornering stiffnesses, center of gravity location, mass, and moment of inertia of the vehicle on the steering performance, yaw damping rate, and yaw natural frequency of the vehicle. The usefulness of a bicycle model is limited to lateral accelerations less than 0.4g, where the vehicle and tire behaviour can be considered to be linear [Wal05]. The results of an analysis of the bicycle model for a vehicle with the same tires on the front and rear is illustrated in Figure A-6.

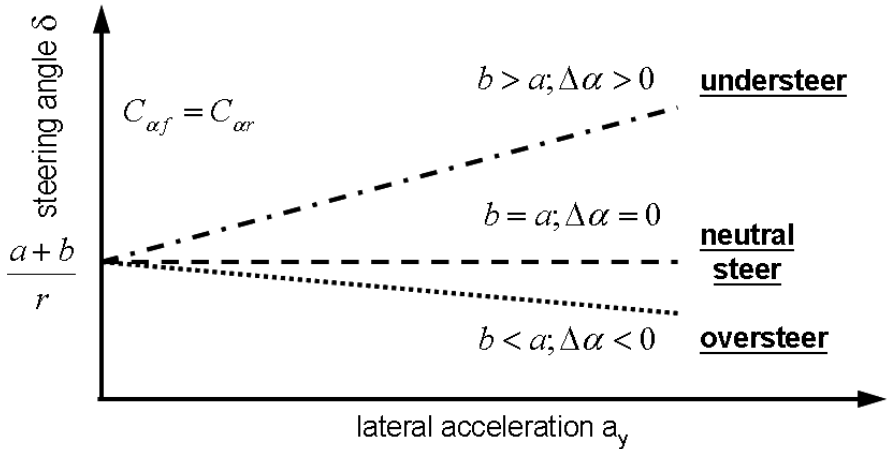

Figure A-6: Self-steering characteristics of the bicycle model when the position of the vehicle center of gravity varies and the tire lateral stiffnesses are the same on both axles

If the vehicle center of gravity position is closer to the front axle, traction is first lost at the front wheels and, consequently, an increasing steering angle is required at higher speeds in order to keep the vehicle on the desired path, as compared to a neutral-

steered vehicle. In addition, an understeered vehicle possesses a characteristic speed at which the vehicle is most 'responsive', reacting quickly and accurately to any steering inputs with no overshoot or delay. The AUTO21EV center of gravity is located at 0.82 m behind the front axle and 0.98 m from the rear axle and, therefore, it has an understeered characteristic with a characteristic speed of 105 km/h. Note that most available passenger cars on the market are designed as understeered vehicles with characteristic speeds between 65 and 100 km/h, which is the speed range in which vehicles are driven most often and, thus, require the best responsiveness [Wal05]. Transient skid-pad testing is used to describe the behaviour of the vehicle. The transient behaviour of a vehicle can be analyzed by writing the equations of motion of the linearized bicycle model as functions of sideslip angle (Figure A-6).

The yaw natural frequency and yaw damping rate of the vehicle can be calculated by comparing the coefficients of the resulting homogeneous differential equation with a spring-damper system. Figure A-7 illustrates the range of yaw damping rates and natural frequencies for available passenger cars. Normal passenger cars (mid-performance vehicles) have an average yaw damping rate of approximately 0.8 and a yaw natural frequency between 2 and 4 Hz. These values correspond to typical speed ranges between 60 and 100 km/h [Wal05]. The yaw damping rate and natural frequency of the AUTO21EV are illustrated in Figure A-8. As can be seen, the high steering responsiveness of the AUTO21EV is set to be between the speed ranges of 60 and 90 km/h, reflecting the predominant driving situation for an urban vehicle. Comparing the AUTO21EV transient behaviour with Figure A-7, it can be confirmed that the yaw damping rate and natural frequency of the AUTO21EV are defined to be in the typical range of normal passenger cars, with a tendency towards sports cars.

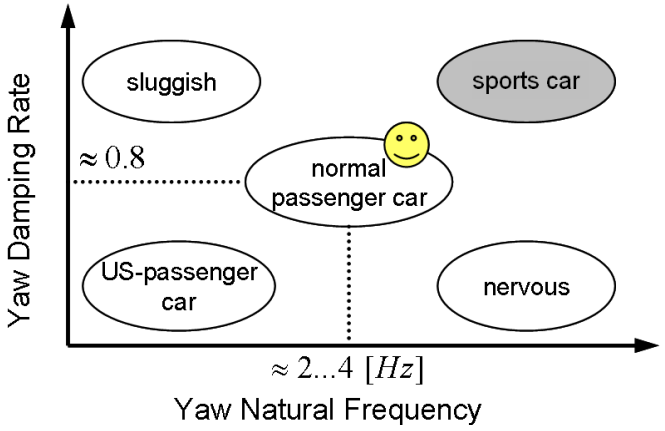

Figure A-7: Typical range of yaw damping rate and natural frequency for available passenger cars [Wal05]

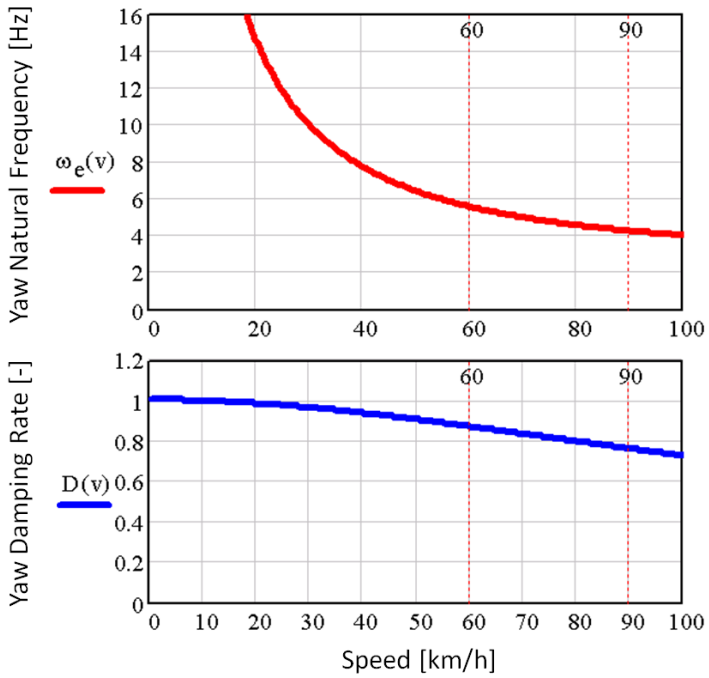

Figure A-8: Yaw natural frequency (top) and damping rate (bottom) of the AUTO21EV as functions of forward speed

A.1.3 Vertical dynamics

The spring and damper rates of the AUTO21EV suspension system are estimated by considering a quarter-car model, and are further refined using a formal optimization procedure. The suspension system spring rates are designed to provide a frequency for the sprung mass that lies within the comfort range for the human body, which is considered to be between 1 and 4 Hz [Rei02]. The rear suspension is designed for a target sprung mass frequency of 1 Hz. The front suspension is designed to have a 30 percent lower ride rate than the rear suspension, based on Olley's recommendation for a comfortable ride [Gil92].

The design of a vehicle suspension is generally a compromise between competing design requirements, aiming to simultaneously provide a comfortable ride as well as safe handling performance. There are multiple excitation sources for vehicle ride vibrations, but these can generally be divided into two classes: road roughness and on-board sources [Wal05]. For an electric vehicle, on-board sources are restricted to tires, rims, and the rotating parts of the electric motors, as there is no powertrain. These excitations are considered to be insignificant in the following analysis, which considers only road roughness as the excitation source. The suspension parameters are selected based on an optimization of the half-car model shown in Figure A-9. The ride performance of the

vehicle is described by the root mean square (RMS) of the chassis vertical acceleration (which is based on the evaluation of the transfer function of the chassis acceleration with respect to the road excitation) and the Laplace transform of the temporal power spectral density (PSD) of the road surface profile [Guo82, Hro81]. The optimization problem is limited by four design constraints. The first design constraint requires that the vehicle holds to the ground by minimizing the fluctuation of the adhesion force between the tire and road. In other words, the probability of the tire leaving the ground must remain below some acceptable limit. The second design constraint is defined based on the allowable roll angle of the vehicle. Assuming that no anti-roll bar is included in the suspension, the suspension stiffness is directly limited by the allowable roll angle. An empirical value for the acceptable roll angle for a normal passenger car is used: less than about 3^o for a lateral acceleration of 0.5g [Wal05]. The third constraint limits the maximum suspension dynamic displacement to avoid hitting the bump stops. The fourth and final constraint concerns the life of the tire: the smaller the tire stiffness, the larger its deflection and the shorter its life. The tire static deflection should be less than 8 to 13 percent of the profile height of the tire [Jal07].

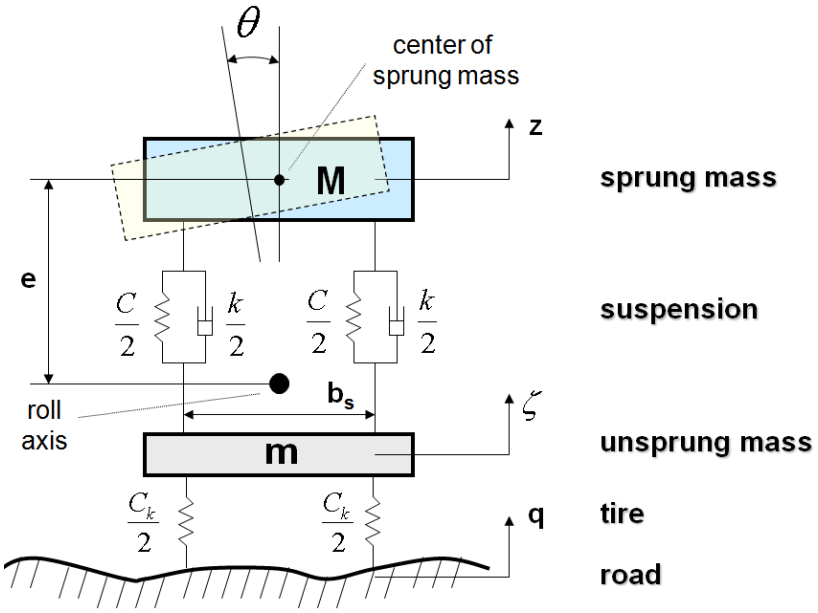

Figure A-9: Half-car suspension model when assuming an equal static mass distribution on the front and rear axles [Jal07]

A genetic algorithm (GA) optimization tool is developed to calculate the optimal suspension and tire parameters based on the above considerations. Figure A-10 illustrates the results of the GA tool for the AUTO21EV when it is driven with an initial speed of 36

km/h on a rough road. The suspension stiffness and damping rates are determined by setting the stiffness of the tires to the same values as those used on the Smart *fortwo*: 130.5 kg/cm. The optimal suspension stiffness and damping rate are calculated to be 51.7 kg/cm and 5.7 kg/cm/s, respectively. The resulting probability of the tire leaving the ground is equal to 0.13 percent, and the RMS of the vertical chassis acceleration is 0.355g. Both values are reasonable for passenger cars.

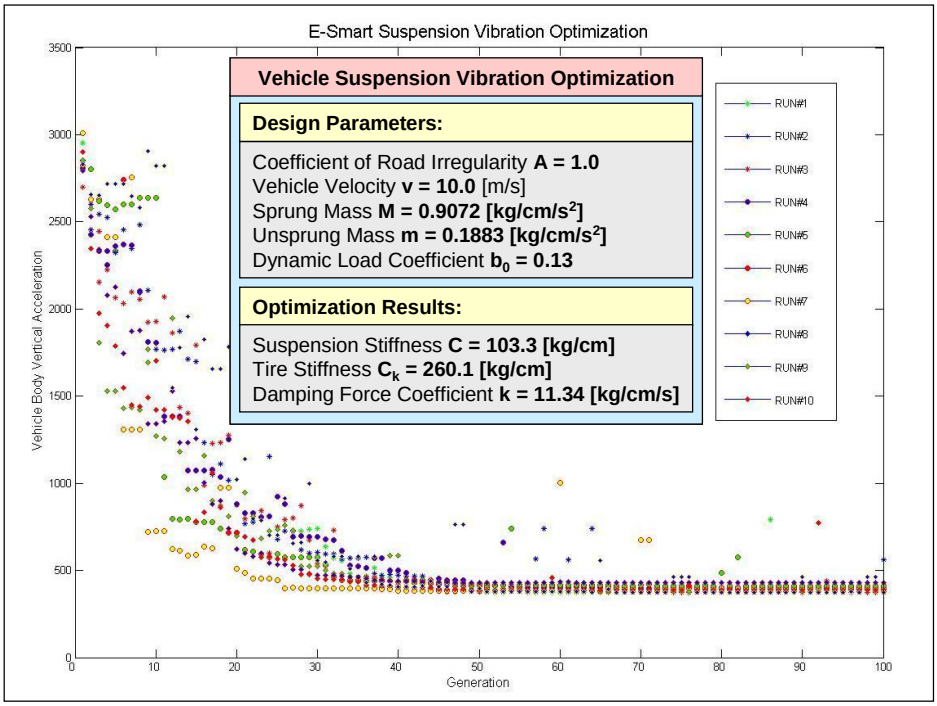

Figure A-10: Optimization results for the AUTO21EV suspension system

A.2 Detailed suspension design

Double-wishbone suspension configurations are selected for the front and rear axles of the AUTO21EV. Specific suspension characteristics (Figure A-11), such as toe-in angle, camber angle, caster angle, and track width changes during vertical wheel travel, are chosen to optimize the cornering behaviour. The suspensions are designed to provide desirable self-steering characteristics for the vehicle, such as camber thrust, roll steer, and lateral load transfer. Other considerations include mechanisms to reduce body pitch angle during acceleration and braking, and roll motion during cornering. By designing a passive suspension with ideal characteristics, the stability control systems do not need to correct for faulty suspension system behaviour, and can focus on improving the driving dynamics of the vehicle. Extensive analyses are performed on various suspension configurations by German exchange students directly supervised by the author. Detailed analyses are

performed on trailing arm and semi-trailing arm [Pet05], double-wishbone [Jal05], and multi-link [Bod06] suspension systems.

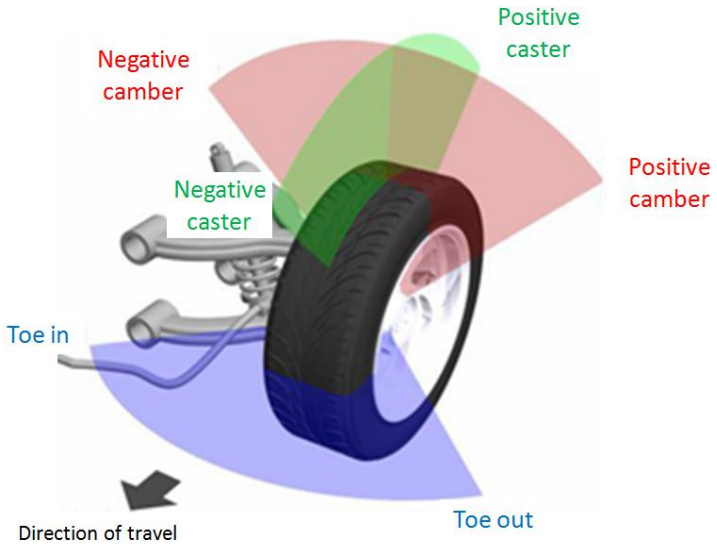

Figure A-11: Sign convention for camber, caster, and toe angle on a double-wishbone suspension [Jal05]

Since the parameters of an independent suspension system are interrelated, virtual prototyping software (ADAMS/View) is used to model the suspension systems. The double-wishbone suspensions of the front and rear axles are illustrated in Figure A-12. The following steps are performed during the design process of the suspension system on each axle:

1) Redistribution of forces: The kingpin inclination, kingpin offset, caster angle, and caster trail are adjusted to fall in the ranges found on commercial vehicles in order to reduce the amount of force acting on the steering axis and tie rods (Figure A-13). The front and rear suspensions are designed to have a kingpin inclination of $\sigma = 15.5^{o}$ and a negative kingpin offset of $r_{\sigma} = -21.7$ mm at static ride height. The front double-wishbone suspension has a caster angle of $\tau = 7.5^{o}$ and a positive caster trail of $r_{\tau,k} = 18.4$ mm, whereas the rear suspension is designed to have zero caster angle and zero caster trail in the design position.

2) Modification of the control arms to define a desirable roll axis: The determination of the roll center height on each axle is done at static ride height by changing the control arm slopes in the front view. The target values are chosen based on Olley's recommendations [Mil02], where a desirable roll center height of less than 127 mm is recommended for the front axle and a roll center height below 410 mm is recommended for the rear axle. A higher roll center height at the rear axle provides a roll understeering

effect. The final vehicle model has a front roll center height of 89.4 mm and a rear roll center height of 94.7 mm in the static design position.

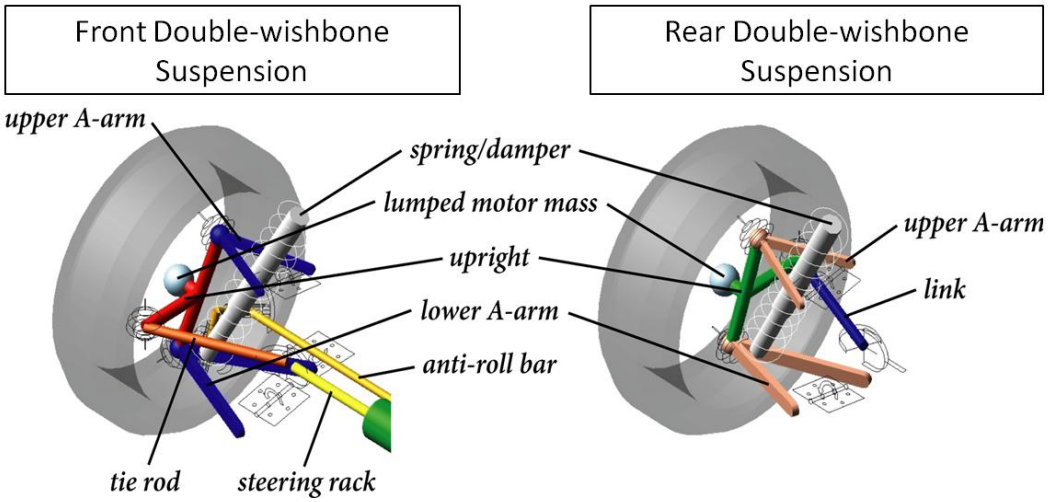

Figure A-12: Front and rear suspension systems of the AUTO21EV

3) Incorporation of anti-pitch characteristics: By inclining the suspension control arms towards one another on both axles, the body pitch motion can be reduced during acceleration and braking. The inclined angles cause part of the additional vertical force created by the dynamic weight shift during braking or acceleration to reduce spring deformation [Bod06]. Three rules are considered to determine the desired positions of the front and rear suspension pitch poles, O_f and O_r (Figure A-14-a). First, to provide the driver with some feedback during acceleration and braking, the complete elimination of the pitch motion is avoided [Gil92]. A pitch angle reduction of 60% was chosen, compared to a vehicle without an anti-pitch mechanism. Figure A-14-b illustrates the effect of the anti-pitch mechanism during acceleration and braking for the AUTO21EV. Secondly, the resultant force due to the control arms should be located as close to the center of gravity as possible. Finally, for independent wheel suspensions, it is important for the pitch poles to be higher than the wheel center of the driven axle [Rei02].

4) Design of an appropriate steering geometry: An electric-motor-driven rack-and-pinion principle has been chosen for the steering system. The location, length, and angle of the tie rods on the front axle and suspension links on the rear axle are analyzed and set to values that provide the best handling properties, including a roll understeering effect, reduced wheel fight and rolling resistance, and minimal toe angle change during bump travel. The vertical position of the inner hard-points of the tie rods and links are defined based on Olley's recommendations for an 'ideal' steering geometry [Mil02], using a

graphical method introduced by Reimpell [Rei02]. Figure A-15 illustrates the roll understeering behaviour of the vehicle when driving in a turn. At the front axle, the outer bump-travelling wheel experiences a toe-out situation and the inner rebounding wheel experiences a toe-in situation. At the rear axle, the opposite phenomenon occurs to realize roll understeering at high speeds.

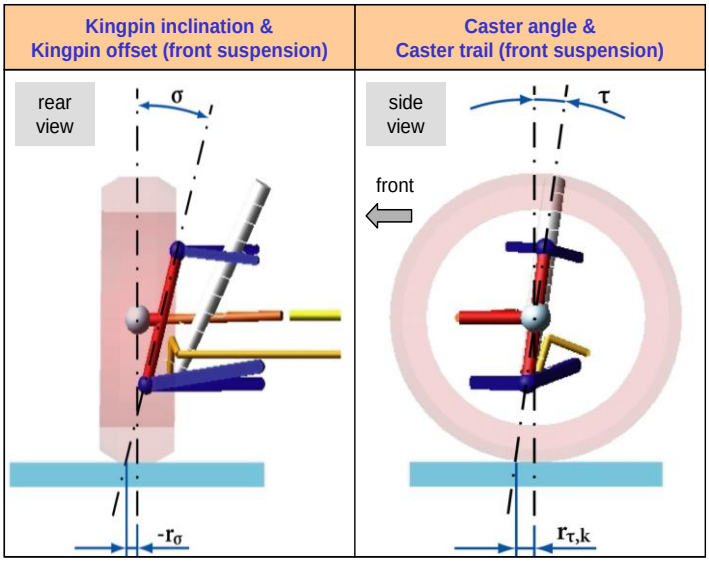

Figure A-13: Illustration of kingpin inclination (σ), kingpin offset (r_σ), caster angle (τ), and caster trail ($r_{\tau,k}$) in front suspension of the AUTO21EV

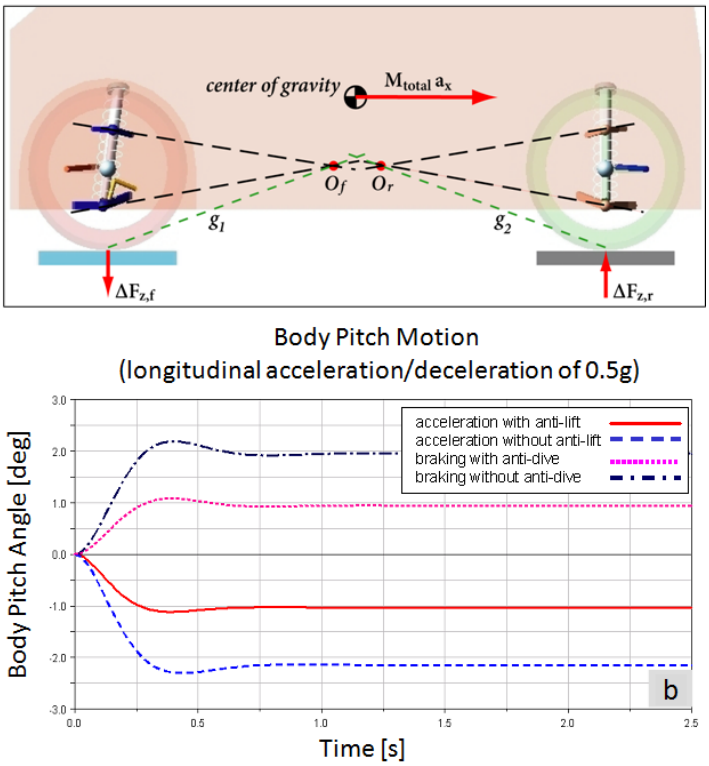

Figure A-14: (a) Pitch poles of the front and rear axles, and (b) AUTO21EV body pitch motion for accelerating and braking with and without the anti-pitch mechanism

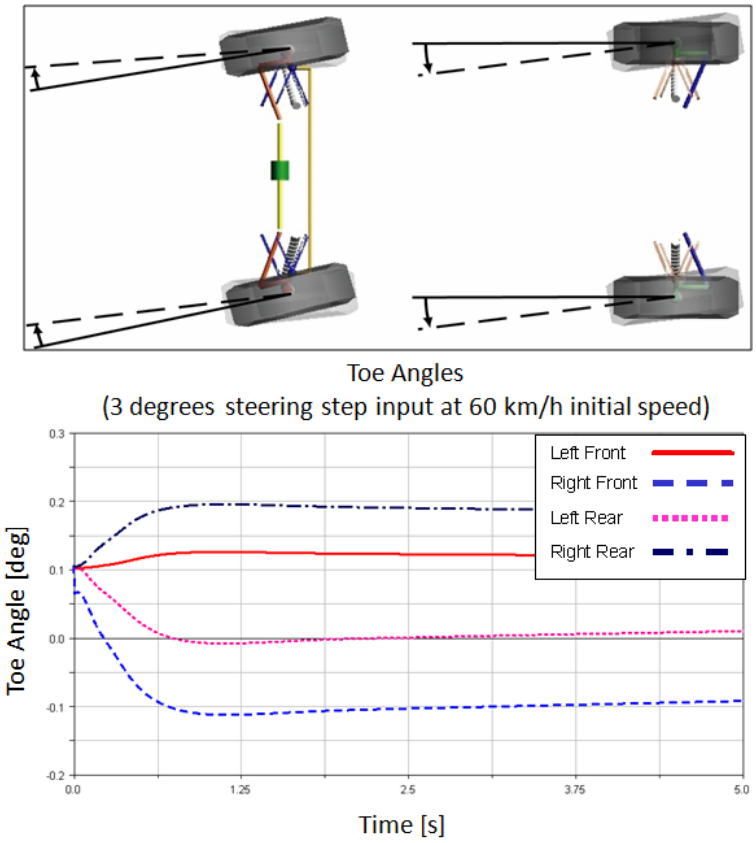

Figure A-15: Roll understeering behaviour through toe angle changes on the front and rear suspensions when driving in a curve

In the next step, the steering rack position in the horizontal direction is determined based on the Ackermann differential steering angle $\Delta\delta_A$, which describes the difference between the inside δ_i and outside $\delta_{o,A}$ steering angles (Figure A-16-a). Perfect Ackermann steering describes the situation in which the front tires have the same instantaneous center of rotation in a turn. In practice, however, a smaller differential steering angle is used because the tires must not come into contact with the wheel arch or other components of the front axle [Rei02]. On the other hand, the smallest possible turning circle for the vehicle can only be achieved if the steer angle of the outside wheel is as large as possible. In order to avoid impairing the cornering behaviour of the vehicle while simultaneously increasing the lateral force capacity of the front outside tire and decreasing the cornering radius, the steering angle on the outside wheel is designed to be larger than that calculated by Ackermann. In this regard, a reduction to 55% Ackermann is chosen as the target for the preliminary design, which is close to the setup of the BMW 3-Series [Rei02]. Figure A-16-b illustrates the influence of the steering rack location on the differential steering angle.

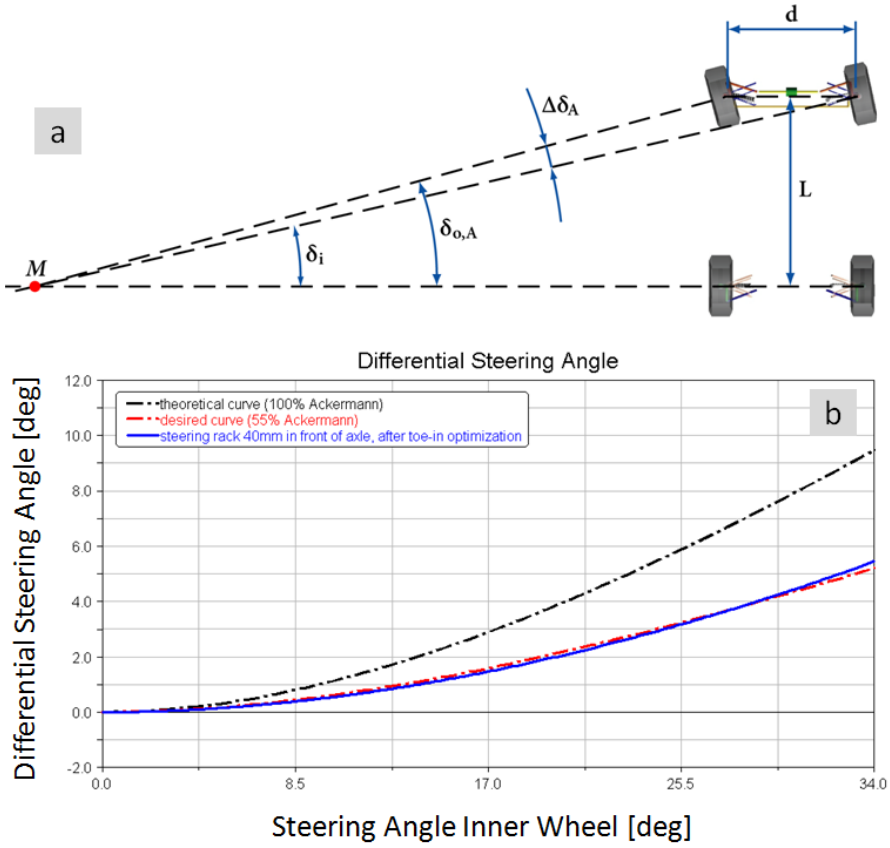

Figure A-16: (a) Differential steering angle ($\Delta\delta_A = \delta_i - \delta_{o,A} > 0$) according to Ackermann, and (b) influence of steering rack position on differential steering angle

5) Adjustment of suspension kinematics: Since negative camber angles on the tires of an axle increase the lateral force potential on that axle, it is important to provide the tires with negative camber angles during all driving maneuvers [Wal05]. Therefore, suspensions are designed to have a negative camber angle at the static ride height. Furthermore, the kinematics of the front and rear suspensions are designed such that the outer wheels are pushed into more negative camber and the inner wheels are pushed into positive camber when cornering. In this way, the suspension system not only counteracts the effects of body roll on tire camber, but also increases the lateral force potential of the more heavily-loaded outside tires. Finally, the wheel track change is reduced by changing the upper control arm length.

A.3 Dynamic model of the AUTO21EV

In order to simulate test maneuvers to investigate different control strategies, full kinematic and dynamic models of the AUTO21EV are developed in ADAMS/View (Figure A-17). ADAMS is a comprehensive multi-body dynamic simulation package that

is used in this project. The extension of the kinematic model into a dynamic model requires the development and adoption of appropriate tire and road models in ADAMS/View. These data are used by subroutines to calculate the forces and moments that tires exert on a vehicle as a result of the interaction between the tires and the road surface. ADAMS/Tire can be employed to model tires for either vehicle handling or vehicle durability analyses. Handling analyses are advantageous for studying vehicle dynamic responses to steering, braking, and throttle inputs, whereas durability analyses are suitable for generating road load histories as well as stress and fatigue studies requiring component forces and accelerations. Figure A-18 illustrates the different tire models available in ADAMS and the typical applications for each tire model.

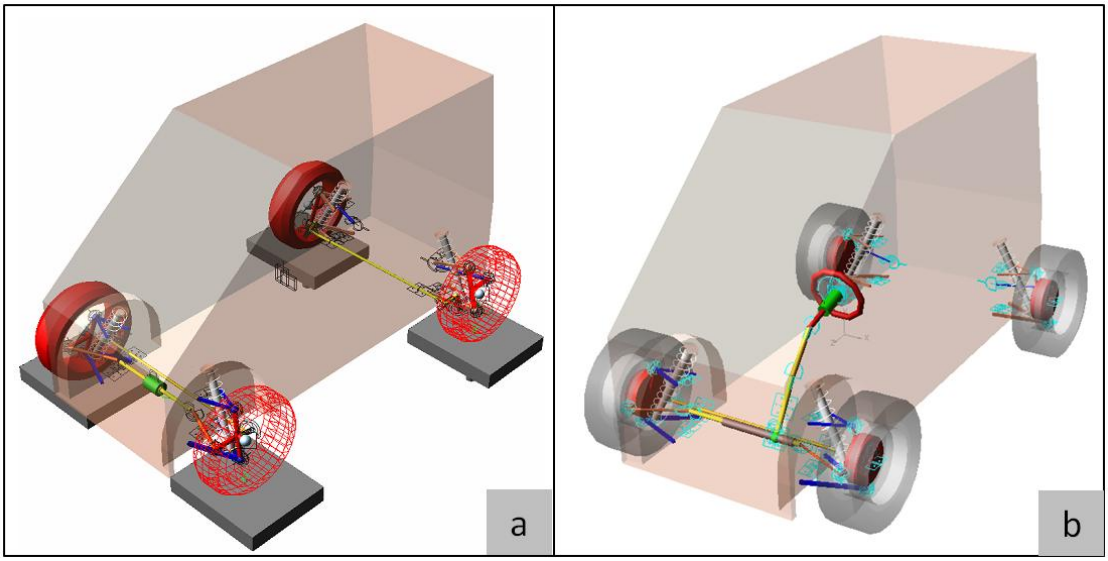

Figure A-17: (a) Kinematic and (b) dynamic models of the AUTO21EV

Based on this information, a Pacejka 2002 tire model is chosen for this project. The Pacejka 2002 tire model is the most recommended model for handling and real-time control studies [Pac02]. The yaw, roll, and pitch moments of inertia of the vehicle are estimated based on the vehicle weight and center of gravity height, as well as geometric measurements, including the track width, roof height, wheelbase, and overall vehicle length. The accuracy of this estimation procedure has been confirmed by experimental results obtained from the Inertial Parameter Measurement Device located at the Vehicle Research and Test Center in East Liberty, Ohio [Bix95]. The moments of inertia of other vehicle parts, such as the suspension and steering system components, are calculated using the ADAMS software, based on the component shape and constituent material. The moments of inertia of the in-wheel motors, tires, and rims are determined by hand

calculation [Vog07]. To fine-tune the understeering characteristic of the vehicle, an anti-roll bar is added to the front axle of the vehicle prior to running the simulations. The stiffness of the anti-roll bar is chosen to be 1.1 Nm/deg, which provides an understeering effect and a maximum roll angle of 3^{o} for the vehicle.

ADAMS v2005 r2	Event / Maneuver	ADAMS/ Handling Tire							Specific Models		
		PAC2002[1]	PAC-TIME[1]	PAC89	PAC94	FIALA	5.2.1.	UA Tire[1]	PAC-MC[1]	SWIFT	FTire
Handling	Stand still and start	+	o/+	0	0	0	0	0	o/+	+	+
	Parking (standing steering effort)	+	-	-	-	-	-	-	-	+	+
	Standing on tilt table	+	+	0	0	0	0	0	+	+	+
	Steady state cornering	+	+	0	+	0	0	0	+	+	0
	Lane change	+	+	0	o/+	0	0	0	+	+	0
	ABS braking distance	+	0	-	-	-	-	-	0	+	+
	Braking/power-off in a turn	+	+	0	0	0	0	0	+	+	0
	Vehicle Roll-over	+	0	0	0	0	0	0	0	+	+
	On-line scaling tire properties	+	-	-	-	-	-	-	-	-	0
Ride	Cornering over uneven roads *	0	0	-	-	-	-	0	0	+	0
	Braking on uneven road *	0	0	-	-	-	-	-	0	+	+
	Crossing cleats / obstacles	-	-	-	-	-	-	-	-	+	+
	Driving over uneven road	-	-	-	-	-	-	-	-	+	+
	4 post rig (A/Ride)	o/+	o/+	-	-	-	-	o/+	o/+	o/+	o/+
Chassis Control	ABS braking control	0	0	-	-	-	-	-	0	+	+
	Shimmy[2]	o/+	0	-	-	-	-	0	0	+	+
	Steering system vibrations	o/+	0	-	-	-	-	-	0	+	+
	Real-time	+	-	-	-	-	-	-	-	-	-
	Chassis control systems > 8 Hz	0	-	-	-	-	-	-	-	+	+
	Chassis control with ride	-	-	-	-	-	-	-	-	+	+
Dura-bility	Driving over curb	-	-	-	-	-	0	0	-	0	o/+
	Driving over curb with rim impact	0	-	-	-	-	0	0	-	-	-
	Passing pothole	-	-	-	-	-	0	0	-	0	o/+
	Load cases	-	-	-	-	-	0	0	-	0	o/+

-	Not possible/Not realistic
0	Possible
o/+	Better
+	Best to use

* wavelength > tire diameter
[1] use_mode on transient combined slip
[2] wheel yawing vibration due to supension flexibility and tire dynamic response

Figure A-18: Typical applications for ADAMS tire models [Aks06]

A.4 Permanent magnet synchronous in-wheel motor

As mentioned earlier, the in-wheel motors currently on the market are generally designed as direct-drive permanent magnet synchronous machines (PMSM). Use of PMSMs implies that no gear reduction exists between the motor and the drive shaft of the wheel, which can reduce the weight and size of the system, but also requires that the speed-torque characteristics of the motor meet the performance requirements of the vehicle. These motors generally contain rare-earth permanent magnets in the rotor, which provide a high power density and employ electric commutation through the use of inverters, allowing the design of a robust and reliable brushless, variable-speed PMSM motor with a high power-to-weight ratio [Han94]. PMSMs are designed upside-down, which means that the rotor is the rotating external part (which can also be attached to the rim) and the stator is attached to the wheel shaft. This strategy is primarily used to reduce the moment of inertia of the rotating parts, thereby reducing the amount of energy required to stop or

accelerate the wheels. In addition, PMSMs have the ability to increase performance and efficiency by eliminating the magnetization losses in the field of the motors. The flux-weakening characteristic of the PMSM not only improves the efficiency of the motors, but also prevents overheating of the tires by the rotor. Figure A-19 illustrates two possible examples for PMSM in-wheel motors that are offered by L-3 Communications Magnet-Motor GmbH and TM4.

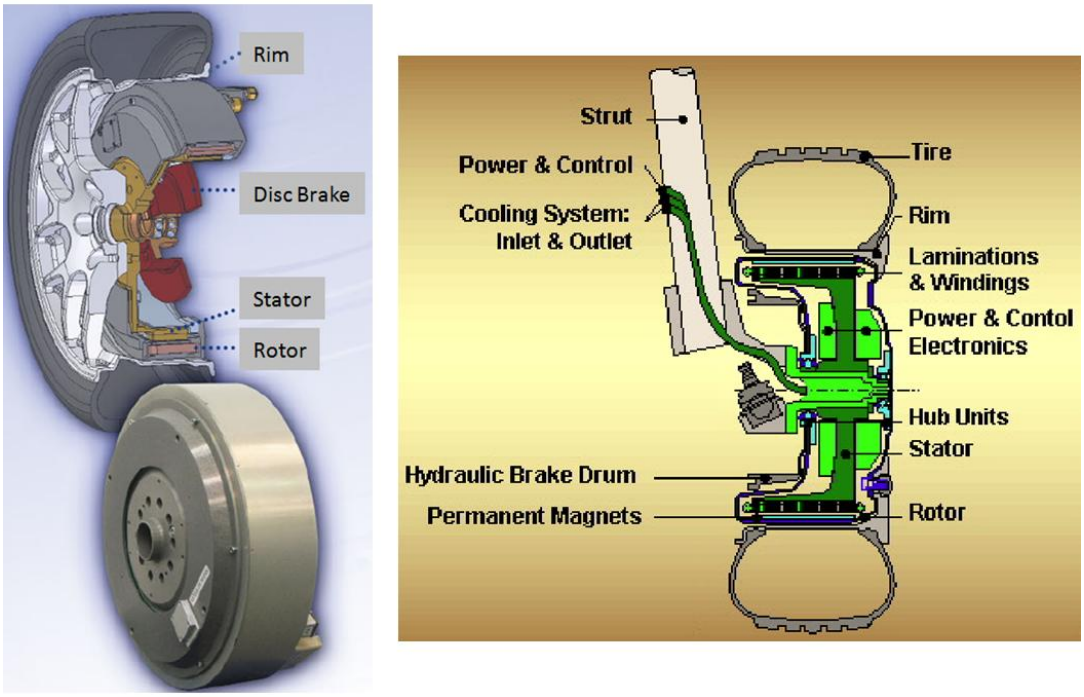

Figure A-19: PMSM in-wheel motor offered by L-3 Communications Magnet-Motor GmbH [MMG10] (left) and TM4 Inc. [TM410] (right)

Details on the modelling, simulation, and analysis of inverter-fed PMSM-type motors can be found in the literature (e.g., [Rah85, Ter97, Pil89]). The PMSM motors used in this model are assumed to consist of a cage-less surface permanent magnet rotor and a stator with three-phase windings and a sinusoidal back electromotive force. A balanced sinusoidal three-phase current is enforced in the stator to achieve synchronous operation and a smooth torque profile [Rah85]. Although these characteristics are usually achieved using an inverter by establishing pulse-width modulation (PWM) control, the switching effects have been neglected here for simplicity; it is assumed that the PWM works like an ideal three-phase variable voltage source. Moreover, saturation, eddy currents, hysteresis losses, and field current dynamics have also been neglected.

The number of pole pairs in a PMSM determines the amount of rotor rotation per complete sine wave in the stator. If the number of pole pairs (*P*) is known, the following equation can be used to relate the (electric) stator angle θ_s and the (mechanical) rotor angle θ_r:

$$\theta_s = P \cdot \theta_r \tag{A.1}$$

or

$$\omega_s = P \cdot \omega_r \tag{A.2}$$

for angular velocities. A common approach for modelling a PMSM is to use the d,q-axis model. This approach uses the Park transformation to reduce a three-phase system to an equivalent two-phase system [Han94]. The inductances in the two-phase system remain constant since the reference frame is assumed to rotate. The Park transformation of voltages from a three-phase system (a-b-c) to a two-phase system (d-q-0) is as follows:

$$\begin{bmatrix} v_q \\ v_d \\ v_0 \end{bmatrix} = \frac{2}{3} \begin{bmatrix} \cos(\theta_s) & \cos(\theta_s - 2\pi/3) & \cos(\theta_s + 2\pi/3) \\ \sin(\theta_s) & \sin(\theta_s - 2\pi/3) & \sin(\theta_s + 2\pi/3) \\ 1/2 & 1/2 & 1/2 \end{bmatrix} \cdot \begin{bmatrix} v_a \\ v_b \\ v_c \end{bmatrix} \tag{A.3}$$

where v_0 is equal to zero in a balanced three-phase system. The Park transformation can also be used to relate the current in a three-phase system (i_a, i_b, i_c) to that in the equivalent two-phase system (i_q, i_d). The governing equations of the latter then take the following form:

$$v_q = R_s \cdot i_q + L_q \cdot \frac{di_q}{dt} + \omega_s \cdot L_d \cdot i_d + \omega_s \cdot B \tag{A.4}$$

$$v_d = R_s \cdot i_d + L_d \cdot \frac{di_d}{dt} - \omega_s \cdot L_d \cdot i_d \tag{A.5}$$

where R_s is the phase resistance, B is the magnetic flux linkage, and L_q and L_d are the q- and d-axis phase inductances, respectively. These four parameters, together with the number of pole pairs (*P*), must be specified for the motor. Although the phase resistances of the two- and three-phase systems are identical, the q- and d-axis phase inductances could be different and are not identical to the phase inductance of the original system (L_s). In the case of surface permanent magnets, however, the following relationship can be assumed:

$$L_q = L_d = \frac{3}{2} L_s \tag{A.6}$$

The magnetic flux linkage represents the effect of the permanent magnets, and can be determined by measuring the no-load line-to-line voltage of the motor while it is externally driven at a constant speed. The motor torque of a PMSM can be determined using the Park transform as follows:

$$T_M = \frac{3}{2} P \cdot \left[B \cdot i_q + (L_d - L_q) \cdot i_q \cdot i_d \right] \tag{A.7}$$

For the special case of surface permanent magnets, this equation simplifies to the following:

$$T_M = \frac{3}{2} P \cdot B \cdot i_q \tag{A.8}$$

Equation (A.8) defines the coupling between the electrical and mechanical domains. In order to calculate the applied torque, equations (A.4) and (A.5) must both be solved. After substituting equations (A.2) and (A.6) into equations (A.4) and (A.5), and rewriting in state-space form, the following equations can be derived:

$$\frac{di_q}{dt} = \frac{1}{L_q} \left(v_q - R_s \cdot i_q - P \cdot \omega_r \cdot \left(\frac{3}{2} L_s \cdot i_d - B \right) \right) \tag{A.9}$$

$$\frac{di_d}{dt} = \frac{1}{L_d} \left(v_d - R_s \cdot i_d - P \cdot \omega_r \cdot \frac{3}{2} L_s \cdot i_q \right) \tag{A.10}$$

Finally, the original phase voltages (v_a, v_b, v_c) must be transformed into the two-phase voltages (v_d, v_q) using equation (A.3), which relies on the vehicle model by means of equation (A.1). In summary, five parameters and two state variables are identified for the motor model. The three-phase voltages are the inputs to the motor model and the motor torque is the output; the mechanical angle and angular velocity, which are state variables in the vehicle model, are treated as external parameters. Further details about the motor model and motor controller units used in this work can be found in [Vog07, Vog09]. In order to address the multidisciplinary nature of the whole system, it is desirable to obtain one model rather than separate mechanical and electrical models [McP05]. This multi-domain approach has been accomplished through the use of linear graph theory. A component template for the PMSM-type motor was developed [Sch04] and added to the existing vehicle model [Vog07]. Table A-II lists the specifications of the PMSM in-wheel motors used in this work.

Specification	Value	Unit
Peak Power	40	kW
Peak Torque	700	Nm
Maximum Speed	3200	rpm
Maximum Voltage	350	V
Maximum Current	311	A
Total Mass	30	kg
Rotor Mass	11.2	kg
Magnetic Flux (B)	0.5	V/rad/s
Phase Inductance (L_s)	4	mH
Phase Resistance (R_s)	0.5	Ω
Number of Pole Pairs (P)	12	–

Table A-II: PMSM in-wheel motor characteristics